CHEMICAL SENSING USING THE LIFE, DEATH, AND REBIRTH OF A PHOTON

by

Nicholas Lewis Peter Andrews

A thesis submitted to the Department of Chemistry

In conformity with the requirements for

the degree of Doctor of Philosophy

Queen's University

Kingston, Ontario, Canada

(January, 2017)

Abstract

In this thesis, optical sensing platforms using the "life, death and rebirth" of a photon are utilised to quantify and characterise chemicals in various samples. In this analogy, the "life" of a photon is characterised by its interactions with the propagation media, since they alter its speed and direction through the refractive index. The "death" of the photon can be observed by its absorption into an analyte, and after this process the "rebirth" of the photon can exist in the form of fluorescence. The instruments described here are based on fundamental optical techniques that were adapted for use with optical waveguides, thus allowing for compact inexpensive instrumentation that is able to characterise samples on-line and within small volumes. Characterising liquids in small volumes reduces both cost and waste, possibly increasing a company's potential profit.

This thesis presents a hollow core in-fibre photonic crystal fibre interferometer used to measure the refractive index and polarisability of gas in small volumes down to 1.2 μL. Similarly, a new amplified fibre loop cavity ring-down spectrometer is used to measure liquid alkynes through an overtone absorption band to a detection limit of 19% v/v in volumes of about 1 pL. Another instrument was built based on the well-known fluorescence excitation emission matrix (EEM) spectroscopy method. Fluorescence EEM is shown here to have great versatility in monitoring the kinetics involved in the degradation of complex fluorescent samples such as lubrication oil and liquid scintillators. When EEM spectroscopy is combined with multivariate analysis techniques, including parallel factor analysis, the full advantages of the technique are realised as all the fluorescent chemical components can be measured quantitatively. However, as it takes a long time to acquire a single EEM spectrum using commercial instruments, this method was not capable of conducting real-time on-line measurements. In this thesis we therefore developed a Hadamard-transform EEM spectrometer, which through simultaneous modulation of all excitation wavelengths, was able to acquire full EEM spectra in a fraction of the time. This instrument realises the potential of using EEM spectroscopy in real time — a first step towards the goal of a commercial on-line sensor.

Co-Authorship

Unless explicitly stated, all the work presented in this thesis has been conducted by the author for the degree of Doctor of Philosophy under the supervision of Dr. Hans-Peter Loock. The author had a significant contribution in the design and supervision of experiments, analysis of the data and preparation of published manuscripts. Permission of all co-authors and publishers has been obtained regarding all published material presented in this thesis.

Many of the optical sensing techniques discussed in this thesis have been published in the literature. The in-fibre hollow core photonic crystal fibre experiments, described in Chapter 3 were co-authored with Ms. Rachel Ross, Dr. Dorit Munzke, Mr. Camiel van Hoorn, Dr. Andrew Brzezinski, Dr. Jack Barnes, Dr. Oliver Reich, and Dr. Hans-Peter Loock and have been previously published in Optics Express, 2016.[1] The amplified fibre loop cavity ring down spectroscopy experiments described in Chapter 4 were co-authored by Dr. Jessica Litman, Mr. Daniel Stroh, Dr. Jack Barnes and Dr. Hans-Peter Loock and have been published in Optical Fiber Technology, 2013.[2]

The lubrication oil degradation studies described in Chapter 6 using fluorescence excitation emission matrix spectroscopy were co-authored by Mr. James Fan, Dr. Hanna Omrani, Dr. Alex Dudelzak, and Dr. Hans Peter Loock and published in Tribology International, 2016.[3] The scintillator degradation studies using the similar method described in Chapter 7 were co-authored by Mr. James Fan, Ms. Rebecka Forward, Dr. Mark Chen, and Dr. Hans-Peter Loock, and is published as the front cover article for the 100 year anniversary edition of the Canadian Society for Chemistry for Physical Chemistry Chemical Physics, 2017.[4]

The application of parallel factor analysis with absorption spectra on acetone water mixtures described in Chapter 8 were co-authored by Ms. Amy Maclean, Dr. John Saunders, Dr. Jack Barnes, Dr. Hans-Peter Loock, Mr. Mohammad Saad, Mr. Chenglai Jia, Mr. Kishor Ramaswamy, and Dr. Lawrence Chen and was

published in Optics Express, 2014.[5] The development of the Hadamard transform multiplex excitation emission matrix spectrometer presented in Chapter 9 was co-authored by Ms. Alana Rangaswamy, Mr. Travis Ferguson, Mr. Adam Bernicky, Mr. Niklas Henning, Dr. Alex Dudelzak, Dr. Oliver Reich, Dr. Jack Barnes, and Dr. Hans Peter Loock. A manuscript on this work has been submitted to Analytical Chemistry.[6] However, the same instrument is described in US and Canadian patent application No. 15/216,296 filed 21 July 2016 with the co-inventors as myself, Dr. Oliver Reich and Dr. Hans-Peter Loock.[7]

1. N. L. P. Andrews, R. Ross, D. Munzke, C. van Hoorn, A. Brzezinski, J. A. Barnes, O. Reich and H.-P. Loock, In-fiber Mach-Zehnder interferometer for gas refractive index measurements based on a hollow-core photonic crystal fiber. *Optics Express* **2016,** *24*, 14086.
2. N. L. P. Andrews, J. Litman, D. Stroh, J. A. Barnes and H.-P. Loock, Near-infrared absorption detection in picolitre liquid volumes using amplified fibre loop ring-down detection. *Optical Fiber Technology* **2013,** *19*, 822-827.
3. N. L. P. Andrews, J. Z. Fan, H. Omrani, A. Dudelzak and H.-P. Loock, Comparison of lubricant oil antioxidant analysis by fluorescence spectroscopy and linear sweep voltammetry. *Tribology International* **2016,** *94*, 279-287.
4. N. L. P. Andrews, J. Z. Fan, R. L. Forward, M. C. Chen and H.-P. Loock, Determination of the thermal, oxidative and photochemical degradation rates of scintillator liquid by fluorescence EEM spectroscopy. *Physical Chemistry Chemical Physics* **2017,** *19* (1), 73-81.
5. N. L. P. Andrews, A. G. MacLean, J. E. Saunders, J. A. Barnes, H. P. Loock, M. Saad, C. L. Jia, K. Ramaswamy and L. R. Chen, Quantification of different water species in acetone using a NIR-triple-wavelength fiber laser. *Optics Express* **2014,** *22* (16), 19337.
6. N. L. P. Andrews, T. G. Ferguson, A. M. Rangaswamy, A. R. Bernicky, N. Henning, O. Reich, A. Dudelzak and H.-P. Loock, Hadamard fluorescence excitation emission matrix spectrometer. *Analytical Chemistry* **Manuscript submitted for publication**.
7. H.-P. Loock, O. Reich and N. L. P. Andrews,*United States and Canada Provisional Pat.*, 15/216,296, 2016.

Acknowledgements

First and foremost, I'd like to thank my supervisor Dr. Hans-Peter Loock. Your enthusiasm and genuine interest in my work and abilities are truly inspiring. You have continuously challenged me and kept me stimulated and occupied with a multitude of projects. I am truly grateful for your thoughtful and insightful comments and for the amazing opportunities you have given me. You have actively promoted me to go on conferences and collaborative trips both at home and abroad to broaden my horizons and to shape my future career. I am also grateful for your support in welcoming me to Canada and ensuring that I have the best time here exploring and experiencing Canada's wilderness. Thank you Peter, your advice and mentorship over these last years have been invaluable.

I'd like to also acknowledge my supervisory committee Dr. Stephen Brown and Dr. Suning Wang for your ideas and insightful suggestions towards my projects. Your discussions have made me think critically of my work ensuring I work at the best of my ability. Furthermore, I am very grateful for equipment and the very charitable donations used in my projects. Additionally, I'd like to thank Dr. Igor Kozin for your intuitive comments regarding my work and your encouragement to use equipment in the undergraduate labs. This access to equipment has been instrumental to my work and understanding of my projects. Additionally, I'd like to thank both you and Tom Hunter for your support and guidance as a teaching assistant for second year labs.

I also want to acknowledge the incredible support from the staff in the Department of Chemistry. Your kindness and care towards me has been very welcoming during my time here at Queen's. I'd like to especially thank Annette Keyes and Michelle Boutilier for all their assistance as graduate coordinators in the department and all those who work in the office. Additionally, I'd like to thank Kim Mackinder and everyone who works at stores for their help in purchasing equipment invaluable for my research.

For all the present and past laser jocks and jockettes who have worked with me in the Loock lab, I'd like to thank you. You have all been amazing and I am truly grateful for your support as both peers and friends. Dr. Jack Barnes, you have been outstanding and I am truly indebted to you. Without your patience,

expertise and guidance over these years, my research would be severely lacking. I also want to thank James Fan and all the undergraduate and visiting students who have worked with me over the years. Your continued dedication towards my research has outshone my expectations and allowed me to produce truly great work.

I'd like to thank my wonderful amazing wife Yoon. Your love and support has been instrumental during my time here, giving me the drive to continue and complete my degree. I love you very much and am truly grateful for your support. I am also grateful for the support from my parents, Jane and Derek, and brother Chris who have supported me to come across the pond and pursue Doctor of Philosophy degree. I'd also like to thank my new family, 엄마, 아빠, and Hyukjin here in Canada for your continued and generous support. 감사합니다!

I'd like to further thank all the friends I have gained during my time here in Canada. You all have made it a very welcoming country to live in and I have had some of my best years here. John and Gillian, I want to especially thank you both for your sincere friendship from my very first day in Canada. You both made me feel very welcome and have supported and guided me throughout my degree. I also want to acknowledge those involved in the winery cellars of Linton. I had numerous adventures with you all and it's been a great number of years.

I'd like to also thank Dr. Dorit Munzke and all those at the University of Potsdam. I am truly grateful for your friendship and support during my trip to Germany and it made me feel really welcome. I'd also like to thank Dr. Alex Dudelzak for your support and useful critique towards my research. Furthermore, I'd like to thank Dr. Jess Ford and those who work at Weatherford International for their support and generous in-kind contribution of the Varian Cary Eclipse spectrometer. Finally, I'd like to thank the generous funding from the national science and engineering research council (NSERC), the Ontario graduate scholarship (OGS), the R.T. Mohan award, in addition to GasTOPS who made my research and time here possible.

Statement of Originality

I hereby certify that all of the work described within this thesis is the original work of the author. Any published (or unpublished) ideas and/or techniques from the work of others are fully acknowledged in accordance with the standard referencing practices.

Nicholas Lewis Peter Andrews

January, 2017

Table of Contents

List of Figures

List of Tables

List of Abbreviations

$0\nu\beta\beta$	neutrinoless double beta decay
bis-MSB	bis(2-methylstyryl)benzene
BHT	3,5-di-*t*-butyl-4-hydroxytoluene
BPF	Bandpass filter
CCD	Charged coupled device
CMOS	Complementary metal oxide semiconductor
CRDP	Cavity ring-down polarimetry
CRDS	Cavity ring-down spectroscopy
CRS	Conventional raster scan
DABCO	1,4-diazabicyclo[2.2.2]octane
DOM	Dissolved organic matter
DMA	Digital micromirror array
DMD	Digital micromirror device
ECL	External cavity laser
EDFA	Erbium doped fibre amplifier
EEM	Excitation emission matrix
EEMS	Excitation emission matrix spectroscopy
FBG	Fibre Bragg grating
FCRDS	Fibre cavity ring-down spectroscopy
FLCRDS	Fibre loop cavity ring-down spectroscopy
FoM	Figure of merit
FRET	Förster resonance energy transfer
FFT	Fast Fourier transform
FT	Fourier transform
FT-NIR	Fourier transform near-infrared
FWHM	Full width at half maximum
GUI	Graphical user interface
GC/MS	Gas chromatography mass spectrometry
HC-PCF	Hollow-core photonic crystal fibre
HPLC	High performance liquid chromatography
HT	Hadamard transform

HT-EEM	Hadamard transform excitation emission
ICLAS	Intracavity laser absorption spectroscopic
ICP-MS	Inductively-coupled-plasma mass-spectrometry
iHT	Inverse Hadamard transform
LAB	Linear alkylbenzene
LC/MS	Liquid chromatography mass spectrometry
LED	Light emitting diode
LIBS	Laser induced breakdown spectroscopy
LOD	Limit of detection
LS	Linear sweep
LSV	Linear sweep voltammetry
NIR	Near-infrared
NMR	Nuclear magnetic resonance
MC	Max and Chapados
MIR	Mid-infrared
MRI	Magnetic resonance imaging
OSA	Optical spectrum analyser
PAH	Polycyclic aromatic hydrocarbon
PAN	phenyl-α-naphthylamine
PARAFAC	Parallel factor
PBG	Photonic band gap
PC	Polarisation controller
PCA	Principle component analysis
PCF	Photonic crystal fibre
PPO	2,5-diphenyloxazole
PMT	Photomultiplier tube
RAM	Random access memory
RENO	Reactor experiment for neutrino oscillations
RUL	Remaining useful life
RULER	Remaining useful lifetime evaluation routine
RULET	Remaining useful lifetime evaluation technique
SMF	Single mode fibre
SNO	Sudbury Neutrino Observatory
SNR	Signal-to-noise ratio

TAN	Total acid number
TBN	Total base number
TBF	Tuneable bandpass filter
TDL	Tuneable diode laser
TIR	Total internal reflection
TTL	Transistor-transistor logic
UV	Ultraviolet
VOA	Variable optical attenuator
WDM	Wave division multiplexing
YDFL	Ytterbium doped fibre laser
ZDDP	Zinc dialkyldithiophosphate
XRF	X-ray fluorescence

Chapter 1

Introduction

Our society has become increasingly reliant on machinery for the production of goods, for transport, and for energy generation — such as in windfarms, hydroelectric power or solar plants. It is, therefore, important to monitor these machines and evaluate whether they are functioning properly. Additionally, it is increasingly important to monitor our environment through tracking the progress of climate change and detecting environmental contamination with pollutants. Using real-time and on-line detection of chemicals can help us characterise these problems better, which might allow for early intervention and thereby contribute to an eventual solution. Additionally, there is a requirement for these sensors to be compact, accurate and inexpensive.

Chemical sensing can be performed with a wide variety of analytical techniques. These include but are not limited to electrochemical, colorimetric, mass-spectrometric and optical methods. In this thesis, a multitude of chemical sensing optical techniques that use the life, death, and rebirth of a photon, are presented. Using this analogy of a photon, its "life" as it travels through various media at differing speeds can be tracked using refractive index. The "death" of the photon is then perceived as it is absorbed by an analyte, and the "rebirth" can be imagined through the process of fluorescence.

Optical instruments can frequently be made from inexpensive and compact components.[1, 2] A simple optical sensor can be constructed using e.g. a light source such as a light emitting diode (LED),[3] and a detector such as a charged coupled device (CCD),[4] which are both small and inexpensive. Given the ubiquity and low cost of imaging systems (driven by the exploding market in inexpensive digital cameras, e.g. for smartphones) and of light sources (driven to similar extent by requirements in lighting and illumination as

well as in telecommunication) the cost for many optical detection systems has been reduced to those of consumer electronics.

Using optical sensors, it is therefore possible to monitor a large system requiring many sensors such as a pipeline. This would not be possible using mass-spectrometric methods, which despite their superior detection limits are very expensive techniques.[5] Additionally, optical techniques can be combined with optical waveguides allowing them to be used for sample detection at inaccessible sites, over large distances, on several spots along an optical fibre, and can be used in strong electric and magnetic fields or in harsh environments.[1, 6]

Optical techniques monitor analytes through their interaction with light. This can be accomplished through absorption, emission, scattering, or refractive index measurements. These processes are discussed in more detail in Chapter 2. One of the major challenges with optical techniques is to tailor the light source and detector to the correct wavelengths required for absorption or fluorescence. This is not a problem for refractive index measurements, which are non-selective and thus can be used when sensing all molecules. However, the non-selectivity of refractive index measurements poses its own problems as *any* analyte will give a response, and the substrate used for detection requires modification to selectively bind the analyte of interest. With all optical techniques, it can be difficult to measure analytes in opaque systems. A method to overcome this challenge is described in Chapter 5 by using well-designed fibre probes when detecting the fluorescence in opaque solutions with zero sample preparation — in this case in machinery oils.[7-9]

Below a few examples are given where compact and inexpensive chemical sensors may have an enormous impact on the safety and quality of machinery use. These examples pertain to different aspects of the work presented in this thesis.

Machinery such as combustion engines, generators, pumps, cooling systems, tools, etc., require lubrication oil to function properly by reducing friction between the moving parts, removing debris and dissipating heat.[10] As the oil degrades, its properties change making the lubricant oil less efficient in lubricating the engine. This can lead to damage of the engine and fuel system parts resulting in high repair costs and potential disastrous consequences from engine failure. A prominent example of this includes the commercial Delta Air Lines flight 1288 on July 6th 1996, which resulted in two fatalities as the compressor hub penetrated the left aft fuselage after a catastrophic turbine engine failure.[11] More recently the British Airways flight 2276 on the 8th September 2015 caught fire during take-off from Las Vegas-McCarran International Airport prompting an aborted take-off and evacuation of all passengers and crew.[12] Furthermore, in 2008, 20% of the US Naval fleet of EA-6B Prowler jets were grounded due to problems related to the quality of the lubricating oil.[13] These cases only represent a handful of recent examples resulting in major financial cost and even loss of life. To prevent these occurrences, oil changes occur after a defined number of miles or operation time, which is typically set conservatively and frequently wastes good quality, usable oil. However, this strategy is not able to alert the user if the oil degrades faster than expected and so potential catastrophic engine failures may still occur. A real-time chemical sensor could continually report on the quality of the oil. This sensor should determine the oil's remaining useful life — as the engine operates —, and an alarm could be triggered alerting the user to carry out an oil change when a threshold signal is reached. The development of such a sensor could therefore, reduce waste of good oil, lessen cost due to down-time of the engine, prevent irreversible damage, and potentially save lives. The development of a lubricant quality sensor based on the fluorescent properties of antioxidant additives is described in this work.

Overall, optical sensors have the potential for use as on-line real-time chemical sensors for many different applications. Because of this, they are able to detect a problem as soon as it occurs and prevent costly and potential life threatening situations. In this thesis multiple optical techniques are presented and are used to

quantify complex chemical systems. Ongoing work on these techniques is leading to the development of smaller, faster instruments such as a new fluorescence excitation emission matrix (EEM) spectrometer, which should have potential as a commercial instrument for on-line real-time chemical detection.

1.1 Thesis outline

A comprehensive literature review is presented in Chapter 2 with the aim to give the reader an understanding of the techniques and concepts discussed in all the subsequent chapters presented in this thesis. These techniques include refractive index measurements as well as absorption and fluorescence spectroscopy.

In Chapter 3, an in-fibre interferometer using a hollow-core photonic crystal fibre as the sample cell is presented and its application is demonstrated through the measurement of the refractive index of nine gases. Using this in-fibre interferometer, the polarisabilities of nine gases are determined from an observed phase-shift in the near infrared spectrum and are attributed to the beating of two low lying core modes that propagate along the fibre.

In Chapter 4, an absorption spectrometer using a technique known as cavity ring-down spectroscopy is evaluated for the detection of liquids in volumes down to 1 pL through weak near infrared overtone vibrational transitions. The system presented is entirely designed using optical fibres and constructed using commercial off-the-shelf telecommunication equipment.

Chapter 5 describes the analytical method that is used to evaluate the fluorescence EEM spectra degradation studies presented in Chapter 6 and Chapter 7. Chapter 6, describes the degradation studies of lubrication oil and serves as a comparative analysis to the ASTM standard electrochemical method. Chapter 7, presents a thorough characterisation of the degradation of a liquid scintillator solution using both EEM and absorption

studies. Chapter 8, applies the similar analysis procedures presented in Chapter 6 and Chapter 7, but applies them to absorption spectra used to quantify multiple water solvation species mixed with acetone.

Chapter 9 introduces the fluorescence EEM spectroscopy instrument that was designed and built in our lab. This instrument uses Hadamard transforms to multiplex the excitation light and obtain EEM spectra in a fraction of the time when compared with the commercial instrument used in Chapter 6 and Chapter 7. In Chapter 10, the Hadamard transform EEM spectrometer is used to monitor the dissolution of tea as it brews in water. This is the first study where EEM spectra have been obtained on a system in real-time and this example serves to highlight the technique's potential for real-time on-line sample analysis.

The work in this thesis is concluded in Chapter 11, which also summarises the work presented therein. This chapter also proposes the future directions that the projects may take towards the goal of realising commercial on-line real-time chemical sensors.

1.2 Bibliography

1. X.-D. Wang and O. S. Wolfbeis, Fiber-optic chemical sensors and biosensors (2008–2012). *Analytical Chemistry* **2013,** *85*, 487-508.
2. X.-D. Wang and O. S. Wolfbeis, Fiber-optic chemical sensors and biosensors (2013–2015). *Analytical Chemistry* **2016,** *88*, 203-227.
3. http://www.cree.com/Xlamp, 2016.
4. S. Casado-Terrones, J. F. Fernández-Sánchez, A. Segura-Carretero and A. Fernández-Gutiérrez, Simple luminescence detectors using a light-emitting diode or a Xe lamp, optical fiber and charge-coupled device, or photomultiplier for determining proteins in capillary electrophoresis: A critical comparison. *Analytical Biochemistry* **2007,** *365*, 82-90.
5. C. A. Noble and K. A. Prather, Real-time single particle mass spectrometry: A historical review of a quarter century of the chemical analysis of aerosols. *Mass Spectrometry Reviews* **2000,** *19*, 248-274.
6. J. Villatoro and J. Zubia, New perspectives in photonic crystal fibre sensors. *Optics & Laser Technology* **2016,** *78, Part A*, 67-75.
7. N. L. P. Andrews, J. Z. Fan, H. Omrani, A. Dudelzak and H.-P. Loock, Comparison of lubricant oil antioxidant analysis by fluorescence spectroscopy and linear sweep voltammetry. *Tribology International* **2016,** *94*, 279-287.
8. R. E. Kauffman, Remaining useful life measurements of diesel engine oils, automotive engine oils, hydraulic fluids, and greases using cyclic voltammetric methods. *Lubrication engineering* **1995,** *51* (3), 223-229.

9. E. Bakker and M. Telting-Diaz, Electrochemical sensors. *Analytical Chemistry* **2002,** *74*, 2781-2800.
10. R. M. Mortier, M. F. Fox and S. T. Orszulik, *Chemistry and technology of lubricants*, Springer Netherlands, Dordrecht, 2010.
11. *NTSB identification: DCA96MA068*, National Transportation Safety Board Office of Public Affairs, 1998.
12. *NTSB issues update on the British Airways engine fire at Las Vegas*, National Transportation Safety Board Office of Public Affairs, 2015.
13. M. Vasconcelos, *Civil airworthiness certification: Former military high-performance aircraft*, Stickshaker Pubs, 2013.

Chapter 2

Literature Review

This chapter is composed of an overview of the theory and techniques used in the subsequent chapters of this thesis. The thesis includes a multitude of optical techniques used for chemical sensing, which all utilise optical fibre waveguides to direct the interacting light to and from the sample. The three main optical sensing platforms use refractive index, absorption, and fluorescence spectroscopy. Therefore, this chapter covers the theory of each technique along with a literature overview with the aim of allowing the reader to gain a fundamental understanding of the optical techniques involved.

2.1 Introduction

Chemical sensing can be performed with a wide variety analytical techniques. These include but are not limited to electrochemical, mass-spectrometric, and optical methods. Electrochemical techniques measure current, voltage, or conductivity to quantify and monitor analytes as they are oxidised or reduced.[1, 2] Although electrochemical methods are generally simple, highly selective and can comprise of low cost detection devices, they are plagued by long term instability, limited reproducibility and slow response of the detectors.[3] Additionally, due to the electrical contact, electrochemical techniques are not recommended for the detection of flammable or explosive analytes.

Mass-spectrometric techniques ionise chemical species and separate the ions based on their mobility or mass-to-charge ratio. These techniques, which include all conventional mass-spectrometric methods but also, for example, inductively-coupled-plasma mass-spectrometry (ICP-MS) are very sensitive in detecting trace elements and determining the structure of molecules through fragmentation.[4, 5] The ultra-low detection limits obtained using these instruments make them the standard reference in most analytical chemistry labs. Since these techniques generally involve bulky and expensive equipment with high vacuum systems they

are typically not used in the field [6] even though some mass spectrometers have been miniaturised and installed in planes, ships, and automobiles for atmospheric monitoring or in handheld devices at airports for the detection of explosive or drugs.[7-13] Additionally, as these techniques involve ionising the sample, they are destructive methods as the samples are consumed in the analytical process.

Optical techniques monitor analytes through their interaction with light. This can be through absorption, emission, scattering, or through refractive index measurements. These measurements involve the analyte's interaction with light, they are typically non-destructive techniques — unless the absorption of light causes the molecule to degrade.[14-16] Analytical optical techniques can also be modified to use optical waveguides, which include on-chip optical waveguides [17-19] and optical fibres.[20-23] Optical waveguides constrain the light within the waveguide via total internal reflection (TIR) making for an easier alignment without the need for complex free space optical components. Light can be coupled into fibre optic probes, which can be simply immersed into a sample for direct sample analysis.[22] Additionally, using waveguides allows for smaller and relatively inexpensive optical components making them more applicable for on-line field detection.[24, 25] However, as with all techniques there are some limitations. Absorption measurements require the desired analyte to have a noticeable extinction coefficient at the chosen detection wavelength. Our group has used cavity enhanced absorption methods to amplify the optical losses of a sample placed in an optical waveguide loop.[26-31] Techniques involved in measuring fluorescence are even more selective as the analyte must be a chemical species capable of emitting fluorescence, i.e. a fluorophore. Refractive index measurements on the other hand are non-selective and can be used for all molecules. However, this poses its own problems as any component will give a response and so refractive index techniques require modification of the substrate used for detection to selectively bind the analyte of interest.

Optical fibres are a very useful branch of optical waveguides that guide light using TIR along a glass fibre. The light that propagates along the fibre is trapped using TIR as the refractive index of the core is larger

than that of the cladding. When light is coupled into a fibre, this allows for easy manipulation of the light path without the need of aligning complex free-space optical components. Additionally, because optical fibres have low losses they are able to guide light over long distances, especially in the telecommunication region.[32] Optical fibres are also very applicable for analytical measurements. Spectroscopy using optical fibres can be conducted at sites unsuitable to conventional spectroscopy as fibres allow for optical spectroscopy at inaccessible sites, over large distances, on several spots along an optical fibre, in strong electric and magnetic fields and in harsh environments.[33, 34]

Photonic crystal fibres (PCFs) developed by Philip Russell and co-workers are a novel branch of optical fibres with a transverse periodic microstructure.[35, 36] PCFs can be classified into two types; solid and hollow core. Solid core PCFs guide light predominately through TIR as the index of the core is greater than the cladding, but further modes are confined by the photonic band gap (PBG). Hollow-core PCFs (HC-PCFs) with the index of the core being less than the cladding, $n_{\text{core}} < n_{\text{cladd}}$, are not able to guide light using TIR. HC-PCFs guide light entirely using the PBG, which confines the light to only propagate along the hollow core.[37] Being that the light propagates through the hollow core rather than within a solid glass structure makes them applicable for extremely low loss waveguides or for guiding very high-power light.[36] Additionally, as the light propagates in the hollow core, this makes HC-PCFs a perfect sample platform to be used for chemical sensing.

The optical sensing techniques described in subsequent chapters in this thesis utilise fibre optics. Measurements to monitor the refractive index uses a PCF as the sample medium, the cavity ring-down absorption measurements utilise a fibre loop made of single mode fibres and the fluorescence measurements use a bifurcated fibre optic probe that is simply immersed into the sample without any prior sample preparation. The subsequent sections of this chapter aim to discuss each optical sensing method in turn to give a literature background and overview of the techniques involved in the later chapters of this thesis.

2.2 Refractive index sensing

2.2.1 Introduction

There is a huge assortment of chemical sensing techniques that measure refractive index. One can imagine that the life of a photon occurs when it interacts and travels through various media. A measure of describing how the photon interacts with the media is to use the refractive index. Refractive index is a label-free universal parameter that can be used to detect every molecule at any wavelength.[34, 38-41] This is as opposed to absorption which can only be used at specific wavelengths for particular molecules and fluorescence which requires molecules to act as fluorophores. However, because refractive index is inherently non-selective, the sensing platform needs to be modified to selectively bind the analyte of interest.

The refractive index, *n*, is defined as the ratio of the velocity of light in a vacuum, c_0, to its velocity in a medium, *c*,[42]

$$n = \frac{c_0}{c}. \tag{2.1}$$

The refractive index is related to the relative permittivity, ε_r, also known as the dielectric constant of the medium,

$$n^2 = \varepsilon_r. \tag{2.2}$$

The relative permittivity is large if the substance is polar or highly polarisable. Therefore, if an analyte is highly polarisable, then it will have a larger refractive index. The relationship of relative permittivity and polarisability, α, is given with the Clausius-Mossotti equation assuming ε_r, is real and positive,

$$\frac{\varepsilon_r - 1}{\varepsilon_r + 2} = \frac{\rho N_A \alpha}{3M\varepsilon_0}, \tag{2.3}$$

where ρ is the mass density of the sample, N_A is Avogadro's number, *M* is the molar mass, and ε_0 is the permittivity of free space. The Clausius-Mossotti equation is used when there is no contribution from

permanent electric dipole moments to the polarisation, which is a valid assumption when visible or near-infrared (NIR) light is applied as the frequency is so high that the molecules cannot orient quickly enough to align in the direction of the field.[42] Additionally, the value for ε_r is assumed to be real with no imaginary component such as absorption occurring. Substituting equation (2.2) into (2.3) gives the Lorentz-Lorenz equation that relates refractive index and the polarisability,

$$\frac{n^2-1}{n^2+2}=\frac{\rho N_A \alpha}{3M\varepsilon_0}. \tag{2.4}$$

Therefore, through measurement of the refractive index at frequencies typical to visible and NIR light, one can acquire the polarisability. When light passes through a medium, some fraction will be attenuated through absorption. This can be described using the complex description of the refractive index,

$$\tilde{n}=n+ik. \tag{2.5}$$

The real part, *n*, is the phase refractive index and is related to the phase velocity of the photon, which is the speed at which the phase of the wave propagates through space. The imaginary part is related to absorption, where *k* is the extinction coefficient. The refractive index can further be described using the group index, n_g, which is defined as the ratio of the speed of light in a vacuum, c_0, to its group velocity in a medium, c_g,

$$n_g=\frac{c_0}{c_g}. \tag{2.6}$$

The phase index is related to the group index, n_g, with the following relationship,

$$n_g=n-\lambda_0\frac{\mathrm{d}n}{\mathrm{d}\lambda_0}, \tag{2.7}$$

where λ_0 is the wavelength and $\mathrm{d}n/\mathrm{d}\lambda_0$ is the dispersion term, being that the refractive index is wavelength dependant.[43]

Refractive index can be measured using Snell's law and the angle of refraction or by measuring the critical angle from total internal reflection of a prism.[44-48] Additionally, the refractive index can be determined from on-chip optical waveguides [17-19] and by using interferometric optical fibre systems.[20-23]

2.2.2 Interferometry

2.2.2.1 Theory

Interferometry is a family of techniques in which waves are superimposed, creating destructive and constructive interference. The measured interferogram in the time domain, $f(t)$, can then be converted to the frequency domain, $F(\omega)$, using a Fourier transform (FT),[49-51]

$$F(\omega) = \frac{1}{\sqrt{2\pi}} \int_{-\infty}^{\infty} f(t) \mathrm{e}^{-i\omega t}\, dt\,. \qquad \textbf{(2.8)}$$

If two waves recombine, interference occurs when the two fields are coherently combined and give rise to a wavelength-dependent interferogram of intensity, *I*, [52-54]

$$I = I_1 + I_2 + 2\sqrt{I_1 I_2}\cos(\phi_1 - \phi_2)\,, \qquad \textbf{(2.9)}$$

where I_1 and I_2 are the respective intensities and ϕ_1 and ϕ_2 are the phases of the two waves. A common configuration of an interferometer is the Michelson interferometer as shown in **Figure 2.1(a)**.[42, 43, 55-57] A Michelson interferometer uses a beam splitter to split light into two arms. In each arm, light is reflected back towards the beam splitter and the combined signal is detected. One mirror is then translated, which changes the relative phase between both waves producing an interferogram. Michelson interferometers are widely used in commercial FT infrared spectrometers [58, 59] and have been used to determine the refractive index of substances such as air, glass and DMSO in water.[43, 57, 60]

A second typical interferometer configuration is the Sagnac interferometer as shown in **Figure 2.1(b)**.[61-65] In the Sagnac interferometer, light is split into two paths using a beam splitter as with the Michelson configuration. The two beams are made to follow the same path but in opposite directions. When the two

beams return at the entry of the ring, they recombine as they exit the ring producing the interference. Sagnac interferometers have been widely used as laser gyroscopes as the clockwise and anticlockwise paths will undergo a difference in effective round-trip optical pathlength if the interferometer itself rotates.[63]

A third typical interferometer configuration is the Mach-Zehnder interferometer as shown in **Figure 2.1(c)**.[17, 20, 23, 52, 66, 67] Here, light is separated into two beams using a beam splitter, as with both the Michelson and Sagnac interferometers. Both beams of light are guided along a different path and subsequently recombine at the second beam splitter producing interference in the recombined light. If there is a sample in one arm of the interferometer the light will undergo a phase shift and this can be measured to determine the refractive index and polarisability of the sample.

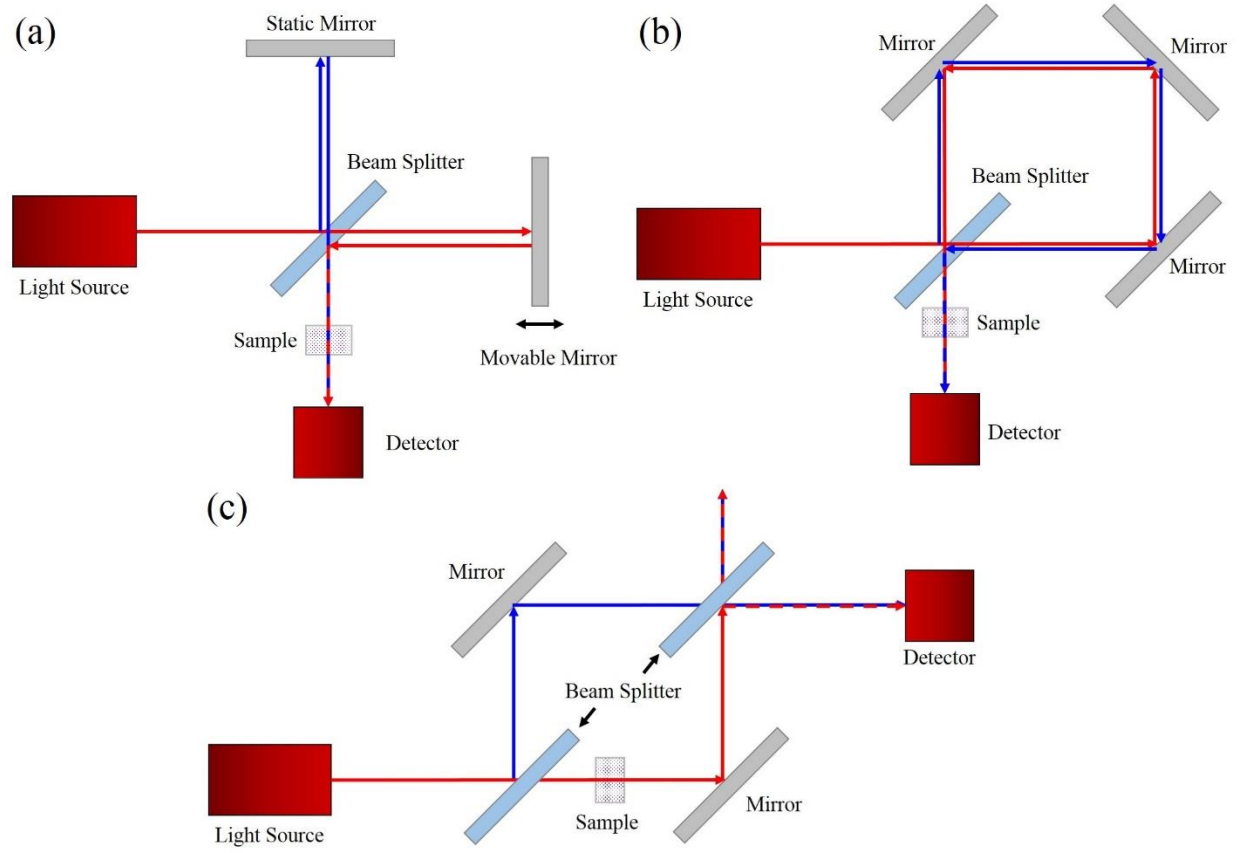

Figure 2.1: Typical schematics for interferometers. **(a)**, **(b)**, and **(c)** represent a Michelson, Sagnac, and Mach-Zehnder interferometer respectively. The red and blue arrows represent the two paths that the interfering beams of light travel.

2.2.2.2 Fibre interferometry

Interferometers can also be built up using waveguides such as optical fibres and therefore, apply interferometry to fibre optic probes. This allows detection of analytes in locations that are difficult to access. Example schematics for these fibre based systems, which are analogous to the free space instruments in **Figure 2.1**, are given in **Figure 2.2**.[68-70]

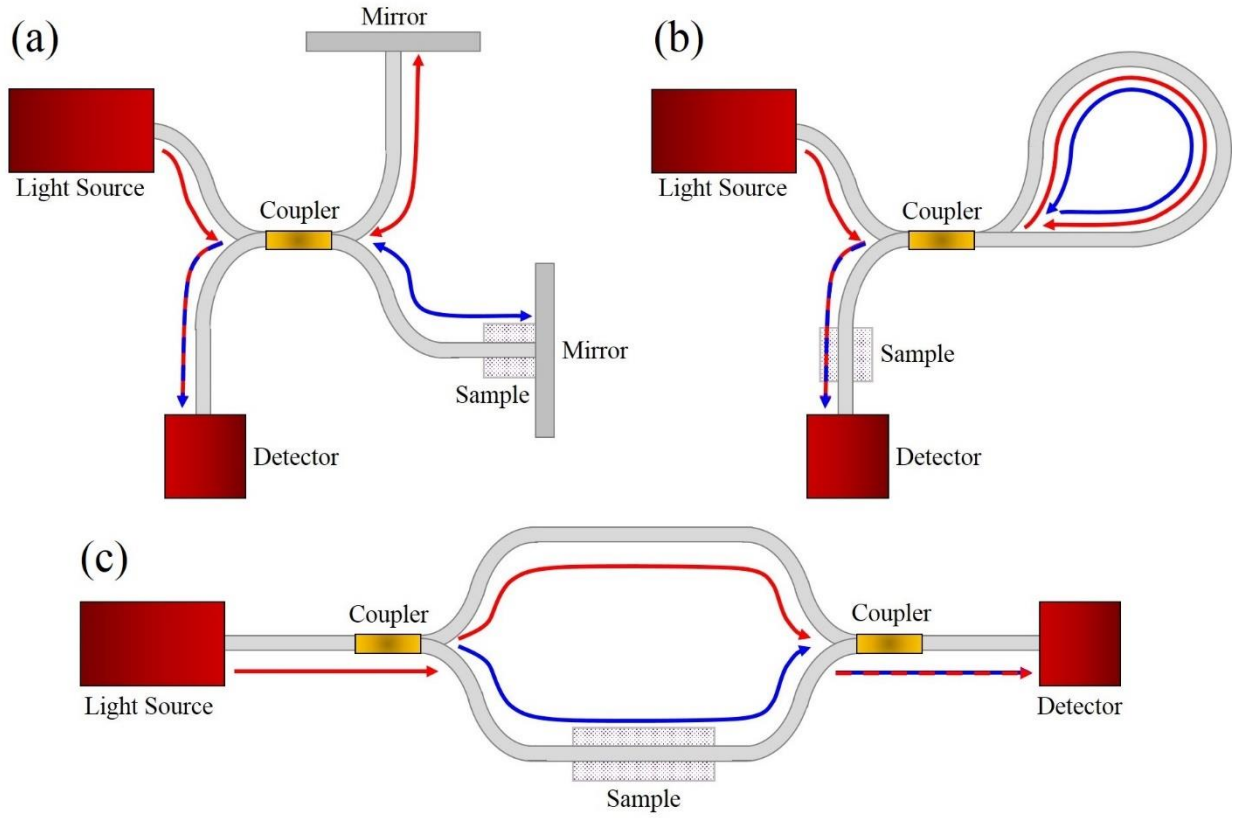

Figure 2.2: Typical schematics for fibre interferometers that are analogous to those in **Figure 2.1**. **(a)**, **(b)**, and **(c)** represent a fibre Michelson, Sagnac, and Mach-Zehnder interferometer respectively. The red and blue arrows represent the two paths that the interfering beams of light travel.

In addition to using two separate fibre optic arms, many interferometers used for chemical sensing are based on either the Michelson or Mach-Zehnder configuration where one of the interferometer arms is the core of the fibre waveguide and the other arm consists of the cladding material, which propagates one or more cladding modes.[20, 52, 57, 71] In all in-fibre interferometers the incoming core mode is split into two (groups

of) modes using a taper or long period fibre gratings (See **Figure 2.3**).[72, 73] These tapers can be drawn down to a diameter of 15 μm from a fibre of diameter 125 μm through heating and slowly drawing out the fibre.[73] In the Michelson configuration, a mirror or retroreflector is used to reflect the light so the modes recombine back at the coupler (**Figure 2.3(a)**).[57] For the Mach-Zehnder configuration a second taper combines these two co-propagating modes (**Figure 2.3(b)**).[20] In both cases, the accumulated phase shift in each arm depends on the length of the arm and the effective refractive index of the propagated mode(s). In-fibre interferometers are inherently "balanced interferometers", i.e. the geometrical lengths (but not necessarily the optical paths) of the two arms are identical, $L_1 = L_2$, and the two arms expand and contract identically with temperature and strain.[74]

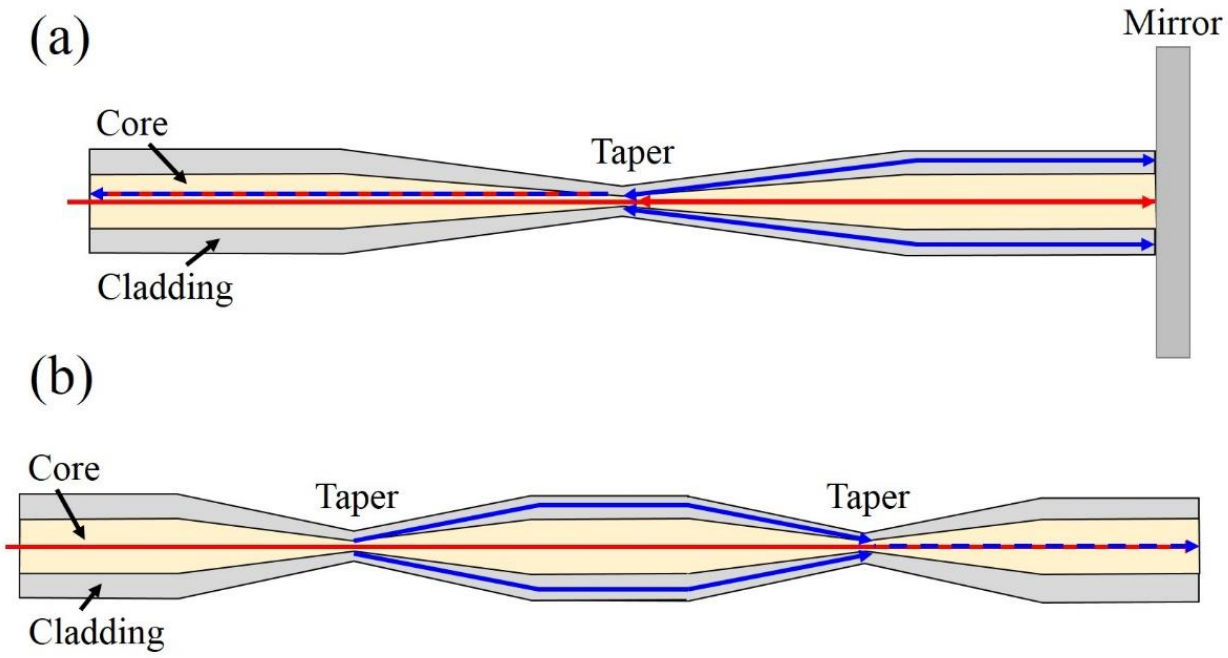

Figure 2.3: In-fibre interferometers using a taper to couple light between the core and cladding. **(a)** represents the Michelson and **(b)** the Mach-Zehnder configuration.

In addition to single mode fibres (SMFs), photonic crystal fibres PCFs have been used to construct in-fibre Mach-Zehnder interferometers (See **Figure 2.4**).[22, 52, 75, 76] As with many SMF in-fibre interferometers, PCF

interferometry, has been applied to measure strain, temperature, and pressure.[64, 65, 77] Conversely, the holey structure of PCFs add further sensing applications as they can be infiltrated with liquids, gases or nanomaterials.[33, 78-82] The holes in a typical HC-PCF have diameters in the order of only a few microns, which reduces the sample volume to microlitre levels and thus significantly reduces the amount of liquid or gas required for sensing. In addition, as the PCFs holes are transverse along the entire fibre length, the light-matter interaction length is strong leading to high detection sensitivities.

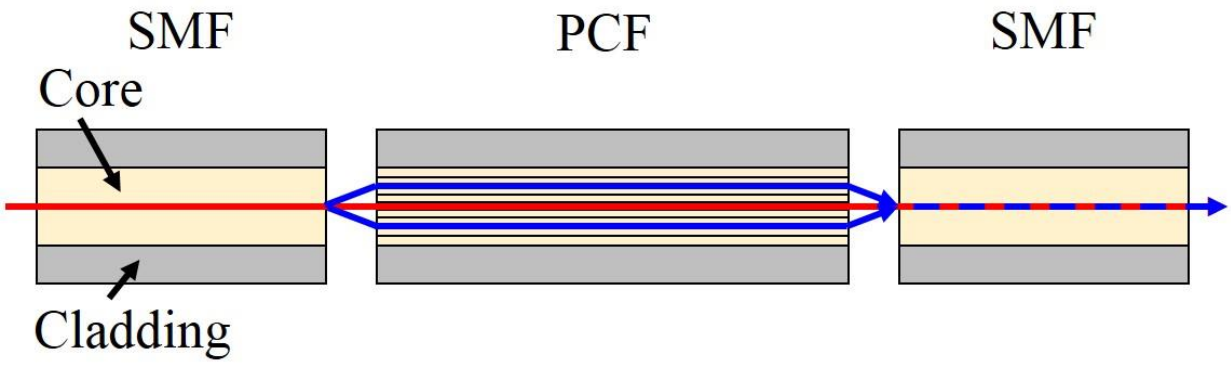

Figure 2.4: An in-fibre PCF interferometer. There is a small air gap to ensure coupling of light into other modes guided along the PCF. These are recombined at the second SMF producing interference.

An instrument based on the configuration sketched in **Figure 2.4**. will be described in detail in Chapter 3.

2.3 Absorption

2.3.1 Introduction

Absorption spectroscopy is a very simple and widely used optical technique for sensing and quantifying chemical species. One could associate the refractive index with the speed of a photon as it travels through different media during its "life", and by this analogy the process of absorption can be thought of the "death of a photon". Conventional spectrometers used to be bulky with expensive components and scanning monochromators, but recently, compact fibre-coupled monolithic spectrometers that are based on diode array detectors have emerged.[83, 84] In addition, the telecommunications industry has made vast

advancements with the development of waveguides and optical components in the NIR region.[85] Spectrometers that feature these advanced optical components can be designed relatively inexpensive and compact. The NIR region of the spectrum shows mostly weakly absorbing features (overtone and combination bands) of almost all compounds, which makes this spectral window ideal for telecommunications, since light signals are only weakly attenuated.[42] For the same reason NIR spectroscopy is challenging for spectroscopic applications — while most compounds show absorption features, so do almost all solvent or solid matrices. To detect the very weak bands, sensitive absorption techniques must be utilised such as cavity ring-down spectroscopy (CRDS).

Absorption spectroscopy is a very simple technique used to quantify the amount of a particular chemical species in a sample. Most chemical compounds can absorb light and thus absorption spectroscopy is applicable to most if not all chemical species.[42] When light passes through a sample of length *l* some photons are absorbed and the resultant intensity is decreased as a result. The transmission, *T*, of the light relates to the absorption, *A*, via the Beer-Lambert law,

$$A = -\log(T) = \varepsilon c l \,, \qquad \textbf{(2.10)}$$

where ε is the molar extinction coefficient and *c* is the concentration of the analyte. From the Beer-Lambert law, absorption is directly proportional to the concentration and molar extinction coefficient of an analyte. If the sample absorbs weakly or is low in concentration, as is the case for some gases, the optical pathlength must be increased for a detectable reading to be obtained. One practical way of increasing the optical pathlength is through use of a multi-pass device, where light is passed through the same sample cell multiple times. Many multi-pass cells have been developed to increase the optical pathlength whilst minimising the footprint of the device; examples include the White and Herriot cells.[86, 87] A very sensitive technique known as CRDS, places a sample of interest within an optical cavity so that light passes through the sample many times. The decay rate of the light leaving the cavity is then measured and related to the concentration of the analyte.[88]

2.3.2 Cavity ring-down spectroscopy

CRDS is a highly sensitive absorption technique developed by O'Keefe and Deacon in 1988.[88] In CRDS, light is coupled into a high finesse optical cavity made up of two highly reflective mirrors as shown in **Figure 2.5**.

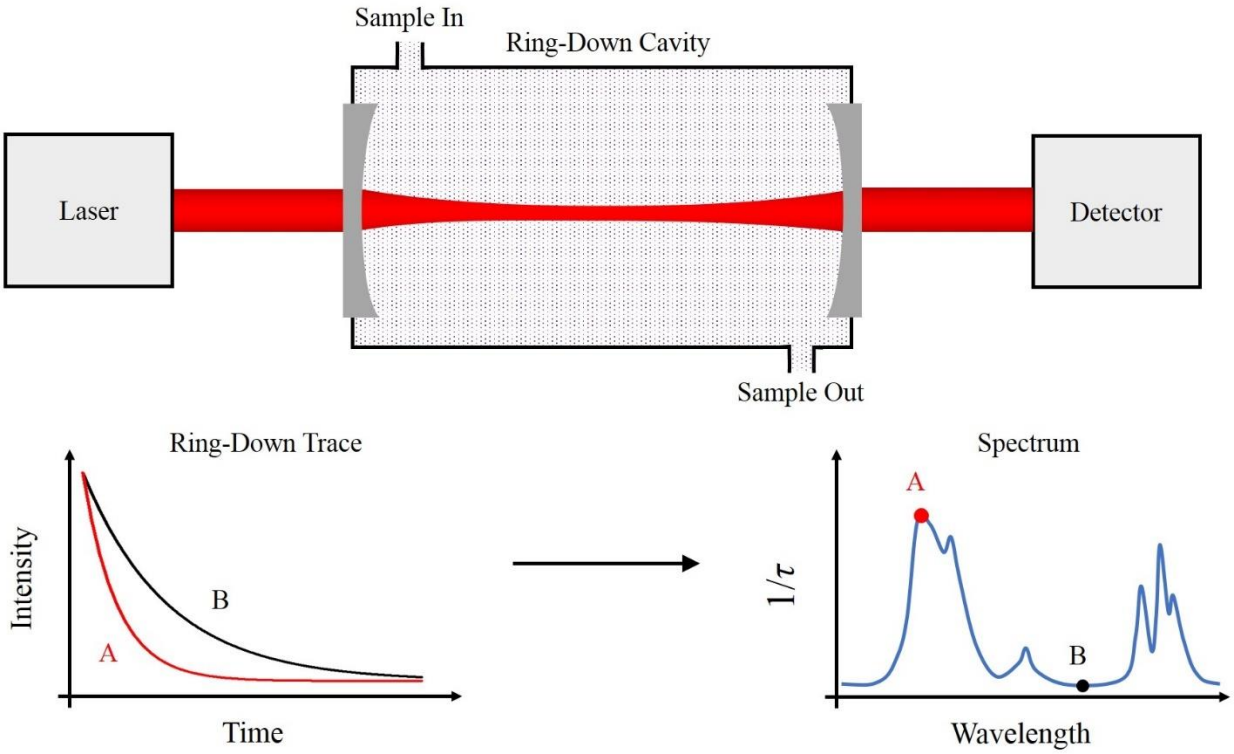

Figure 2.5: Typical schematic of a CRDS setup. A pulse from the tuneable laser is coupled into the high finesse optical cavity. The light that leaks out of the cavity is detected. When the sample within the cavity absorbs light as is the case for A, the optical losses are greater and the light rings-down faster. When the sample doesn't absorb as is the case for B, longer ring-down times are achieved. This is done over a range of wavelengths to produce the spectrum.This figure is based on a similar figure in the paper by Zalicki et al.[89]

The fraction of light that is trapped within the cavity is reflected back and forth between the two mirrors. At each reflection, a small portion of light leaks out of the cavity and is detected.[90] The lifetime of the photon as it is trapped within the cavity is defined by the ring-down time, τ ,

$$\tau = -\frac{t_{\mathrm{rt}}}{\ln\left(T_{\mathrm{sys}}\right)}, \tag{2.11}$$

where T_{sys} and t_{rt} are the transmittance of light and roundtrip time of the cavity prior to the sample introduction, respectively. t_{rt} is related to the cavity length, l, and speed of light, c_0,

$$t_{\mathrm{rt}} = \frac{2l}{c_0}, \tag{2.12}$$

τ is therefore only dependent on the losses of intensity within the optical cavity. Thus, it is immune to error from intensity fluctuations of the light source, which is a major advantage over other multi-pass absorption techniques. Placing an absorbing sample within the cavity creates additional losses that correlate with the Beer-Lambert term, εcl,

$$\tau = -\frac{t_{\mathrm{rt}}}{\ln\left(T_{\mathrm{sys}}\right) - \varepsilon cl}. \tag{2.13}$$

By monitoring the change in decay rates of the cavity, one can obtain the concentration of the chemical compound of interest,[89] as long as the temporal pulse width is less than the roundtrip time of the cavity to avoid interference effects. This requires fast lasers or other fast light sources as well as similarly fast detection and data acquisition systems.

CRDS is not limited to measurements in the time-domain and can also be carried out in the frequency domain. In this case the incident light to the cavity can be modulated as a sinusoidal or square wave and the phase-shift resulting from the standing wave cavity resonance is monitored. Phase-shift measurements were initially demonstrated in 1980 by Herbelin et al.[91] and the method was later applied to absorption measurements by Engeln et al. in 1996.[92] The phase-shift, ϕ, and modulation frequency, ω, are related to the ring-down time as follows,[26]

$$\tan\left(\phi\right) = -\omega\tau. \tag{2.14}$$

By knowing the source modulation frequency and detecting a change in the phase-shift, both the ring-down time and hence the sample concentration can be obtained. Phase-shift CRDS is capable of monitoring very rapid ring-down times through sinusoidal modulation on the order of tens of MHz. In addition, it can be easily implemented for a variety of cheap continuous wave light sources and lasers. However, unlike time-domain CRDS, phase-shift CRDS cannot distinguish multi-exponential decays caused from additional modes within a cavity from a single measurement.[26] If the signal decays as a multi-exponential, phase-shift CRDS can be carried out however, through multiple measurements at a range of frequencies.[26]

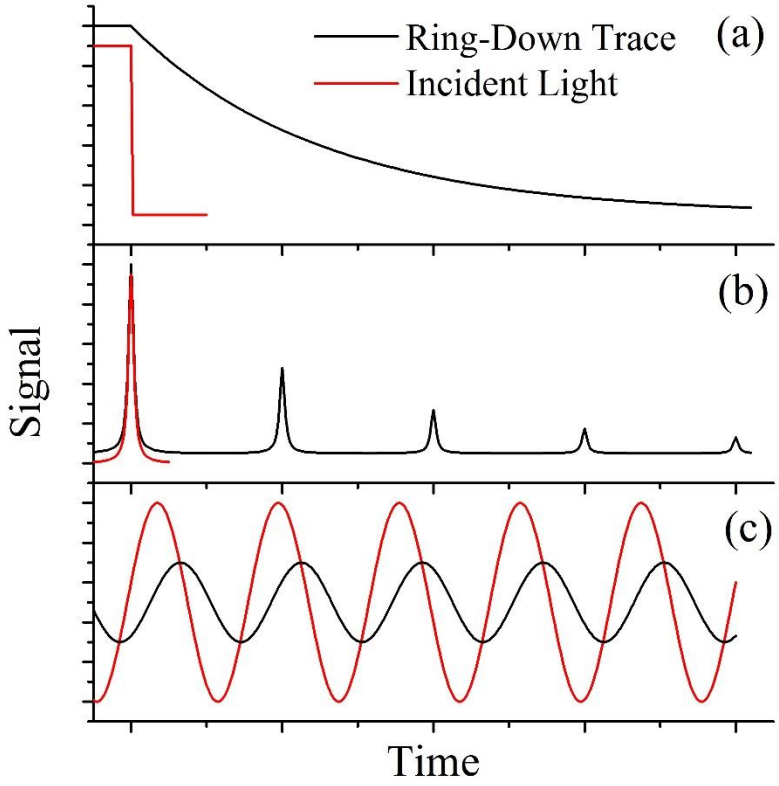

Figure 2.6: Ring-down traces of differing CRDS techniques where the incident light is shown as red and the ring-down trace is black**. (a)** Time-resolved continuous wave CRDS where the incident light entering the cavity is rapidly switched off and the intensity decay in the cavity is measured. **(b)** Pulsed CRDS where the pulse length is much shorter than the roundtrip time. An exponential decay function is fit to the amplitudes of the peaks giving the ring-down time. **(c)** Phase-shift CRDS with the incident light modulated

with a sinusoidal pattern. The resultant, measured waveform has an alternate phase due to the losses in the cavity. This figure is based on a similar figure in the paper by Waechter et al.[90]

Since its conception in 1988, CRDS and related cavity enhanced techniques have gained a large following. This is due to their inherent ability to detect trace gases [93-95] and aerosols.[96, 97] Using CRDS with a 1 metre cavity, the effective optical pathlength of several kilometres can be achieved. Measurements on liquids, however, prove to be more difficult due to additional scattering losses at the sample container interfaces. Despite this difficulty, impressive detection limits have been obtained on liquid samples by using Brewster orientations of the cell [98-101] or by filling the entire cavity with the sample to minimise scatter.[102]

2.3.3 Fibre cavity ring-down spectroscopy

An alternative approach to conventional mirror-based CRDS is to construct the optical cavity using optical waveguides.[103] Fibre CRDS (FCRDS) cavities are readily aligned and are relatively compact compared to their free space counterparts. FCRDS is also capable of analysing samples on the pL/nL scale,[28, 29, 104] as opposed to the several μLs.[102, 105]

FCRDS is generally done in one of two ways: using either a linear cavity or a ring cavity. In a linear fibre cavity the light is guided through an optical waveguide where the cavity is comprised of two fibre Bragg gratings (FBGs) [103] or two gold coated fibre ends [106] rather than highly reflective mirrors. FBGs are wavelength specific dielectric mirrors that reflect a narrow wavelength range corresponding to the period grating. Alternatively, a ring cavity can be easily made by connecting the two ends of the fibre to form a loop as shown in **Figure 2.7**.[28, 29, 107]

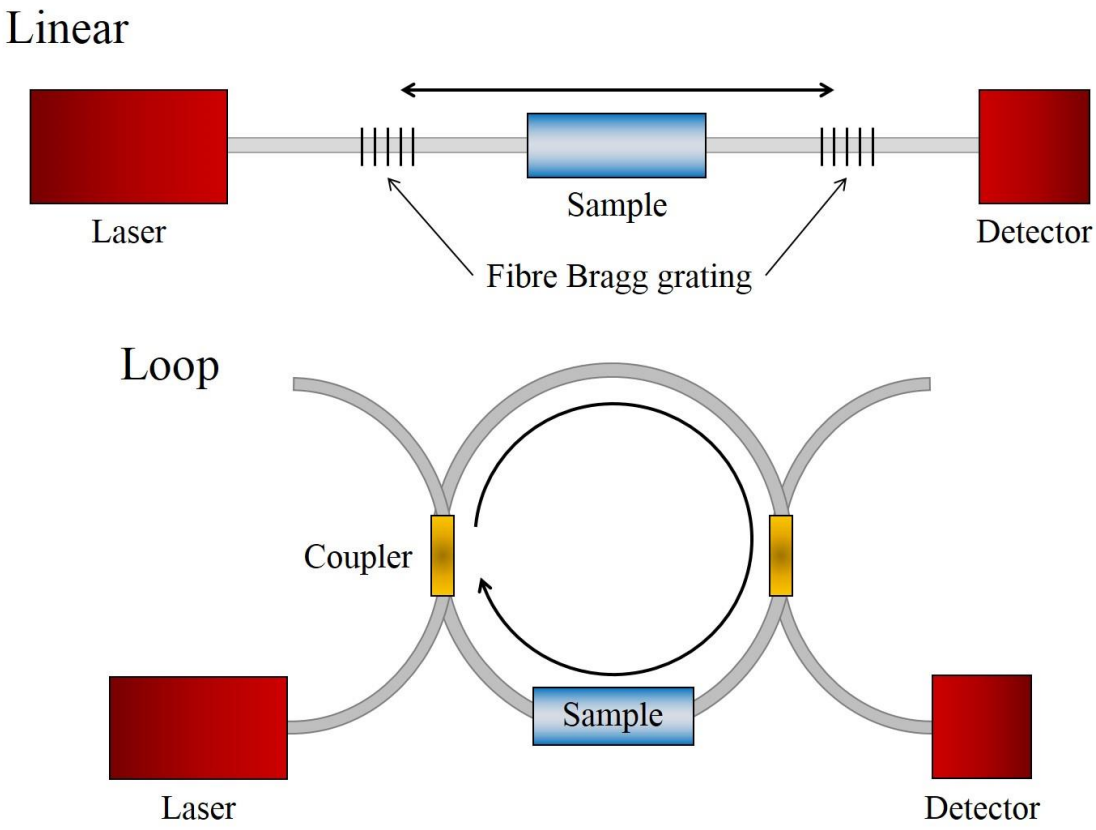

Figure 2.7: Schematic of both a linear and loop FCRDS setup. In the linear version, two fibre Bragg gratings are used to form an optical cavity where as in the loop version, the cavity is made when the light circulates around the loop.

Coupling light into a fibre loop has been carried out in a variety of ways, including commercial fibre-fibre couplers (see **Figure 2.7**),[108] small notches in the fibre cladding [109] or a by shining a light source into a bend in the fibre.[28] Loop cavities are advantageous as the loop may be tens of metres long allowing lasers with longer pulse widths to be used. The round trip time of fibre loop CRDS (FLCRDS) is shown below:

$$t_{\mathrm{RT}} = \frac{nL}{c_0}, \qquad \textbf{(2.15)}$$

where n is the refractive index of the waveguide and L is the circumference of the loop. Whereas high reflectivity mirrors and FBGs usually have a very narrow bandwidth over which they reflect light, loop

cavities are inherently broadband as they are only limited by the optical transmission of the fibre loop and the components within it. This is advantageous if multiple analytes have to be detected simultaneously.

In FCRDS and FLCRDS, there are two common methods of introducing the sample of interest into the cavity (See **Figure 2.8**). One can either cleave the fibre, placing the sample between the two fibre ends, or one can utilise the evanescent wave of the core mode to probe an external sample. The evanescent wave can be easily probed by etching away the cladding [103, 110] or by tapering down the fibre.[107, 111]

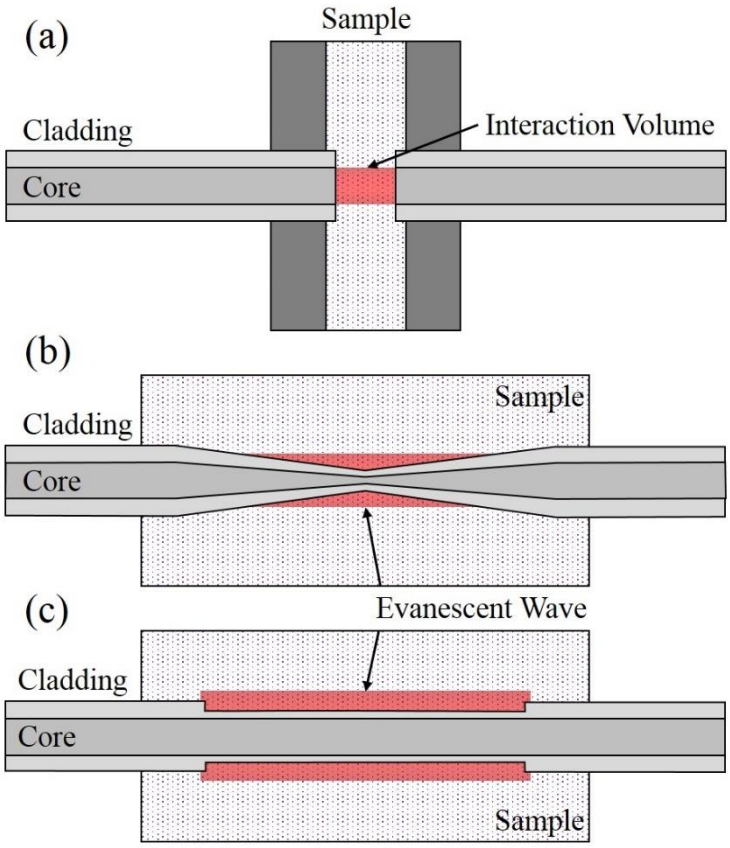

Figure 2.8: Absorption sensor elements typically used in FCRDS. **(a)** The fibre is cleaved and the sample is placed between the fibre ends. Direct absorption of the propagated light. **(b)** A tapered fibre where the evanescent field extends into the sample volume. **(c)** A fibre where the cladding is removed through etching so that the evanescent wave probes the sample.

2.3.4 Amplified fibre cavity ring-down spectroscopy

Despite the advantages of FLCRDS over other linear CRDS methods, it is plagued with comparatively high round-trip losses. This is due to optical losses by the implementation of splices, couplers, sample interfaces and loss within the fibre cavity itself. These high losses cause light to rapidly leak out of the cavity, producing very short ring-down times, which are detrimental for optical sensing. Stewart *et al.* proposed that these losses can be compensated by introducing a gain element, G, such as an erbium doped fibre amplifier (EDFA) into the loop as shown in **Figure 2.9**.[112, 113] The wavelength used for sample detection was selected using a band pass filter (BPF).

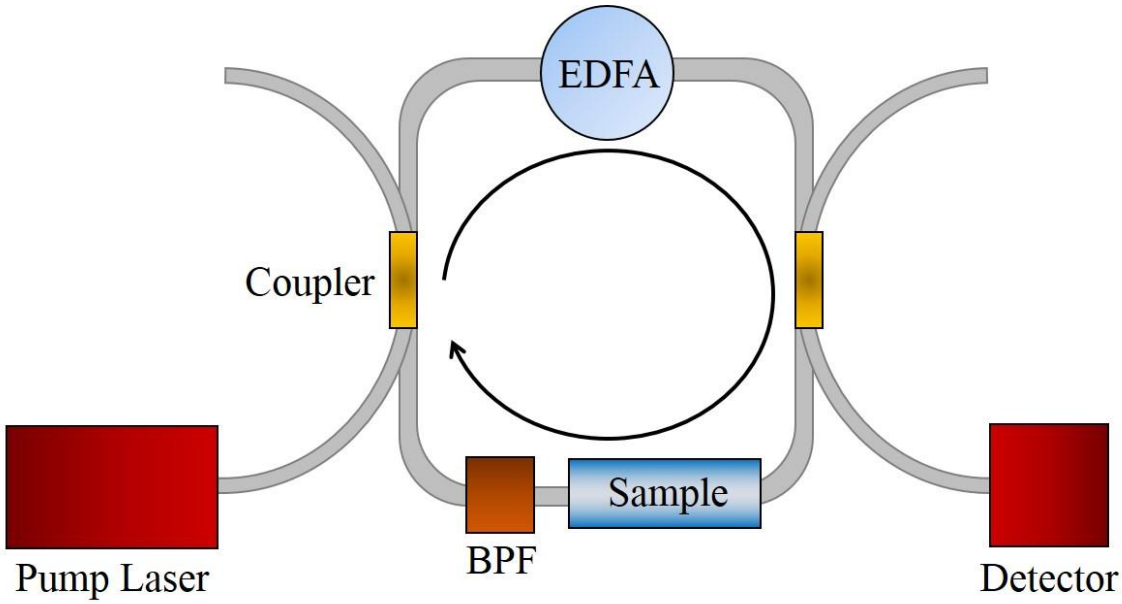

Figure 2.9: Schematic of the amplified fibre CRDS setup carried out by Stewart et al.[113] The EDFA is used as the gain element and light from the laser is coupled into the loop and the wavelength for absorption is selected using the BPF. The sample is placed in the gas cell and the ring-down time is detected at the output.

The ring-down time from equation (2.13) then becomes,

$$\tau = -\frac{t_{\mathrm{RT}}}{\ln\left(T_{\mathrm{sys}}\right) + \ln\left(T_{\mathrm{sample}}\right) + \ln\left(G\right)}. \qquad \textbf{(2.16)}$$

In the ideal case the gain exactly matches the losses of the system: $T_{sys} \times G = 1$. This will simplify the expression to,

$$\tau = -\frac{t_{RT}}{\ln\left(T_{sample}\right)}. \quad \textbf{(2.17)}$$

Thus, in this special case, the ring-down time is only dependent on the losses from the sample. This generates much larger ring-down times enhancing the system's sensitivity and detection limit. Furthermore, Zhang et al. discovered that the sensitivity is at its highest when the laser is working near its lasing threshold as the gain matches the losses of the system.[114] However, the sensitivity varies significantly around the threshold region, which is problematic experimentally as very stable laser sources are required. Alternatively, a two-loop system can be used, as proposed by Stewart et al. and is shown in **Figure 2.10**.[113] The inner loop with the gain element is set above threshold and the outer loop contains the sample. Into each loop separate BPFs are inserted that select different wavelengths to be within a few nanometres from each other. This "clamps" the gain to the required threshold, stabilising the system.

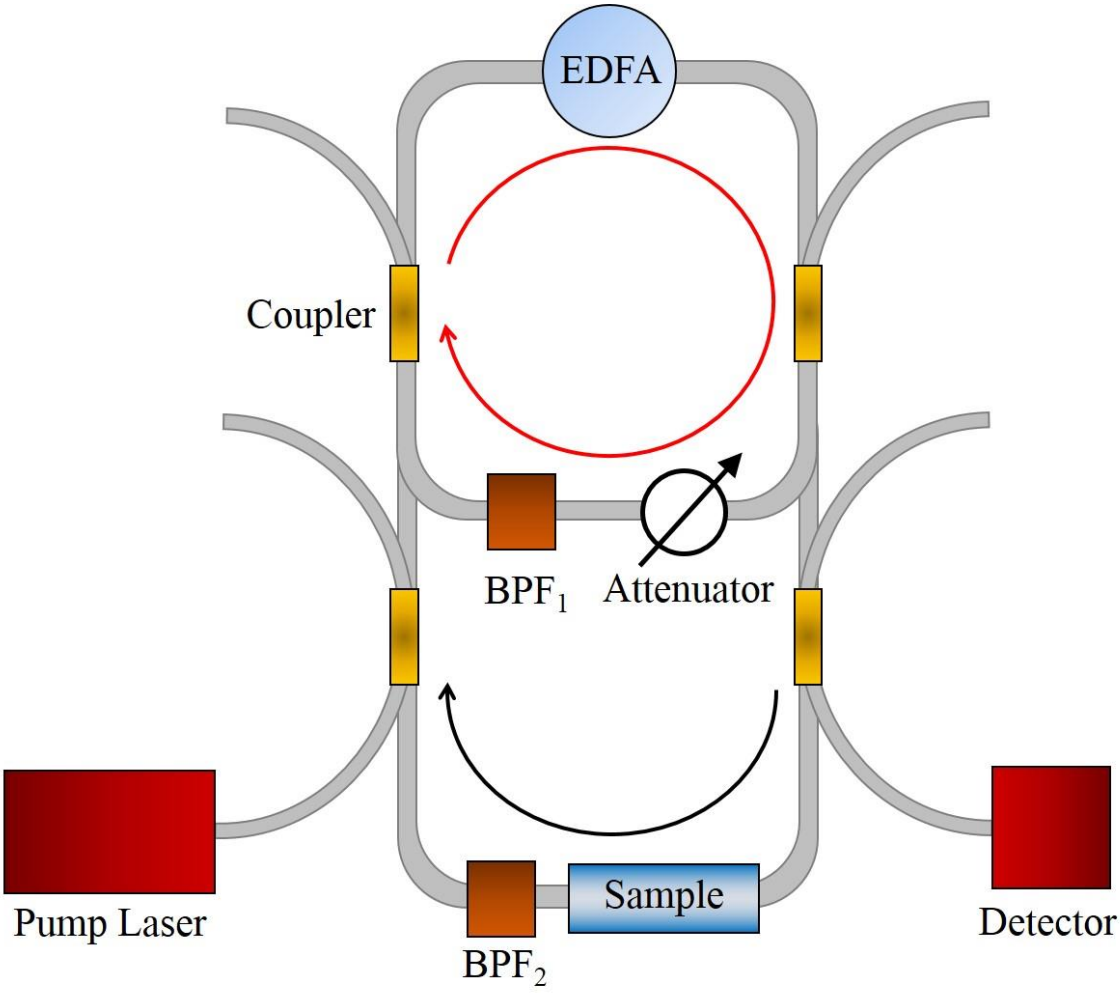

Figure 2.10: Schematic of a two loop amplified fibre CRDS setup proposed by Stewart *et al.* to account for gain stabilisation.[113] The setup is similar to the one loop (**Figure 2.9**) but with the addition of an attenuator and a BPF located within the inner loop to select the lasing wavelength that circulates. The inner loop shown with the red circular arrow is used to continuously lase at a wavelength selected by BPF_1. The wavelength used in the outer loop used for sample detection is chosen by BPF_2.

An example of the instrument sketched in **Figure 2.10** will be discussed and fully characterised in Chapter 4.

2.4 Fluorescence

2.4.1 Introduction

If absorption is understood to be the death of a photon, "the rebirth of a photon" can be through fluorescence as a new photon is emitted. As with absorption, fluorescence can be used to optically detect chemical samples. When a photon is absorbed by a fluorescent analyte, an electron is excited to a higher energy state. This excited electron can subsequently relax to a lower energy state via various non-radiative and radiative pathways, as observed in **Figure 2.11**. When relaxation occurs with overall spin conservation, a photon is emitted through fluorescence. This results in an emission that is longer in wavelength than the initial excitation wavelength.

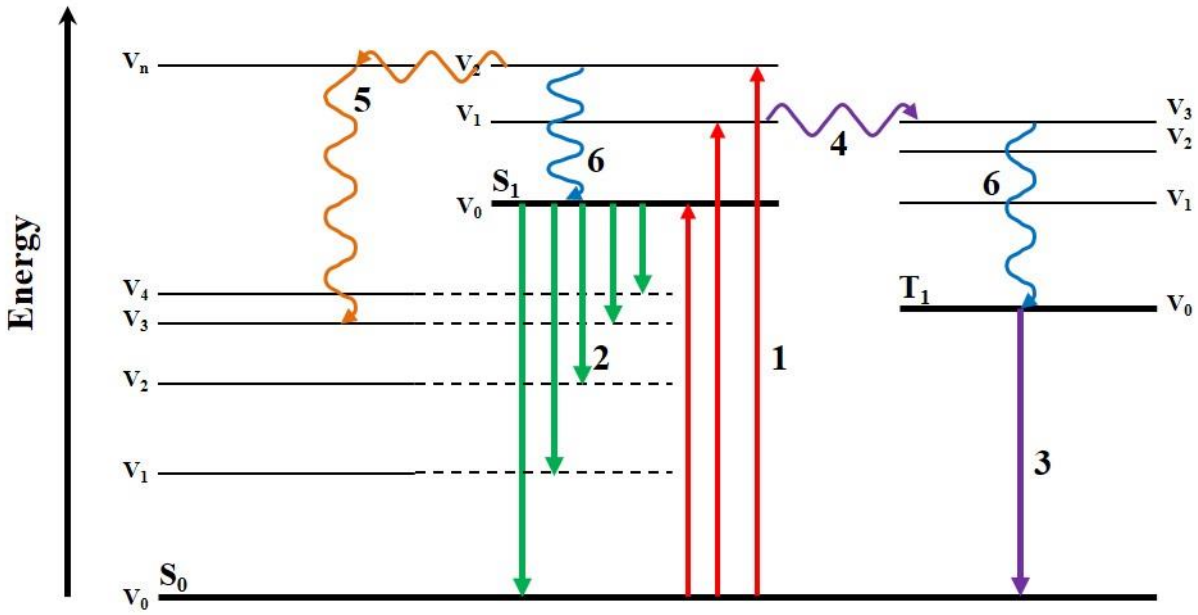

Figure 2.11: Jablonski diagram showing various relaxation processes after absorption of a photon. (1) absorption, (2) fluorescence, (3) phosphorescence, (4) intersystem crossing, (5) internal conversion and (6) vibrational relaxation. The curly and straight arrows represent non-radiative and radiative processes, respectively.

Fluorescence is a highly sensitive, background-free technique as the emitted light is detected separately from incident radiation. However, not all molecules fluoresce, and so fluorescence is only useful when observing chemical species that either are or contain fluorophores. Furthermore, when using a single excitation wavelength, it is difficult to distinguish between individual analytes in complex mixtures, such as oil or foodstuff as the broad fluorescence peaks overlap each other. This problem is exacerbated when the sample contains many similar fluorophores. A superior analytical method collects the entire fluorescence spectrum for a large number of excitation wavelengths and emission wavelengths. The resultant excitation emission matrix (EEM) can be used to generate a two-dimensional topographical map that allows one to distinguish different fluorophores within a complex mixture.[115, 116]

2.4.2 Excitation emission matrix spectroscopy

EEM spectroscopy (EEMS) is a very powerful tool for distinguishing different chemical species within a mixture.[117-119] EEMS is a fluorescence technique where the entire emission spectrum is collected while scanning over a series of excitation wavelengths. The intensity at each excitation and emission wavelength coordinate can be collected and displayed as a two-dimensional topographical map. With the help of an EEM spectrum, one can visually separate the broad fluorescent features into key dominant fluorophores; a difficult procedure when collecting a single fluorescence spectrum at one excitation wavelength.[120] Much more quantitative methods are described in section 2.4.3 below.

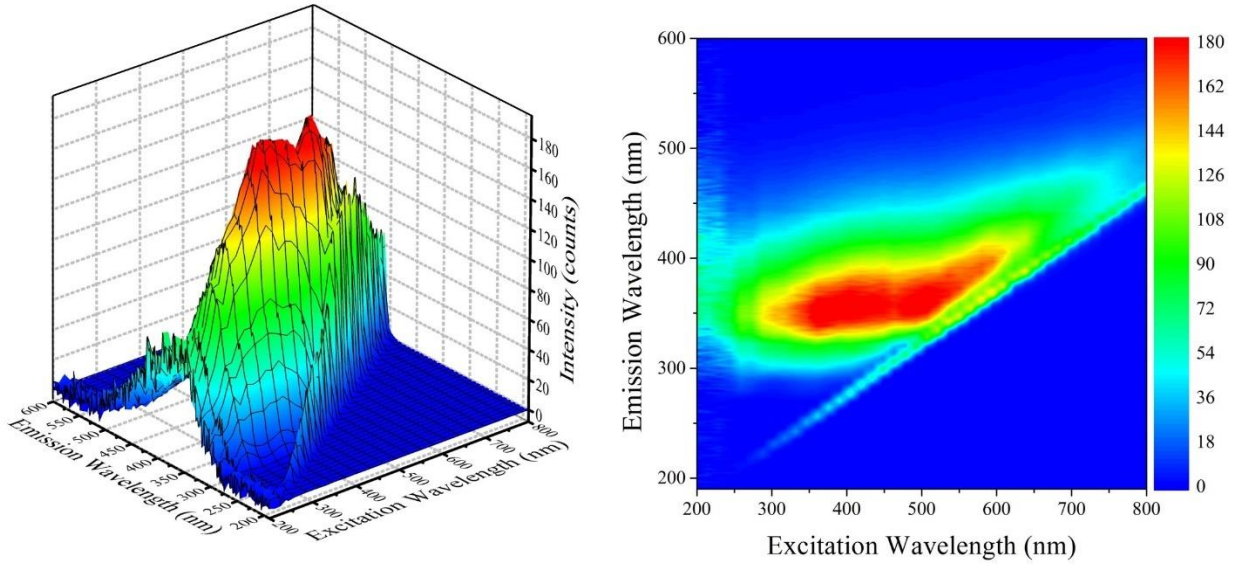

Figure 2.12: Excitation emission matrix spectrum represented as both a surface and contour plot of a crude oil sample. The spectrum was obtained using an in-house bifurcated fibre probe submerged in the sample and attached to a Varian Cary Eclipse spectrometer.

The amount of information that can be extracted reliably from a data set increases with the order of the instrumentation.[121] Zero-order sensors such as a single photomultiplier tube (PMT) signal or temperature measurement provide less information compared to first-order instrumentation such as an absorption spectrum, which is in turn, less informative than second-order techniques. As EEMS is a second-order technique, it is analytically more powerful than first-order single wavelength excitation fluorescence spectroscopy. All second-order techniques, such as EEMS but also 2D-NMR, have the advantage over first- and zero-order instrumentation, that they can analyse and quantify spectroscopic components in a data set that are not explicitly included in the calibration model. Additionally, it is possible to form a calibration model when there are multiple spectral interferences present from unknown compounds.[121] Furthermore, EEMS generates much more information on the measured analyte as compared to fluorescence using only a single excitation wavelength, and can be used to investigate the vibrational structure and potential energy surfaces of both the ground and excited states that lead to fluorescence.[122]

Determining the concentration of specific fluorophores within a mixture can prove difficult, especially when the broad fluorescence peaks overlap. This problem can be solved using multivariate data analysis, such as principle component analysis (PCA) or parallel factor (PARAFAC) analysis. In many cases PARAFAC analysis is able to decompose the complex EEM spectra into its various fluorescent components.[123] After PARAFAC analysis these fluorescent components can be attributed to the concentration of the fluorescent analytes present in each mixture. Being able to monitor and distinguish the concentration of multiple analytes in a system as it reacts is very useful as it allows us determine kinetic information.[118, 124] However, one must be aware that the determined fluorescent components obtained using PARAFAC analysis are not necessarily related to specific chemical fluorophores. It is then entirely possible that a single spectroscopic component will represent multiple similar fluorophores that are indistinguishable from each other. Furthermore, inner filter effects and reabsorption of fluorescence may result in artificially attenuated fluorescence signal causing the score of one component to be artificially lower.[119]

Due to their inherent ability to distinguish between analytes, both EEMS and multivariate analysis are invaluable analytical tools in chemometrics and are widely used in a range of research fields. Applications include water quality assessment through detection of dissolved organic matter,[125-128] pesticides,[129, 130] membrane foulants in wastewater effluent,[131] and the characterisation of different culinary liquids such as tea,[132, 133] wine,[134, 135] brandy,[136] sherry vinegar,[137] and cooking oils.[138-140] Furthermore, EEMS has been used in the medical field for characterising bacteria [117, 141, 142] and determining drugs in urine.[143-145] EEMS has also been widely applied for sensing oil samples ranging from monitoring crude oil spills [146, 147] and oil degradation [118, 124] to measuring contamination of oil and fuel.[148, 149]

Although EEMS is frequently used to quantify compounds in many chemical environments systems, the technique is hindered by long acquisition times. Many commercial EEM spectrometers consist of two monochromators that individually step over all excitation and emission wavelength pairs to build up the

entire EEM spectrum.[150] Long acquisition times prevent EEMS to be used in real-time and so offline sample analysis is required.[118] Obviously, this is not ideal as it prevents EEMS to be used for its main potential of kinetic analysis. Acquisition times of several minutes per EEM spectrum allow kinetic measurements only for slow reactions, or for reactions in which reaction mixtures can be easily quenched. Therefore, many groups have worked to improve the rate at which EEM spectra can be acquired. The excitation monochromator can be replaced by spatially resolving the excitation light, and the fluorescence is then directly measured on a two dimensional charged coupled device (CCD) array.[151-153] This reduced the EEM spectral acquisition time to 4 mins [152] and in some cases to tens of seconds.[151, 153] Although spatially exciting the sample enhanced the rate at which EEM spectra are acquired, doing this requires a homogeneous sample and very careful optical alignment. Alternatively, the excitation and emission monochromators can be replaced with acousto-optical filters [154] and linear interference filters to obtain low-resolution EEM spectra within a few seconds.[155, 156] Dye lasers with fast-switching dye cells have also been used to replace the monochromators.[157, 158] In these instruments, a laser is used to pump ten dyes that are rapidly switched sequentially on a wheel. The lasing emission of each dye provides a narrow-band excitation wavelength and the emission of the sample is then collected and dispersed onto a CCD array for detection. Although this method achieved EEM spectral acquisition rates down to 5 EEM spectra per second (200 ms per spectrum), the technique is limited to only 11 excitation wavelengths. One can envision enlarging the wheel so that more laser dyes can be selected and therefore more excitation wavelengths used. However, this would obviously increase the EEM spectral acquisition time.

An alternative method to enhance the acquisition rate of EEM spectra is to utilise wavelength division multiplexing (WDM), which generates a higher signal-to-noise ratio (SNR) leading to faster acquisition rates as compared to dispersive techniques.[159-162] WDM techniques exploit both the Fellgett advantage [163, 164]— each point of the collected data contains information from all the wavelengths of the input light — and the Jacquinot advantage — more energy reaches the detector as 50% of the light is used to excite the

sample.[56, 165] Hirschberg et al. utilised WDM through the use of a Michelson interferometer to modulate the excitation light and obtain excitation spectra of rhodamine B.[166] In a similar setup designed by Peng et al., used a Michelson interferometer to modulate the excitation light and obtain fluorescence lifetimes.[167] The same group then developed this further and built an EEM spectrometer that uses FTs for both the excitation and emission light.[120] Their instrument consists of two Michelson interferometers, the first modulates the excitation wavelength and the second is used to modulate the emission. To calibrate for the wavelengths, both interferometers are calibrated using two separate lasers. Using the FT-EEM spectrometer, Peng et al. were able to acquire EEM spectra in only 40 s while having a spectral resolution of 81 cm^{-1} (approx. 1-5 nm) over a 425-550 nm excitation and 580-750 nm emission range.[120] The complexity of the setup was somewhat reduced by Yuan et al. who demonstrated high speed-measurements of Förster Resonance Energy Transfer (FRET) using a double-pass FT fluorescence EEM spectrometer.[168] In Chapter 9 of this thesis we demonstrate yet another variation of WDM based EEM spectral acquisition. Our method is based on Hadamard transforms — a binary equivalent to FTs [169] — which can be used to greatly enhance the rate at which EEM spectra are acquired with only minimal loss of spectral information. Using Hadamard transform EEM spectroscopy will open up new possibilities of monitoring chemical reaction kinetics using EEMS where using the conventional instrument is otherwise impossible.

2.4.3 Multivariate analysis techniques

2.4.3.1 Principle component analysis

Although the added dimensionality of second order spectra such as EEMS, provides a much more powerful tool to quantify a chemical system, it correspondingly makes it more difficult to extract useful information.[170] However, with second order techniques one can use multivariate analysis methods to simplify and extract useful information that can then be used to characterise a chemical mixture. One such procedure is principal component analysis (PCA), which is a simple and fast method of emphasising the variation and extract strong patterns within a dataset.

PCA is a multivariate analysis technique that simplifies second or higher order data by reducing dimensionality.[171] In PCA, a new orthogonal coordinate system is generated to best describe the data set. The projection of the experimental data is obtained using a unit vector in the direction of the highest variance as shown in **Figure 2.13**. This unit vector is known as the first eigenvector and also known as the first principal component. The new projection of the data along the first principal component gives the score for each data point. The second eigenvector or principal component is orthogonal to the first and describes the highest level of remaining variance that is not accounted for by the first eigenvector. Additional principal components are then created for higher dimensional data to account for further remaining variance. The principal component describing the smallest variance can then be omitted, reducing the dimensionality and simplifying the data set.

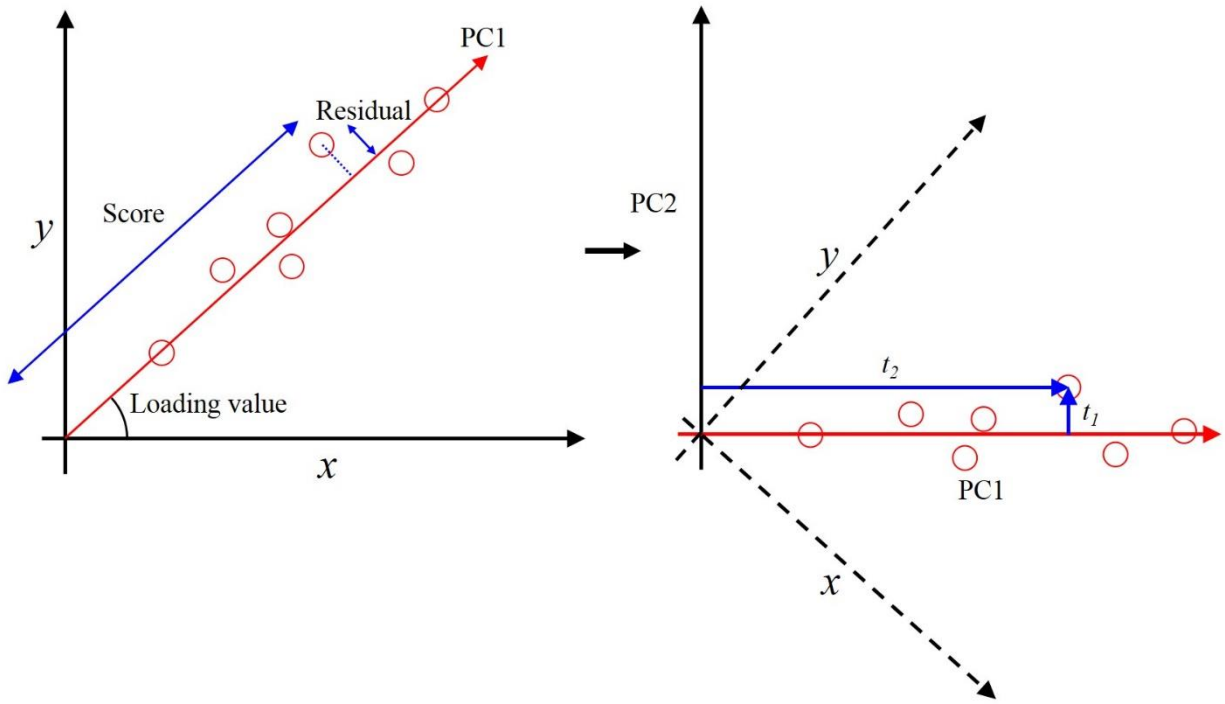

Figure 2.13: PCA on a two-dimension data set. The data is aligned along the first principal component dimension to reduce dimensionality. PC1 and PC2 represent the first and second principle components, respectively.

PCA approximates the original matrix of data, **X** , as a product of two smaller matrices so,

$$\begin{aligned}\mathbf{X} &= \mathbf{T}\mathbf{P}^{\mathrm{T}} + \mathbf{E} \\ &= t_1 p_1^{\mathrm{T}} + t_2 p_2^{\mathrm{T}} + \ldots + \mathbf{E}\end{aligned}, \qquad \textbf{(2.18)}$$

where $\mathbf{T}$ is the score matrix, $\mathbf{P}$ is the weight or loading matrix, and $\mathbf{E}$ is the residual signal that is not described by any principal component. Now each data point in the set is described in relation to the original variables using the loading profile, *p*, with a quantification along the principal component with score, *t*.

PCA has been widely used to characterise EEM spectra and is able to determine similarities between samples. For example, PCA has been used to discriminate between black teas,[133] characterise different wine distillates,[136] and distinguish between various olive oils.[172] Although in these cases, PCA is useful in distinguishing between various samples by finding similarities in the EEM spectra, it does not allow us to determine the fluorescent chemical compounds that are present in the samples. A more appropriate approach to characterise fluorophores in EEM spectra is to use trilinear models such as PARAFAC analysis as the loadings correspond directly to the fluorescent excitation and emission spectra of fluorescent chemical species.[121]

2.4.3.2 Tucker3 model

The Tucker3 model is a decomposition method, which deconstructs complex EEM spectra into individual components.[173] To carry out a three-way Tucker3 analysis, multiple EEMs of a mixture of fluorescent samples in various ratios are collected. These are then stacked to form a data cube, $\mathbf{X}$, with dimensions *i*, *j*, and *k* which represent the excitation wavelength, emission wavelength, and sample number, respectively. The sample number can represent a parameter that is either controlled or measured such as reaction time, concentration, or temperature for example. The Tucker3 model for the data cube $\mathbf{X} = x_{ijk}$, can be written as,

$$x_{ijk} = \sum_{p=1}^{P}\sum_{q=1}^{Q}\sum_{r=1}^{R} a_{ip} b_{jq} c_{kr} g_{pqr} + e_{ijk}, \qquad \textbf{(2.19)}$$

where $\mathbf{A} = a_{ip}$ is the $I \times P$ component matrix for the 1st mode, $\mathbf{B} = b_{jq}$ is the $J \times Q$ component matrix for the 2nd mode, $\mathbf{C} = c_{kr}$ is the $K \times R$ component matrix for the 3rd mode, $\mathbf{G} = g_{pqr}$ is the three-way $P \times Q \times R$ core array, and $E = e_{ijk}$ is the $I \times J \times K$ residual.[174] For EEM spectra the 1st, 2nd and 3rd modes represent the respective excitation wavelength, emission wavelength and fluorophore concentration respectively. The core array, $\mathbf{G}$, is used to weight the sum of the outer products used for the model. When the Tucker3 analysis is conducted on the matrix, $\mathbf{X}$, the best model is identified by modifying the sum in equation (2.19) such that the residual array, $\mathbf{E}$, is at its minimum. A graphical representation for the Tucker3 model is given in **Figure 2.14**.

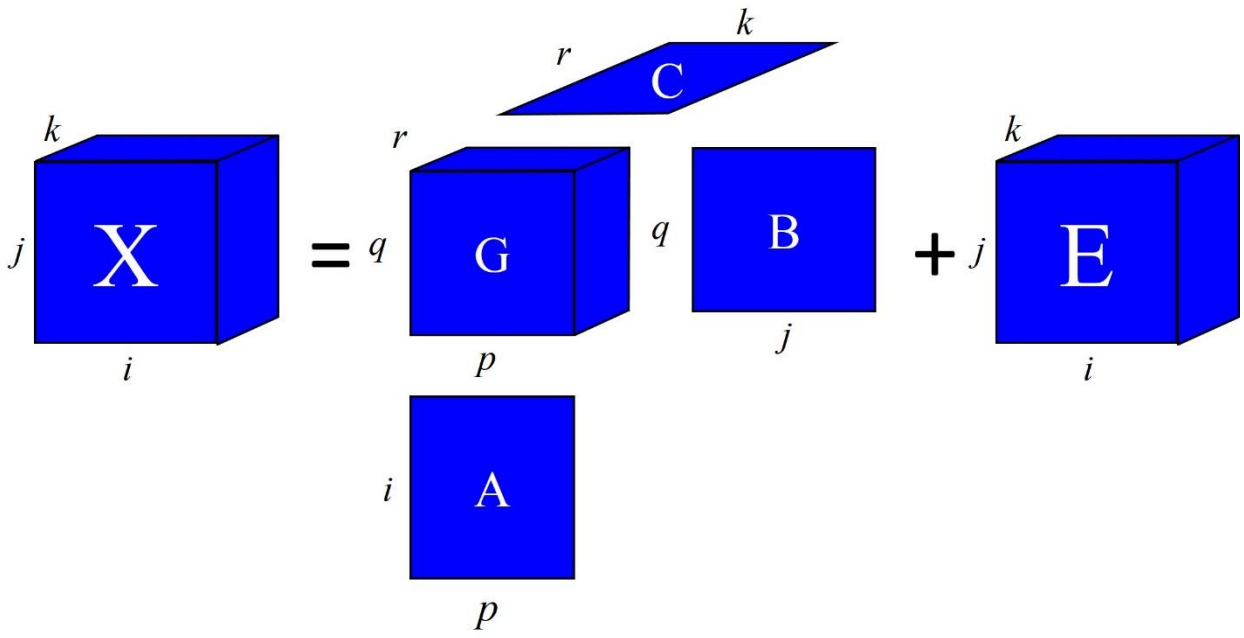

Figure 2.14: Graphical representation of the Tucker3 model. The model is a sum of outer products between the factors stored as columns in **A**, **B** and **C** weighted by the core matrix **G**. The matrix **E** represents the residual that is minimised in the model.

Although using the Tucker3 model on an array of EEM spectra provides an accurate model to the data, because each mode can have a different number of components and separate core weighting, it is difficult to correlate the mathematical components to real chemical fluorophores. This complexity reduces the

model's effectiveness in describing chemical systems. A simpler more appropriate model to describe a chemical system is to use PARAFAC analysis.

2.4.3.3 Parallel factor analysis

PARAFAC analysis is a more constrained version of the Tucker3 technique and is more applicable to describe chemical systems.[170] In PARAFAC analysis the core array, $\mathbf{G}$, is constrained to be a cubic superdiagonal array with component dimensions where $P = Q = R = F$.[174] Equation (2.19) used to describe the Tucker3 model can be rewritten for the PARAFAC model as,

$$x_{ijk} = \sum_{f=1}^{F} a_{if} b_{jf} c_{kf} g_{fff} + e_{ijk}, \qquad \textbf{(2.20)}$$

The confinement that $\mathbf{G}$ is a cubic superdiagonal matrix means that it can be omitted and equation (2.20) can be simplified to be,

$$x_{ijk} = \sum_{f=1}^{F} a_{if} b_{jf} c_{kf} + e_{ijk}. \qquad \textbf{(2.21)}$$

In PARAFAC analysis, each mode or loading matrix has the same number of components, *F*. For example, if a correct and appropriate number of PARAFAC components is chosen, then the value of *F* is identical to the number of fluorophores within the mixture.[123, 170] As with the Tucker3 model, the trilinear model obtained using PARAFAC analysis on the data cube, $\mathbf{X}$, aims to minimise the sum of the squares of the residuals, $\mathbf{E}$, as shown in equation (2.21). A graphical representation for a two component (*F*=2) PARAFAC model is given in **Figure 2.15**. An alternative form of equation (2.21) is shown below,

$$\mathbf{X} = \sum_{f=1}^{F} \mathbf{a}_f \otimes \mathbf{b}_f \otimes \mathbf{c}_f + \mathbf{E}_{ijk}, \qquad \textbf{(2.22)}$$

where, $\mathbf{a}_f$, $\mathbf{b}_f$ and $\mathbf{c}_f$ are the *f*th columns of the loading matrices $\mathbf{A}$, $\mathbf{B}$, and $\mathbf{C}$, respectively.

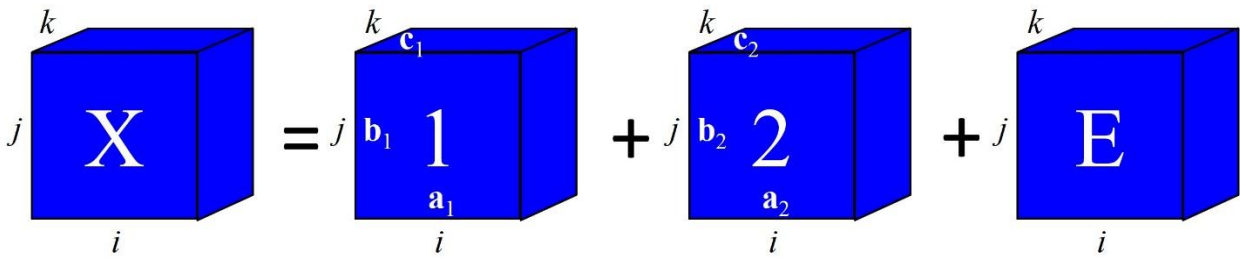

Figure 2.15: Graphical representation of the PARAFAC model of a two component fit. To generate the matrix X, the PARAFAC model generates components 1 and 2 with dimensions *ijk* from the loading matricies A, B, and C, and aims to minimise the residual matrix E. This figure is based on a similar figure in the paper by Bro.[170]

A major advantage of PARAFAC analysis over the PCA or Tucker3 techniques is that the loadings reflect the pure spectra of the analytes measured.[170] Furthermore, the concentration of each analyte is directly proportional the component scores. This is because PARAFAC models are constrained to fewer degrees of freedom that will precisely describe the trilinear system. For PCA or Tucker3 techniques, the models are unconstrained so the dimensions are free to rotate to further minimise the residual. Although the fits produced using Tucker3 and PCA are mathematically more accurate and have a smaller residual value, it is hard to extract the pure spectra from such a model. If the correct number of components is chosen, the PARAFAC model will best describe the chemical system in a way that is easy to interpret and will produce loadings that correlate to true spectra of chemical fluorophores in the system.

Additionally, as PARAFAC analysis is a mathematical multivariate analysis procedure as with Tucker3 and PCA, no assumptions on the spectral shape are required except that the different fluorophores have different spectra.[170] This obviously poses a small problem if the fluorophores have similar spectra. Furthermore, no chemical knowledge of the system of interest is required prior to a PARAFAC analysis run as the model with the most appropriate number of components and thus chemical fluorophores will provide the best model.[123, 175]

We will demonstrate the power of the PARAFAC analysis method when applied to fluorescence EEM spectra, when discussing the degradation of lubrication oil in Chapter 6 and the thermal, photochemical, and oxidative degradation of SNOLAB scintillator liquids in Chapter 7.

2.5 Concluding remarks

Now that an overview of the background optical techniques has been described, the objectives of the thesis can be revealed. Although the optical techniques used in this thesis are broad in scope including refractive index, absorption and fluorescence measurements, they encompass a central theme of optical methods using fibre optic waveguides for chemical detection. The PCF interferometer is used to measure the refractive index of nine gases with a range of polarisabilities within a volume of a microlitre. The amplified fibre loop cavity ring-down is used to detect samples in even smaller volumes down to 1 picolitre. Both these techniques are used for detection of analytes within small volumes, which is only made possible using optical fibres. The small volumes are beneficial as they reduce waste and the cost impact of measuring expensive analytes.

The fluorescence EEMS technique additionally uses fibre optics in the form of a bifurcated fibre optic probe. The front face fluorescence detection obtained using the fibre probe ensures that fluorescence EEM spectra are acquired with zero sample preparation. This allows for on-line detection of analytes and does not require a skilled worker to prepare the sample for subsequent analysis. However, with the conventional EEM spectrometer, it takes a long time to acquire a single spectrum preventing it to be used for real-time and on-line analysis. We therefore developed a method to accelerate the acquisition EEM spectra using Hadamard modulation, and reduce the acquisition time of EEM spectra from ~30 mins to a few seconds. This thesis highlights the usefulness of EEM spectroscopy as applied for kinetic measurements and shows the construction and development of a multiplexed EEM spectrometer used to hasten the fluorescence EEM spectral acquisition. The brewing of tea is monitored using the multiplexed EEM spectrometer and is used to highlight its potential for real-time and on-line analysis of fluorescent systems.

2.6 Bibliography

1. E. Bakker and M. Telting-Diaz, Electrochemical sensors. *Analytical Chemistry* **2002,** *74*, 2781-2800.
2. J. Wang, Electrochemical detection for microscale analytical systems: A review. *Talanta* **2002,** *56*, 223-231.
3. K. Štulík, Challenges and promises of electrochemical detection and sensing. *Electroanalysis* **1999,** *11*, 1001-1004.
4. E. de Hoffmann, in *Kirk-Othmer encyclopedia of chemical technology*, ed. I. John Wiley & Sons, John Wiley & Sons, Inc., Hoboken, NJ, USA, 2005.
5. G. A. Jenner, H. P. Longerich, S. E. Jackson and B. J. Fryer, ICP-MS — A powerful tool for high-precision trace-element analysis in Earth sciences: Evidence from analysis of selected U.S.G.S. reference samples. *Chemical Geology* **1990,** *83*, 133-148.
6. C. A. Noble and K. A. Prather, Real-time single particle mass spectrometry: A historical review of a quarter century of the chemical analysis of aerosols. *Mass Spectrometry Reviews* **2000,** *19*, 248-274.
7. R. G. Cooks, Z. Ouyang, Z. Takats and J. M. Wiseman, Ambient mass spectrometry. *Science* **2006,** *311*, 1566-1570.
8. Z. Ouyang and R. G. Cooks, Miniature mass spectrometers. *Annual Review of Analytical Chemistry* **2009,** *2*, 187-214.
9. Z. Ouyang, R. J. Noll and R. G. Cooks, Handheld miniature ion trap mass spectrometers. *Analytical Chemistry* **2009,** *81*, 2421-2425.
10. H. F. Hemond, US5155357 A, 1992.
11. M. R. Canagaratna, J. T. Jayne, J. L. Jimenez, J. D. Allan, M. R. Alfarra, Q. Zhang, T. B. Onasch, F. Drewnick, H. Coe, A. Middlebrook, A. Delia, L. R. Williams, A. M. Trimborn, M. J. Northway, P. F. DeCarlo, C. E. Kolb, P. Davidovits and D. R. Worsnop, Chemical and microphysical characterization of ambient aerosols with the aerodyne aerosol mass spectrometer. *Mass Spectrometry Reviews* **2007,** *26*, 185-222.
12. C. C. Mulligan, D. R. Justes, R. J. Noll, N. L. Sanders, B. C. Laughlin and R. G. Cooks, Direct monitoring of toxic compounds in air using a portable mass spectrometer. **2006,** *131*, 556-567.
13. R. T. Short, D. P. Fries, S. K. Toler, C. E. Lembke and R. H. Byrne, Development of an underwater mass-spectrometry system for in situ chemical analysis. *Measurement Science and Technology* **1999,** *10*, 1195.
14. A. G. Mignani, L. Ciaccheri, A. A. Mencaglia, H. Ottevaere, E. E. S. Báca and H. Thienpont, Optical measurements and pattern-recognition techniques for identifying the characteristics of beer and distinguishing Belgian beers. *Sensors and Actuators B: Chemical* **2013,** *179*, 140-149.
15. A. G. Mignani, L. Ciaccheri, B. Gordillo, A. A. Mencaglia, M. L. González-Miret, F. J. Heredia and B. Culshaw, Identifying the production region of single-malt Scotch whiskies using optical spectroscopy and pattern recognition techniques. *Sensors and Actuators B: Chemical* **2012,** *171–172*, 458-462.
16. M. Fischer, M. Wahl and G. Friedrichs, Design and field application of a UV-LED based optical fiber biofilm sensor. *Biosensors & bioelectronics* **2012,** *33* (1), 172-178.
17. Y. Dattner and O. Yadid-Pecht, Analysis of the effective refractive index of silicon waveguides through the constructive and destructive interference in a Mach-Zehnder interferometer. *IEEE Photonics Journal* **2011,** *3*, 1123-1132.
18. A. L. Washburn and R. C. Bailey, Photonics-on-a-chip: Recent advances in integrated waveguides as enabling detection elements for real-world, lab-on-a-chip biosensing applications. *The Analyst* **2011,** *136*, 227-236.
19. O. Kononchuk and B.-Y. Nguyen, *Silicon-on-insulator (SOI) technology: Manufacture and applications*, Elsevier, 2014.

20. Z. Tian, S. S.-H. Yam, J. Barnes, W. Bock, P. Greig, J. M. Fraser, H.-P. Loock and R. D. Oleschuk, Refractive index sensing with Mach-Zehnder interferometer based on concatenating two single-mode fiber tapers. *IEEE Photonics Technology Letters* **2008,** *20*, 626-628.
21. I. Shavrin, S. Novotny, A. Shevchenko and H. Ludvigsen, Gas refractometry using a hollow-core photonic bandgap fiber in a Mach-Zehnder-type interferometer. *Applied Physics Letters* **2012,** *100*, 051106.
22. N. L. P. Andrews, R. Ross, D. Munzke, C. van Hoorn, A. Brzezinski, J. A. Barnes, O. Reich and H.-P. Loock, In-fiber Mach-Zehnder interferometer for gas refractive index measurements based on a hollow-core photonic crystal fiber. *Optics Express* **2016,** *24*, 14086.
23. L. Li, L. Xia, Z. Xie and D. Liu, All-fiber Mach-Zehnder interferometers for sensing applications. *Optics Express* **2012,** *20*, 11109.
24. T. K. Liang, M. Friedrich, D. Lala and K. B. Ozanyan, Proceedings of IEEE Sensors, 2004.
25. J. Ma, Y. Chiniforooshan, W. Hao, W. J. Bock and Z. Y. Wang, Easily fabricated, robust fiber-optic probe for weak fluorescence detection: modeling and initial experimental evaluation. *Optics Express* **2012,** *20*, 4805-4811.
26. K. Bescherer, J. A. Barnes, S. Dias, G. Gagliardi, H.-P. Loock, N. R. Trefiak, H. Waechter and S. Yam, Measurement of multi-exponential optical decay processes by phase-shift cavity ring-down. *Applied Physics B-Lasers and Optics* **2009,** *96*, 193-200.
27. K. Bescherer, J. A. Barnes and H.-P. Loock, Absorption measurements in liquid core waveguides using cavity ring-down spectroscopy. *Analytical Chemistry* **2013,** *85*, 4328-4334.
28. R. S. Brown, I. Kozin, Z. Tong, R. D. Oleschuk and H.-P. Loock, Fiber-loop ring-down spectroscopy. *The Journal of Chemical Physics* **2002,** *117*, 10444-10447.
29. Z. Tong, M. Jakubinek, A. Wright, A. Gillies and H.-P. Loock, Fiber-loop ring-down spectroscopy: A sensitive absorption technique for small liquid samples. *Review of Scientific Instruments* **2003,** *74*, 4818-4826.
30. Z. Tong, A. Wright, T. McCormick, R. Li, R. D. Oleschuk and H.-P. Loock, Phase-shift fiber-loop ring-down spectroscopy. *Analytical Chemistry* **2004,** *76*, 6594-6599.
31. H.-P. Loock, Ring-down absorption spectroscopy for analytical microdevices. *TrAC Trends in Analytical Chemistry* **2006,** *25*, 655-664.
32. T. Miya, Y. Terunuma, T. Hosaka and T. Miyashita, Ultimate low-loss single-mode fibre at 1.55 μm. *Electronics Letters* **1979,** *15*, 106-108.
33. J. Villatoro and J. Zubia, New perspectives in photonic crystal fibre sensors. *Optics & Laser Technology* **2016,** *78, Part A*, 67-75.
34. X.-D. Wang and O. S. Wolfbeis, Fiber-optic chemical sensors and biosensors (2008–2012). *Analytical Chemistry* **2013,** *85*, 487-508.
35. P. Russell, Photonic crystal fibers. *Science* **2003,** *299*, 358-362.
36. P. S. J. Russell, Photonic-crystal fibers. *Journal of Lightwave Technology* **2006,** *24*, 4729-4749.
37. R. S. Quimby, *Photonics and lasers: An introduction*, John Wiley & Sons, 2006.
38. X.-D. Wang and O. S. Wolfbeis, Fiber-optic chemical sensors and biosensors (2013–2015). *Analytical Chemistry* **2016,** *88*, 203-227.
39. S. Roh, T. Chung and B. Lee, Overview of the characteristics of micro- and nano-structured surface plasmon resonance sensors. *Sensors* **2011,** *11*, 1565-1588.
40. H. H. Nguyen, J. Park, S. Kang and M. Kim, Surface plasmon resonance: A versatile technique for biosensor applications. *Sensors* **2015,** *15*, 10481-10510.
41. J. Homola, Present and future of surface plasmon resonance biosensors. *Analytical and Bioanalytical Chemistry* **2003,** *377*, 528-539.
42. P. Atkins and J. d. Paula, *Physical chemistry*, W H Freeman & Co, New York, 2009.
43. Z. Bor, K. Osvay, B. Rácz and G. Szabó, Group refractive index measurement by Michelson interferometer. *Optics Communications* **1990,** *78*, 109-112.
44. D. T. F. Marple, Refractive index of GaAs. *Journal of Applied Physics* **1964,** *35*, 1241-1242.

45. W. L. Bond, Measurement of the refractive indices of several crystals. *Journal of Applied Physics* **1965,** *36*, 1674-1677.
46. J. Valentine, S. Zhang, T. Zentgraf, E. Ulin-Avila, D. A. Genov, G. Bartal and X. Zhang, Three-dimensional optical metamaterial with a negative refractive index. *Nature* **2008,** *455*, 376-379.
47. J. E. Saunders, C. Sanders, H. Chen and H.-P. Loock, Refractive indices of common solvents and solutions at 1550 nm. *Applied Optics* **2016,** *55*, 947.
48. J. E. Saunders, H. Chen, C. Brauer, M. Clayton, W. Chen, J. A. Barnes and H.-P. Loock, Quantitative diffusion and swelling kinetic measurements using large-angle interferometric refractometry. **2015,** *11*, 8746-8757.
49. G. Kaiser, *A friendly guide to wavelets*, Springer Science & Business Media, 2010.
50. M. Rahman, *Applications of Fourier transforms to generalized functions*, WIT Press, 2011.
51. P. Griffiths, *Transform techniques in chemistry*, Springer Science & Business Media, 2012.
52. H. Y. Choi, M. J. Kim and B. H. Lee, All-fiber Mach-Zehnder type interferometers formed in photonic crystal fiber. *Optics Express* **2007,** *15*, 5711.
53. B. H. Lee and J. Nishii, Dependence of fringe spacing on the grating separation in a long-period fiber grating pair. *Applied Optics* **1999,** *38*, 3450.
54. B. E. A. Saleh and M. C. Teich, *Fundamentals of photonics*, 2nd Edition edn., John Wiley & Sons, Inc., 1991.
55. G. Horlick and W. Yuen, Modular Michelson interferometer for Fourier-transform spectrochemical measurements from mid-infrared to ultraviolet. *Applied Spectroscopy* **1978,** *32*, 38-46.
56. P. Jacquinot, New developments in interference spectroscopy. *Reports on Progress in Physics* **1960,** *23*, 267.
57. Z. Tian, S. S.-H. Yam and H.-P. Loock, Refractive index sensor based on an abrupt taper Michelson interferometer in a single-mode fiber. *Optics Letters* **2008,** *33*, 1105-1107.
58. https://www.newport.com/c/ft-ir-spectrometers, 2016.
59. *Specification sheet: Nicolet iG50 FT-IR spectrometer product specifications*, ThermoFisher Scientific, 2016.
60. B. Edlén, The refractive index of air. *Metrologia* **1966,** *2*, 71.
61. D. H. Hurley and O. B. Wright, Detection of ultrafast phenomena by use of a modified Sagnac interferometer. *Optics Letters* **1999,** *24*, 1305.
62. T. Eberle, S. Steinlechner, J. Bauchrowitz, V. Händchen, H. Vahlbruch, M. Mehmet, H. Müller-Ebhardt and R. Schnabel, Quantum enhancement of the zero-area Sagnac interferometer topology for gravitational wave detection. *Physical Review Letters* **2010,** *104*, 251102.
63. T. Qu, K. Yang, X. Han, S. Wu, Y. Huang and H. Luo, Design of a superluminal ring laser gyroscope using multilayer optical coatings with huge group delay. *Scientific Reports* **2014,** *4*, 7098.
64. D.-H. Kim and J. Kang, Sagnac loop interferometer based on polarization maintaining photonic crystal fiber with reduced temperature sensitivity. *Optics Express* **2004,** *12*, 4490-4495.
65. A. N. Starodumov, L. A. Zenteno, D. Monzon and E. D. L. Rosa, Fiber Sagnac interferometer temperature sensor. *Applied Physics Letters* **1997,** *70*, 19-21.
66. R. Chevalerias, Y. Latron and C. Veret, Methods of interferometry applied to the visualization of flows in wind tunnels. *Journal of the Optical Society of America* **1957,** *47*, 703.
67. S. Liu, N. Liu, M. Hou, J. Guo, Z. Li and P. Lu, Direction-independent fiber inclinometer based on simplified hollow core photonic crystal fiber. *Optics Letters* **2013,** *38*, 449.
68. M. Imai, T. Ohashi and Y. Ohtsuka, Fiber-optic Michelson interferometer using an optical power divider. *Optics Letters* **1980,** *5*, 418.
69. B. Culshaw, The optical fibre Sagnac interferometer: An overview of its principles and applications. *Measurement Science and Technology* **2006,** *17*, R1.

70. Y. Cao, W. Jin, F. Yang and H. L. Ho, Phase sensitivity of fundamental mode of hollow-core photonic bandgap fiber to internal gas pressure. *Optics Express* **2014,** *22* (11), 13190-13201.
71. Z. Tian, S. S.-H. Yam and H.-P. Loock, Single-mode fiber refractive index sensor based on core-offset attenuators. *IEEE Photonics Technology Letters* **2008,** *20*, 1387-1389.
72. J. H. Lim, H. S. Jang, K. S. Lee, J. C. Kim and B. H. Lee, Mach–Zehnder interferometer formed in a photonic crystal fiber based on a pair of long-period fiber gratings. *Optics Letters* **2004,** *29*, 346.
73. J. Villatoro, V. P. Minkovich and D. Monzon-Hernandez, Compact modal interferometer built with tapered microstructured optical fiber. *IEEE Photonics Technology Letters* **2006,** *18*, 1258-1260.
74. K. T. V. Grattan and B. T. Meggitt, *Optical fiber sensor technology: Fundamentals*, Springer US, Boston, MA, 2013.
75. D. Barrera, J. Villatoro, V. P. Finazzi, G. A. Cardenas-Sevilla, V. P. Minkovich, S. Sales and V. Pruneri, Low-loss photonic crystal fiber interferometers for sensor networks. *Journal of Lightwave Technology* **2010,** *28*, 3542-3547.
76. R. Jha, J. Villatoro, G. Badenes and V. Pruneri, Refractometry based on a photonic crystal fiber interferometer. *Optics Letters* **2009,** *34*, 617-619.
77. J. Villatoro, V. Finazzi, V. P. Minkovich, V. Pruneri and G. Badenes, Temperature-insensitive photonic crystal fiber interferometer for absolute strain sensing. *Applied Physics Letters* **2007,** *91*, 091109-091109-091103.
78. J. Villatoro, M. P. Kreuzer, R. Jha, V. P. Minkovich, V. Finazzi, G. Badenes and V. Pruneri, Photonic crystal fiber interferometer for chemical vapor detection with high sensitivity. *Optics Express* **2009,** *17*, 1447-1453.
79. J. Mathew, Y. Semenova and G. Farrell, Photonic crystal fiber interferometer for dew detection. *Journal of Lightwave Technology* **2012,** *30*, 1150-1155.
80. J. Mathew, Y. Semenova and G. Farrell, Relative humidity sensor based on an agarose-infiltrated photonic crystal fiber interferometer. *IEEE Journal of Selected Topics in Quantum Electronics* **2012,** *18*, 1553-1559.
81. S. H. Kassani, R. Khazaeinezhad, Y. Jung, J. Kobelke and K. Oh, Suspended ring-core photonic crystal fiber gas sensor with high sensitivity and fast response. *IEEE Photonics Journal* **2015,** *7*, 1-9.
82. P. Pinkhasova, H. Chen, J. Kanka, P. Mergo and H. Du, Nanotag-enabled photonic crystal fiber as quantitative surface-enhanced Raman scattering optofluidic platform. *Applied Physics Letters* **2015,** *106*, 071106.
83. http://www.oceanoptics.com/products/benchoptions_usb4.asp, 2016.
84. http://www.avantes.com/company, 2016.
85. N. Tessler, V. Medvedev, M. Kazes, S. Kan and U. Banin, Efficient near-infrared polymer nanocrystal light-emitting diodes. *Science* **2002,** *295*, 1506-1508.
86. J. U. White, Long optical paths of large aperture. *Journal of the Optical Society of America* **1942,** *32*, 285-285.
87. D. R. Herriott and H. J. Schulte, Folded optical delay lines. *Applied Optics* **1965,** *4*, 883-889.
88. A. O'Keefe and D. A. G. Deacon, Cavity ring-down optical spectrometer for absorption measurements using pulsed laser sources. *Review of Scientific Instruments* **1988,** *59*, 2544-2551.
89. P. Zalicki and R. N. Zare, Cavity ring-down spectroscopy for quantitative absorption measurements. *The Journal of Chemical Physics* **1995,** *102*, 2708.
90. H. Waechter, J. Litman, A. H. Cheung, J. A. Barnes and H.-P. Loock, Chemical sensing using fiber cavity ring-down spectroscopy. *Sensors* **2010,** *10*, 1716-1742.
91. J. M. Herbelin, J. A. McKay, M. A. Kwok, R. H. Ueunten, D. S. Urevig, D. J. Spencer and D. J. Benard, Sensitive measurement of photon lifetime and true reflectances in an optical cavity by a phase-shift method. *Applied Optics* **1980,** *19*, 144-147.

92. R. Engeln, G. von Helden, G. Berden and G. Meijer, Phase shift cavity ring down absorption spectroscopy. *Chemical Physics Letters* **1996,** *262*, 105-109.
93. A. O'Keefe and O. Lee, Trace gas-analysis by pulsed laser-absorption spectroscopy. *American Laboratory* **1989,** *21*, 19-22.
94. K. E. Whittaker, L. Ciaffoni, G. Hancock, R. Peverall and G. A. D. Ritchie, A DFG-based cavity ring-down spectrometer for trace gas sensing in the mid-infrared. *Applied Physics B-Lasers and Optics* **2012,** *109*, 333-343.
95. S. S. Brown, H. Stark and A. R. Ravishankara, Cavity ring-down spectroscopy for atmospheric trace gas detection: Application to the nitrate radical (NO_3). *Applied Physics B: Lasers & Optics* **2002,** *75*, 173.
96. T. J. A. Butler, D. Mellon, J. Kim, J. Litman and A. J. Orr-Ewing, Optical-feedback cavity ring-down spectroscopy measurements of extinction by aerosol particles. *The Journal of Physical Chemistry A* **2009,** *113*, 3963-3972.
97. T. J. A. Butler, J. L. Miller and A. J. Orr-Ewing, Cavity ring-down spectroscopy measurements of single aerosol particle extinction. I. The effect of position of a particle within the laser beam on extinction. *The Journal of Chemical Physics* **2007,** *126*, 174302.
98. S. Xu, G. Sha and J. Xie, Cavity ring-down spectroscopy in the liquid phase. *Review of Scientific Instruments* **2002,** *73*, 255-258.
99. A. J. Alexander, Reaction kinetics of nitrate radicals with terpenes in solution studied by cavity ring-down spectroscopy. *Chemical Physics Letters* **2004,** *393*, 138-142.
100. K. L. Snyder and R. N. Zare, Cavity ring-down spectroscopy as a detector for liquid chromatography. *Analytical Chemistry* **2003,** *75*, 3086-3091.
101. K. L. Bechtel, R. N. Zare, A. A. Kachanov, S. S. Sanders and B. A. Paldus, Moving beyond traditional UV−visible absorption detection: Cavity ring-down spectroscopy for HPLC. *Analytical Chemistry* **2005,** *77*, 1177-1182.
102. A. J. Hallock, E. S. F. Berman and R. N. Zare, Ultratrace kinetic measurements of the reduction of methylene blue. *Journal of the American Chemical Society* **2003,** *125*, 1158-1159.
103. M. Gupta, H. Jiao and A. O'Keefe, Cavity-enhanced spectroscopy in optical fibers. *Optics Letters* **2002,** *27*, 1878-1880.
104. N. L. P. Andrews, J. Litman, D. Stroh, J. A. Barnes and H.-P. Loock, Near-infrared absorption detection in picolitre liquid volumes using amplified fibre loop ring-down detection. *Optical Fiber Technology* **2013,** *19*, 822-827.
105. D. James, B. Oag, C. M. Rushworth, J. W. L. Lee, J. Davies, J. T. Cabral and C. Vallance, High-sensitivity online detection for microfluidics via cavity ringdown spectroscopy. *RSC Advances* **2012,** *2*, 5376-5384.
106. T. v. Lerber and M. W. Sigrist, Cavity-ring-down principle for fiber-optic resonators: Experimental realization of bending loss and evanescent-field sensing. *Applied Optics* **2002,** *41*, 3567-3575.
107. P. B. Tarsa, P. Rabinowitz and K. K. Lehmann, Evanescent field absorption in a passive optical fiber resonator using continuous-wave cavity ring-down spectroscopy. *Chemical Physics Letters* **2004,** *383*, 297-303.
108. J. Barnes, M. Dreher, K. Plett, R. S. Brown, C. M. Crudden and H.-P. Loock, Chemical sensor based on a long-period fibre grating modified by a functionalized polydimethylsiloxane coating. *Analyst* **2008,** *133*, 1541-1549.
109. C. M. Rushworth, D. James, J. W. L. Lee and C. Vallance, Top notch design for fiber-loop cavity ring-down spectroscopy. *Analytical Chemistry* **2011,** *83*, 8492-8500.
110. B. D. Gupta, C. D. Singh and A. Sharma, Fiber optic evanescent field absorption sensor: Effect of launching condition and the geometry of the sensing region. *Optical Engineering* **1994,** *33*, 1864-1868.

111. P. B. Tarsa, A. D. Wist, P. Rabinowitz and K. K. Lehmann, Single-cell detection by cavity ring-down spectroscopy. *Applied Physics Letters* **2004,** *85*, 4523-4525.
112. G. Stewart, K. Atherton and B. Culshaw, Cavity-enhanced spectroscopy in fiber cavities. *Optics Letters* **2004,** *29*, 442-444.
113. G. Stewart, K. Atherton, H. Yu and B. Culshaw, An investigation of an optical fibre amplifier loop for intra-cavity and ring-down cavity loss measurements. *Measurement Science and Technology* **2001,** *12*, 843-849.
114. Y. Zhang, M. Zhang, W. Jin, H. L. Ho, M. S. Demokan, B. Culshaw and G. Stewart, Investigation of erbium-doped fiber laser intra-cavity absorption sensor for gas detection. *Optics Communications* **2004,** *232*, 295-301.
115. R. M. B. O. Duarte, C. A. Pio and A. C. Duarte, Synchronous scan and excitation-emission matrix fluorescence spectroscopy of water-soluble organic compounds in atmospheric aerosols. *Journal of Atmospheric Chemistry* **2004,** *48*, 157-171.
116. M. M. Schachter and E. O. Haenni, Automatic triparametric recording in fluorometry of polynuclear hydrocarbons. *Analytical Chemistry* **1964,** *36*, 2045-2047.
117. L. R. Dartnell, T. A. Roberts, G. Moore, J. M. Ward and J.-P. Muller, Fluorescence characterization of clinically-important bacteria. *PLoS ONE* **2013,** *8*, e75270.
118. N. L. P. Andrews, J. Z. Fan, H. Omrani, A. Dudelzak and H.-P. Loock, Comparison of lubricant oil antioxidant analysis by fluorescence spectroscopy and linear sweep voltammetry. *Tribology International* **2016,** *94*, 279-287.
119. A. Andrade-Eiroa, M. Canle and V. Cerda, Environmental applications of excitation-emission spectrofluorimetry: An in-depth review I. *Applied Spectroscopy Reviews* **2013,** *48*, 1-49.
120. L. Peng, J. A. Gardecki, B. E. Bouma and G. J. Tearney, Fourier fluorescence spectrometer for excitation emission matrix measurement. *Optics Express* **2008,** *16*, 10493.
121. K. S. Booksh and B. R. Kowalski, Theory of analytical chemistry. *Analytical Chemistry* **1994,** *66*, 782A-791A.
122. J. W. Hofstraat and U. P. Wild, Constant-Energy Synchronous Scan and Excitation Emission Matrix Shpol'skii Spectroscopy for Characterization of PAHs. *Journal of Fluorescence* **1998,** *8*, 319-325.
123. C. A. Stedmon, S. Markager and R. Bro, Tracing dissolved organic matter in aquatic environments using a new approach to fluorescence spectroscopy. *Marine Chemistry* **2003,** *82*, 239-254.
124. H. Omrani, A. E. Dudelzak, B. P. Hollebone and H.-P. Loock, Assessment of the oxidative stability of lubricant oil using fiber-coupled fluorescence excitation–emission matrix spectroscopy. *Analytica Chimica Acta* **2014,** *811*, 1-12.
125. P. G. Coble, Characterization of marine and terrestrial DOM in seawater using excitation emission matrix spectroscopy. *Marine Chemistry* **1996,** *51*, 325-346.
126. W. Chen, P. Westerhoff, J. A. Leenheer and K. Booksh, Fluorescence excitation−emission matrix regional integration to quantify spectra for dissolved organic matter. *Environmental Science & Technology* **2003,** *37*, 5701-5710.
127. F. Jiang, F. S.-C. Lee, X. Wang and D. Dai, The application of excitation / emission matrix spectroscopy combined with multivariate analysis for the characterization and source identification of dissolved organic matter in seawater of Bohai Sea, China. *Marine Chemistry* **2008,** *110*, 109-119.
128. C. Guéguen, D. C. Burns, A. McDonald and B. Ring, Structural and optical characterization of dissolved organic matter from the lower Athabasca River, Canada. *Chemosphere* **2012,** *87*, 932-937.
129. R. D. JiJi, G. A. Cooper and K. S. Booksh, Excitation-emission matrix fluorescence based determination of carbamate pesticides and polycyclic aromatic hydrocarbons. *Analytica Chimica Acta* **1999,** *397*, 61-72.

130. M. L. Nahorniak and K. S. Booksh, Excitation-emission matrix fluorescence spectroscopy in conjunction with multiway analysis for PAH detection in complex matrices. *The Analyst* **2006,** *131*, 1308.
131. X. Zhu, Z. Wang and Z. Wu, Characterization of membrane foulants in a full-scale membrane bioreactor for supermarket wastewater treatment. *Process Biochemistry* **2011,** *46*, 1001-1009.
132. L. N. Seetohul, M. Islam, W. T. O'Hare and Z. Ali, Discrimination of teas based on total luminescence spectroscopy and pattern recognition. *Journal of the Science of Food and Agriculture* **2006,** *86*, 2092–2098.
133. L. N. Seetohul, S. M. Scott, W. T. O'Hare, Z. Ali and M. Islam, Discrimination of Sri Lankan black teas using fluorescence spectroscopy and linear discriminant analysis. *Journal of the Science of Food and Agriculture* **2013,** *93*, 2308–2314.
134. D. Airado-Rodríguez, I. Durán-Merás, T. Galeano-Díaz and J. P. Wold, Front-face fluorescence spectroscopy: A new tool for control in the wine industry. *Journal of Food Composition and Analysis* **2011,** *24*, 257-264.
135. D. Airado-Rodríguez, T. Galeano-Díaz, I. Durán-Merás and J. P. Wold, Usefulness of fluorescence excitation−emission matrices in combination with PARAFAC, as fingerprints of red wines. *Journal of Agricultural and Food Chemistry* **2009,** *57*, 1711-1720.
136. J. Sádecká, J. Tóthová and P. Májek, Classification of brandies and wine distillates using front face fluorescence spectroscopy. *Food Chemistry* **2009,** *117*, 491-498.
137. R. M. Callejón, J. M. Amigo, E. Pairo, S. Garmón, J. A. Ocaña and M. L. Morales, Classification of sherry vinegars by combining multidimensional fluorescence, parafac and different classification approaches. *Talanta* **2012,** *88*, 456-462.
138. E. Sikorska, A. Gliszczynska-Swiglo, I. Khmelinskii and M. Sikorski, Synchronous fluorescence spectroscopy of edible vegetable oils. Quantification of tocopherols. *Journal of Agricultural and Food Chemistry* **2005,** *53*, 6988-6994.
139. E. Sikorska, A. Romaniuk, I. V. Khmelinskii, R. Herance, J. L. Bourdelande, M. Sikorski and J. Kozioł, Characterization of edible oils using total luminescence spectroscopy. *Journal of Fluorescence* **2004,** *14*, 25-35.
140. N. Tena, R. Aparicio and D. L. García-González, Chemical changes of thermoxidized virgin olive oil determined by excitation–emission fluorescence spectroscopy (EEFS). *Food Research International* **2012,** *45*, 103-108.
141. M. Sohn, D. S. Himmelsbach, F. E. Barton and P. J. Fedorka-Cray, Fluorescence spectroscopy for rapid detection and classification of bacterial pathogens. *Applied Spectroscopy* **2009,** *63*, 1251-1255.
142. A. Calvet, B. Li and A. G. Ryder, A rapid fluorescence based method for the quantitative analysis of cell culture media photo-degradation. *Analytica Chimica Acta* **2014,** *807*, 111-119.
143. M. C. Ortiz, L. A. Sarabia, M. S. Sánchez and D. Giménez, Identification and quantification of ciprofloxacin in urine through excitation-emission fluorescence and three-way PARAFAC calibration. *Analytica Chimica Acta* **2009,** *642*, 193-205.
144. J. Mazina, V. Aleksejev, T. Ivkina, M. Kaljurand and L. Poryvkina, Qualitative detection of illegal drugs (cocaine, heroin and MDMA) in seized street samples based on SFS data and ANN: Validation of method. *Journal of Chemometrics* **2012,** *26*, 442–455.
145. J. A. Murillo Pulgarín, A. Alañón Molina and N. Boras, Application of non-linear angle synchronous spectrofluorimetry to the determination of complex mixtures of drugs in urine: A comparative study. *Spectrochimica Acta Part A: Molecular and Biomolecular Spectroscopy* **2012,** *98*, 190-198.
146. Z. Zhou, L. Guo, A. M. Shiller, S. E. Lohrenz, V. L. Asper and C. L. Osburn, Characterization of oil components from the Deepwater Horizon oil spill in the Gulf of Mexico using fluorescence EEM and PARAFAC techniques. *Marine Chemistry* **2013,** *148*, 10-21.

147. Z. Zhou, Z. Liu and L. Guo, Chemical evolution of Macondo crude oil during laboratory degradation as characterized by fluorescence EEMs and hydrocarbon composition. *Marine Pollution Bulletin* **2013,** *66*, 164-175.
148. O. Divya and A. K. Mishra, Multivariate methods on the excitation emission matrix fluorescence spectroscopic data of diesel–kerosene mixtures: A comparative study. *Analytica Chimica Acta* **2007,** *592*, 82-90.
149. H. Omrani, J. A. Barnes, A. E. Dudelzak, H.-P. Loock and H. Waechter, Fluorescence excitation–emission matrix (EEM) spectroscopy and cavity ring-down (CRD) absorption spectroscopy of oil-contaminated jet fuel using fiber-optic probes. *The Analyst* **2012,** *137*, 2782.
150. http://www.agilent.com/en-us/products/fluorescence/fluorescence-systems/cary-eclipse-fluorescence-spectrophotometer, 2016.
151. A. R. Muroski, K. S. Booksh and M. L. Myrick, Single-measurement excitation / emission matrix spectrofluorometer for determination of hydrocarbons in ocean Water. 1. Instrumentation and background correction. *Analytical Chemistry* **1996,** *68*, 3534-3538.
152. A. F. Zuluaga, U. Utzinger, A. Durkin, H. Fuchs, A. Gillenwater, R. Jacob, B. Kemp, J. Fan and R. Richards-Kortum, Fluorescence excitation emission matrices of human tissue: A system for in vivo measurement and method of data analysis. *Applied Spectroscopy* **1999,** *53*, 302-311.
153. S. J. Hart and R. e. D. JiJi, Light emitting diode excitation emission matrix fluorescence spectroscopy. *The Analyst* **2002,** *127*, 1693-1699.
154. W. Wang, Z. Wu, J. Zhao, H. Lui and H. Zeng, A rapid excitation-emission matrix fluorometer utilizing supercontinuum white light and acousto-optic tunable filters. *Review of Scientific Instruments* **2016,** *87*, 063117.
155. M. Gouzman, N. Lifshitz, S. Luryi, O. Semyonov, D. Gavrilov and V. Kuzminskiy, Excitation-emission fluorimeter based on linear interference filters. *Applied Optics* **2004,** *43*, 3066.
156. C. D. Tran and R. J. Furlan, Spectrofluorometer based on acousto-optic tunable filters for rapid scanning and multicomponent sample analyses. *Analytical Chemistry* **1993,** *65*, 1675-1681.
157. M. G. Müller, A. Wax, I. Georgakoudi, R. R. Dasari and M. S. Feld, A reflectance spectrofluorimeter for real-time spectral diagnosis of disease. *Review of Scientific Instruments* **2002,** *73*, 3933-3937.
158. R. A. Zângaro, L. Silveira, R. Manoharan, G. Zonios, I. Itzkan, R. R. Dasari, J. Van Dam and M. S. Feld, Rapid multiexcitation fluorescence spectroscopy system for in vivo tissue diagnosis. *Applied Optics* **1996,** *35*, 5211.
159. A. Oriana, J. Réhault, F. Preda, D. Polli and G. Cerullo, Scanning Fourier transform spectrometer in the visible range based on birefringent wedges. *Journal of the Optical Society of America A* **2016,** *33*, 1415.
160. R. Kellner and G. Gidály, Fourier-transform infrared versus conventional grating-infrared-attenuated total reflectance spectroscopic investigation of the adsorption of blood proteins on polymer surfaces. *Microchimica Acta* **1981,** *75*, 119-129.
161. J. A. Decker, Experimental realization of the multiplex advantage with a Hadamard-transform spectrometer. *Applied Optics* **1971,** *10* (3), 510-514.
162. K. W. Busch and L. D. Benton, Multiplex methods in atomic spectroscopy. *Analytical Chemistry* **1983,** *55*, 445A-460A.
163. P. B. Fellgett, On the ultimate sensitivity and practical performance of radiation detectors. *Journal of the Optical Society of America* **1949,** *39*, 970.
164. R. H. Brown and R. Q. Twiss, Interferometry of the intensity fluctuations in light. I. Basic theory: The correlation between photons in coherent beams of radiation. *Proceedings of the Royal Society of London A: Mathematical, Physical and Engineering Sciences* **1957,** *242*, 300-324.
165. P. G. Lucey, K. A. Horton and T. Williams, Performance of a long-wave infrared hyperspectral imager using a Sagnac interferometer and an uncooled microbolometer array. *Applied Optics* **2008,** *47*, F107.

166. J. G. Hirschberg, G. Vereb, C. K. Meyer, A. K. Kirsch, E. Kohen and T. M. Jovin, Interferometric measurement of fluorescence excitation spectra. *Applied Optics* **1998,** *37*, 1953.
167. L. Peng, J. T. Motz, R. W. Redmond, B. E. Bouma and G. J. Tearney, Fourier transform emission lifetime spectrometer. *Optics Letters* **2007,** *32*, 421.
168. J. Yuan, L. Peng, B. E. Bouma and G. J. Tearney, Quantitative FRET measurement by high-speed fluorescence excitation and emission spectrometer. *Optics Express* **2010,** *18*, 18839.
169. K. W. Henderson, Some notes on the walsh functions. *IEEE Transactions on Electronic Computers* **1964,** *EC-13*, 50-52.
170. R. Bro, PARAFAC. Tutorial and applications. *Chemometrics and Intelligent Laboratory Systems* **1997,** *38*, 149-171.
171. S. M. Scott, D. James and Z. Ali, Data analysis for electronic nose systems. *Microchimica Acta* **2006,** *156*, 183-207.
172. F. Guimet, J. Ferré, R. Boqué and F. X. Rius, Application of unfold principal component analysis and parallel factor analysis to the exploratory analysis of olive oils by means of excitation–emission matrix fluorescence spectroscopy. *Analytica Chimica Acta* **2004,** *515*, 75-85.
173. L. R. Tucker, Some mathematical notes on three-mode factor analysis. *Psychometrika* **1966,** *31*, 279-311.
174. P. M. Kroonenberg and J. M. F. ten Berge, The equivalence of Tucker3 and Parafac models with two components. *Chemometrics and Intelligent Laboratory Systems* **2011,** *106*, 21-26.
175. K. R. Murphy, C. A. Stedmon, D. Graeber and R. Bro, Fluorescence spectroscopy and multi-way techniques. PARAFAC. *Analytical Methods* **2013,** *5*, 6557-6566.

Chapter 3

In-Fibre Interferometer Using a Hollow-Core Photonic Crystal Fibre

This chapter is based on the paper entitled "In-fiber Mach-Zehnder interferometer for gas refractive index measurements based on a hollow-core photonic crystal fiber" Optics Express, Vol. 24, Iss. 13 (2016) P. 14086, N. L. P. Andrews, R. Ross, D. Munzke, C. van-Hoorn, A. Brzezinski, J. A. Barnes, O. Reich and H.-P. Loock. Permission to reproduce the material for this chapter has been acquired from OSA. Rachel Ross obtained the pressure response spectral data under my supervision. Camiel van Hoorn and Andrew Brzezinski performed preliminary studies and Dorit Munzke helped with the theory and further experiments. With these exceptions all work presented below is that of the author.

3.1 Introduction

In this chapter, an interferometer is used to detect gaseous samples within small volumes. Measuring samples in small volumes, reduces both cost and waste associated in detecting samples. The interferometer uses a hollow-core photonic crystal fibre (HC-PCF) that is filled with various gases as a single mode absorption cell having typically a volume of only 1.2 μL for a fibre length (and absorption length) of 34.6 cm.

HC-PCFs guide light entirely using the photonic band gap (PBG) with the condition that, $\beta < \omega n_{\text{core}}/c$, where β is the axial wave vector, ω is the frequency of light and c is speed of light in a vacuum.[1, 2] While this condition is obeyed, light is free to propagate within the hollow core but is unable to escape into the cladding. Since light propagates through the air — or even vacuum — in the core of a HC-PCF rather than being guided by a solid glass structure, HC-PCFs found interest as low-loss waveguides or for guiding very high-power light.[2] Additionally, as the light propagates in the hollow core, HC-PCFs are an ideal absorption cell to be used for gas spectroscopy and sensing. Gases can be filled into the small volume of the hollow

channels in the PCF and the loss of transmitted light is detected. The very long interaction path of the sample with the light can also be used to enhance other weak non-linear phenomena [3, 4] including the Raman effect.[5, 6]

In this chapter HC-PCFs are used as in-fibre interferometers. When light from a single mode fibre (SMF) is coupled to a HC-PCF multiple core modes are excited. After propagating through the HC-PCF the modes are coupled into a second SMF, and due to their different phase delays they produce an interferogram. Each of the modes propagation phase is affected differently when the concentration of the gas in the hollow core alters the effective refractive index of the propagating modes. This results in a shift of the interferogram and through this shift, the concentration of the gas in the PCF may be determined. Here, we use a HC-PCF as a simple in-fibre interferometer to determine the refractive index of several different gaseous samples in a small volume.

3.2 In-fibre interferometry

In the past seven years several hundred articles have been published that describe the use of simple in-fibre interferometers to determine the change of the refractive index of liquids. Most interferometers are based on either the Michelson or Mach-Zehnder configuration where one of the interferometer arms is the core of the fibre waveguide and the other arm consists of the cladding material which propagates one or more cladding modes.[7-9] In all in-fibre interferometers a coupler splits the incoming core mode into two (groups of) modes. In the Mach-Zehnder configuration a second coupler then combines these two co-propagating modes into a single mode, whereas in the Michelson configuration a retroreflector doubles the interaction length and the recombination occurs at the same coupler. In either case, the accumulated phase shift in each arm depends on the length of the arm and the effective refractive index of the propagated mode(s),

$$\phi_i = \frac{2\pi}{\lambda} n_i^{eff} L_i , \qquad \textbf{(3.1)}$$

where n_i^{eff} is the phase index of the propagated mode, i, L_i is the geometrical length of the respective arm, and λ is the wavelength of the light in vacuum. If only two modes (i = 1, 2) co-propagate, interference occurs when the two fields are coherently combined and give rise to a wavelength-dependent interferogram of intensity, I, [10, 11]

$$I = I_1 + I_2 + 2\sqrt{I_1 I_2}\cos\left(\phi_1 - \phi_2\right), \tag{3.2}$$

where I_1 and I_2 are the respective intensities and ϕ_1 and ϕ_2 are the phases of the co-propagating modes. The difference in the effective phase indices, Δn^{eff}, is therefore directly related to the difference of the propagation phase $\Delta\phi = \phi_1 - \phi_2$,

$$\Delta n^{eff} = \frac{\lambda\Delta\phi}{2\pi L}. \tag{3.3}$$

In-fibre interferometers are inherently "balanced interferometers", i.e. the geometrical lengths (but not necessarily the optical paths) of the two arms are identical, $L_1 = L_2$, and the two arms expand and contract identically with temperature and strain.[12]

It is straightforward to derive the sensitivity with which an interferometer can measure the refractive index of a sample, n_s. The sensitivity of the phase shift measurement of the sample's refractive index depends on the extent with which either one of the two modes can interact with the sample medium. We define a sensitivity coefficient f_i such that,

$$n_i^{eff} = \left(1 - f_i\right)n_i^w + f_i n_s. \tag{3.4}$$

In equation (3.4) we assume that the effective phase index in each arm, n_i^{eff}, is a weighted sum of the indices of the sample, $f_i n_s$, and the waveguide material $\left(1 - f_i\right)n_i^w$. Equation (3.4) allows us to express the sensitivity of the phase measurement in terms of the relative interaction of the two modes with the sample,

$$\begin{aligned}\frac{d\Delta\phi}{dn_s} &= \frac{2\pi L}{\lambda}\frac{d}{dn_s}\left(n_1^{eff} - n_2^{eff}\right) \\ &= \frac{2\pi L}{\lambda}\frac{d}{dn_s}\left(\left[\left(1-f_1\right)n_1^{w} + f_1 n_s\right] - \left[\left(1-f_2\right)n_2^{w} + f_2 n_s\right]\right). \\ &= -\frac{2\pi L}{\lambda}\left(f_1 - f_2\right)\end{aligned} \tag{3.5}$$

The sensitivity of the interferometer's phase measurement is therefore greatest, if one mode propagates completely through the sample $\left(f_1 = 1\right)$ and the other one remains fully contained in the waveguide $\left(f_2 = 0\right)$. Of course, the sensitivity depends also on the length of the interferometer arms, and the wavelength, λ. Only the magnitude of the phase shift, $\left|\Delta\phi\right|$, can be measured experimentally and, since the sign of the phase is arbitrary, equation (3.5) can be written as,

$$\frac{d\Delta\phi}{dn_s} = \frac{2\pi L}{\lambda}\left|f_1 - f_2\right|. \tag{3.6}$$

In most previously reported works the sensitivity is given as the wavelength shift of an interferometer fringe (i.e. at constant $\Delta\phi$) as a function of sample index. Following a similar route, the corresponding expression is derived as,

$$\frac{d\lambda}{dn_s} = \frac{2\pi L}{\Delta\phi}\left|f_1 - f_2\right|, \tag{3.7}$$

where for attenuation maxima $\Delta\phi = 2\pi\left(m + 1/2\right)$ with m being an integer. By substituting equation (3.3) into equation (3.6) or (3.7), $f = \left|f_1 - f_2\right|$ can be given as,

$$f = \frac{d\Delta n^{eff}}{dn_s}. \tag{3.8}$$

When two neighbouring attenuation maxima at λ_1 and λ_2 and $d\lambda/dn_s$ are known, using equations (3.7) and (3.3) the sensitivity coefficient f is readily determined as,

$$f = \frac{d\lambda}{dn_s}\frac{1}{\lambda L}\frac{1}{\lambda_1^{-1} - \lambda_2^{-1}}. \tag{3.9}$$

Equation (3.5) illustrates that the sensitivity does not depend on the materials' refractive indices of either of the interferometer arms, n_1^w and n_2^w, but it does depend on how strongly the modes are interacting with the sample. For example, if the index of the sample liquid n_s is probed through the sample's interactions with the evanescent field of the cladding modes, the sensitivity coefficient *f* depends on the depth of the evanescent field, i.e. on the mode number, which is associated with the total internal reflection angle. Importantly, the sensitivity — and therefore the limit of detection (LOD) — is in this approximation independent on the type of couplers that are used as long as they excite the same fibre modes. The sensitivity also does not depend on the interference contrast (the visibility) which depends on the relative intensity of the modes, although low contrast may make it difficult to distinguish the interferometer fringes and thereby also reduces the reliability of the measurements. Equation (3.6) shows that the route to high sensitivity measurements involves increasing the "effective interaction length", *fL*, i.e. a parameter that is related to the actual length of the interferometer and to the fraction of light that interacts with the sample.

Equally important for the practical use of an interferometer is the "figure of merit (*FoM*)", i.e. the ratio of the sensitivity and the full-width-at-half-maximum (FWHM) of the spectral feature, $\delta\lambda$. In optical resonators the linewidth, $\delta\lambda$, of a cavity resonance is used and in interferometers it would be most practical to use the width of an interference fringe, $\delta\phi = \pi/2$ which results with Eq. (3.3) in,

$$\delta\lambda = 4\Delta n^{eff} L\,, \tag{3.10}$$

and the *FoM* is therefore simply,

$$FoM = \frac{d\Delta\phi}{dn_s}\frac{1}{\delta\phi} = \frac{4fL}{\lambda}\,. \tag{3.11}$$

In this work we follow the route to maximal sensitivity and largest *FoM*, i.e. we attempt to increase the effective interaction length by maximising the overlap of the mode volume with the sample. This may be done most efficiently in a HC-PCF, where the core mode propagates through the sample-filled hollow core of a microstructured fibre.[2, 13] The many cladding modes in HC-PCF propagate in the patterned silica-walled

microholes surrounding the hollow core, but their phase indices are so different from the core modes (and from each other) that an interferogram is not analysable. We therefore co-propagate two low-lying core modes with different phase indices and measure their interference. In this case the two values of f_1 and f_2 are both near unity, but unfortunately they are quite similar so that the overall sensitivity coefficient $f = f_1 - f_2 = 0.0078$ and is far from the maximal value of $f = 1$. Nevertheless, our simple design is able to outperform nearly all existing in-fibre interferometers and measure the refractive index of several microliter-sized gas samples with an accuracy of better than 1 ppm.

To demonstrate the capabilities of the setup we measure the refractive indices of several gases as a function of their pressure. Even polarisable gases do not exhibit a refractive index change of more than $\Delta n_s / P = 10^{-3}/\text{bar}$ thereby requiring great sensitivity of the interferometer setup. In particular, we measure the refractive indices of several gases at pressures from 0.07 bar to about 0.6 bar. In the near-infrared the refractive index of some molecular gases is a complicated function of wavelength, due to absorption features of overtones and combination bands and their corresponding dispersion behaviour. Additionally, for some molecular gases we observe absorption phenomena in our wavelength window. Below we demonstrate that it is possible to detect refractive index variations as small as 10^{-7} refractive index units. These miniscule changes would be buried in thermal fluctuations for denser samples such as liquids, but in dry gases they remain detectable due to the gases' lower thermal sensitivity of their refractive indices.

3.3 Mode interferometry

3.3.1 Theory

To understand the phase shifts in the interferogram in response to gas pressure, *P*, and temperature, *T*, changes we consider the interdependence of all relevant variables in equation (3.1) above,

$$\Delta\phi = 2\pi \frac{\left(n_1^{eff}\left(P,T,\lambda\right) - n_2^{eff}\left(P,T,\lambda\right)\right)L\left(P,T\right)}{\lambda}. \qquad \textbf{(3.12)}$$

The refractive indices of the propagated modes n_1^{eff} and n_2^{eff} are a function of pressure, temperature and wavelength, and the length of the PCF is also pressure- and temperature-dependent. Assuming only small and linear dependencies equation (3.1) can be written in partial derivatives,

$$\Delta\phi = \sum_i \frac{\partial \Delta\phi}{\partial X_i} \Delta X_i, \quad X_i = P, T, \lambda, \tag{3.13}$$

and therefore,

$$\begin{aligned} d\Delta\phi = & \frac{2\pi\Delta P}{\lambda}\left[\left(\frac{\partial n_1^{eff}}{\partial P} - \frac{\partial n_2^{eff}}{\partial P}\right)L + \frac{\partial L}{\partial P}\left(n_1^{eff} - n_2^{eff}\right)\right] \\ & + \frac{2\pi\Delta T}{\lambda}\left[\left(\frac{\partial n_1^{eff}}{\partial T} - \frac{\partial n_2^{eff}}{\partial T}\right)L + \frac{\partial L}{\partial T}\left(n_1^{eff} - n_2^{eff}\right)\right] \\ & + 2\pi L\Delta\lambda\left[\left(\frac{\partial n_1^{eff}}{\partial \lambda} - \frac{\partial n_2^{eff}}{\partial \lambda}\right)\frac{1}{\lambda} - \frac{\partial L}{\partial P}\left(n_1^{eff} - n_2^{eff}\right)\frac{1}{\lambda^2}\right] \end{aligned} . \tag{3.14}$$

Equation (3.14) accounts for the pressure-induced expansion of the fibre waveguide, $\partial L/\partial P$, as well as its thermal expansion $\partial L/\partial T$, the dependence of the mode index on the gas pressure, $\partial n_i^{eff}/\partial P$, the thermooptic coefficients, $\partial n_i^{eff}/\partial T$, and the dispersion terms $\partial n_i^{eff}/\partial \lambda$.

The pressure-induced length expansion was obtained using $\Delta L = LF/\left(A_{\text{fibre}}E\right)$, where L = 0.346 m is the length of the fibre and $A_{\text{fibre}} = 3.8\times10^{-8}$ m^2 is the surface area of the glass and acrylate coating. The force applied to the fibre by the gas is calculated using $F = \Delta P A_{\text{hole}}$ where $A_{\text{hole}} = 3.4\times10^{-9}$ m^2 is the cross sectional area of all holes in the HC-PCF, i.e. the area of the centre hole with diameter 10 µm and of 294 holes with a diameter of 3.8 µm. The Young modulus of the fibre E = 16.56 ± 0.39 GPa was previously determined for a fibre coated by a polymer jacket.[14] The contribution of the pressure-induced expansion of the HC-PCF is $\Delta L/\Delta P = 1.9\times10^{-12}$ m Pa^{-1} and is negligible compared to the $\partial n_i^{eff}/\partial P$ terms.

The thermal expansion of the fibre, $\partial L/\partial T = a_L L = 2.1\times10^{-5}$ m K^{-1}, was obtained from L = 0.346 m and $a_L = 6.0\times10^{-5}$ K^{-1}. The value a_L is the cross-section-weighted average of the linear thermal expansion coefficients of the hollow-core fibre material, $a_{\text{silica}} = 5.5\times10^{-7}$ K^{-1},[15, 16] and its 50 μm acrylate coating, approximated with $a_{\text{PMMA}} = 7.6\times10^{-5}$ K^{-1}.[16, 17] With Δn^{eff} = 0.0096 (see section 3.5.1) we determine $\partial L/\partial T\left(n_1^{eff} - n_2^{eff}\right) = 2.0\times10^{-7}$ m K^{-1}. This value almost offsets the contribution from the difference of the thermooptic coefficients, $\left(\partial n_1^{eff}/\partial T - \partial n_1^{eff}/\partial T\right)L = -2.04\times10^{-7}$ m K^{-1}, which was calculated using the eigenmode solver, *Lumerical*, with the thermooptic coefficients of Corning 7980 glass (see section 3.3.2).

The dispersion of gas and fibre material $\partial n^{eff}/\partial\lambda$ could be neglected, since the phase shifts were obtained in wavelength windows that were as narrow as 100 pm. The term $\partial n^{eff}/\partial P$ corresponds to the pressure dependence on the modes' effective refractive index. Changing the pressure of the gas inside the PCF has a strong effect of the sample's index, n_s, inside the holes. This index can be related to temperature and pressure as well as the gases' polarisability, α_s, through the Lorentz-Lorenz equation,[18]

$$\frac{n_s^2 - 1}{2 + n_s^2} = \frac{PN_A\alpha_s}{3RT\varepsilon_0}, \qquad \textbf{(3.15)}$$

where N_A is Avogadro's constant, α_s is the polarisability of the gas, R is the gas constant, T is the temperature, and ε_0 is the vacuum permittivity. Of course, changing the hole medium's index also affects the mode volume, and therefore the phase index of the mode. Even in the linear approximation the term $\Delta n/\Delta P$ is therefore difficult to predict. The problem is exacerbated by the fact that in our setup the fibre is bent. We therefore performed a computational modal analysis of the $\partial n^{eff}/\partial P$ term using the *Lumerical* eigenmode solver software.

3.3.2 Modelling of the eigenmodes

To model the modes within the PCF an eigensolver analysis program (*MODE Solutions*, *Lumerical*) was used. The PCF (HC-1550-02, NKT Photonics) was modelled as a patterned structure made from Corning 7980 glass at 23 °C having a bulk index of 1.445034.[19] In the model the central core has a radius of 4.8 µm and the surrounding holes have radii of 1.7 µm and a pitch of 3.8 µm, corresponding to the values given by the manufacturer of the HC-PCF. The calculated five dominant core modes near 1532 nm are shown in **Figure 3.1** along with our scanning electron microscope image of the PCF (Quanta 250, *FEI*, SEM spectrometer). According to Aghaie et al. these modes are best labelled as "quasi-$TEM_{m,n}$ modes" as they are not distinctly soley TEM being that there are 3 symmetry components, but for convenience we will simply refer to them as $TEM_{m,n}$ modes.[20, 21] The TEM designation represents transverse electromagnetic modes and the values for m and n represent their order.

The TEM_{01} mode and the TEM_{10} are not degenerate, since the fibre's hole pattern does not have C_4 symmetry. Also, when the PCF is bent in the horizontal plane the TEM_{01} mode is expected to be more affected than the TEM_{10} mode. Even the TEM_{00} mode has two polarisation components that are not degenerate. We denote the horizontally polarised mode as TEM_{00} and the vertically polarised mode as TEM_{00}*.

To compare with our experimental studies at different gas pressures, mode calculations were performed using different indices of the medium inside the holes in the range of 1.0000 to 1.0006 in steps of 10^{-4}. The temperature dependence of the holes was modelled to contain a gas with a polarisability $\alpha_s = 6.57\times10^{-40}$ $J^{-1}C^2m^2$ (similar to ClF_2CH) and a temperature dependence according to equation (3.15) while the glass portion of the PCF was modelled as Corning 7980 glass with respective Sellmeier coefficients.[19]

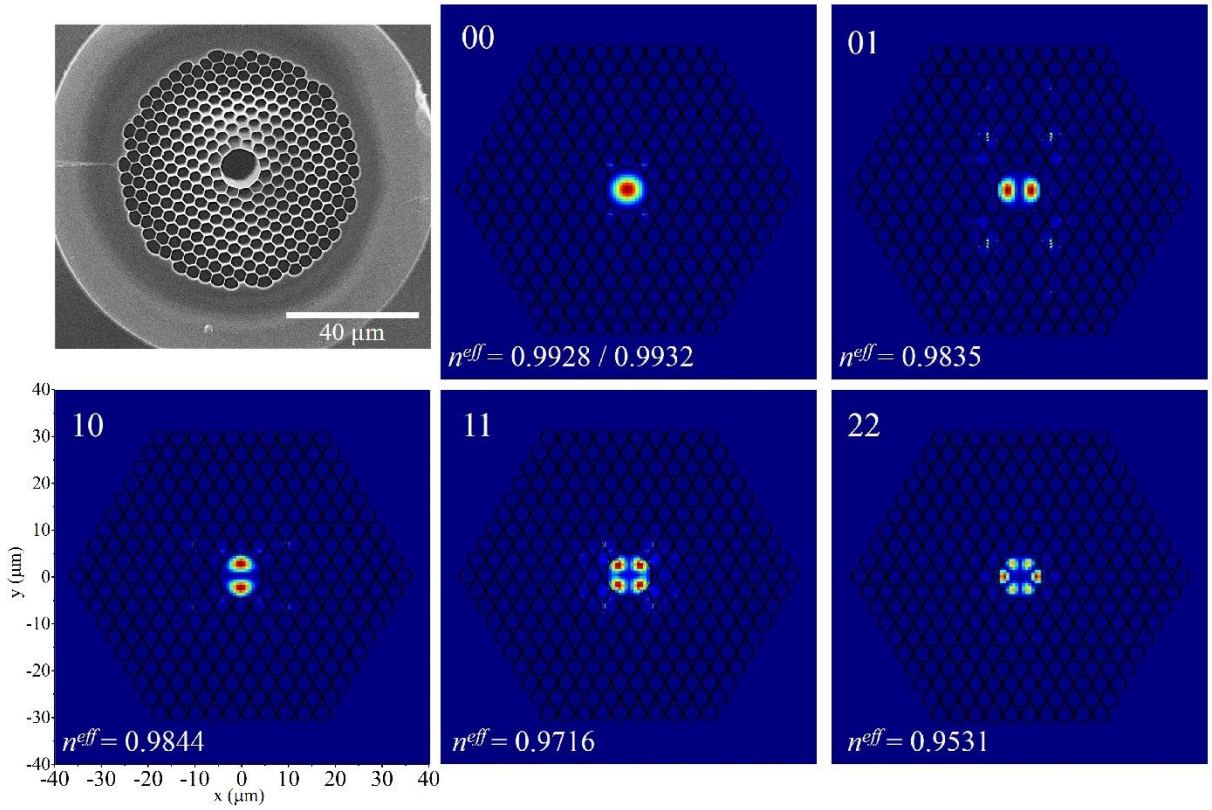

Figure 3.1: The first five core modes that are guided through the PCF (HC-1550 NKT). The top left image of the PCF used was obtained using a scanning electron microscope. The other images show five of the core modes simulated using the eigensolver modal analysis. The effective indices were obtained setting the hole interiors at vacuum, the bend radius to R = 30 mm, and the temperature to T = 23°C. The two polarisation states of the core TEM_{00} mode give different effective indices. The dimensions used for the calculations were to match those of the HC-1550C PCF given by *NKT photonics*.

We identified the modes responsible for the interference patterns from their accumulated phase difference and their experimentally measured $\Delta n^{eff} \approx 0.010$ (see section 3.5). It is apparent that the core modes cannot interfere with any of the cladding modes, since then the respective value for Δn^{eff} would be much larger.

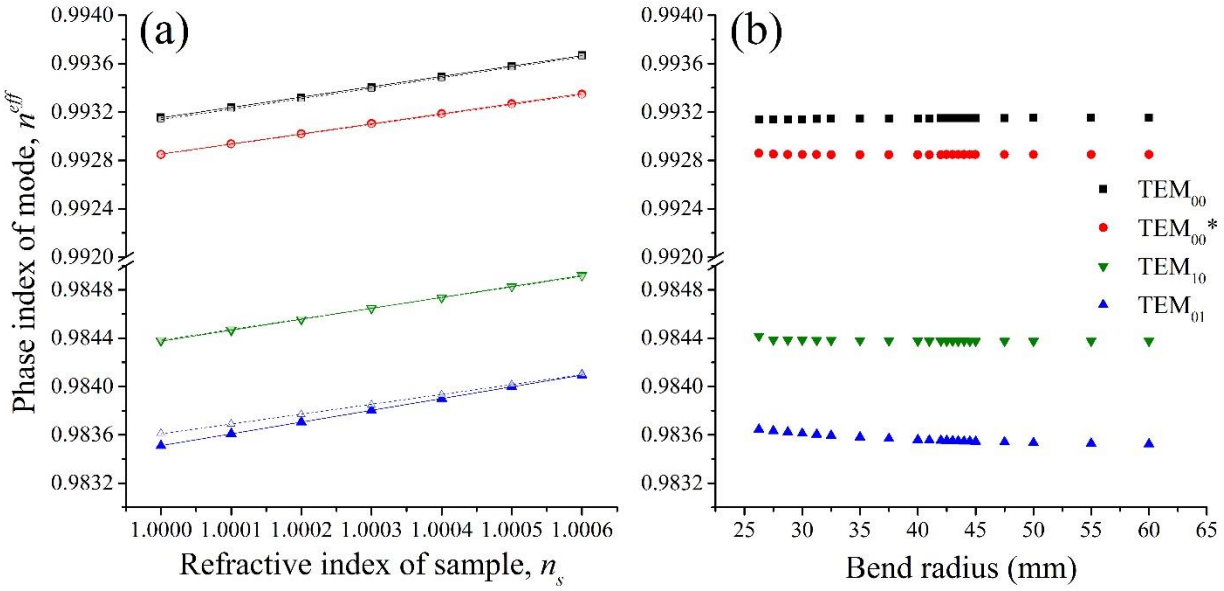

Figure 3.2: Phase index of the core modes that propagate along the HC-PCF shown in **Figure 3.1**. **(a)** The calculated phase indices, n^{eff}, of the four lowest lying core modes of **Figure 3.1** as the sample's index in the holes, n_s, was increased. The hollow data points are the effective index with a bend radius of 30 mm and the solid data points represent the effective index of the modes in a straight fibre. For the TEM_{00}*, TEM_{00}, and TEM_{10} modes the phase index is nearly independent on the bend radius. **(b)** The phase indices, n^{eff}, as a function of bending radius calculated as in **(a)** but for n_s = 1.0.

We further assume that only modes carrying light of the same polarisation can interfere, i.e. that the interferograms arise from interference of either the horizontally polarised TEM_{00}:TEM_{01} mode pair or the vertically polarised TEM_{00}*:TEM_{10} mode pair.

The phase index associated with these modes was calculated as a function of material index inside the holes and the PCF bend radius (**Figure 3.2**). It is found that the phase indices of the TEM_{00} (polarised in the bend plane) and the equivalent TEM_{00}* mode (polarised normal to bend plane) change approximately linearly with increasing refractive index of the medium inside the holes, but do not vary greatly when the fibre is bent (**Figure 3.2(a)**). Note that, perturbation theory could be used to calculate the phase indicies of the modes but was not used here. It would then be very interesting if this was investigated. Similarly, the TEM_{10}

mode index increases linearly with the index of the sample gas, but is largely insensitive to the bend radius. On the other hand, the index of the TEM_{01} mode, which is polarised in the bend plane, strongly depends on the bend radius as the fibre is bent in the polarisation plane. When the empty PCF is bent to 30 mm the TEM_{01} mode index increases from $n_2^{eff} = 0.98351$ to 0.98361.

More importantly, the *difference* of the horizontally polarised TEM_{00} and TEM_{01} mode indices, $\Delta n^{eff} = 0.0095$ (**Figure 3.3(a)**), is consistent with the experimentally obtained index difference of $\Delta n^{eff} = 0.010$ associated with the 1.43 nm^{-1} peak in the Fourier transform (FT) of the interferogram (**Figure 3.3(a)** and **Figure 3.5** and **Figure 3.6** below). It is not impossible that the vertically polarised mode pair, TEM_{00}*:TEM_{10}, is contributing to the interference pattern giving $\Delta n^{eff} = 0.0088$, but we have not seen experimental evidence for this effect.

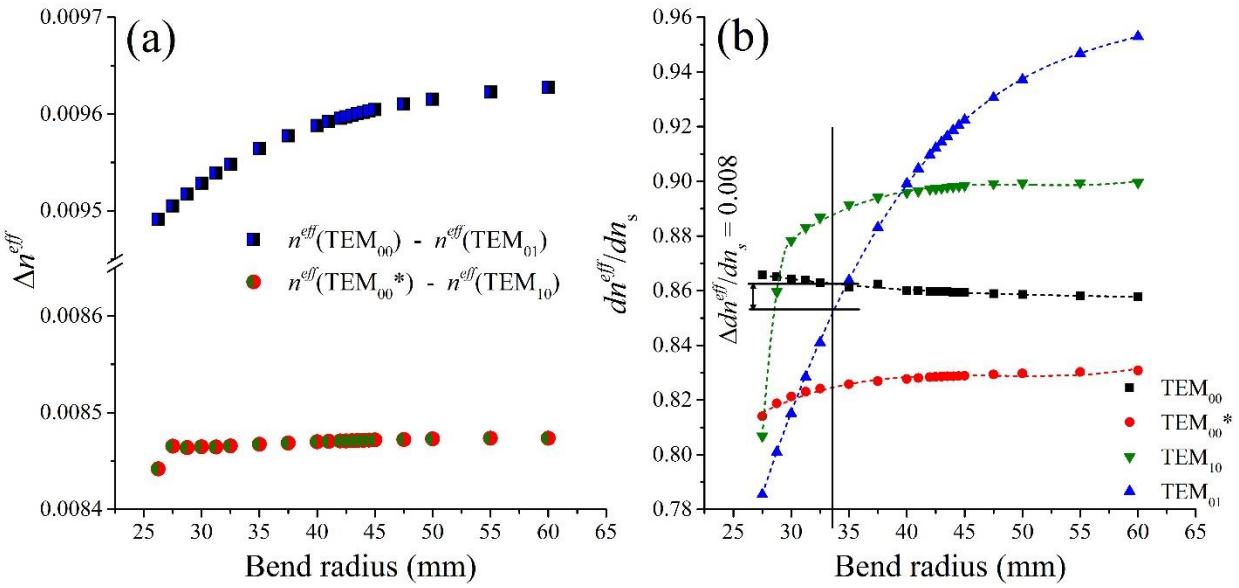

Figure 3.3: The effect on the phase index of the main core propagating modes as the PCF is bent. **(a)** The difference in phase index responsible for the interference spectrum, Δn^{eff}, is shown for the two modes polarised in the bending plane $\Delta n^{eff} = n^{eff}(TEM_{00}) - n^{eff}(TEM_{01})$ in blue and black squares and the two out-of-plane polarised modes $\Delta n^{eff} = n^{eff}(TEM_{00}*) - n^{eff}(TEM_{10})$ in red and green circles. **(b)** The sensitivity dn^{eff}/dn_s for the core modes as the bend radius is increased is calculated from the first derivative of **Figure**

3.3(a). The dashed lines are meant to guide the eye. The short black arrow corresponds to a sensitivity of the interference measurement $f = \Delta dn^{eff}/dn_s = d\Delta n^{eff}/dn_s = 0.008$.

Table 3.1: Polarisabilities of the gases investigated with references. For He, Ar, N_2, and C_2H_2 the polarisability was calculated using known dispersion and refractive indices at 1532 nm. The static average electric dipole polarisabilities for the ground state of all gases are also shown.

Gas	**α from n at 1532 nm ($\times 10^{-40}$ J^{-1}C^{2}m^2)**		**Average α ($\times 10^{-40}$ J^{-1}C^{2}m^2)**		**Grade, purity (company)**
He	0.229	[22]	0.228	[23]	Ultra-high purity 5.0, 99.999% (*Praxair*)
Ne			0.44	[23, 24]	5.0 grade, 99.999% (*Linde*)
Ar	1.74	[25]	1.82	[23, 26]	4.8 grade, 99.998% (*Praxair*)
N_2	1.95	[27]	1.96	[28]	4.8 grade, 99.998% (*Praxair*)
NH_3			2.47	[28]	Anhydrous 4.5 grade, 99.995% (*Praxair*)
C_2H_2	3.86	[29]	3.88	[28, 29]	Dissolved 2.6 grade, 98% (*Praxair*)
CF_4			4.27	[23, 30]	>99.9% (*Sigma Aldrich*)
Xe			4.50	[23, 31]	5.0 research grade, 99.999% (*Praxair*)
ClF_2CH			6.58	[23, 32]	99.95-99.999% (*Matheson*)

Changing the index of the material inside the holes from n_s = 1.0 to 1.0006, allows us to estimate the sensitivity of measurement depending on the pair of beating modes that is involved as well as the bend radius. **Figure 3.3(b)** shows the dependence of the sensitivity dn^{eff}/dn_s on the bending radius. It is apparent that the modes that have no nodes along the bend axis are hardly affected by bending the waveguide, whereas the TEM_{01} mode that has a nodal plane along the axis of the bend is strongly affected. Especially for the TEM_{01} mode (and at very small bend radii the TEM_{10} mode) the sensitivities depend strongly on the bend radius. At the experimental bend radius of approximately 34 mm the TEM_{00}:TEM_{01} mode pair shows a sensitivity of the interference measurement $f = \Delta dn^{eff}/dn_s = 0.008$ (see also equation (3.5)).

3.4 Experimental

The experimental setup is shown in **Figure 3.4**. The experiments were carried out using a tuneable laser source (AQ4320D, ANDO, linewidth <1 MHz and typically 200 kHz), which was coupled to a SMF. The HC-PCF (L = 346 mm, HC-1550-02, NKT Photonics) was coupled to the SMF using ceramic ferrules with a small gap of a few µm to allow gas to vent in and out of the PCF. The output from the PCF was coupled into a second SMF and detected using an InGaAs amplified detector (PDA 10CS, Thorlabs) set to 10 dB. The setup required that the fibre was bent with a bend radius of about 30-35 mm.

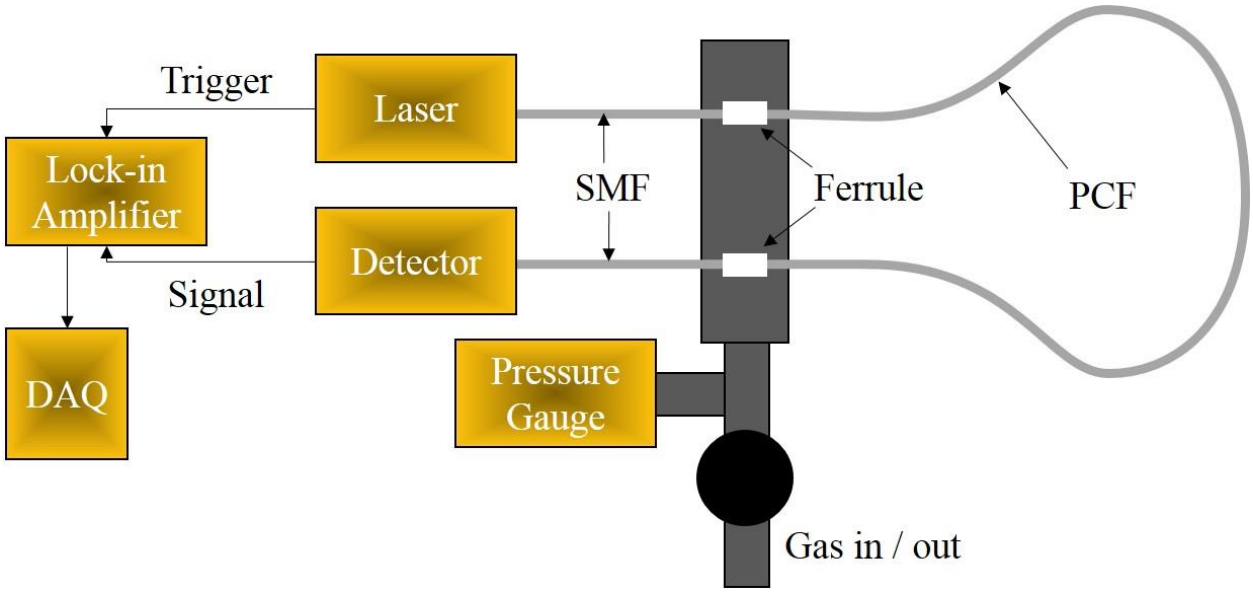

Figure 3.4: Experimental setup of the in-fibre PCF interferometer. Laser light is coupled into a single mode fibre (SMF). Using gas-permeable ferrules the light is then coupled into the hollow-core photonic crystal fibre (length 346 mm). The photodetector signal is recorded through a lock-in amplifier.

The laser was chopped with a frequency of 300 kHz and was scanned from 1527 nm to 1537 nm with a step increment of 1 pm (about 12 MHz). At each wavelength, 15 data points were collected and averaged. The detector output was sampled by a lock-in amplifier (Mode 5202, Princeton Applied Research) that was synchronised to the laser. The lock-in amplitude was recorded using a digital data acquisition card (USB-

201, Measurement Computing). While the laser was polarised in the bending plane, polarisation was not actively measured or controlled.

3.5 Results and discussion

3.5.1 In-fibre PCF interferometer pressure dependence

The in-fibre PCF interferometer of **Figure 3.4** was filled with nine different gases having different polarisabilities (

Table 3.1); for each gas, interferograms were obtained at nine different pressures between 0.07 bar and 0.6 bar. To remove any residual gas, the system was flushed with the new gas three times before each measurement. The system was then filled with the gas to a pressure of up to approximately 0.6 bar and allowed to settle for 20 min to ensure that the gas completely diffused along the photonic crystal fibre before measurements were taken. The volume of the PCF holes is only $A_{hole}L$ = 1.2 μL. The temperature was kept at 296 ± 1 K.

Figure 3.5 shows normalised spectra collected for all nine gases as the pressure within the fibre was decreased. The spectra show interference patterns that are caused by the TEM_{00} core modes of the PCF beating with either one or several higher-order core modes. The panels in **Figure 3.5** are arranged in order of increasing gas polarisabilities (

Table 3.1) and accordingly show an increase in phase shift with pressure. Ammonia and acetylene are the only two gases with obvious vibrational overtone absorption features. As expected the transmission spectra show a linear increase of the absorption with increasing gas pressure.

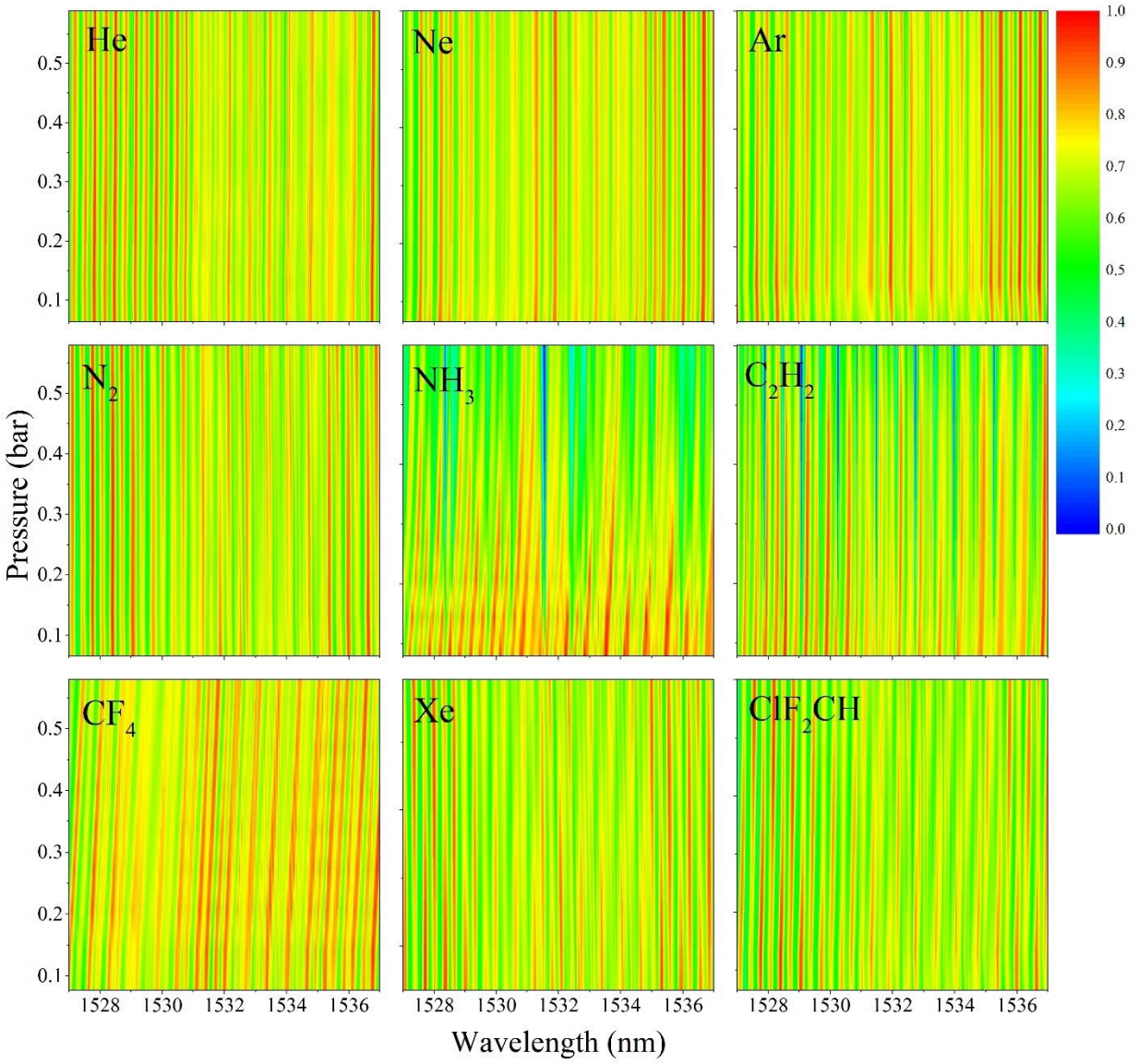

Figure 3.5: Normalised intensities of all nine gases measured using the in-fibre interferometer so that the maximum intensity equals 1. The gases are presented in the order of increasing polarisability, from top left to bottom right corners and were chosen to encompass a range of polarisabilites. To generate these plots the pressure of the gas within the PCF was selected and the wavelength of the tuneable diode laser was scanned from 1527-1537 nm, and repeated for a range of pressures. The normalised intensity is coloured from blue to red to show 0 to 1.

To quantify the pressure-dependent phase shift in the interferograms, we perform a fast Fourier transform (FFT). The delta peak was reduced by subtracting the constant background and multiplying the spectra with a cosine function, where cos(0) is placed at the start wavelength and cos(π/2) at the end wavelength. The data was padded with 20,000 extra zeros to increase the Fourier transform resolution. **Figure 3.6** shows the resulting FT of chlorodifluoromethane and acetylene interferograms recorded at three different pressures. The peaks at 1.43 nm^{-1} and 3.1 nm^{-1} in the chlorodifluoromethane and acetylene interferograms correspond to two mode pairs, i.e. TEM_{00}:TEM_{01} (**Figure 3.3(a)**) and probably TEM_{00}:TEM_{11}. The corresponding wavelength difference can either be obtained by fitting the interference fringes of **Figure 3.5** using equation (2.9) or from the reciprocal values of the peaks in the FT and equation (3.3). Using equation (3.12) both methods give the effective phase index differences of $\Delta n^{eff} = 0.010$ and 0.021, respectively. The other peaks in **Figure 3.6(b)** arise from harmonics and combinations in the interferogram and are multiples of the beat frequencies of 1.43, 3.1 and 1.6 nm^{-1}. Minor peaks appear to be beats of higher order core modes in the fibre. In contrast to these interference fringes the amplitude of the peak in the acetylene interferograms at 1.6 nm^{-1} increases with pressure and corresponds to the $\nu_1+\nu_3$ combination absorption band with a line-to-line separation of ~0.63 nm. It is apparent in the interferograms as well as in their Fourier transform that the phase of this latter peak does not change with pressure.

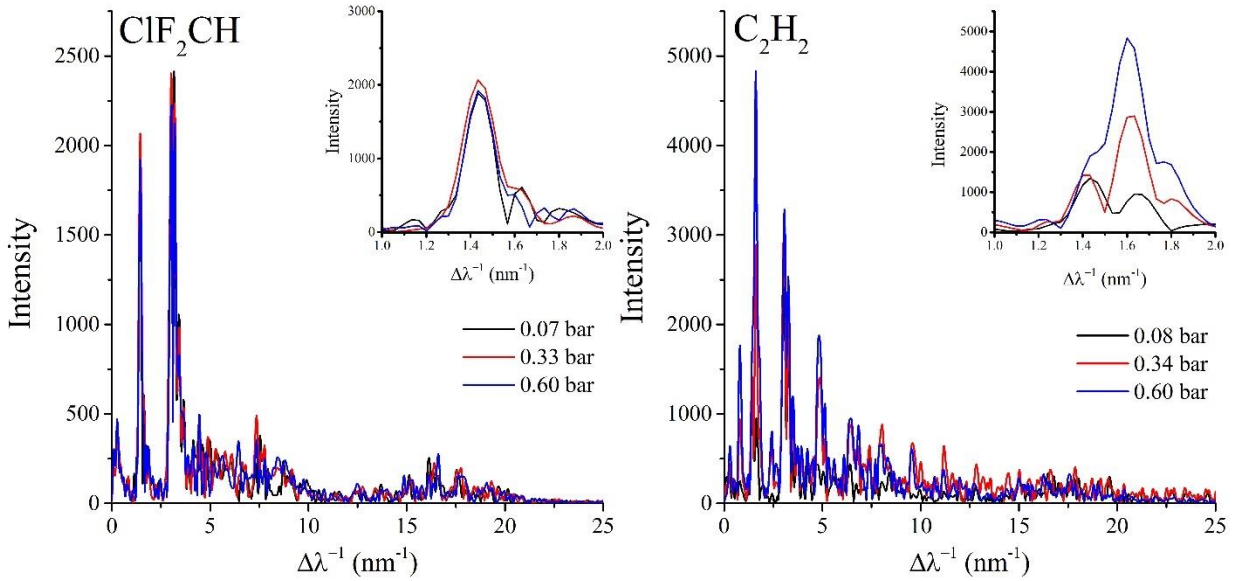

Figure 3.6: Spatial frequencies obtained using a FFT of the chlorodifluoromethane acetylene spectra. The black, red, and blue lines represent the gases at low medium and high pressure. The inset shows the peak located at 1.43 nm^{-1}, which corresponds to the interference pattern separated by 0.69 nm as shown in **Figure 3.5**. Acetylene has a structured absorption band at 1527-1537 nm and this is apparent in the FT by a concentration dependent peak at 1.60 nm^{-1}.

To investigate how the interferograms shift as a function of gas pressure, the phase of the FFT was extracted using (3.16) and unwrapped to remove the steps caused by the discontinuity of the tangent function,

$$\phi = -\arctan\left(\frac{\Im\left(F(\omega)\right)}{\Re\left(F(\omega)\right)}\right). \qquad \textbf{(3.16)}$$

For the prominent 1.43 nm^{-1} peak the unwrapped phases are shown in **Figure 3.7(a)** as a function of pressure. All nine gases show a linear dependence of the interferometric phase on the gas pressure. For small changes of the gas index, n_s the Lorentz-Lorenz equation (3.15) predicts an approximately linear dependence on pressure. Accordingly, the interferometric phase changes from equation (3.6) depend linearly on gas pressure and on the polarisability.

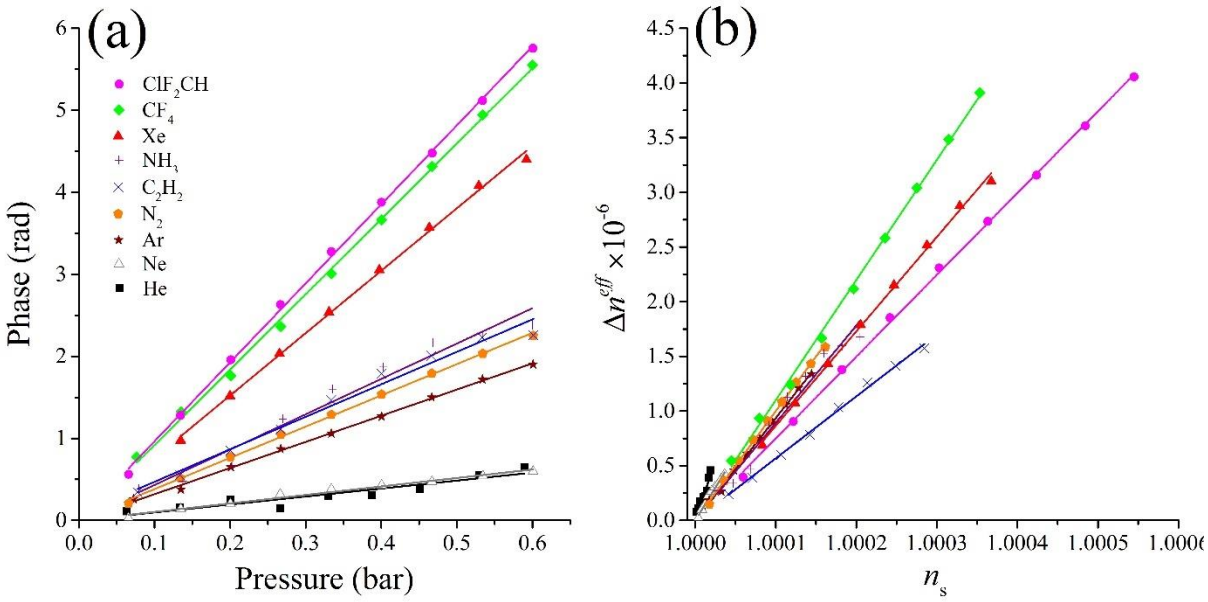

Figure 3.7: Phase dependence for all nine gases as the pressure in the PCF was decreased. **(a)** Phase as a function of pressure for each of the nine gases. The slope increases with the polarisability of the gas. **(b)** The dependence of the effective index difference between the beating modes and the index of the gas in the holes. Δn^{eff} was calculated using equation (3.3) from the phase at the centre wavelength of 1532 nm. The index of the gas in the holes, n_s, was obtained using equation (3.15) from the pressure and polarisability (**Table 3.1**) of each gas.

3.5.2 In-fibre PCF interferometer sensitivity characterisation

The measured sensitivities may be compared to previously reported polarisabilities of the nine gases (**Table 3.1**). **Figure 3.7(b)** uses the experimentally obtained phase shift from the Fourier analysis and equation (3.3) to obtain Δn^{eff}. The index of the gas inside the holes, n_s, was calculated from the experimental pressure, the previously reported polarisabilities and the Lorentz-Lorenz equation (3.15). We expect all data to fall on the same straight line. Its slope corresponds to the sensitivity coefficient, f, and is expected to be between 0.05 and zero depending on the exact fibre bend radius (see section 3.3.2). The slopes in **Figure 3.7(b)** vary in the range of $f = 0.022 \pm 0.003$ for helium to 0.0052 ± 0.0003 for acetylene with an average value near $f = 0.0078$ for all nine gases. For comparison, if one assumes a phase shift corresponding to an "effective bend radius" of 33.5 mm, the calculated sensitivity $f = 0.008$ (**Figure 3.3(b)**) is very close to that experimentally observed.

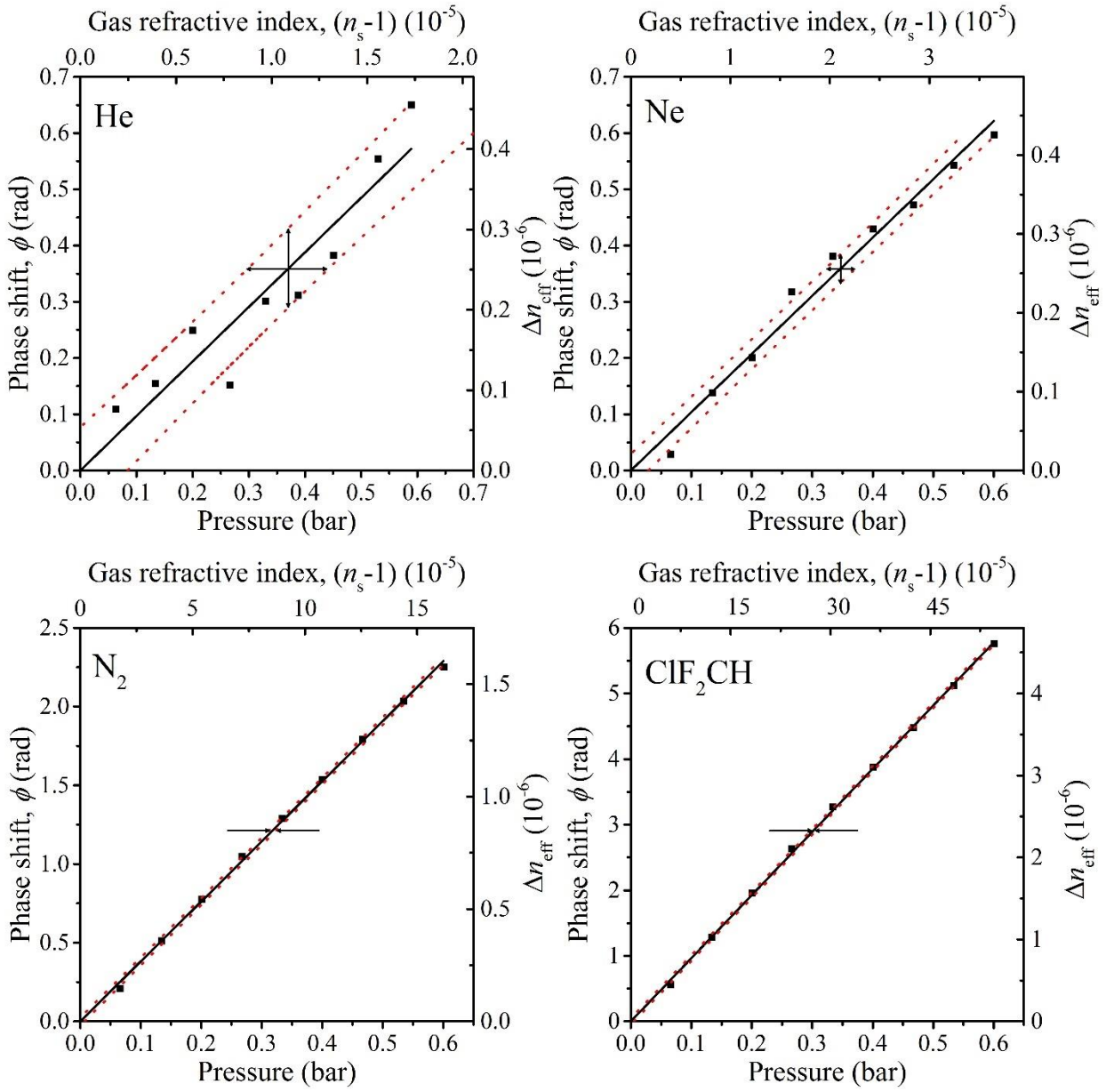

Figure 3.8: Interferometric phase measured for helium, neon, nitrogen and ClF_2CH at different pressures (From **Figure 3.7(a)**). The corresponding Δn^{eff} was calculated using equation (3.6) from the phase at the centre wavelength of 1532 nm. The index of the gas in the holes, n_s, was obtained from the pressure and polarisability (

Table 3.1) of each gas from the pressure using equation (3.15). The minimal detectable gas refractive index change δn_s = 0.5-1.0 $\times 10^{-6}$ is indicated by horizontal arrows and corresponds to the width of the 1σ-confidence interval (95%).[33]

The variation of the observed sensitivity coefficients, *f*, may point to inadequacies of the reported polarisabilities in predicting the refractive index at 1532 nm. In addition, absorption features in acetylene and ammonia cause strong wavelength-dependent index changes [34] and for most gases the polarisability was obtained from an average value in the infrared region of the spectrum. It is also possible that the variation of the sensitivity coefficients observed for the different gases points towards our difficulty to control the polarisation states in our experiment given that the fibre is bent and may also be under torsion. The smallest detectable refractive index change at the 1σ level can be calculated from the calibration curves following [33] and is shown for 4 typical gases to be 0.5-1.0 $\times 10^{-6}$ (**Figure 3.8**). This corresponds to a minimal detectable phase change of $\delta\Delta\phi \approx 0.1$ rad. The sensitivity coefficients of the measurement which depends on the sensitivity of the phase indices of the beating modes towards the refractive index of the sample was calculated as $f = 0.008$ for a bend radius of 33.5 mm and was experimentally measured to be $f = 0.0078$.

Figure 3.9 shows a calibration curve where the instrument-specific sensitivity coefficient $f = 0.0078$ (the average *f* value for all 9 gases) was used to correlate the pressure-corrected interferometric phase against previously measured gas polarisabilities (

Table 3.1). Such a calibration curve may be used to determine the refractive index of an unknown gas at known pressure.

These sensitivity coefficients *f* permit the calculation of the figure of merit, $FoM = 4fL/\lambda = 7050$, calculated from equation (3.11) and with $f = 0.0078$. This figure of merit implies that an interference fringe shifts by $d\Delta\phi = \pi/2$ when the sample's index changes by $dn_s = 1/7050 = 1.4 \times 10^{-4}$. In more conventional terms the sensitivity of an attenuation minimum to the gases index change is 1233 nm/RIU.

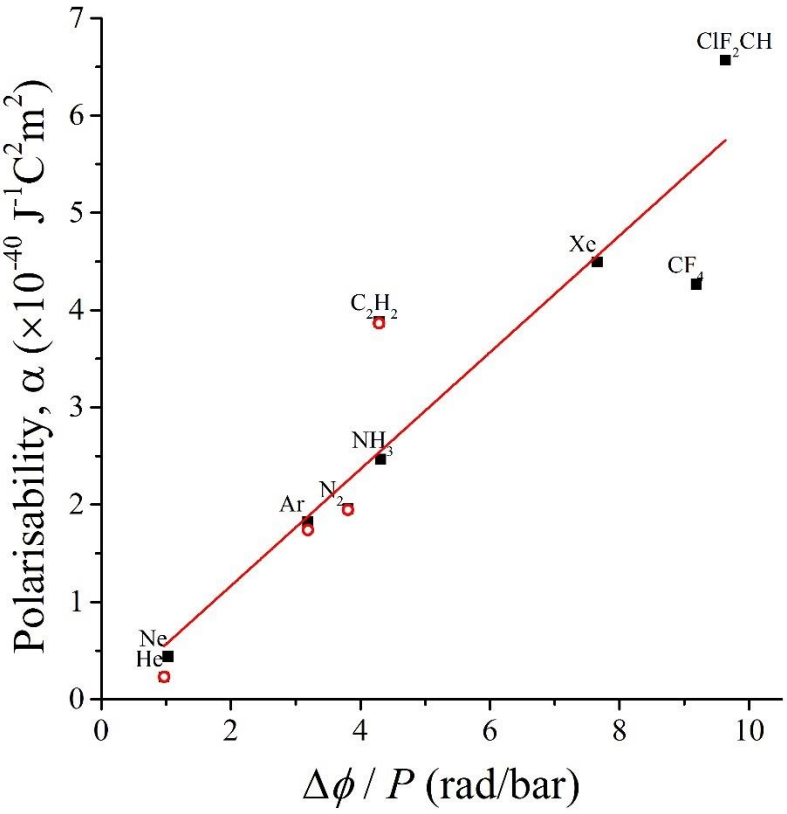

Figure 3.9: Experimental calibration to determine the polarisability from the phase-pressure dependence. The solid black squares and hollow red circles represent the static average electric dipole polarisabilities for the ground state and the true polarisability at 1532 nm calculated from dispersion, respectively. The line is a linear fit of the data with a slope and intercept of $6.00 \pm 0.84\times10^{-41}$ $J^{-1}C^2m^2bar$ and $-0.4 \pm 4.9\times10^{-41}$ $J^{-1}C^2m^2$, respectively.

3.6 Concluding remarks

The in-fibre PCF interferometer discussed in this chapter, has shown a dependence on the pressure of the gas present in the hollow cavities in the fibre. As the hollow core is filled with a gas its index increases, which affects the modes that are guided through the core of the PCF and hence their interference with each other. The sensitivity coefficient for the in-fibre PCF interferometer was obtained to be $f = 0.0078$ as an average for all 9 gases and the *FoM* was determined to be 7050. While these are respectable results by any measure, they are not optimal. The sensitivity, *f*, and accordingly the *FoM* and detection limit could all be improved, if the two modes that are beating were not both core modes, i.e. if they were not both propagating

to a similar extent through the sample gas. Note that the sensitivty factor f = 0.78 % is far below the optimal value of 100 % expected for two modes in which one travels exclusively through the sample and the other one travels through material that is not affected by the sample medium. Such a setup would require a balanced in-fibre Mach-Zehnder interferometer consisting of one mode traveling entirely through the hollow core, which also contains the sample gas, and beating against a single second mode that propagates through, for example, a solid glass core contained in the same fibre. To our knowledge such a fibre does not exist, yet.

One might propose that a hollow-core PCF operating at longer wavelength, when it supports only a single core mode might act as such a Mach-Zehnder-interferometer. Here the second mode would be a cladding mode. However, it would be difficult to set up such an instrument as it would require filling the hole with an inert gas of low index (ideally helium) sealing the holes and then launching a single cladding mode of well-defined phase index together with the core mode. Alternatively, one can devise an unbalanced MZ-interferometer similar to the Young interferometer described by Shavrin et al.[34] Here the two modes travelled through approximately identical lengths of HC-PCF and regular SMF and were beating when they recombined. The differential response to temperature and birefringence would likely make it difficult to increase the experimental sensitivity, however.

Almost all previous variants of in-fibre interferometers are designed to measure the refractive indices of liquid samples, n_s.[35-38] Typically, one of the interfering modes is the core mode of a single mode fibre with effective (phase) index n_1^{eff} which does not interact with the sample (the reference arm). In the sensing arm one propagates either a single cladding mode or the superposition of many similar cladding modes, with effective index n_2^{eff}, that may interact with the sample through the evanescent field. The interaction may be enhanced by, e.g., the use of tapers [39] or field access blocks.[7-9, 40] Usually, the sensitivity is reported as an interference wavelength shift with sample index. Typical values are $d\lambda/dn_s \approx 25$ nm/RIU for 38 and 62 mm

tapers,[8] 200 nm/RIU for a 12 mm taper,[39] and 1600 nm/RIU for a 0.66 mm taper.[41] The sensitivity coefficients may then be estimated with equation (3.9) and are between $f = 7\times10^{-5}$, 5×10^{-4} and 4×10^{-2}, showing that it is difficult to obtain strong interaction of the propagated modes in the sensing arm with the sample liquid.

Our setup is quick to construct and simple to use. The interpretation of the interferograms requires no more than a phase analysis using Fourier transforms. The setup is uniquely suited to measure the refractive index of small gas volumes of about a microliter (1.2 μL in our case), and could be adapted to measurements of liquid indices. It is nevertheless limited to *relative* measurements of refractive index, i.e. the interferometric phase at a given partial pressure has to be compared to either the phase at vacuum, or the phase with a different partial pressure of the same gas, or to that of a reference gas at the same pressure. This is a common limitation of interferometric measurements, however. We note that the sensitivity might simply be increased by careful control of the bending radius and polarisation as **Figure 3.3(b)** indicates. Both values may be improved by decreasing the bending radius beyond 30 mm and launching light that is polarised in the bending plane. Trivially, it is also possible to simply increase the length of the fibre interferometer.

3.7 Bibliography

1. R. S. Quimby, *Photonics and lasers: An introduction*, John Wiley & Sons, 2006.
2. P. S. J. Russell, Photonic-crystal fibers. *Journal of Lightwave Technology* **2006,** *24*, 4729-4749.
3. F. Benabid, J. C. Knight, G. Antonopoulos and P. S. J. Russell, Stimulated Raman scattering in hydrogen-filled hollow-core photonic crystal fiber. *Science* **2002,** *298*, 399–402.
4. F. Benabid, P. S. Light, F. Couny and P. S. J. Russell, Electromagnetically-induced transparency grid in acetylene-filled hollow-core PCF. *Optics Express* **2005,** *13*, 5694.
5. A. Khetani, A. Momenpour, E. I. Alarcon and H. Anis, Hollow core photonic crystal fiber for monitoring leukemia cells using surface enhanced Raman scattering (SERS). *Biomedical Optics Express* **2015,** *6*, 4599-4609.
6. T. Jochum, L. Rahal, R. J. Suckert, J. Popp and T. Frosch, All-in-one: A versatile gas sensor based on fiber enhanced Raman spectroscopy for monitoring postharvest fruit conservation and ripening. *Analyst* **2016,** *141*, 2023-2029.
7. Z. Tian, S. S.-H. Yam and H.-P. Loock, Single-mode fiber refractive index sensor based on core-offset attenuators. *IEEE Photonics Technology Letters* **2008,** *20*, 1387-1389.
8. Z. Tian, S. S.-H. Yam and H.-P. Loock, Refractive index sensor based on an abrupt taper Michelson interferometer in a single-mode fiber. *Optics Letters* **2008,** *33*, 1105-1107.

9. Z. Tian, S. S.-H. Yam, J. Barnes, W. Bock, P. Greig, J. M. Fraser, H.-P. Loock and R. D. Oleschuk, Refractive index sensing with Mach-Zehnder interferometer based on concatenating two single-mode fiber tapers. *IEEE Photonics Technology Letters* **2008,** *20*, 626-628.
10. H. Y. Choi, M. J. Kim and B. H. Lee, All-fiber Mach-Zehnder type interferometers formed in photonic crystal fiber. *Optics Express* **2007,** *15*, 5711.
11. B. H. Lee and J. Nishii, Dependence of fringe spacing on the grating separation in a long-period fiber grating pair. *Applied Optics* **1999,** *38*, 3450.
12. K. T. V. Grattan and B. T. Meggitt, *Optical fiber sensor technology: Fundamentals*, Springer US, Boston, MA, 2013.
13. Y. Cao, W. Jin, F. Yang and H. L. Ho, Phase sensitivity of fundamental mode of hollow-core photonic bandgap fiber to internal gas pressure. *Optics Express* **2014,** *22* (11), 13190-13201.
14. P. Antunes, F. Domingues, M. Granada and P. Andr, in *Selected Topics on Optical Fiber Technology*, ed. M. Yasin, InTech, 2012.
15. W. Wei and Y. Bo, Analysis of temperature effect in fiber optics ring resonator based on photonic crystal fiber. *Optik - International Journal for Light and Electron Optics* **2015,** *126*, 2094-2098.
16. S.-C. Her and C.-Y. Huang, Thermal strain analysis of optic fiber sensors. *Sensors* **2013,** *13*, 1846-1855.
17. M. Esposito, S. Buontempo, A. Petriccione, M. Zarrelli, G. Breglio, A. Saccomanno, Z. Szillasi, A. Makovec, A. Cusano, A. Chiuchiolo, M. Bajko and M. Giordano, Fiber Bragg Grating sensors to measure the coefficient of thermal expansion of polymers at cryogenic temperatures. *Sensors and Actuators A: Physical* **2013,** *189*, 195-203.
18. J. E. Saunders, C. Sanders, H. Chen and H.-P. Loock, Refractive indices of common solvents and solutions at 1550 nm. *Applied Optics* **2016,** *55*, 947.
19. D. B. Leviton and B. J. Frey, Temperature-dependent absolute refractive index measurements of synthetic fused silica. *arXiv:0805.0091 [physics]* **2008**.
20. M. J. F. Digonnet, H. K. Kim, G. S. Kino and S. Fan, Understanding air-core photonic-bandgap fibers: Analogy to conventional fibers. *Journal of Lightwave Technology* **2005,** *23*, 4169.
21. K. Z. Aghaie, V. Dangui, M. J. F. Digonnet, S. Fan and G. S. Kino, Classification of the core modes of hollow-core photonic-bandgap fibers. *IEEE Journal of Quantum Electronics* **2009,** *45*, 1192-1200.
22. C. R. Mansfield and E. R. Peck, Dispersion of helium. *Journal of the Optical Society of America* **1969,** *59*, 199.
23. W. M. Haynes, *CRC handbook of chemistry and physics, 92nd edition*, CRC Press, 2011.
24. C. Gaiser and B. Fellmuth, Experimental benchmark value for the molar polarizability of neon. *EPL (Europhysics Letters)* **2010,** *90*, 63002.
25. E. R. Peck and D. J. Fiisier, Dispersion of argon. *Journal of the Optical Society of America* **1964,** *54*, 1362.
26. A. C. Newell and R. C. Baird, Absolute determination of refractive indices of gases at 47.7 gigahertz. *Journal of Applied Physics* **1965,** *36*, 3751-3759.
27. E. R. Peck and B. N. Khanna, Dispersion of nitrogen. *Journal of the Optical Society of America* **1966,** *56*, 1059.
28. N. J. Bridge and A. D. Buckingham, The polarization of laser light scattered by gases. *Proceedings of the Royal Society of London A: Mathematical, Physical and Engineering Sciences* **1966,** *295*, 334-349.
29. R. L. Kelly, R. Rollefson and B. S. Schurin, The infrared dispersion of acetylene and the dipole moment of the C–H bond. *The Journal of Chemical Physics* **1951,** *19*, 1595-1599.
30. T. K. Bose, J. S. Sochanski and R. H. Cole, Dielectric and pressure virial coefficients of imperfect gases. V. Octopole moments of CH_4 and CF_4. *The Journal of Chemical Physics* **1972,** *57*, 3592-3595.
31. T. M. Miller and B. Bederson, *Advances in atomic & molecular physics*, Academic, 1989.

32. F. Buckley and A. A. Maryott, *Tables of dielectric constants and electric constants and electric dipole moments of substances in the gas phase*, National Bureau of Standards, Washington DC, 1953.
33. H.-P. Loock and P. D. Wentzell, Detection limits of chemical sensors: Applications and misapplications. *Sensors and Actuators B: Chemical* **2012,** *173*, 157-163.
34. I. Shavrin, S. Novotny, A. Shevchenko and H. Ludvigsen, Gas refractometry using a hollow-core photonic bandgap fiber in a Mach-Zehnder-type interferometer. *Applied Physics Letters* **2012,** *100*, 051106.
35. R. Jha, J. Villatoro, G. Badenes and V. Pruneri, Refractometry based on a photonic crystal fiber interferometer. *Optics Letters* **2009,** *34*, 617-619.
36. G. Cárdenas-Sevilla, F. Fávero and J. Villatoro, High-visibility photonic crystal fiber interferometer as multifunctional sensor. *Sensors* **2013,** *13*, 2349-2358.
37. J. Mathew, Y. Semenova and G. Farrell, Photonic crystal fiber interferometer for dew detection. *Journal of Lightwave Technology* **2012,** *30*, 1150-1155.
38. J. Mathew, Y. Semenova and G. Farrell, Relative humidity sensor based on an agarose-infiltrated photonic crystal fiber interferometer. *IEEE Journal of Selected Topics in Quantum Electronics* **2012,** *18*, 1553-1559.
39. J.-F. Ding, A. P. Zhang, L.-Y. Shao, J.-H. Yan and S. He, Fiber-taper seeded long-period grating pair as a highly sensitive refractive-index sensor. *IEEE Photonics Technology Letters* **2005,** *17*, 1247-1249.
40. T. K. Gangopadhyay, Prospects for Fibre Bragg Gratings and Fabry-Perot Interferometers in fibre-optic vibration sensing. *Sensors and Actuators A: Physical* **2004,** *113*, 20-38.
41. R. Yang, Y.-S. Yu, Y. Xue, C. Chen, Q.-D. Chen and H.-B. Sun, Single S-tapered fiber Mach–Zehnder interferometers. *Optics Letters* **2011,** *36*, 4482.

Chapter 4

Amplified Fibre Loop Cavity Ring-Down Spectroscopy

This chapter is based on the invited paper entitled "Near-infrared absorption detection in picolitre liquid volumes using amplified fibre loop ring-down detection" Optical Fiber Technology, Vol. 19, Iss. 6 (2013) P. 822-827, N. L. P. Andrews, J. Litman, D. Stroh, J. A. Barnes and H.-P. Loock. Material from this article is included in this chapter according to Elsevier's fair use policy. Initial experiments on acetylene gas samples were conducted by Jessica Litman and published in her M.Sc. thesis (2011). Daniel Stroh completed his B.Sc. thesis in 2010-2011 on some of the aspects of the work shown below and assisted specifically with initial work on the fibre–liquid interface (similar to **Figure 4.2**). With these exceptions all work presented below is that of the author.

4.1 Introduction

Over recent years, cavity ring-down spectroscopy (CRDS) and related cavity-enhanced absorption techniques have gained a large following. In CRDS, light is coupled into a high finesse optical cavity and one measures the optical loss from the rate at which light escapes from the cavity.[1] The decay time or "ring-down time", τ, represents the lifetime of a photon trapped within a cavity and is a direct measure of the optical loss in the cavity.[2] The photons trapped in the optical cavity can undergo multiple roundtrips in the optical cavity leading to an effective optical pathlength in the order of several kilometres. This allows CRDS to be used to detect samples with very low concentrations such as gases or samples in very small volumes.[3, 4] Additionally, as CRDS is dependent on the rate at which light decays from the optical cavity, it is immune to intensity variations.[1] Adding an absorbing sample into the cavity creates additional losses to the cavity and this additional loss allows for an accurate determination of the concentration of the sample.[5]

Fibre optic loops can be used to produce optical cavities as light is coupled into and out of the loop via fibre-fibre couplers.[6] The main advantage of fibre-CRDS over mirror-based setups is that it only requires

sample volumes of nL or even pL,[7, 8] rather than volumes of several μL.[4, 9-12] Loop cavities are also preferred when a very large spectral bandwidth is required. Here, the bandwidth is only limited by the optical transmission of the fibre loop and its components and can be as large as 300-1650 nm. This is advantageous if multiple analytes have to be detected simultaneously in a wide wavelength range.[13] Furthermore, fibre loop CRD spectrometers are readily aligned and comparably compact. The ring-down time can be determined from the roundtrip losses and roundtrip time,

$$t_{\mathrm{rt}} = nL/c_0 \,, \tag{4.1}$$

where n is the refractive index of the optical fibre, L is the length of the loop and c_0 is the speed of light in vacuum,

$$\tau = -\frac{t_{\mathrm{rt}}}{\ln\left(T_{\mathrm{sys}}\right) + \ln\left(T_{\mathrm{sample}}\right)} \,, \tag{4.2}$$

where the roundtrip losses of the system and sample are $\ln\left(T_{\mathrm{sys}}\right)$ and $\ln\left(T_{\mathrm{sample}}\right)$, respectively. However, loop cavities do have the problem of far larger system losses caused by the implementation of couplers, splices and absorption cells which may add up to a total loss that is larger than the loss introduced by the absorption of the sample.[14] This results in shorter ring-down times leading to poorer detection limits. To overcome this, one can utilise amplified CRDS. Amplified CRDS is a technique that adds a gain element to the fibre loop cavity to compensate for the high losses of the system resulting in longer ring-down times and improved detection limits. This chapter, evaluates the amplified CRDS technique as a tool to measure samples in the near-infrared spectral region and in very small volumes. The application of the same method to gas samples is described in an article from our group.[15, 16]

4.2 Amplified cavity ring-down spectroscopy

In 2001, Stewart *et al.* proposed and implemented a conceptually simple method to compensate for the losses in a fibre loop cavity by introducing a gain element into the loop.[14, 17] The ring-down time then becomes,

$$\tau = -\frac{t_{rt}}{\ln\left(T_{\text{sys}}\right) + \ln\left(T_{\text{sample}}\right) + \ln\left(G\right)}. \qquad \textbf{(4.3)}$$

Ideally, the gain, G, is tuned to $T_{\text{sys}} \times G = 1$, so that it exactly matches the undesired losses of the system. The ring-down time, τ, is then only dependent on the losses of the sample and equation (4.3) simplifies to,

$$\tau = -\frac{t_{rt}}{\ln\left(T_{\text{sample}}\right)}. \qquad \textbf{(4.4)}$$

The sensitivity enhancement of the technique was further described by Zhang *et al*. in a combined experimental and theoretical study.[18] In these experiments of intra cavity absorption of a fibre laser it was determined the sensitivity is highest when the laser is working near its lasing threshold as the gain matches the loss of the system. However, the sensitivity varies significantly around the threshold as a function of even slight variations of pump laser power due to the spontaneous emission noise. Therefore, to attain stable and sensitive absorption measurements a stable pump source is crucial. Alternatively, we propose to use a two loop system where the inner loop is set above threshold and thereby forms part of a fibre laser that lases at a wavelength within a few nanometres of the sample (outer) loop. This "clamps" the gain to the required threshold, stabilising the system and thus fixing the sensitivity.[14, 17] In our setup the outer loop contains the sample and a variable attenuator to set the gain level such that it matches that of the losses of the system, thereby generating a high and stable sensitivity.

While Zhang *et al.* and Stewart *et al.* performed a thorough characterisation of the amplified fibre loop cavity ring-down setup, they did not report on (micro-) analytical measurements. Our work is inspired by these early experiments and we set out to explore the advantages and limitations of using an additional gain element in the fibre loop as a micro-analytical sensor for liquids. As mentioned above, the same setup

described herein was combined with phase-shift CRDS and used to detect acetylene down to 50 ppm using the P(13) line of the $\nu_1+\nu_3$ combination band.[15, 16]

4.3 Experimental

The amplified fibre ring-down setup shown in **Figure 4.1** uses a two loop system as proposed by Stewart *et al*..[14] The two loops share the same erbium doped fibre amplifier (EDFA, *Keopsys* KPS-BT-C-18-LN-FA), but operate at two different wavelengths within the EDFA's gain spectrum, which are set by a tuneable bandpass filter (TBF, *Newport* TBF-1550-1.0) and a fibre Bragg grating (FBG, *Advanced Optics Solutions GmbH* FBG 28080940). The relative optical loss is set by a variable optical attenuator (VOA, *OZ Optics Ltd.* DD-100) that is placed in the inner loop, whereas the sample and photodetector are placed in the outer loop. In such a setup the gain of the EDFA is "clamped" to the free running lasing threshold of the inner loop, and the outer loop is allowed to "ring up" or "ring down", when driven with a long square light pulse from the tuneable diode laser (TDL, *ANDO* AQ4320D). As Stewart *et al.* previously mentioned a set up based on gain clamping is expected to provide larger stability compared to the simple intracavity laser absorption spectroscopic (ICLAS) measurements.[14, 17]

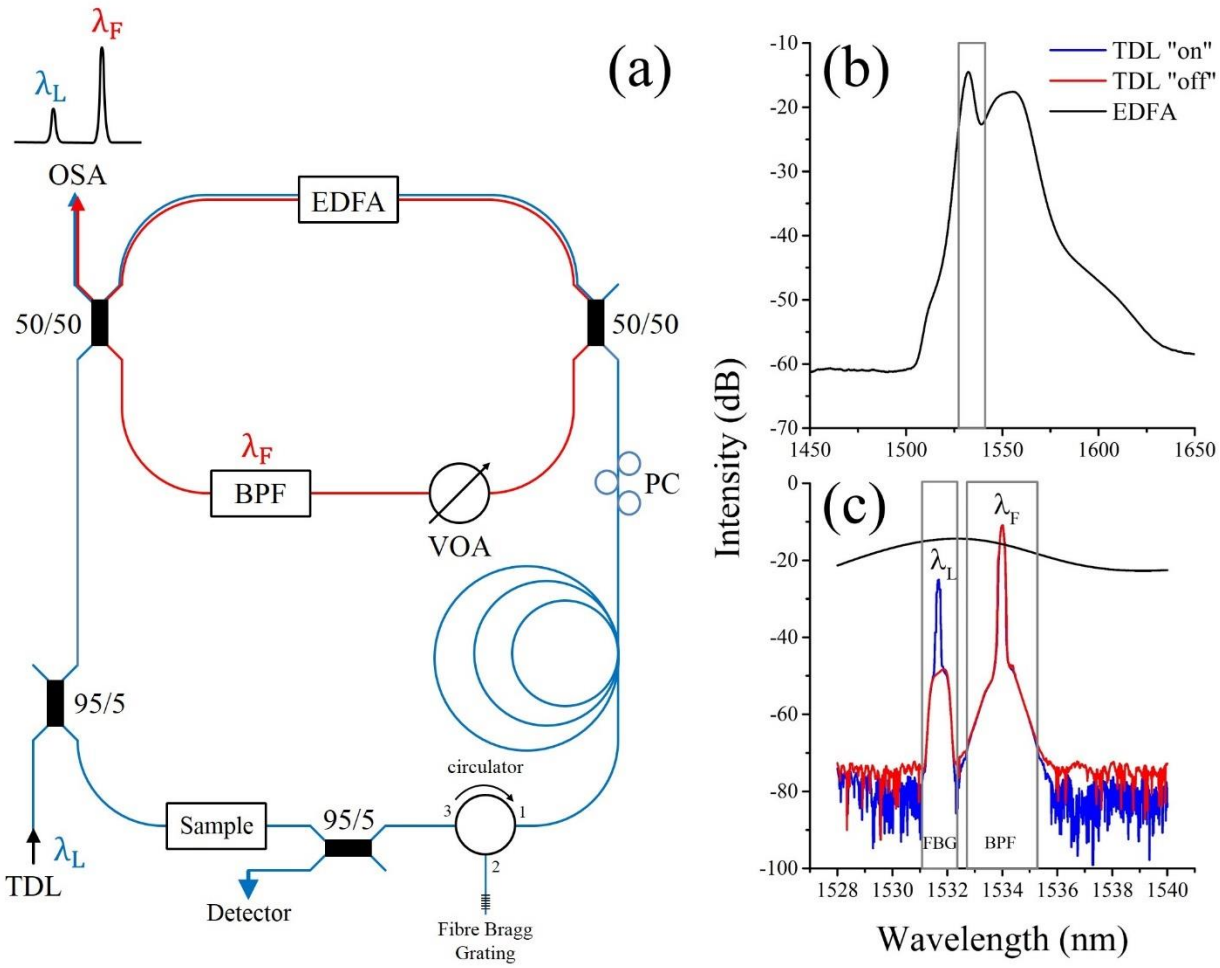

Figure 4.1: Two loop amplified CRDS setup. **(a)** Represents a schematic of the two loop amplified CRDS setup. The inner loop shown in red is used to "gain-clamp" the EDFA. The outer loop shown in blue contains the sample and detector. **(b)** The emission spectrum of the EDFA. The grey box shows the section that is enlarged in panel **(c)**. **(c)** Near the maximum of the EDFA emission spectrum (black line) are the transmission windows of the FBG and bandpass filter (BPF) shown as grey boxes. The inner loop lases near 1534 nm (red) and shows constant power regardless of whether the TDL is turned on (blue line) or turned off (red line).

In the experiments, the inner loop lases at 1534.05 nm within the gain curve of the EDFA; this wavelength is selected using the tuneable BPF. The outer loop is used for the ring-down sample detection. The sample loop contains a polarisation controller (PC) to compensate for birefringence in the fibre. Polarisation changes affect the splitting ratio of the 50/50 couplers that couple light between the inner and outer loop.

A spool of ~150 m fibre optic cable is added to increase the ring-down times by increasing the optical roundtrip path length. The wavelength of the outer loop and thus the wavelength used for the absorbing medium is given as 1532.03 nm by the FBG (*Advanced Optics Solutions GmbH*, FBG 28080940). The TBF and FBG were set to different wavelengths to prevent cross talk between the two loops. Light from both loops was coupled to an optical spectrum analyser (OSA, *Anritsu* MS9710) so that the relative intensity of the signals could be monitored in addition to their respective wavelengths.

The liquid sample sensing interface was used to detect the 1532 nm overtone bands of 1-octyne (Sigma-Aldrich, 97%) and 1-dodecyne (Sigma-Aldrich, 98%) in a non-interacting solvent such as dodecane (Sigma-Aldrich, ≥99%) and was constructed out of two single mode fibres with core diameter of 8 μm set 19 μm apart with an interrogation volume of 0.96 pL (**Figure 4.2**).

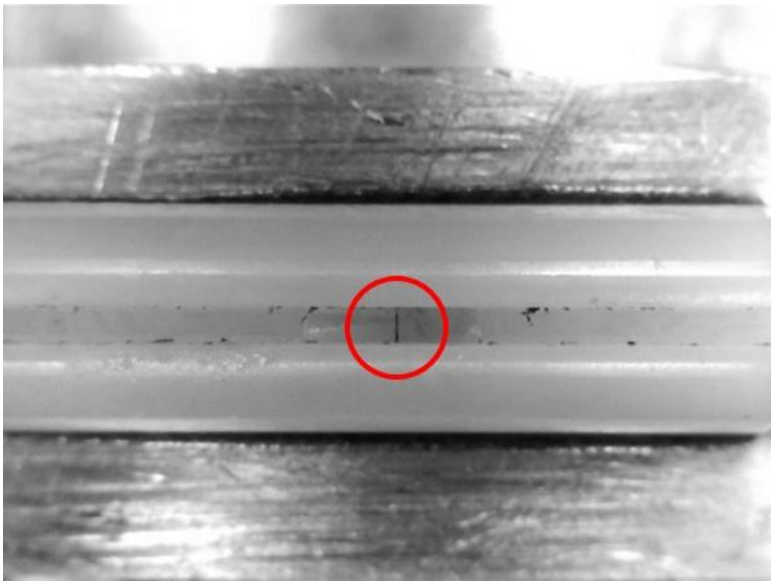

Figure 4.2: Liquid interface showing a 19 μm gap (circled) between two SMF ends. This interface is located at the sample region in the outer loop of **Figure 4.1(a)**.

4.4 Results and discussion

4.4.1 Characterisation of the amplified fibre loop CRDS setup

Long ring-down times can be obtained using the setup of **Figure 4.1(a)**. In **Figure 4.3(a)** the ring up process as light builds in the cavity during a square input pulse from the TDL is shown. The rise can be fit using a single exponential rise function (equation (4.5)) with a ring-up time of 10.8 μs. The steps correspond to one roundtrip time of the 158 m fibre loop. The decay process following the TDL pulse can also be fit to an exponential decay function (equation (4.6)) to obtain the ring down time of τ = 13.1 μs (**Figure 4.3(b))**,

$$I = I_0\left(1-\exp\left(-\frac{t}{\tau}\right)\right), \qquad \textbf{(4.5)}$$

$$I = I_0\exp\left(-\frac{t}{\tau}\right). \qquad \textbf{(4.6)}$$

In a passive (non-amplified) CRD scheme we would expect the ring-up time and the ring-down time to be identical. Their differences may point to non-linear gain effects of the EDFA, i.e. the round trip gain may depend on the intensity of the seed light and be higher when the intensity of the light is high at the beginning of a ring-down event.

Furthermore, in previous studies on non-amplified fibre-loop CRD spectroscopy, it was observed that the ring down process usually involves two independent decay processes corresponding to those occurring in the core and the cladding of the single mode fibre.[19] However, when inserting a sample cell in the loop, the cladding modes decay quickly causing their relative contribution to be minimal. Therefore, a single-exponential function is able to provide an excellent fit to the cavity ring-up and ring-down curves. The ring-up is caused by the build-up of the transient field within the cavity as it is excited from the pulsed laser.

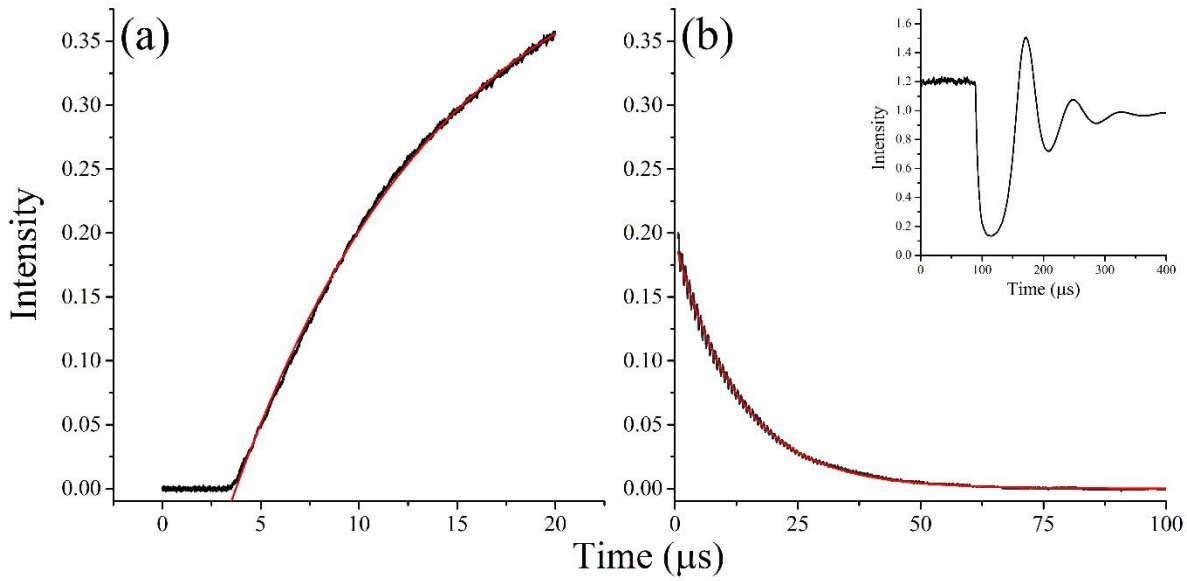

Figure 4.3: Ring up/down traces without a sample using the amplified fibre loop CRDS setup with the liquid interface implemented within the outer loop. **(a)** Represents the cavity build-up waveform. The red line is a fit using a single exponential rise function with time constant τ = 10.8 μs. **(b)** Cavity ring-down waveform of the fibre loop. The solid red line represents a single exponential decay curve with τ = 13.1 μs. The cavity decay inset shows the relaxation oscillations following the cavity decay that are observable on longer timescales.

The length of the fibre loop can be obtained from the steps in the ring-up trace, or — more clearly observable — in the "ring-down" trace of **Figure 4.3(b)**. The width of each step is about 760 ns, which corresponds to 158 m length of the outer loop in **Figure 4.1(a)** using equation (4.1) — assuming a refractive index, *n*, of the glass fibre to be 1.44. As noted by Stewart *et al.* relaxation oscillations can be observed whenever the probe laser wavelength coincided with the wavelength of the inner loop which is dominated by lasing.[17] These relaxation oscillations occur from the drop in pump power used for the ring-down event and lead back towards a steady state. Fortunately, as shown in the inset of **Figure 4.3(b)**, these relaxation oscillations decay much slower compared to the ring-down decay. Therefore, the influence of relaxation oscillations can be reduced by carefully adjusting the relative gain and loss in the two loops using the VOA. Relaxation oscillations can be suppressed entirely by increasing the difference in wavelengths circulating in the two

loops. However, since the stability of the ring-down measurement depends on the relative gain of the EDFA in these two wavelength regions, the wavelengths cannot be different by more than a few nanometres. In practice, we set the bandpass filters such that their pass bands do not overlap but are as close as possible. The gain in the outer loop was then increased by adjusting the VOA and by adjusting the amplification of the EDFA, through the pump laser power, such that the relaxation oscillations are visible but fall outside the 100 μs time window needed to make ring-down measurements.

As might be expected it was found that when the sample loop was operated at very long ring-down times, and the net loss was close to zero ($T \times G \approx 1$), the system became very sensitive to mechanical perturbations that might modulate the optical loss. For example, bending the fibre induces not only macrobending losses but also birefringence. The changes of polarisation seem to also change the optical loss in the two loops, possibly because the transmission through the bandpass filters or through fibre-fibre couplers is polarisation sensitive.

4.4.2 Detection of 1-alkynes in picolitre liquid volumes

In an attempt to detect liquid samples through weak vibrational overtones in unprecedentedly small detection volumes we opened the fibre-loop and separated the single mode fibre ends by about 19 μm (**Figure 4.2**). The volume between the two fibre end faces is then 230 pL, but only a cylinder with a 1.0 pL volume (8 μm diameter and 19 μm length) is interrogated by the circulating light. Experiments were conducted using 1-octyne and 1-dodecyne in dodecane at different concentrations.

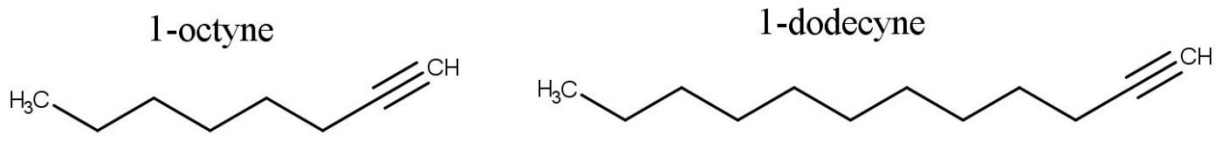

Figure 4.4: Chemical structure of 1-octyne and 1-dodecyne.

Figure 4.5 shows the detection of 1-octyne and 1-dodecyne in the non-absorbing solvent dodecane at 1532.03 nm. Five different concentrations of 1-octyne in dodecane ranging from 100% to 10% were sampled pseudo-randomly to demonstrate the repeatability of the measurement and to check for slow drifts and cross talk between samples. The solid red lines correspond to the 3σ level of the background signal and it is apparent that the detection limit is better than 20% of 1-octyne in dodecane. Similar responses are obtained for 12 injections of 1-dodecyne in dodecane at 4 different concentrations — 100% to 20% — and are also shown in **Figure 4.5**. As observed, 1-dodecyne has a lower absorptivity than that of 1-octyne at the same % by volume. Despite 1-dodecyne being slightly denser than 1-octyne due to stronger dispersion forces — 0.778 to 0.747 g/ml, respectively — in its neat form it is less concentrated — 4.7 mM compared to 6.8 mM, respectively.[20, 21] As there are less molecules in a given volume %, there will be less absorbing alkyne groups resulting in a lower absorption value.

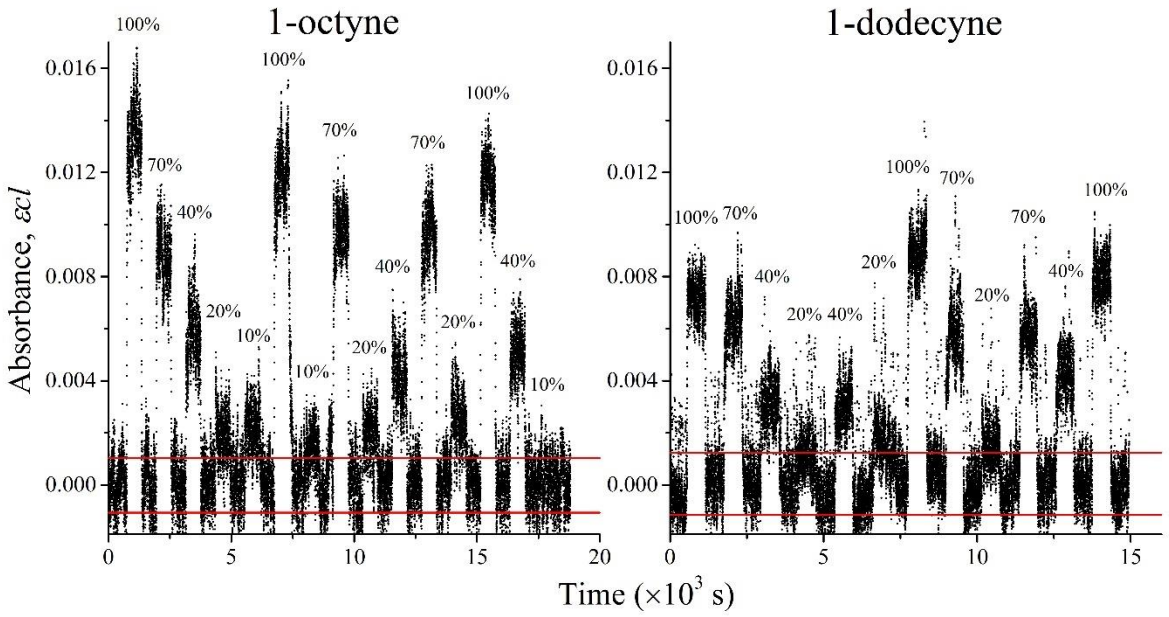

Figure 4.5: Absorption of 1-octyne and 1-dodecyne in dodecane using the amplified fibre loop CRDS setup. Concentrations of 100%, 70% ,40%, 20%, and 10% (for 1-octyne) were injected into the liquid interface of **Figure 4.2**. The solid red lines signify the background noise at the 3σ level.

Figure 4.6 shows linear relationships between the measured absorption loss and the concentration for both absorbers. In **Figure 4.5** and **Figure 4.6** the absorption of the sample is calculated from equation (4.2) and the Beer-Lambert law, $-\ln\left(T_{\text{sample}}\right)=\varepsilon cl$ using,

$$-\ln\left(T_{\text{sample}}\right)=\frac{t_{\text{rt}}}{\tau}-\frac{t_{\text{rt}}}{\tau_0}, \tag{4.7}$$

where c is the concentration. The pathlength through the sample, $l \approx 19$ μm, was determined from the absorption cross section of 1.6×10^{-19} cm^{-2} of the C-H stretch overtone located at around 1532 nm.[22] The roundtrip time, t_{rt} = 760 ns was calculated from the steps in the ring-down curve (**Figure 4.3(b)**) and the ring-down time of the system without absorber, τ_0, was determined from the baseline,

$$\tau_0=-\frac{t_{\text{rt}}}{\ln\left(G\right)+\ln\left(T_{\text{sys}}\right)}. \tag{4.8}$$

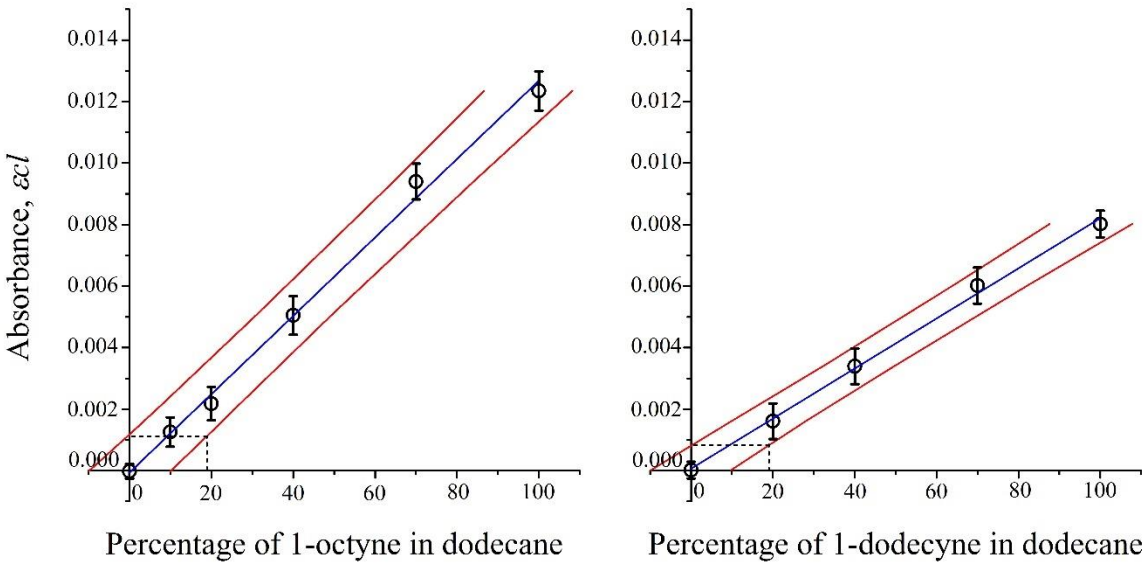

Figure 4.6: Measured absorption at 1532 nm as a function of concentration for 1-octyne and 1-dodecyne in dodecane. The blue lines represent linear fits through the data and the red lines signify the 3σ confidence intervals. The error bars shown were obtained as the 3σ value from all three separate measurements at each concentration and combined using error propagation. The dashed black lines signify the limit of detection, which is the minimal detectable absorption.[23]

The limits of detection can be determined from the calibration curves and are given as dashed black lines in **Figure 4.6**. The error bars (3σ) shown in **Figure 4.6** were calculated from propagation of the 3σ values obtained for all three signal levels at each of the 5 or 4 concentrations. The confidence intervals for the linear fit were obtained from 3σ using the fit.[23] The limits of detection in this case are calculated using the minimal detectable absorption and correspond to 19% of alkyne in dodecane in both cases. This value is in good agreement with the estimate of **Figure 4.5**. We note that the minimal detectable absorptivity of $< 10^{-3}$ is comparable with the lowest values obtained to date for micro-analytical liquid absorption spectroscopy.[8] The minimal detectable absorptivity, $(\varepsilon c)_{min} = 0.034$ cm^{-1} — obtained using a pathlength of 19 μm with 1-dodecyne — is comparable to that of many devices based on either fibre loops or liquid core waveguides. The minimal detectable absorption cross section $V_{det}(\varepsilon c)_{min} = 0.035$ μm^2 — obtained using a detection volume of $V_{det} = 0.96$ pL — is to the best of my knowledge lower than that of any previously reported absorption technique by more than one order of magnitude.

4.5 Concluding remarks

Amplified fibre-loop CRDS was used to determine detection limits of liquid samples in a minute detection volume. Similar to earlier work, two nested fibre loops that shared a fibre amplifier were used to stabilise the gain. The system was built from commercial off the shelf equipment and equipped with a home-built sample introduction liquid interface. Despite the weak overtone band of the 1-alkyne samples, amplified CRDS was able to quantify liquid samples of 1-octyne and 1-dodecyne to a limit of detection corresponding to 19% in a non-absorbing solvent dodecane. While the minimal detectable concentration is 20-fold higher than what had been achieved before,[22] please note that the detection volume is close to 1 pL and orders of magnitude smaller compared to previous work. Despite being somewhat sensitive to polarisation changes and mechanical perturbations, amplified CRDS shows resilience to light intensity changes and a greatly enhanced absorption path using cavities that may exhibit very high (passive) roundtrip loss.

Additionally, using the same amplified CRDS setup the detection of the weak P(13) line of the v_1+v_3 combination band was used to detect acetylene down to concentrations of 50 ppm.[15] Although this work is not presented in this thesis, — please refer to the thesis of J. Litman [16] — it highlights the versatility of the amplified CRDS technique to detect both liquids and gases in a spectral region of very weak absorption.

4.6 Bibliography

1. A. O'Keefe and D. A. G. Deacon, Cavity ring-down optical spectrometer for absorption measurements using pulsed laser sources. *Review of Scientific Instruments* **1988,** *59*, 2544-2551.
2. H. Waechter, J. Litman, A. H. Cheung, J. A. Barnes and H.-P. Loock, Chemical sensing using fiber cavity ring-down spectroscopy. *Sensors* **2010,** *10*, 1716-1742.
3. A. O'Keefe and O. Lee, Trace gas-analysis by pulsed laser-absorption spectroscopy. *American Laboratory* **1989,** *21*, 19-22.
4. C. M. Rushworth, J. Davies, J. T. Cabral, P. R. Dolan, J. M. Smith and C. Vallance, Cavity-enhanced optical methods for online microfluidic analysis. *Chemical Physics Letters* **2012,** *554*, 1-14.
5. P. Zalicki and R. N. Zare, Cavity ring-down spectroscopy for quantitative absorption measurements. *The Journal of Chemical Physics* **1995,** *102*, 2708.
6. J. Barnes, M. Dreher, K. Plett, R. S. Brown, C. M. Crudden and H.-P. Loock, Chemical sensor based on a long-period fibre grating modified by a functionalized polydimethylsiloxane coating. *Analyst* **2008,** *133*, 1541-1549.
7. D. James, B. Oag, C. M. Rushworth, J. W. L. Lee, J. Davies, J. T. Cabral and C. Vallance, High-sensitivity online detection for microfluidics via cavity ringdown spectroscopy. *RSC Advances* **2012,** *2*, 5376-5384.
8. K. Bescherer, J. A. Barnes and H.-P. Loock, Absorption measurements in liquid core waveguides using cavity ring-down spectroscopy. *Analytical Chemistry* **2013,** *85*, 4328-4334.
9. L. van der Sneppen, A. Wiskerke, F. Ariese, C. Gooijer and W. Ubachs, Improving the sensitivity of HPLC absorption detection by cavity ring-down spectroscopy in a liquid-only cavity. *Analytica Chimica Acta* **2006,** *558*, 2-6.
10. K. L. Snyder and R. N. Zare, Cavity ring-down spectroscopy as a detector for liquid chromatography. *Analytical Chemistry* **2003,** *75*, 3086-3091.
11. K. L. Bechtel, R. N. Zare, A. A. Kachanov, S. S. Sanders and B. A. Paldus, Moving beyond traditional UV−visible absorption detection: Cavity ring-down spectroscopy for HPLC. *Analytical Chemistry* **2005,** *77*, 1177-1182.
12. B. Bahnev, L. van der Sneppen, A. E. Wiskerke, F. Ariese, C. Gooijer and W. Ubachs, Miniaturized cavity ring-down detection in a liquid flow cell. *Analytical Chemistry* **2005,** *77*, 1188-1191.
13. H. Waechter, D. Munzke, A. Jang and H.-P. Loock, Simultaneous and continuous multiple wavelength absorption spectroscopy on nanoliter volumes based on frequency-division multiplexing fiber-loop cavity ring-down spectroscopy. *Analytical Chemistry* **2011,** *83*, 2719-2725.
14. G. Stewart, K. Atherton, H. Yu and B. Culshaw, An investigation of an optical fibre amplifier loop for intra-cavity and ring-down cavity loss measurements. *Measurement Science and Technology* **2001,** *12*, 843-849.

15. N. L. P. Andrews, J. Litman, D. Stroh, J. A. Barnes and H.-P. Loock, Near-infrared absorption detection in picolitre liquid volumes using amplified fibre loop ring-down detection. *Optical Fiber Technology* **2013,** *19*, 822-827.
16. J. Litman, Queen's University, 2011.
17. G. Stewart, K. Atherton and B. Culshaw, Cavity-enhanced spectroscopy in fiber cavities. *Optics Letters* **2004,** *29*, 442-444.
18. Y. Zhang, M. Zhang and W. Jin, Sensitivity enhancement in erbium-doped fiber laser intra-cavity absorption sensor. *Sensors and Actuators A: Physical* **2003,** *104*, 183-187.
19. Z. Tong, M. Jakubinek, A. Wright, A. Gillies and H.-P. Loock, Fiber-loop ring-down spectroscopy: A sensitive absorption technique for small liquid samples. *Review of Scientific Instruments* **2003,** *74*, 4818-4826.
20. Sigma-Aldrich, *1-Octyne, 244465 safety data sheet*, 2016.
21. Sigma-Aldrich, *1-Dodecyne, 244406 safety data sheet*, 2016.
22. P. B. Tarsa, P. Rabinowitz and K. K. Lehmann, Evanescent field absorption in a passive optical fiber resonator using continuous-wave cavity ring-down spectroscopy. *Chemical Physics Letters* **2004,** *383*, 297-303.
23. H.-P. Loock and P. D. Wentzell, Detection limits of chemical sensors: Applications and misapplications. *Sensors and Actuators B: Chemical* **2012,** *173*, 157-163.

Chapter 5

Fluorescence Excitation Emission Matrix Spectroscopy Analysis Technique

This chapter is based on the technique used in the papers entitled "Comparison of lubricant oil antioxidant analysis by fluorescence spectroscopy and linear sweep voltammetry" published in Tribology International Feb 2016 and "Determination of the thermal oxidative and photochemical degradation rates of the scintillator liquid by fluorescence EEM spectroscopy" which has been accepted for publication in Physical Chemistry Chemical Physics, 2017. Please refer to Chapter 6 and Chapter 7 for each of the authors contributions to these papers. This material has been added according to Elsevier's and the RSC's fair use policy.

5.1 Introduction

Excitation emission matrix (EEM) spectroscopy is a powerful fluorescence technique. Being that the entire excitation and emission landscape are obtained makes it easier to distinguish between multiple fluorescent species as compared to simply exiting at a single wavelength.[1] In addition, 2nd order techniques contain far more information and can be combined with multivariate analysis techniques such as parallel factor (PARAFAC) analysis.[2, 3] Using PARAFAC analysis on a data set of EEM spectra can generate a thorough characterisation of the kinetics involved, which is otherwise impossible for a single excitation wavelength setup.[4-6]

The instrument used to acquire all EEM spectra is a *Varian* Cary Eclipse spectrometer. This is a scanning grating spectrofluorometer, and steps over each excitation and emission wavelength combination to generate the full EEM spectrum. The parameters used such as the step size, slit size, photomultiplier tube (PMT) voltage, and filters were chosen to optimise the fluorescence signal while generating a fluorescence EEM spectrum in approximately 30 mins. The settings are discussed in more detail in section 5.2.1.

This chapter evaluates the methodologies applied to the EEM spectroscopy analysis method used to determine degradation rates of lubricants and scintillator solutions as explained in Chapter 6 and Chapter 7. In addition, discussion of the custom made bifurcated fibre probe used to acquire all the EEM spectra is also included.

5.2 EEM spectroscopy method

5.2.1 EEM acquisition

All EEM spectra were acquired using the commercial *Varian* Cary Eclipse spectrometer which permits the recording of the entire fluorescence landscape. This instrument scans across both excitation and emission wavelengths using two motors that rotate diffraction gratings to select the wavelengths.[1, 7] The step and slit sizes were set to match each other as to avoid missing or over analysis of spectra. In addition, these settings were chosen to ensure that the fluorescence features were correctly identified while allowing a full EEM spectrum to be acquired in approximately 30 mins. The PMT voltage setting was chosen such that the maximum intensity count was in the region of 800-900 counts —where the maximum is 1000 counts. This ensured a good signal to noise while preventing oversaturation of the detector. In addition, the PMT setting was kept constant for all spectra on similar samples to allow for an easier comparison between samples. Auto filters were applied to all spectra acquisitions to remove second order grating effects and other instrumental artefacts that corrupt the EEM spectrum as shown in **Figure 5.1**. The *Varian* Cary Eclipse was also adapted for use with a custom-built bifurcated fibre probe that was simply submerged into the sample without any prior preparation. The design of the probe is discussed in more detail in section 5.3.

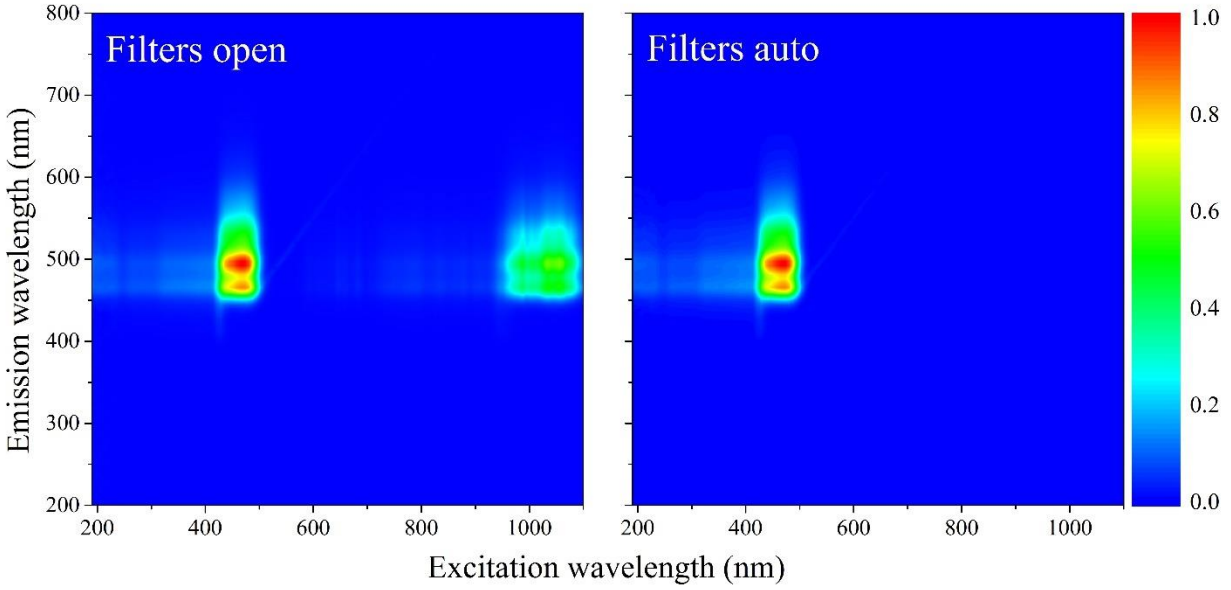

Figure 5.1: EEM spectra of fresh SNO+ scintillator solution with both excitation and emission filters set either to open or to auto. For auto, new high pass filters are applied as the emission and excitation wavelengths are scanned to remove second order excitation light from exciting the sample.

To determine the degradation of lubricants or scintillator liquid for example using fluorescence EEM spectroscopy, samples were first appropriately aged — through heating or via photo-degradation — and typically withdrawn in a logarithmic time scale. These samples were then sealed to reduce contamination and were allowed to cool to room temperature. This ensured that all the samples were analysed with the same conditions. Although sample withdrawal was carried out, in a future application this should not be necessary, as an EEM spectrum can be obtained by our newly developed Hadamard EEM spectrometer (Chapter 9) in a fraction of the time it takes as compared to the commercial instrument used.

5.2.2 Parallel factor analysis

PARAFAC analysis was used to distinguish between the components that comprise the sample set.[8, 9] Although the components obtained using PARAFAC are mathematical by nature and do not correspond to specific chemical compounds, they do relate to a group of similar chemical fluorophores. Therefore,

PARAFAC analysis can be used to distinguish between different chemical compound classes in an EEM for quantitative analysis.

Once all the EEM spectra were collected for a particular sample set, a custom Matlab algorithm was written to combine all spectra into a three-dimensional data cube with dimensions of sample number, emission wavelength, and excitation wavelength (**Figure 5.2**). To help the fit, the Rayleigh scatter effects were removed from the data cube by using the EEMCut command in the DOMFluor toolbox in Matlab.[10] This data cube was subsequently analysed with PARAFAC analysis using the drEEM toolbox in Matlab.[11] The data sets were normalised prior to analysis as to give the weakly fluorescent samples the same weighting in the fit as the strongly fluorescent samples. This was required to reduce the noise of the highly fluorescent components so that the weaker components could be measured and distinguished from this noise. After PARAFAC analysis the normalisation of the model is reversed to retrieve the correct scores.

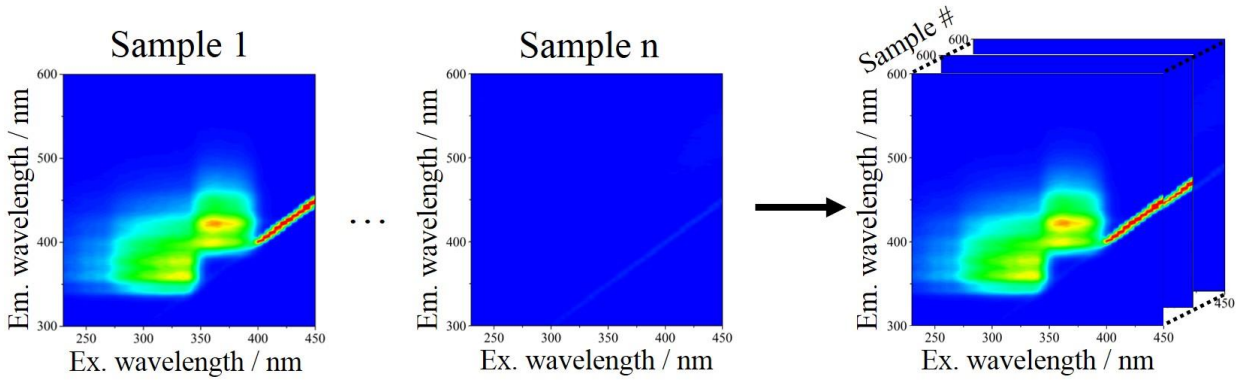

Figure 5.2: Generation of three-dimensional data cube for use with PARAFAC analysis. A number of spectra are recorded and are combined into a three dimensional data cube with dimensions of excitation wavelength, emission wavelength, and sample number. The spectra shown are of the degraded SNO+ scintillator solution described in chapter 7.

PARAFAC analysis was run ten times using random initialisation, and the fit with the least sum of squared errors was chosen for the model. The random initialisation evaluates the robustness of the model and it was

determined to be good, if there was no large deviation in the sum of squared error for all random initial starting vectors. A convergence criterion of 10×10^{-10} was used to ensure the model converged to an appropriate level. Nonnegativity constraints were added being that fluorescence data is expected to be positive. The constraint helped the fit to find an appropriate model for the chemical system that was analysed.

To determine the number of components that best describes the data, we need to consider both the core consistency and "percentage explained". The core consistency is a diagnostic tool for the appropriateness of the PARAFAC model. It is a measure of superdiagonality and is calculated using equation (5.1),[8]

$$\text{core consistency} = 100\left(1-\frac{\sum_{p=1}^{F}\sum_{q=1}^{F}\sum_{r=1}^{F}\left(g_{pqr}-t_{pqr}\right)^2}{F}\right), \qquad \textbf{(5.1)}$$

where t_{pqr} are the elements of a superdiagonal array of ones, **T**, with dimensions p, q and r. g_{pqr} are the elements of the core array **G** using F components. (Chapter 2 section 2.4.3.2) If the superdiagonal elements of **G** are similar to the elements of **T** and the off-superdiagonal elements of **G** are zero, the model is appropriate. This is because, in PARAFAC analysis the core array, **G**, is defined as a superdiagonal matrix and thus should not have any off-diagonal elements (Chapter 2 section 2.4.3.2).[8] A value close to 100% for the core consistency is then a measure that the PARAFAC model is appropriate and agrees with PARAFAC. A core consistency value near 0% or even negative implies an unsuitable model, as more of the variation is associated with the off-diagonal core elements than with the superdiagonal. As the number of components, F, increases, the core consistency decreases monotonically. As soon as the maximal number of components is exceeded, the core consistency will decrease dramatically as the additional components mainly describe noise, leading to high off-diagonal core values.[8] The decrease of core consistency with the number of components for the set of 101 samples of SNO+ scintillator solution is shown in **Figure 5.3**.

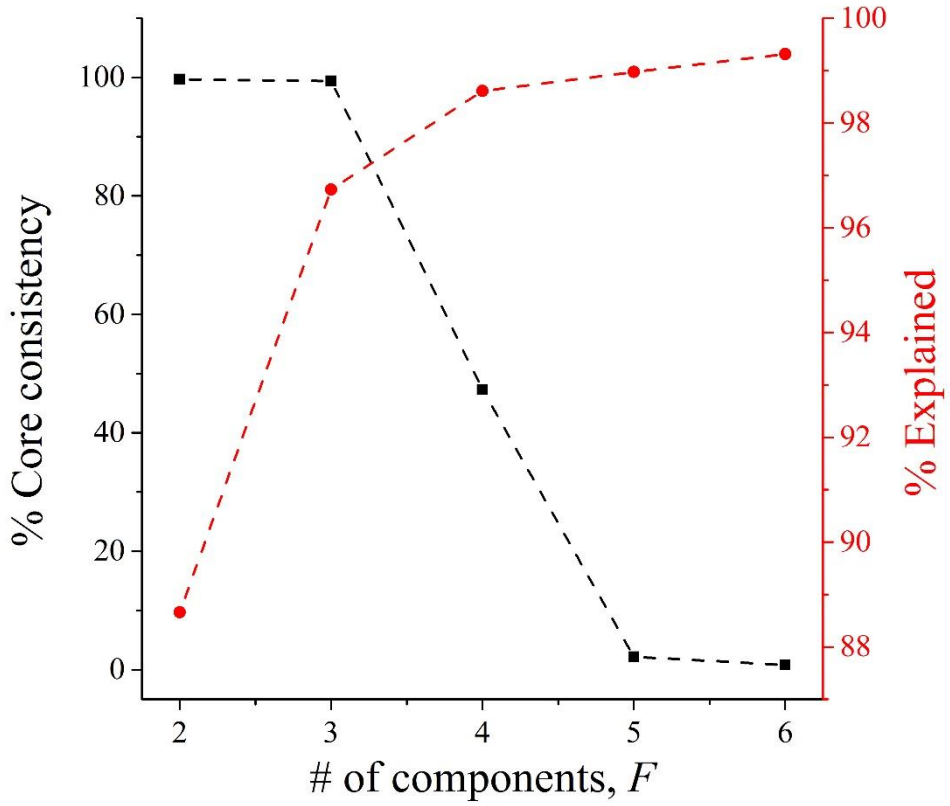

Figure 5.3: Core consistency and % explained for a set of degraded 101 SNO+ scintillator with increasing number of components, *F*. As observed the core consistency decreases sharply as the fit becomes over analysed and the % explained increases with components. Therefore, in this case the best PARAFAC model uses 3 components.

The "percentage explained" diagnostic is a measure of how well the model describes the data through the least squares fit — a small error will produce a high % explained. As the number of components increase the % explained will also increase as the model has more adaptability to describe the data. However, when the maximal number of components is surpassed, the rate at which the "percentage explained" value improves, decreases as the additional components predominantly fit the noise. From **Figure 5.3** it can be concluded that a 3-component model is the most appropriate for the sample set. This is due to the fact that there is a sharp drop of core consistency from 3 to 4 components and the increase in "percentage explained" is small for any additional components. After knowing the most appropriate model from PARAFAC using

the core consistency and "percentage explained" diagnostics, the spectra of the components themselves are investigated. This ensures that the PARAFAC components describe fluorophores that are present in the sample with known or at least recognisable EEM Spectra. This information is then used to possibly improve the PARAFAC model to best describe the data.

5.3 Fibre probe design

5.3.1 Bifurcated fibre probe

Being that EEM spectroscopy is a fluorescence technique, it can be applied for use with fibre optic probes. These can simply be submerged into an analyte without any prior sample preparation.[4, 5] In addition, fibre probes have a small cross-section and can be used to analyse samples in places that are hard to reach, delicate, or dangerous for an employee such as *in vivo* or a pipeline.[12, 13] Measuring fluorescence with fibre probes is non-destructive and there is no loss or alteration of the sample. Furthermore, being that fibre probes are typically made from silica, they are generally inert and unaffected by high electric or magnetic fields.

For fluorescence measurements, custom-built bifurcated fibre probes were used as shown in **Figure 5.4**. The fibre bundle consists of 6 excitation fibres **Figure 5.4(a)** that are used to guide light from a light source to the sample at the probe end **Figure 5.4(b)**. The sample absorbs the excitation light and subsequently fluoresces. Some of the emission is collected by 13 collection fibres that are co-aligned and interspersed with the excitation fibres. These fibres guide the light to the detector (**Figure 5.4(c))**. This front-face fluorescence detection scheme was preferred as a fibre bundle setup as it provides the best acceptance cone overlap for fluorescence detection while using separate excitation and emission fibres.[14] Of course, the largest overlap acceptance cones occurs when the same fibre is used for both excitation and emission, but this is impractical as it would require to separate the fluorescence from the intense excitation light in a separate optical element.

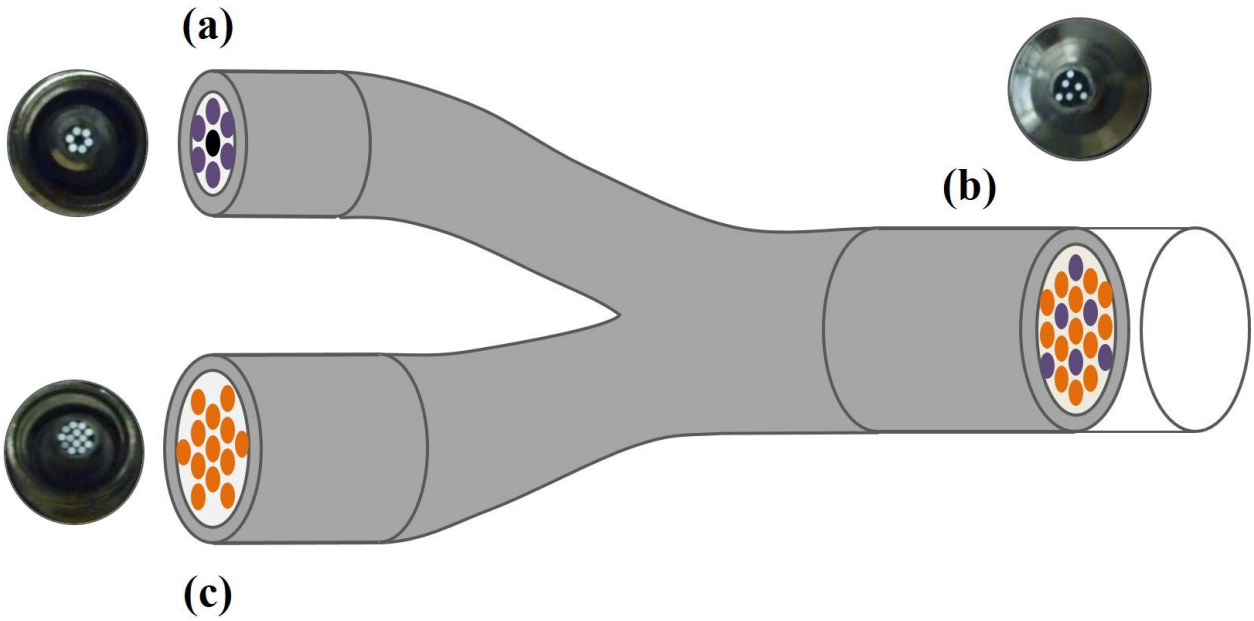

Figure 5.4: Schematic of the bifurcated fibre probe used to collect EEM spectra. **(a)** represents the excitation end that is coupled to the xenon flash lamp of the *Varian* Cary Eclipse and is comprised of 6 excitation fibres (purple). **(b)** shows the probe end that is submerged in the sample with all 19 fibres used for collection and excitation. **(c)** represents the emission end that is coupled to the spectrometer with a total of 13 collection fibres (orange).

The bifurcated fibre bundle was then attached to the commercial *Varian* Cary Eclipse fluorescence spectrometer for all the EEM spectral acquisition.

5.3.2 Addition of transparent spacer

As can be observed in **Figure 5.4**, there is a transparent spacer attached to the probe end of the fibre bundle. This is added to ensure complete overlap of the acceptance cones of the excitation and emission fibres. This then ensures that the fluorescence which is generated in the sample and irradiates the front face of the fibre probe, falls into the acceptance cones of the collection fibres (See **Figure 5.5**). This spacer is especially important for highly reabsorbing samples as it reduces the distance of reabsorption that the light must travel and thereby enhancing the fluorescence signal measured.

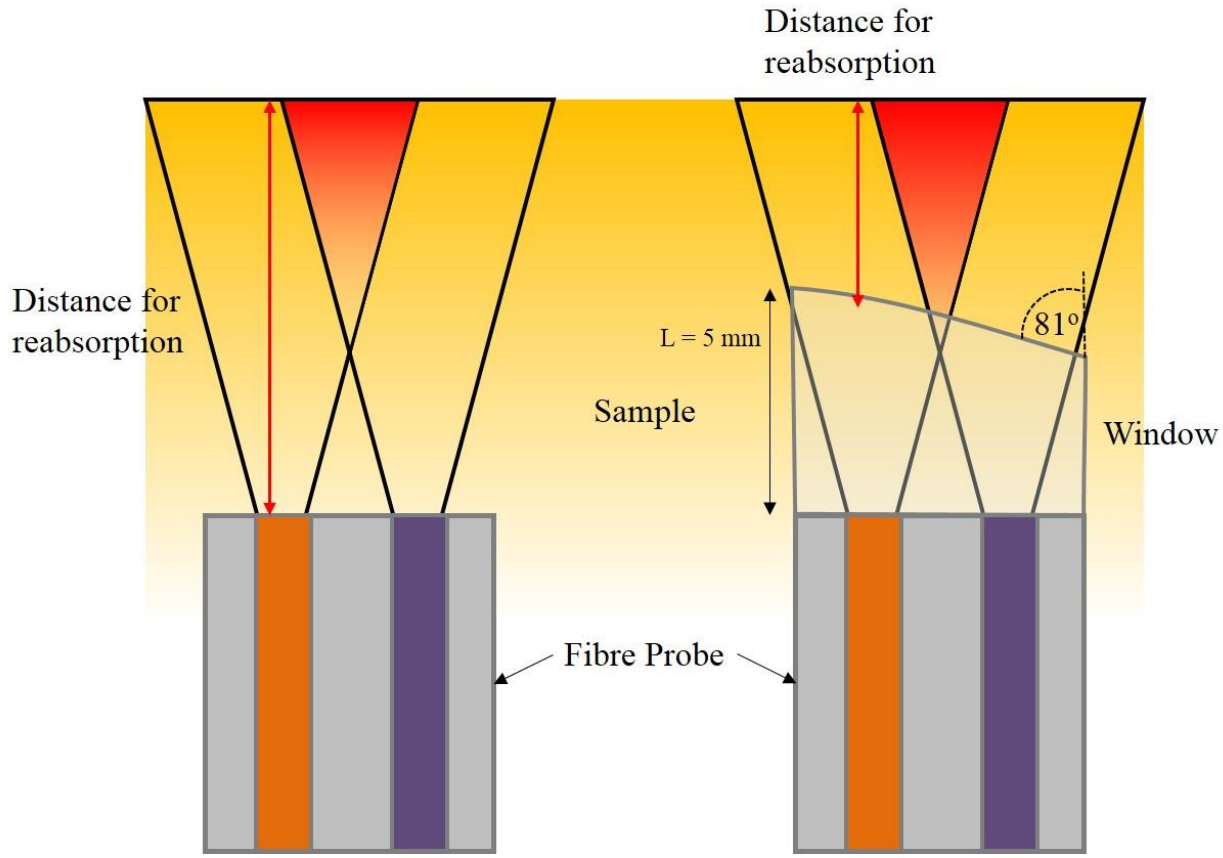

Figure 5.5: Schematic showing the differences between the windowless and windowed fibre bundle. Note the drawing is not drawn to scale and is an over simplification as it doesn't include the refraction effects from the window to the sample. The purple excitation fibre emits light into the sample within its acceptance cone. The red triangle represents the volume of excitation and emission acceptance cone overlap emission. Only fluorescence emitted in this region can be detected and collected by the orange collection fibre. This provides a ~3 mm thick region in which fluorescence is partly invisible to the collection fibres (See **Table 5.1**). The addition of a 5 mm window (not drawn to scale) is used to remove the reabsorption, thereby enhancing the collected fluorescence intensity. The window is also bevelled to reduce back reflections and thus over saturation of the detector from the excitation light.

The acceptance cone overlap is determined by the numerical aperture, NA, of the fibres,

$$\mathrm{NA} = n\sin\left(\theta_{\max}\right), \tag{5.2}$$

where n is the refractive index of the medium such as the sample or transparent spacer and θ is the half angle of the maximum cone of light that can enter or exit the fibre. The numerical aperture is also defined by the total internal reflection in a fibre with the refractive indices of the core, n_{core} and cladding, n_{clad},

$$\text{NA} = \sqrt{n_{core}^2 - n_{clad}^2} \,. \tag{5.3}$$

The fibres used to construct the bifurcated fibre probe are CeramOptec UV400/440P multimode fibres with core / cladding / polyimide coating diameters of 400 / 440 / 470 μm, respectively, and have a NA of 0.22.[15] The refractive index of the fused silica window depends on the wavelength, λ, and can be obtained using the Sellmeier dispersion equation at room temperature,[16]

$$n^2 - 1 = \frac{0.6961663\lambda^2}{\lambda^2 - (0.0684043)^2} + \frac{0.4079426\lambda^2}{\lambda^2 - (0.1162414)^2} + \frac{0.8974794\lambda^2}{\lambda^2 - (9.896161)^2} \,. \tag{5.4}$$

Equation (5.4) can be used to determine the refractive index of the fused silica glass for the typical EEM wavelength range of 200-800 nm and is shown in **Figure 5.6**. The half angle of the maximum acceptance cone, θ_{max}, is calculated from the refractive index using equation (5.2). The minimum practical thickness of the glass window, D, is then calculated using simple trigonometry with equation (5.5),

$$D = \frac{W/2}{\tan(\theta_{\text{max}})}, \tag{5.5}$$

where W is the width of the fibres and jackets. It is apparent from **Figure 5.7** that the value of W = (core diameter of both fibres) + (cladding and jacket thickness) = (400×2) μm + 70 μm = 870 μm. Therefore, the minimum thickness that the window can be to ensure all the possible photons are collected, is calculated from a W of 870 μm and is shown as the intersection of the two dotted yellow lines in **Figure 5.7**. The minimum thicknesses of the glass transparent window are given in **Table 5.1** for the EEM wavelength range. Therefore, a window thickness of 5 mm is more than enough to ensure overlap of the acceptance cones.

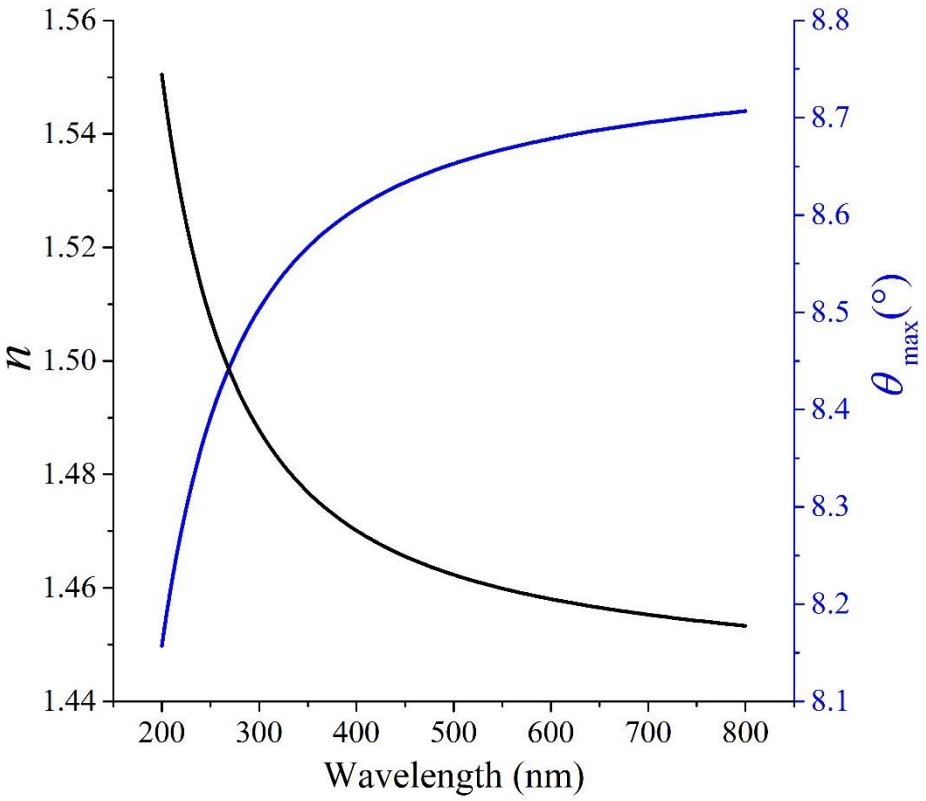

Figure 5.6: Refractive index, *n*, of the fused silica window over the EEM wavelength range using equation (5.4). As plotted on the right axis is the maximum angle in degrees for each wavelength using equation (5.2) with a numerical aperture of 0.22.

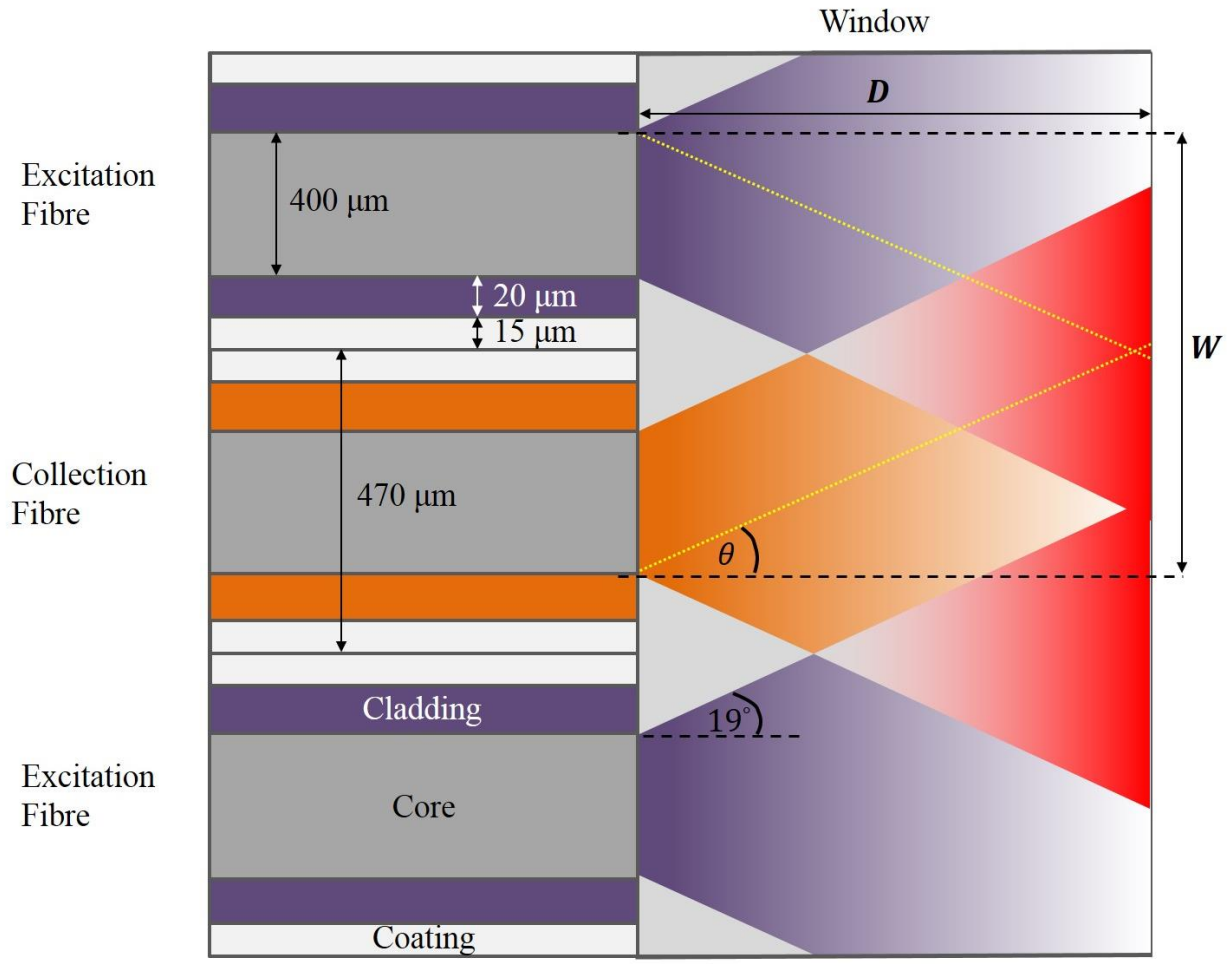

Figure 5.7: Schematic of the window thickness calculation for the UV-fused silica spacer. The shaded areas coloured in purple and orange are the acceptance cones of the excitation and collection fibres, respectively. The area shaded in red is the region at which both the excitation and collection acceptance cones overlap and so fluorescence can be measured. The minimum thickness of the window is shown as the intersection of the yellow dotted lines.

The window was also bevelled to reduce back reflections at the window / sample interface (See **Figure 5.4**). This reduced the amount of Fresnel-reflection into the collection fibres and prevented saturating ("blinding") the detector. Although not optimised, the window was bevelled at an angle of 81° and gave an enhanced fluorescence signal while reducing scattered excitation light from entering the collection fibres (See **Figure 5.8**).

Table 5.1: Minimum thicknesses, *D*, that the UV-fused silica window must have for optimal acceptance cone overlap between excitation and collection fibres.

λ / nm	n	θ / °	*D* / mm
200	1.551	8.16	3.03
500	1.470	8.65	2.86
800	1.453	8.71	2.84

5.3.3 Signal improvement with transparent spacer

This section compares the EEM components and scores that were obtained when using PARAFAC on EEM spectra obtained on lubrication oil (see more information in Chapter 6) using a fibre probe without a window as in Omrani et al.[4] and with a bevelled window.[5] A total of 90 EEM spectra were analysed on oil samples heated to 468 K. Of those, 22 were obtained in 2013 using a fibre probe without window and 19 of these samples were analysed using the windowed fibre probe. From the newer set of oil samples aged in 2014 at the same temperature under reflux, 24 samples were analysed using the old probe and 25 with the new probe. Spectra of the fresh lubrication oil obtained in 2014 using both the windowed and windowless fibre probes are shown in **Figure 5.8**. When the window is applied there is a dramatic increase of signal as the photons are not reabsorbed. The PARAFAC analysis included all 90 EEM spectra in a single dataset and produced 3 components that were very similar to those shown by Omrani et al. (**Figure 5.9**).[4]

Figure 5.10 shows the time evolution for all three components for all the combinations of 2013 and 2014 oil with the windowed and windowless fibre probes. The component scores indicated that component 1, which absorbs at the shortest wavelength $\lambda = 350^{ex} / 400^{em}$ nm is much more strongly represented when a window is placed between the fibre ends and the sample regardless of the data set (Compare **Figure 5.10 (a)** to **Figure 5.10(c)**). Component 3 at the longest wavelengths $\lambda = 420^{ex} / 550^{em}$ nm is least affected by the window and has now a greatly reduced contribution to the spectra.

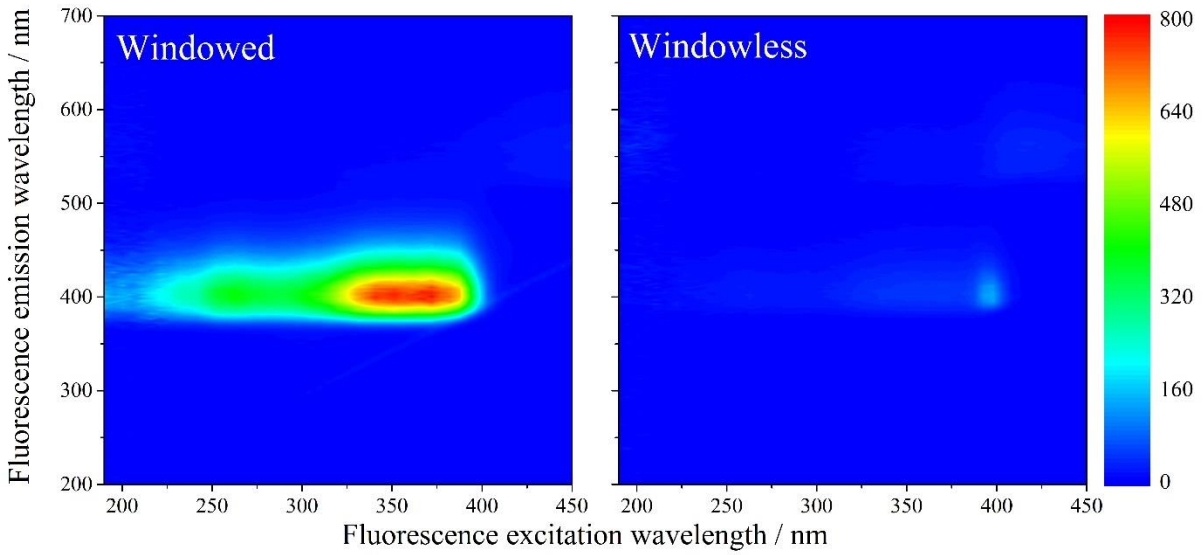

Figure 5.8: EEM spectra of fresh lubrication oil using a windowed and windowless fibre probe. For the windowed EEM spectrum a PMT voltage of 740 V was used as to not saturate the detector and a higher PMT voltage of 800 V was used for the windowless EEM spectrum. As observed the window enhances the fluorescence signal dramatically. The colours from blue to red represent the intensity of the signal.

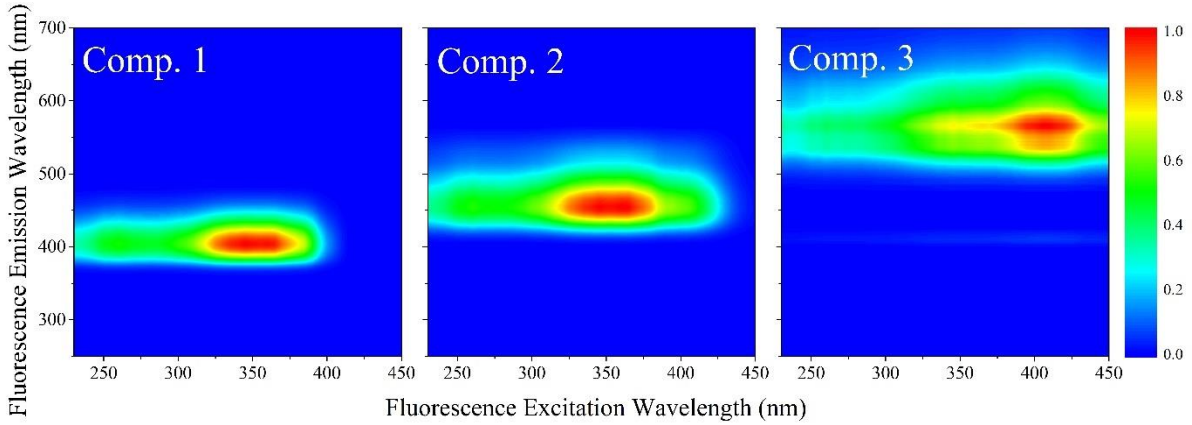

Figure 5.9: Normalised EEM spectra of the three components obtained by running PARAFAC on all 90 EEM spectra of the aged lubrication oil at 468 K using both the windowed and windowless fibre probes in the same analysis. These include both samples obtained in 2014 and recently, in addition to being measured from both the windowed and windowless fibre probes. The colours from blue to red represent the normalised intensity of the signal.

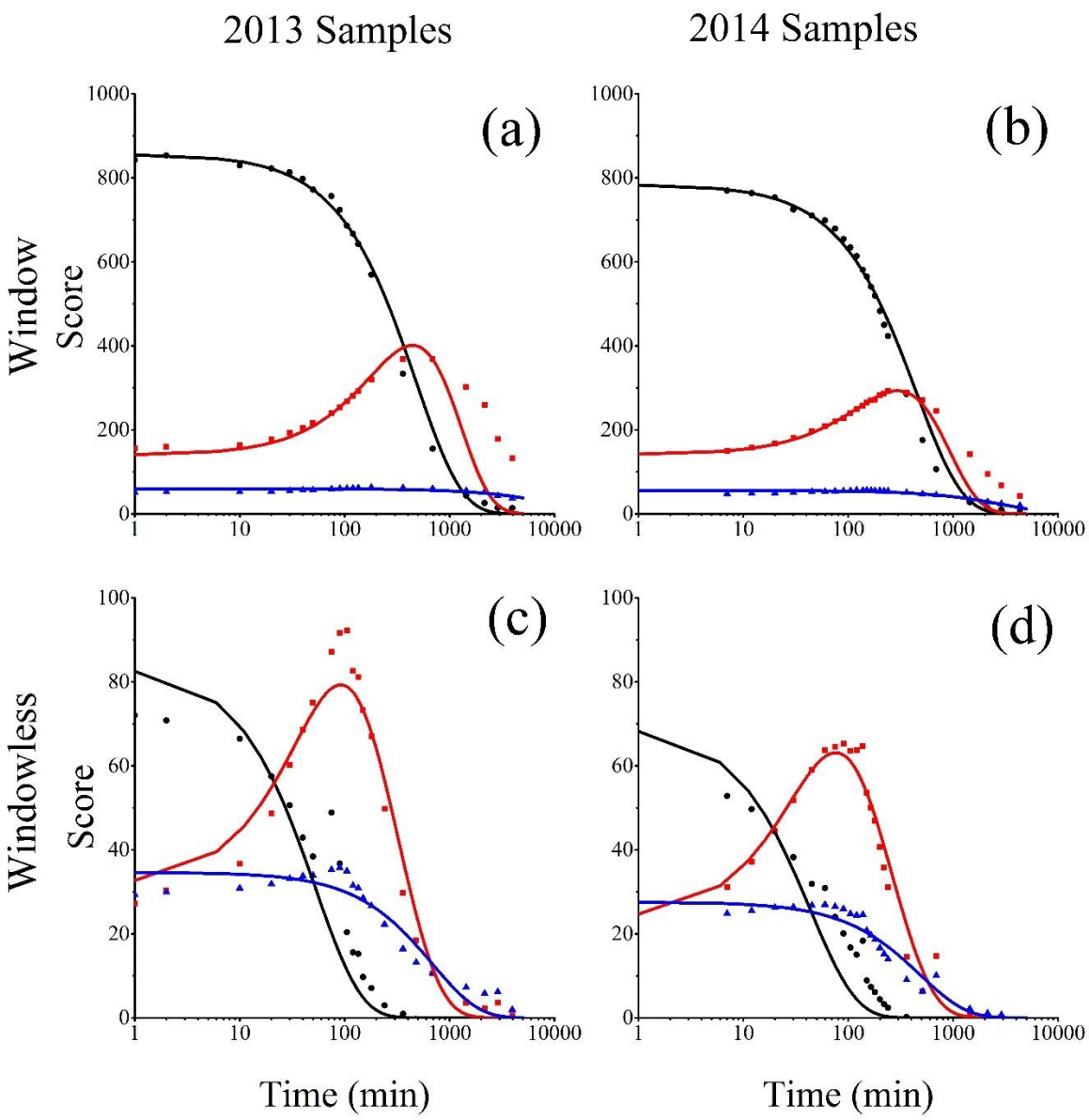

Figure 5.10: Time evolution of the three PARAFAC components obtained of the 468 K aged lubrication oil. **(a)** includes data obtained using the windowed fibre probe on the 2013 samples. **(b)** includes data obtained using the windowed fibre probe on the 2014 samples and windowless fibre probe, respectively. **(c)** includes data obtained using the windowless fibre probe on the 2013 samples. **(d)** includes data obtained using the windowless fibre probe on the 2014 samples. The black circles, red squares, and blue triangles represent the scores of the components shown in figure **Figure 5.9** as component one, two, and three, respectively. The coloured lines are obtained by fitting the data to the kinetic model described in Chapter 6.

From **Figure 5.10** it appears as if the presence of the window on a fibre probe reduces the rate of reaction since both the decay of component 1 and the appearance and decay of component 2 appear at later times. Since both sets of samples aged in 2013 and 2014 show the same effect, the apparent delay of the reaction with the windowed fibre probe is due to inner filter effects and not related to chemical kinetics. In the following section we describe the formation of strongly absorbing degradation products at later times; their absorption reduces the scores of all three components leading to a premature drop-off in the observed fluorescence intensity in Omrani's data.[4]

5.3.4 Filter functions

Filter functions that affect the three components are determined and subsequently used to simulate the effect of fluorescence reabsorption on the spectra obtained with the new fibre probe containing the window. When including inner filter effects the time evolution of the components in **Figure 5.10(a)** and **(b)** are expected to resemble those in **(c)** and **(d)**.

Absorption measurements were carried out on the lubricant oil aged at 468 K. All oils were diluted to 10% in methanol and placed in a 1 mm cuvette for the absorption measurements. The same *Varian* Cary Eclipse spectrometer used for fluorescence measurements was used for the absorption measurements. However, instead of the bifurcated fibre probe, a simple absorption cell was constructed, consisting of two 1 mm diameter multimode fibres, used to guide the light between the spectrometer and the 1 mm thick cuvette. 100% methanol was used as the reference and all spectra were measured 5 times and averaged. The absorption spectra for the 468 K sample series are shown in **Figure 5.11(a)**. The emission loadings for the three components are given in **Figure 5.11(b)** to show the overlap between the increasing absorption and fluorescence as the oil degrades.

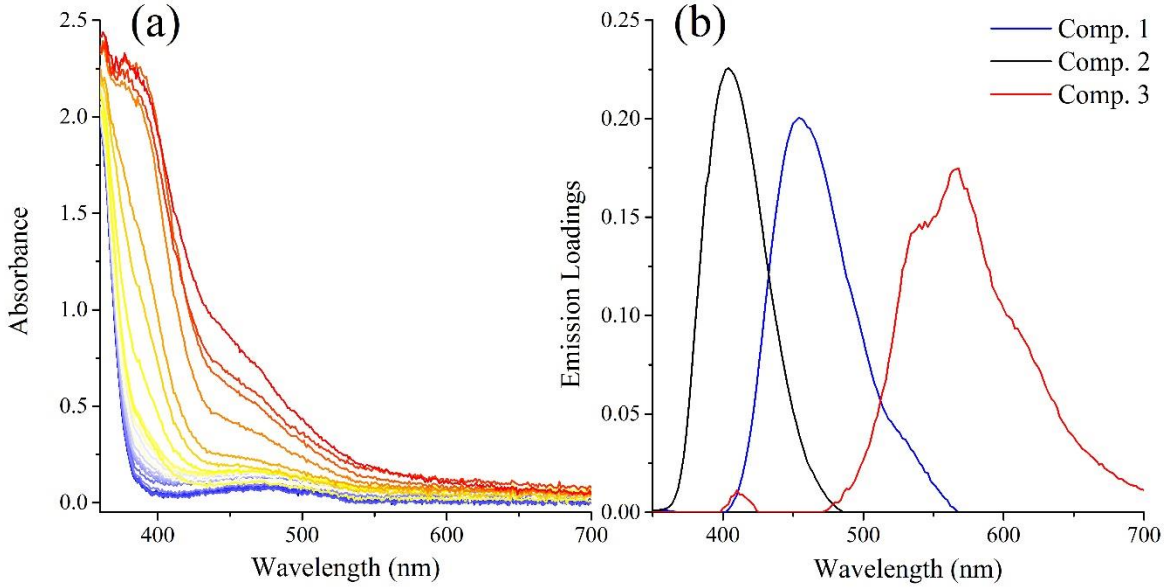

Figure 5.11: Absorption spectra and emission loadings of the turbine oil degraded at 486 K. **(a)** Absorption measurements obtained with a 1 mm cuvette and 10% of the oil samples diluted in Methanol. Blue to red represents fresh oil to degraded oil, respectively. 5 spectra were acquired per sample and averaged to reduce noise and the absorption is calculated using 100% methanol as reference. **(b)** Emission loadings of the three components obtained using PARAFAC analysis on the 90 degraded samples.

To correct the fluorescence scores for reabsorption effects, the following equation was used,

$$\begin{aligned} CorrectedScore_i &= S_i \times C_i \\ &= S_i \times \sum_{\lambda} F_i(\lambda) \times \phi_i \times \exp\left(-L \times A_i(\lambda)\right), \end{aligned} \tag{5.6}$$

where C_i is the component-dependent coefficient required to correct the score. This coefficient is generated by a sum of the three filter functions, which are a product of the emission loading (**Figure 5.11(b)**), $F_i(\lambda)$, with the efficiency factor, ϕ_i, and the absorption. A different efficiency factor, ϕ_i, is required for each component, *i*, to compensate for different emission collection efficiencies of the two probes. The absorption correction factor, *L*, is used to allow for comparison between the absorbance measurements using both the cuvette and fibre probe and accounts for both the ×10 difference in concentration of the oil and the length difference between the 1 mm cuvette and the reabsorption distance of the probe.

The products, $F_i(\lambda)\times\phi_i\times\exp\left(-L\times A_i(\lambda)\right)$, for the three components are shown in **Figure 5.12**. As the oil degrades, the absorption across the spectrum increases and hence the component-dependent coefficient decreases. The effect is less dominant in component 1 as the base stock of the oil absorbs at shorter wavelengths. The scores obtained using the windowed fibre probe are corrected using equation (5.6) to investigate the effect of reabsorption. Separate coefficients were used for all three components to correct for the different decay times of each compound they represent. The corrected scores are shown in **Figure 5.13** and are compared to the scores using the windowless probe. Despite the noise introduced by the weighted absorption data, the scores overlap when the effect of reabsorption is included. Thus the inconsistencies between the two probes are believed to be due to the effective distance of the inner filter effects. The addition of a window to the probe reduces the distance a fluorescence photon must travel from the overlapping acceptance cones and is therefore, less susceptible to re-absorption for highly absorbing samples such as turbine oil. Therefore, introducing a transparent spacer (for example a 5 mm UV-fused silica window, see above) greatly improved the measured fluorescence signal making the technique more robust and sensitive.

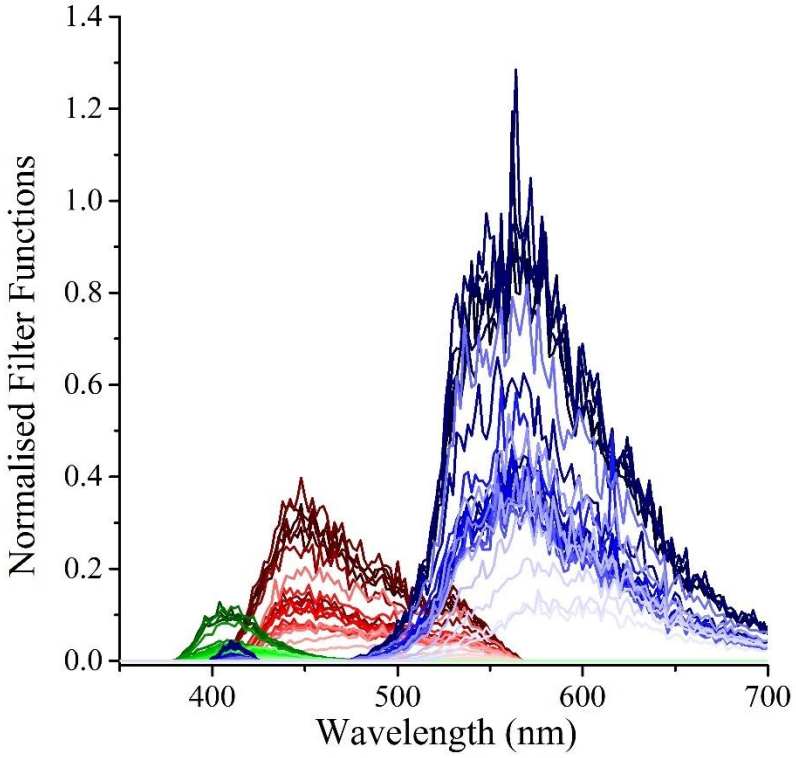

Figure 5.12: The resultant product, $F_i(\lambda)\times\phi_i\times\exp\left(-L\times A_i(\lambda)\right)$, for the three PARAFAC components, *i*. These are summed to determine component dependent coefficient, C_i, that is used to convert the scores obtained using the new windowed fibre probe to the scores obtained previously by Omrani et al. who did not use a spacer window in front of the fibre bundle. The green, red and blue lines correspond to the PARAFAC components, 1, 2, and 3, respectively.

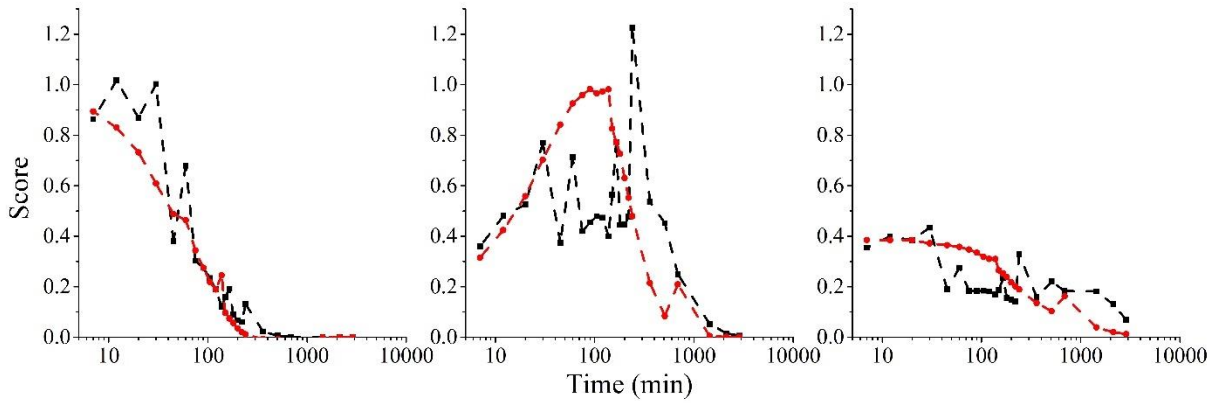

Figure 5.13: Corrected scores (black) of the new windowed probe to account for the reabsorption of fluorescence in the old probe (red) using equation (5.6). From left to right shows components 1, 2, and 3, respectively. The scores are normalised so that component 1 has a maximum of 1 at t_0. The coefficient L was determined to be 15.29 using excel solver. This is reliable being that there is a ×10 difference in concentration of the oil for the absorption measurements between the cuvette and fibre probe. Additionally, the factor includes the excitation beam path depth difference of light into the sample which is approximately 1.8 mm when comparing the 1 mm cuvette and 2.8 mm dead volume of the probe. This obviously depends on the wavelength, refractive index, and age and darkness of the oil, however. The efficiency factor, ϕ_i, was further obtained using solver of each respective component to maximise the fit.

5.4 Concluding remarks

This chapter highlights and evaluates the procedure to collect and analyse the EEM spectra as shown in Chapter 6 and Chapter 7. This involves the settings used to acquire the spectra using the *Varian* Cary Eclipse spectrometer, in addition to the methodology of choosing the correct number of components with PARAFAC analysis.

Here we described how fluorescence-EEM spectroscopy was coupled to a custom-made bifurcated fibre probe that was simply submerged in the sample without any prior sample preparation. In addition, a transparent window was added to the probe end of the fibre to enhance the measured fluorescence in highly reabsorbing media such as lubrication oil.

The procedures herein are utilised for both the analyses used in Chapter 6 and Chapter 7 of this thesis.

5.5 Bibliography

1. J. H. Rho and J. L. Stuart, Automated three-dimensional plotter for fluorescence measurements. *Analytical Chemistry* **1978,** *50*, 620-625.
2. J. H. Christensen, A. B. Hansen, J. Mortensen and O. Andersen, Characterization and matching of oil samples using fluorescence spectroscopy and parallel factor analysis. *Analytical Chemistry* **2005,** *77*, 2210-2217.
3. F. Jiang, F. S.-C. Lee, X. Wang and D. Dai, The application of excitation / emission matrix spectroscopy combined with multivariate analysis for the characterization and source identification of dissolved organic matter in seawater of Bohai Sea, China. *Marine Chemistry* **2008,** *110*, 109-119.
4. H. Omrani, A. E. Dudelzak, B. P. Hollebone and H.-P. Loock, Assessment of the oxidative stability of lubricant oil using fiber-coupled fluorescence excitation–emission matrix spectroscopy. *Analytica Chimica Acta* **2014,** *811*, 1-12.
5. N. L. P. Andrews, J. Z. Fan, H. Omrani, A. Dudelzak and H.-P. Loock, Comparison of lubricant oil antioxidant analysis by fluorescence spectroscopy and linear sweep voltammetry. *Tribology International* **2016,** *94*, 279-287.
6. N. L. P. Andrews, J. Z. Fan, R. L. Forward, M. C. Chen and H.-P. Loock, Determination of the thermal, oxidative and photochemical degradation rates of scintillator liquid by fluorescence EEM spectroscopy. *Physical Chemistry Chemical Physics* **2017,** *19* (1), 73-81.
7. http://www.agilent.com/en-us/products/fluorescence/fluorescence-systems/cary-eclipse-fluorescence-spectrophotometer, 2016.
8. R. Bro and H. A. L. Kiers, A new efficient method for determining the number of components in PARAFAC models. *Journal of Chemometrics* **2003,** *17*, 274-286.
9. R. Bro, PARAFAC. Tutorial and applications. *Chemometrics and Intelligent Laboratory Systems* **1997,** *38*, 149-171.
10. C. A. Stedmon, S. Markager and R. Bro, Tracing dissolved organic matter in aquatic environments using a new approach to fluorescence spectroscopy. *Marine Chemistry* **2003,** *82*, 239-254.
11. K. R. Murphy, C. A. Stedmon, D. Graeber and R. Bro, Fluorescence spectroscopy and multi-way techniques. PARAFAC. *Analytical Methods* **2013,** *5*, 6557-6566.
12. M. G. Shim, B. C. Wilson, E. Marple and M. Wach, Study of fiber-optic probes for in vivo medical Raman spectroscopy. *Applied Spectroscopy* **1999,** *53*, 619-627.
13. T. K. Liang, M. Friedrich, D. Lala and K. B. Ozanyan, Proceedings of IEEE Sensors, 2004.
14. D. Munzke, J. Saunders, H. Omrani, O. Reich and H.-P. Loock, Modeling of fiber-optic fluorescence probes for strongly absorbing samples. *Applied Optics* **2012,** *51*, 6343-6351.
15. http://www.ceramoptec.de/products/fibers/optran-uv-wf.html, 2016.
16. I. H. Malitson, Interspecimen comparison of the refractive index of fused silica. *Journal of the Optical Society of America* **1965,** *55*, 1205.

Chapter 6

Lubricant Oil Analysis

This chapter is based on the paper entitled "Comparison of lubricant oil antioxidant analysis by fluorescence spectroscopy and linear sweep voltammetry" Tribology international, Vol. 94 (2016) P. 279-287, N. L. P. Andrews, J. Z. Fan, H. Omrani, A. Dudelzak, H.-P. Loock. This material has been added according to Elsevier's fair use policy. Under supervision, James Fan helped in ageing the lubricant oil samples and collected some of the EEM spectra. Hanna Omrani and Alex Dudelzak both work at GasTOPS Ltd. and provided useful consultation and preliminary work. With these exceptions all work presented below is that of the author.

6.1 Introduction

Even in the 21st century, and despite all predictions to the contrary, our society is reliant on the use of the internal combustion engine. These engines require lubrication oil as it reduces friction between the moving parts of the engine, removes debris and dissipates heat.[1] As the oil degrades its properties change making it less efficient in lubricating the engine. When excessive oil degradation occurs, this will lead to increased wear of the engine components which in the longer term may result in engine malfunction.[2] Damage to the engine due to insufficient lubrication is often very expensive, due to loss of production time, the need for replacement parts, and hiring contractors to repair the engine. In some cases, the economic cost is eclipsed, since engine malfunction can result in personal injury and even death.

As lubrication oil degrades, free alkyl (R•), hydroxyl (HO•) and alkyl peroxyl (ROO•) radicals are formed via thermally, metal- or oxygen-induced free-radical initiation steps.[3] These radicals further react in chain propagation and branching reactions to form oligomeric compounds and thereby thicken the oil. In the long term insoluble condensates such as sludge and varnish-like deposits are formed.[4] These processes are accelerated at the elevated temperatures in engines and some may be metal catalysed. In addition, hydrogen

peroxides formed as byproducts of peroxyl radical attack that further react to form ketones, alcohols and acids. The presence of acidic compounds cause corrosion of the metallic components of the engine.[3, 5]

The Remaining Useful Life (RUL) is a measure of the operating lifetime of lubrication oil from when it is fresh to when changes to properties of the base-stock render the lubricant useless.[2] RUL can be used to predict the quality of the oil and how long left the oil has until it becomes degraded.

To prolong the RUL of a lubrication oil, additives are added. These include antioxidants, corrosion inhibitors and antiwear agents.[3, 6] However, only low concentrations (typically less than 5%) of these can be used as to not alter the base-stocks lubricating properties. Antioxidants are added to protect the lubricant from oxidative degradation — processes which are catalysed at the elevated temperatures and presence of metals within the internal combustion engine. Antioxidants prolong the RUL of the oil by terminating the active radicals preventing further free-radical polymerisation reactions.[7] There are two major classes of primary antioxidants that are added to lubrication oils. The first are comprised of hindered phenols such as 3,5-di-*t*-butyl-4-hydroxytoluene (BHT). The second major class of antioxidants are aromatic amines such as phenyl-α-naphthylamine (PAN) (See **Figure 6.1**). Both groups consist of highly conjugated species and are able to scavenge the free-radicals that are formed in the engine.

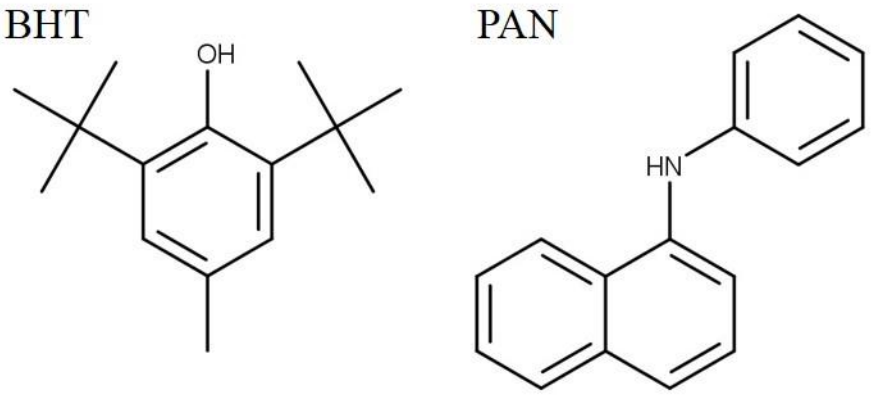

Figure 6.1: Chemical structure of the phenol antioxidant 3,5-di-t-butyl-4-hydroxytoluene (BHT) and aromatic amine phenyl-α-naphthylamine (PAN).

Additives such as corrosion inhibitors, are further added to lubricant oil to reduce the corrosion and rusting of the ferrous metal components in the engine. Corrosion inhibitors are molecules that form a dense protective layer on the metal surfaces preventing oxidative species to react with the metal that cause corrosion and rusting. Another class of additives are antiwear agents. These form films on the metal surfaces to reduce wielding and abrasive wear caused by metal to metal contact in the engine.[8]

Zinc dialkyldithiophosphate (ZDDP) acts as both a corrosion inhibitor and an antiwear agent.[8-10] ZDDP forms protective crosslinked polymeric films on the metal component surfaces that are resistant to being removed through mechanical stress.[11, 12] However, these films are readily broken down by dispersants — additives used to control the lubricant viscosity. Due to the conflicting and potential antagonistic properties of additives, the formulation of lubricant oil additives is specialised to the engine type and running conditions. For example, turbine aviation oil — analysed in this chapter — is an ester based lubrication oil which has amine based antioxidants to hinder the oxidation of the base-stock.[13] Synthetic ester based lubricant oils are appropriate for jet turbines due to their low volatility, high flash points and high thermal stability.[1] By contrast gas and diesel engine lubrication oil are hydrocarbon based lubricants that are

stabilised using hindered phenol-type antioxidants and frequently also contain further additives such as ZDDP.[2]

In addition to degradation of the lubricant and its additives, contamination of the oil with water, combustion products, debris, ethanol, and gasoline will also significantly affect the oils' lubricity and RUL.[1, 14, 15] Consequently, it is vital to monitor these contaminants — ideally while the engine is in use — to ensure a long lifetime of the machine. Water corrodes the engine via rusting, increasing wear. It is typically quantified off-line using infrared spectroscopy at the H_2O absorption lines at 3400 cm^{-1} (2930 nm) and overtones at 6760 cm^{-1} (1480 nm) and 5200 cm^{-1} (1920 nm).[16-23] Contamination of the oil with ethanol from biofuels is also undesired as it is not miscible with the engine oil and thus emulsions will form.[14, 15, 24]

In this chapter, we introduce and evaluate a method of determining the RUL of jet turbine oil through the measurement of the remaining antioxidant concentration using excitation emission matrix (EEM) spectroscopy.[25] Antioxidants scavenge the free-radicals that are formed in the lubrication oil as the engine operates. When the concentrations of antioxidants decrease to below a certain threshold then the base-stock of the oil will start to degrade. Conversely, uncontaminated oil will remain useful as long as it is protected by antioxidants. Thus antioxidant concentration can be used as a proxy for the quality of the lubricant oil.

6.2 Lubricant oil lifetime analysis techniques

As lubrication oil degrades its physical, chemical, and electrical properties are affected. These property changes can be monitored to predict the RUL of the lubricant. Many methods involve the detection of degradation products which are then quantified as the "total acid number" (TAN), "total base number" (TBN), and measurements of particulates such as soot. Other methods determine physical product properties such as viscosity, conductivity or dielectric constant.

Viscosity is frequently used as a measure for the lubricant oil quality. When oil degrades, the viscosity increases due to product formation from the free-radical branching and chain propagation reactions. However, the viscosity may also decrease as the oil ages due to the formation of precipitates. Due to the unpredictabilty on how the lubricants viscosity changes as the oil ages makes it a difficult to measure the remaining useful life of the oil. A lubricant's viscosity is defined in two ways.[1] The kinematic viscosity is defined as its resistance to flow and shear due to gravity and is measured using a capillary tube viscometer.[26] Absolute viscosity is defined as the oil's resistance to flow and shear due to internal friction and is measured using a rotary viscometer.[27]

TAN is a measure of the acidic contamination in oxidised lubrication oil. As oil degrades, acids are formed as a by-product of the radical polymerisation of the base-stock. Acids are quite detrimental to the operation of engines as they can corrode the metallic components of the engine.[28] To prevent corrosion from acids formed as the oil degrades, bases can be added as an additive to react and neutralise any acids that are formed. This is especially important for hydrocarbon mineral based lubricant oils — diesel engines — due to the sulphur and nitrogen acids that are formed as the oil degrades.[29] The TBN is a measure of the amount of base remaining in the oil and decreases as the TAN number increases.[30, 31] Both the TAN and TBN can be determined using potentiometric or colorimetric titration with a base (KOH),[30-32] and using IR spectroscopy combined with chemometrics.[21, 33]

When the oil degrades, its conductivity increases due to the formation of oxidised products such as acids.[34] Consequently, electrochemical sensors have been used to determine the RUL of lubricant oil and have been correlated to the TAN.[34] Another conductivity method, known as Rancimat, involves ageing oil at an elevated temperature and typically under oxidising conditions such as forced air flow.[35] As the oil degrades, volatile acids are produced and are blown into deionised water producing a sharp increase in conductivity,

which can be used to determine the quality of the oil. Rancimat is a destructive method to determine the oxidative stability of the oil.

Also the measurement of particles in the oil can be used to determine the quality of the lubricant.[36] These particles are characterised into two categories: iron and soot. Iron contamination is caused by metal debris as the engine undergoes wear and the formation of iron particles creates an impact on oil electric, and magnetic properties. Iron shavings also promote oxidation of the lubricants. Soot build-up is caused by oxidation of the oil. Iron and soot particles can be removed by filtering the oil and quantified using a microscope.[37] In addition, particle build-up also affects the viscosity and dielectric constant and it has been proposed to infer particle concentrations from these measurements.[36] Trace metals can emerge in lubrication oils from wear due to friction or corrosion of the moving engine components. The amount of trace metals — measured by inductively coupled plasma mass spectrometry (ICP-MS) — can be used to determine the wear of the engine.[38] Metal debris is also quantified using laser induced breakdown spectroscopy (LIBS) in combination with digital image acquisition using a CC120, ChipCHECK by *GasTOPS*.[39] This technique determines the total quantity of particulates, their size, composition and alloy which provides a rapid and reliable assessment of the condition of the working engine. Induction of current is also measured to quantify the concentration of metallic particles within the lubricant using a MetalSCAN device, *GasTOPS*.[39] X-ray fluorescence (XRF) spectroscopy is a further technique that is used to identify and evaluate metal debris through the element specific transitions of inner core electrons (FC400, FilterCHECK, *GasTOPS*).[39, 40]

As can be imagined, detecting the products of lubricant degradation or their properties is not the most effective method for determining the RUL of lubrication oil. When a product is detected the oil has already degraded resulting in irreversible wear to the engine. In addition, the detection of products and their properties is very susceptible to false positives. After an oil change, remnant products will remain in the oil which will give a positive signal of the degradation product even though the oil is fresh and perfectly good.

A more effective method of determining the RUL of lubrication oil is to measure the depletion of reactants. This includes measuring the remaining antioxidant concentration or, alternatively, the TBN.

Antioxidants are added to the oil to prevent oxidation of the base-stock in a free-radical reaction. The concentration of antioxidants therefore decreases as the oil degrades and predicts the RUL of the oil.[2] Currently the best methods to determine the antioxidant concentration are electrochemical methods such as linear sweep voltammetry (LSV).[2, 41] In addition, Fourier transform infrared spectroscopy and chemometric methods have been used to determine the antioxidant concentration of lubrication oil.[42, 43]

An alternative technique, which is presented in this chapter, is based on excitation emission matrix (EEM) spectroscopy — a fluorescence technique — to determine the remaining antioxidant concentration and thus the RUL of the lubrication oil. Antioxidants need to be highly conjugated molecules so that they are able to scavenge the free-radicals that are formed as the oil degrades. This conjugation also makes these molecules fluorescent and fluorescence is a rather specific method of quantifying the antioxidant concentration, since neither the base stock nor its decomposition products strongly fluoresce. Fluorescence can furthermore be measured using fibre probes. These probes can be submerged into a sample without prior sample preparation, thus allowing for in-line measurements. Studies were conducted previously to correlate the fluorescence of lubrication oils with TAN and the mileage of engines at various degrees of oil degradation.[23, 44-46] However, these were only done at a single excitation wavelength and so do not have the additional advantages as with second order fluorescence such as EEMS.

6.3 Remaining antioxidant analysis

6.3.1 Degradation of lubricant oil

To evaluate the remaining antioxidant concentration and hence RUL of lubrication oil, aviation oil (*NYCO*, synthetic aviation turbine oil, Turbonycoil 600, ML-PRF-23699/F) was artificially degraded at elevated temperatures typical of an aviation turbine. The polyol ester-based oil was artificially aged by heating to

three temperatures (468 K, 453 K, and 438 K) typical in a jet turbine engine,[1, 47] while air was bubbled through the oil.[48] The procedure involving heating the oil in a 500 ml round bottom flask in a silicon oil bath was previously done in the work of Omrani et al.[49] Here a condenser was added to prevent evaporation loss of lubricant and lubricant degradation products for a more thorough analysis. Oil samples were withdrawn and allowed to cool in sealed bottles for subsequent analysis. In addition to the artificially aged lubricant, field samples from the main rotor engine (*BCA* Engine Turbo Shaft T58-GE) of a *Sikorsky* Sea King helicopter were obtained at the engine's oil change intervals. All samples were analysed using both LSV and fluorescence EEM spectroscopy.

6.3.2 Kinetic model for antioxidant degradation

The antioxidant concentrations may be described with a simple kinetic model based on pseudo-first order reactions. In the presence of antioxidants such as PAN, the organic radicals, $R^{\bullet}$, that are formed in the oxidation of lubricants are scavenged and converted into stable compounds:[50, 51]

$$PAN + R^{\bullet} \xrightarrow{k_1} PAN^{\bullet} + RH \quad \text{where } R = R,\ RO,\ RCO_2,\ \text{etc}, \tag{R 6.1}$$

$$2PAN^{\bullet} \xrightarrow{k_2} PAN_2, \tag{R 6.2}$$

$$PAN_2 + R^{\bullet} \xrightarrow{k_3} (\text{Product}) + RH. \tag{R 6.3}$$

The concentrations of the fluorescent antioxidants PAN and PAN_2 are therefore governed by the rate equations:

$$\frac{d[PAN]}{dt} = -k_1[PAN][R^{\bullet}], \tag{6.1}$$

$$\frac{d[PAN^{\bullet}]}{dt} = k_1[PAN][R^{\bullet}] - k_2[PAN^{\bullet}]^2, \tag{6.2}$$

$$\frac{d[PAN_2]}{dt} = k_2[PAN^{\bullet}]^2 - k_3[PAN_2][R^{\bullet}]. \tag{6.3}$$

As PAN is present in a large excess over the organic radicals, $\left[\mathrm{R}^{\bullet}\right]$, the concentration of PAN-radicals, $\left[\mathrm{PAN}^{\bullet}\right]$, is assumed to be constant. This allows setting $\frac{d\left[\mathrm{PAN}^{\bullet}\right]}{dt}=0$, which allows setting equation (6.2) to be $k_1[\mathrm{PAN}]\left[\mathrm{R}^{\bullet}\right]=k_2\left[\mathrm{PAN}^{\bullet}\right]^2$. In addition, $\left[\mathrm{R}^{\bullet}\right]$ is small and roughly constant allowing for the assumption that, $k_1^*=k_1\left[\mathrm{R}^{\bullet}\right], k_3^*=k_3\left[\mathrm{R}^{\bullet}\right]$, which is typical for pseudo-first order kinetics. With these assumptions the concentration of PAN in equation (6.1) can be rewritten as,

$$\frac{d[\mathrm{PAN}]}{dt}=-k_1^*[\mathrm{PAN}], \tag{6.4}$$

and solved to give,

$$[\mathrm{PAN}](t)=[\mathrm{PAN}]_0\exp\left(-k_1^*t\right). \tag{6.5}$$

To solve for the concentration of PAN_2, using the above assumptions, equation (6.3) can be rewritten as,

$$\frac{d[\mathrm{PAN}_2]}{dt}+k_3^*[\mathrm{PAN}_2]=k_1^*[\mathrm{PAN}]. \tag{6.6}$$

Substituting equation (6.5) into equation (6.6) gives,

$$\frac{d[\mathrm{PAN}_2]}{dt}+k_3^*[\mathrm{PAN}_2]=k_1^*[\mathrm{PAN}]_0\exp\left(-k_1^*t\right). \tag{6.7}$$

Equation (6.7) is an inhomogeneous differential equation and the solution of the homogeneous form is,

$$\begin{aligned}
\frac{d[\mathrm{PAN}_2]}{dt}&=-k_3^*[\mathrm{PAN}_2]\\
\int_{[\mathrm{PAN}_2]_0}^{[\mathrm{PAN}_2]}\frac{1}{[\mathrm{PAN}_2]}d[\mathrm{PAN}_2]&=\int_0^t -k_3^*dt\\
\ln\left(\frac{[\mathrm{PAN}_2]}{[\mathrm{PAN}_2]_0}\right)&=-k_3^*t\\
[\mathrm{PAN}_2]&=[\mathrm{PAN}_2]_0\exp\left(-k_3^*t\right)
\end{aligned}. \tag{6.8}$$

The solution to the particular equation of (6.8) is found by letting $[\mathrm{PAN}_2]=A\exp(-\alpha t)$ and substituting into equation (6.8),

$$-A\alpha \exp(-\alpha t) + k_3^* A \exp(-\alpha t) = k_1^* [\mathrm{PAN}]_0 \exp(-k_1^* t). \quad \textbf{(6.9)}$$

Now equating the exponent part,

$$\alpha = k_1^*. \quad \textbf{(6.10)}$$

The pre-exponential is,

$$-A\alpha + k_3^* A = k_1^* [\mathrm{PAN}]_0, \quad \textbf{(6.11)}$$

and substituting equation (6.10) into equation (6.11) gives,

$$\begin{aligned} (k_3^* - k_1^*) A &= k_1^* [\mathrm{PAN}]_0 \\ A &= \frac{k_1^* [\mathrm{PAN}]_0}{k_3^* - k_1^*} \end{aligned} \quad \textbf{(6.12)}$$

Adding the homogeneous and particular equations, one obtains,

$$[\mathrm{PAN}_2] = B \exp(-k_3^* t) + \frac{k_1^* [\mathrm{PAN}]_0}{k_3^* - k_1^*} \exp(-k_1^* t). \quad \textbf{(6.13)}$$

With the initial conditions at $t = 0$, $[\mathrm{PAN}_2] = [\mathrm{PAN}_2]_0$ equation (6.13) becomes,

$$\begin{aligned} [\mathrm{PAN}_2]_0 &= B + \frac{k_1^* [\mathrm{PAN}]_0}{k_3^* - k_1^*} \\ B &= [\mathrm{PAN}_2]_0 - \frac{k_1^* [\mathrm{PAN}]_0}{k_3^* - k_1^*} \end{aligned} \quad \textbf{(6.14)}$$

Substituting equation (6.14) into equation (6.13) yields,

$$[\mathrm{PAN}_2] = \left([\mathrm{PAN}_2]_0 - \frac{k_1^* [\mathrm{PAN}]_0}{k_3^* - k_1^*} \right) \exp(-k_3^* t) + \frac{k_1^* [\mathrm{PAN}]_0}{k_3^* - k_1^*} \exp(-k_1^* t), \quad \textbf{(6.15)}$$

which is the solution of the concentration of the PAN dimer. Letting the initial concentration of $[\mathrm{PAN}_2]_0 = 0$ produces,

$$[\mathrm{PAN}_2] = -\left(\frac{k_1^*[\mathrm{PAN}]_0}{k_3^* - k_1^*}\right)\exp\left(-k_3^* t\right) + \frac{k_1^*[\mathrm{PAN}]_0}{k_3^* - k_1^*}\exp\left(-k_1^* t\right)$$
$$[\mathrm{PAN}_2] = \left(\frac{k_1^*[\mathrm{PAN}]_0}{k_3^* - k_1^*}\right)\left\{\exp\left(-k_1^* t\right) - \exp\left(-k_3^* t\right)\right\} \quad , \qquad \textbf{(6.16)}$$

which is the same equation derived by Omrani et al.[49] Later on in this chapter, equations (6.5) and (6.15) are used to fit the antioxidant concentrations as obtained from EEMS.

6.3.3 Linear sweep voltammetry and remaining useful lifetime evaluation routine

6.3.3.1 Overview of technique

The Remaining Useful Lifetime Evaluation Routine (RULER) is an ASTM — American Society of the International Association for Testing and Materials — standard for measuring the remaining antioxidant concentration in oils such as lubrication oil.[41, 52-54] Previously known as Remaining Useful Life of a Lubricant Evaluation Technique (RULLET), RULER is a LSV technique designed to measure the remaining primary antioxidant concentration.[2, 13] The LSV method relies on the difference of the signal from the sample to that obtained from fresh reference oil. The voltammetric technique does not involve titration allowing repeat analysis of each sample and takes less than a minute to perform.[29, 55]

In LSV, the voltage is ramped from low to high voltage — typically from 0 V to 2 V — and the resultant current is measured. If there are any antioxidants in the oil they will become oxidised at a characteristic voltage thereby generating a peak in the voltammogram.[56] The antioxidant concentration is linearly related to the current produced and so the remaining antioxidant concentration can be monitored. The integral of the antioxidant peak is used to calculate the remaining antioxidant concentration using equation (6.17),

$$\%\ \text{remaining antioxidant} = \frac{\text{Used oil}}{\text{Fresh oil}} \times 100\ \%. \qquad \textbf{(6.17)}$$

The RULER instrument consists of a three electrode probe system containing a glassy carbon reference electrode, a platinum wire working electrode and a platinum wire auxiliary electrode. An aliquot of used

oil sample (100 – 500 μL) is diluted in acetone or ethanol which contains 1 g of +325 mesh sand, and an electrolyte. Once the vial is shaken, the antioxidants are extracted into the solution whereas the remaining droplets of oil suspended in the solution are agglomerated by the sand. The sand / droplet suspension is allowed to settle out to the bottom of the flask as to not interfere with the voltammetric analysis.[53]

Being that the lubrication oil's formulation and thus its properties depend on the engine it is designed for, RULER has been modified to work with a number of various lubrication oil types. Turbine ester based lubrication oils with aromatic amine antioxidants use acetone as the solvent and lithium perchlorate as the electrolyte.[13] Diesel hydrocarbon lubrication oils with hindered phenol antioxidants and reserve base use water / ethanol as the solvent and potassium hydroxide as the electrolyte.[29] Standard solutions have been designed for the different lubricant oil and are named as the "red" solution for aviation turbines, "green" solution for hydraulic and industrial lubrication, "blue" solution for gas and diesel engines, and "yellow" solution for steam turbines. These names are not associated with the colour of the solution — they are all colourless — but are simply used to differentiate the standards. Being that aviation lubricant oil is analysed in this report, the red solution was used. The electrode probe must also be cleaned prior to analysis to remove any residual chemical films that will interfere with the voltammetric reading. To account for the conductivity of the electrolyte solution and other variances, the instrument is calibrated using the "red" solution.

6.3.3.2 Experimental

The LSV experiments were carried out using a commercial device (RULER, CE520, *Fluitec*). As jet turbine oil is being evaluated, the RULER "red" solution (*Fluitec*) was used. According to the supplier the "red" solution comprises of 5 ml of acetone, an electrolyte (lithium perchlorate), in addition to coarse and fine sand.[41, 52-54] 100 μL aliquots of turbine oil were added to each "red" solution vial. The vials were shaken so the antioxidants in the oil were extracted into the acetone electrolyte phase and the remaining base stock

oil was agglomerated by the sand. The sand / oil suspension was then allowed to settle to the bottom to not interfere with the measurement. The instrument was calibrated using the neat “red” solution.

The probe consists of a 3-electrode system containing two platinum working and auxiliary electrodes and a glassy carbon reference electrode. The potential across the electrode is increased linearly at a rate of 100 mV/s and the resulting current is converted to a voltage by the voltammetric analyser, using a gain ratio of 1 V / 20 µA. The data is acquired through to an analogue or digital recording device (0 to 1 V full scale) and scaled to a so-called RULER number. **Figure 6.2** shows a typical linear sweep (LS) voltammogram of the fresh turbine oil (Turbonycoil 600, *NYCO*). The antioxidant N-phenylnaphthalen-1-amine (phenyl-α-naphthylamine, PAN) present in the neat oil is oxidised resulting in a peak in the voltammogram at about 900 mV that is used to quantify the antioxidant concentration. Other amine-based antioxidants are also expected to contribute to the peak at 900 mV, whereas hindered phenol-based antioxidants are expected to appear at around 1.5 V

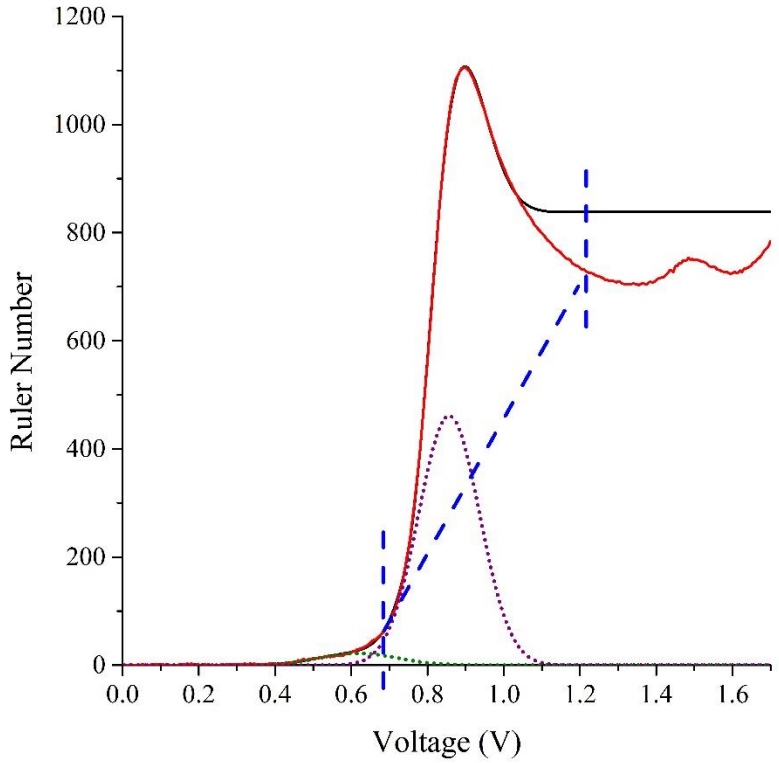

Figure 6.2: Voltammogram of the fresh turbine oil sample shown as solid red. The solid black line represents the fit to the data using equation (6.18) where the green and purple dotted lines represent the two Gaussians in equation (6.18). Although at higher voltages is no longer adequate, it does provide a good representation for the amine-based antioxidant peak at 900 mV. The RULER method of determining the antioxidant concentration is to integrate the area above and between the blue dashed lines.[41]

The LSV data can be fit to a combination of a step function and two Gaussian functions as shown in equation (6.18),

$$f(x) = a \times \exp\left(-\exp\left(-k\left(x - x_a\right)\right)\right) + b \times \exp\left(-\frac{(x - x_b)^2}{w_b}\right) + c \times \exp\left(-\frac{(x - x_c)^2}{w_c}\right), \quad \textbf{(6.18)}$$

where a, b, c, x_a, x_b, x_c, k, w_b, and w_c are fitting parameters (**Figure 6.2**). To obtain the remaining antioxidant concentrations, the larger Gaussian function — centred at 0.9 V — was integrated using the product of $c\sqrt{w_c \pi}$ and compared to that of the fresh sample at t = 0 min. This fit was found to be slightly more

robust and less variable compared to the recommended RULER method, which involves manually setting integration limits at each side of the main feature and thereby defining a sloping baseline before calculating the integral (**Figure 6.2**).

6.3.3.3 Results and discussion

Several LS voltammograms were obtained from aged jet engine lubricant (Turbonycoil 600, *NYCO*), that were withdrawn following a roughly logarithmic time plan (**Figure 6.3**). The figure indicates that after an initial delay the main feature at 900 mV in the LSV decays while a small feature at about 600 mV increases in intensity. As will be shown below in **Figure 6.10**, the main feature is well-correlated to the sum of the PAN and its dimer (PAN_2) antioxidant additives, which are both strongly fluorescing. The smaller feature is currently unassigned and is likely a non-fluorescent degradation product of the PAN antioxidant.

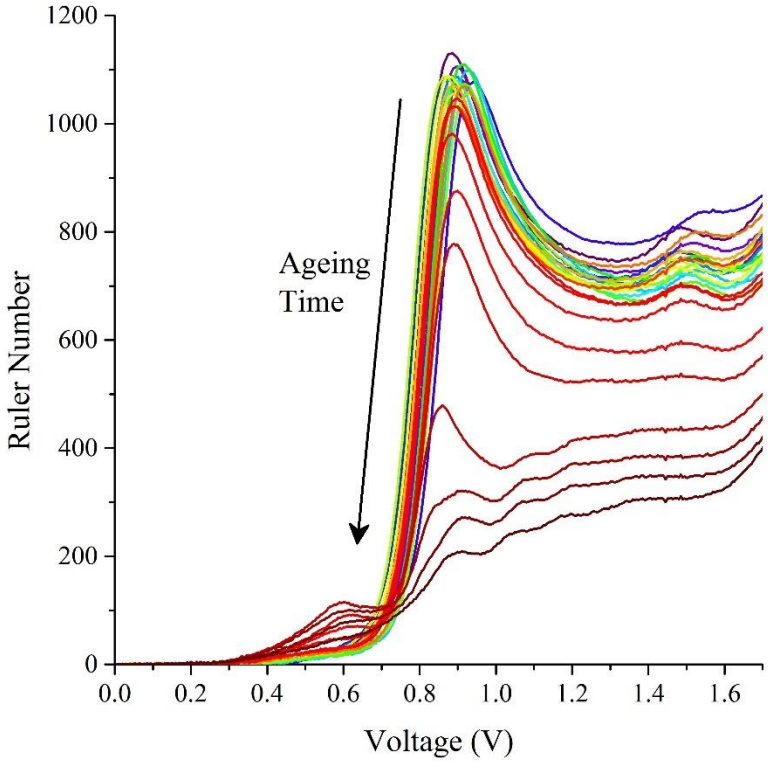

Figure 6.3: Voltammograms of jet turbine oil aged at 468 K. The RULER number is obtained by converting the produced current into a voltage by the RULER CE520 device. The peak located at 900 mV represents

the amine-based antioxidant PAN and PAN_2 and decreases as the oil is aged. The coloured lines from purple to red represent samples withdrawn at increased ageing times. The arrow is used to help highlight that the peak located at 0.9 V decreases as the oil ages.

The relative antioxidant concentration in the artificially aged aviation lubricant using equation (6.17) with the LSV method is shown in **Figure 6.4**. As observed the remaining antioxidant concentration decreases as the oil degrades and the antioxidants are used up by reacting with the free-radicals that are formed in the oil. **Figure 6.4** also shows that both the ASTM RULER cursor and our Gaussian fit (equation (6.18)) methods of determining the remaining antioxidant concentration, agree.

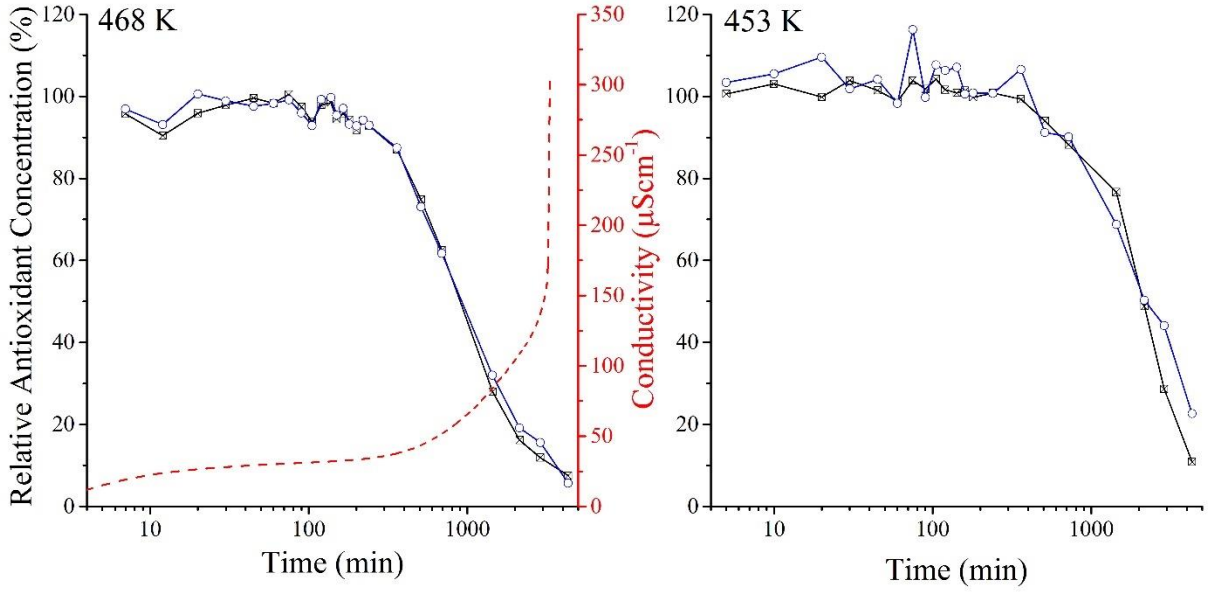

Figure 6.4: Relative remaining antioxidant concentration in aviation turbine oil samples aged at 468 K and 453 K where at t = 0 min the total concentration is set to 100%. The hollow blue circles and crossed black squares represent the LSV data obtained using the Gaussian integral and ASTM RULER cursor method, respectively. The dashed red line plotted using the right axis represents Rancimat data obtained by Omrani et al. and shows the conductivity increase as volatile acids are formed when the same oil is aged at 468 K.[49]

As the relative remaining antioxidant concentration decreases to a point when the oil has degraded there is a sharp increase in the conductance in the Rancimat data. In the Rancimat technique, the oil is aged at a

specific temperature (468 K) and the effluent air from the oil is bubbled through deionised water.[35, 49] When the oil degrades volatile organic acids such as formic acid, are produced and blown into the water resulting in a sharp increase in conductivity. Although Rancimat only measures the volatile acid formation, this rise in acids produced in the oil agrees with the total acid build up and thus TAN, which relates to the RUL of the oil.[2] Thus the remaining antioxidant concentration can be used as a proxy to predict the RUL of the oil.

6.3.4 Excitation emission matrix spectroscopy

6.3.4.1 Overview of technique

Optical techniques, such as fluorescence spectroscopy, are suitable tools for use in lubricant oil monitoring.[25, 49, 57] Many lubrication oils contain aromatic antioxidants such as hindered phenols including BHT or aromatic amines including PAN. These compounds naturally fluoresce and can be used as indicators to monitor the RUL and condition of the oil.[25, 58] Moreover, fluorescence spectroscopy is highly sensitive, allowing for rapid real-time data acquisition while requiring minimal data treatment. However, lubrication oils are complex in composition and because oil samples contain a vast amount of similar fluorophores, specific components are difficult to distinguish using a simple single-wavelength excitation fluorescence measurement.[19, 59] A superior analytical method collects the entire fluorescence spectrum for a large number of excitation wavelengths and emission wavelengths. The resultant EEM can be used to generate a three-dimensional topographical map that allows one to distinguish different fluorophores within a complex mixture.[60, 61] In addition, combining second order fluorescence techniques such as excitation emission matrix spectroscopy with a multivariate analysis method such as parallel factor (PARAFAC) analysis, one can reliably differentiate between the oil's main constituents.[25, 62]

6.3.4.2 Experimental

A double-grating fluorescence spectrometer (*Varian,* Cary Eclipse) was used to collect all the 157 EEM spectra. The instrument was coupled to a custom built bifurcated fibre probe as discussed in Chapter 5. The bifurcated fibre probe (**Figure 6.5**) was built to the same specifications that were used previously and

contains 19 multimode fibres (*CeramOptec*, core/cladding diameters of 400/440 µm).[49] Of those, 6 fibres are used to deliver excitation light to the sample (**Figure 6.5(c)**) and 13 fibres are used to collect the emitted fluorescence light (**Figure 6.5(d)**). The fibre probe was submerged in the neat lubricant samples, without the need for sample preparation. As pointed out in Chapter 5, only the light that is emitted by the sample within the overlap of the acceptance cones of the emission and excitation fibres will be collected.[63] Since the attenuation length in aged ("black") lubricant can be as short as a few hundred micrometres, the distance between the fibre end and the front face of the emitting sample contributes significantly to the reabsorption by the oil, which can affect the resultant fluorescence intensities. This concern can be alleviated by attaching a transparent spacer in front of the fibre end facets. Therefore, a 5 mm thick UV-fused silica window (*Thorlabs* WG41050**)** was cut to size and attached to the probe end. In addition, the window was bevelled at 81° to reduce back reflections from the front face of the window in to the collection fibres (**Figure 6.5(b)**)

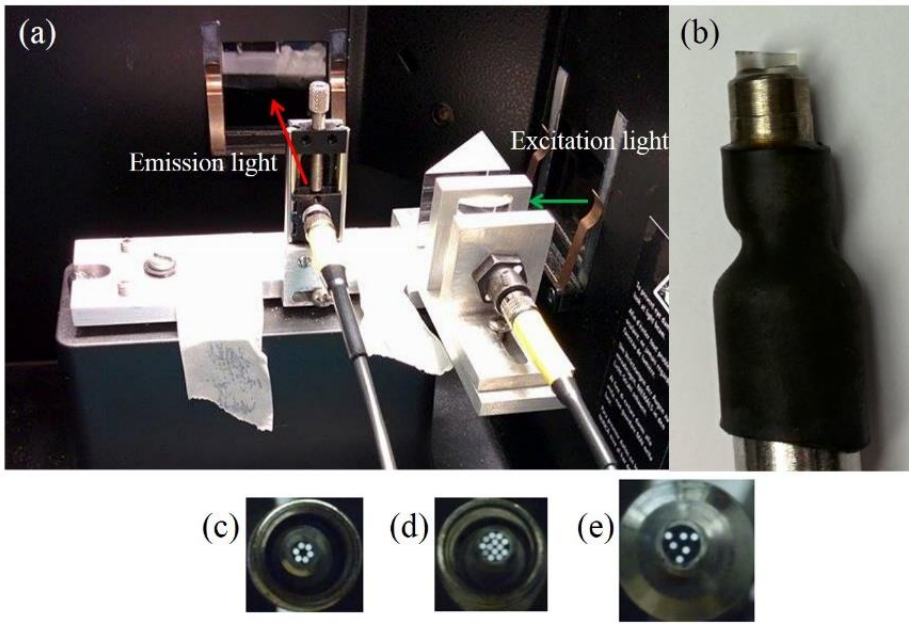

Figure 6.5: Photo of the custom made bifurcated fibre attachment. **(a)** Fibre attachment to the Varian Eclipse spectrometer. **(b)** Fibre probe end with bevelled window to reduce back reflections. **(c)** and **(d)** show the excitation and emission ends of the fibre bundle respectively. **(e)** The 6 excitation fibres illuminated at the probe end of the fibre bundle.

All EEM spectra were collected in the excitation range of 190 – 450 nm and emission range of 200 – 700 nm with step sizes of 5 nm and 2 nm, respectively. Both monochromator slits were set to 5 nm and filters were used remove second order diffraction light from exciting the sample. The collection of each EEM spectrum took around 30 minutes with a scan rate at 1200 nm/min.

6.3.4.3 Parallel factor analysis

All 157 EEM spectra were analysed together using multivariate analysis; they include 79 taken from the main rotor (*BCE* turbo shaft T58-GE) engines used in *Sikorsky* Sea King helicopters, 71 samples obtained by artificial ageing, and 7 samples that were spiked with additional PAN. Given the small number of fluorescent components and the simplicity of the EEM spectra, parallel factor analysis (PARAFAC), was implemented by the drEEM toolbox in Matlab.[64] PARAFAC is preferable over other multivariate methods, since in kinetic measurements its components can frequently be correlated to chemical compounds or compound classes.[62, 65, 66] The PARAFAC algorithm was applied 10 times to normalised data so all samples had equal weighting, with random initialisation for each run, a convergence criterion of 1×10^{-10} and non-negativity constraints. The run with the lowest sum of least square errors was selected as the best fit.[64] Here a two-component fit best represented the data. It had a core consistency of 99.6% and a sum of least square error of 4.1×10^{-4}. Although the three-component fit had an improved sum of least square error of 2.9×10^{-4} it overanalysed the data. The components then overlapped and produced a core consistency of only 51.6%.

6.3.4.4 Results and discussion

Figure 6.6 shows a representative data series of EEM spectra on degraded lubricant oil heated to 468 K. Upon inspection of the spectra in **Figure 6.6** visual identification of two main contributors to the fluorescence spectra — one at an excitation wavelength of λ_{exc} = 350 nm and emission of λ_{em} = 400 nm, and a second one at λ_{exc} = 400 and λ_{em} = 450 nm — can be determined. These components were identified in an earlier publication as PAN and the PAN_2, respectively.[49] Using PARAFAC analysis on all the 157 EEM spectra also gave two components and their reconstructed component spectra are shown in **Figure 6.7**. The component scores of these two fluorescent antioxidants are shown as a function of time in **Figure**

6.8. The scores show that the PAN antioxidant concentration decays as the oil is heated at the same rate that the PAN_2 forms. As the lubricant is further oxidised both concentrations decay to zero and the oil degrades. In addition, at higher temperature the antioxidants react faster, as expected, and hence the oil degrades earlier. As the scores obtained using PARAFAC correlate to the concentration of the components this data can be used to fit to the rate equations (6.5) and (6.15) — shown as the dashed lines in **Figure 6.8** — and agree well over a logarithmic time frame.

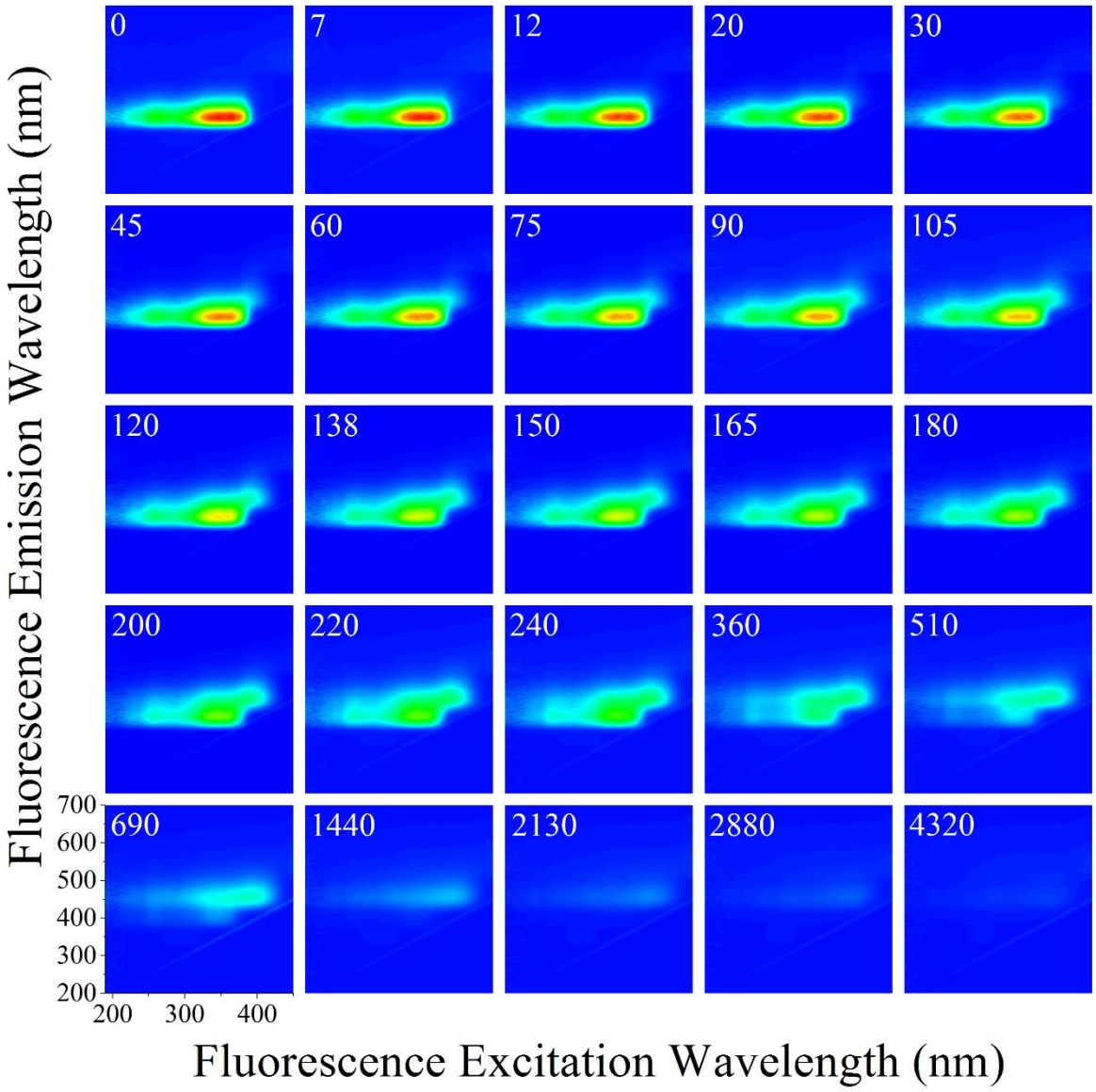

Figure 6.6: EEM spectra of jet turbine oil samples artificially aged though heating to 468 K. The white text in the top left of each spectrum represents the time in minutes at which the sample was withdrawn. The colours from blue to red, represent the normalised intensity from 0 to 1, respectively.

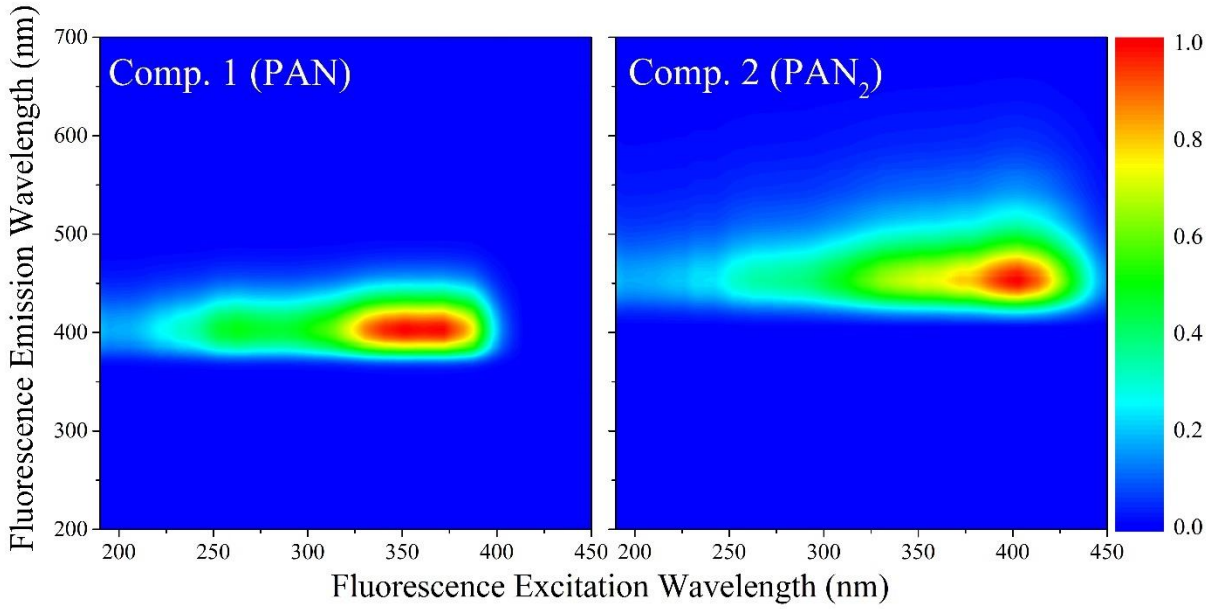

Figure 6.7: Normalised EEM signatures of the two components produced by PARAFAC on all the 157 EEM spectra obtained using the windowed probe as shown in figure **Figure 6.5**. The colours from blue to red, represent the normalised intensity from 0 to 1, respectively.

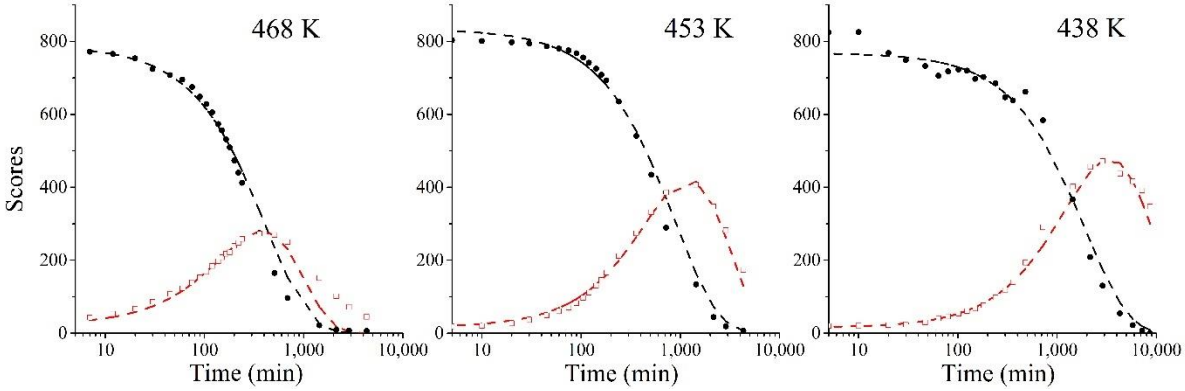

Figure 6.8: Time evolution of the two PARAFAC components using the fibre probe containing a bevelled spacer window. The black circles and red squares represent component 1 (PAN) and component 2 (PAN_2), respectively. The dashed lines are obtained by fitting the data to the kinetic model shown in equations (6.5) and (6.15).

Although the fits of equations (6.5) and (6.15) to the scores of PAN and PAN_2 fit well over the most of the time frame, deviations from the data exist at long times. This is due to the fact that the assumptions used in

the kinetic model (Section 6.3.2) do not hold well at long times, i.e. when the concentration of $\left[\mathrm{PAN}^{\bullet}\right]$ decreases and $\left[\mathrm{R}^{\bullet}\right]$ increases. It is therefore not surprising to see deviations of the experimental data from the fit at times longer than 2000 min, especially for the highest temperature, 468 K (**Figure 6.8**).

The rate constants k_1^* and k_3^* are given in **Table 6.1**. Since rate constants are obtained at three different temperatures, an Arrhenius plot (**Figure 6.9**) can be used to estimate the activation energy and pre-exponential factor associated with these effective rate constants. Comparison of the rate constants with those obtained by Omrani et al. — who aged the same brand of lubrication oil (Turbonycoil 600, *NYCO*) without a condenser and analysed them with a windowless fibre probe — shows that the activation energies are similar. However, the pre-exponential factors and rate constants are considerably different. This was expected since the — presumably constant but unknown — $\left[\mathrm{R}^{\bullet}\right]$ was included in the effective rate constants, $k_1^* = k_1\left[\mathrm{R}^{\bullet}\right], k_3^* = k_3\left[\mathrm{R}^{\bullet}\right]$.

Table 6.1: Rate constants for the decay of PAN and the formation of PAN_2, k_1^*, and decay of PAN_2, k_3^*, in jet turbine oil obtained by fitting the data shown in **Figure 6.8** to equations (6.5) and (6.15).

T / K	**468**	**453**	**438**	**E_a (kJ mol^{-1})**	**E_a (kJ mol^{-1}) Ref [49]**
$[PAN]_0$	787.5	833.0	768.2		
$[PAN_2]_0$	23.2	16.2	15.1		
***k**$_1$ / min^{-1}**	0.00238	0.00113	0.00051	86.9 (0.2)	93 (2)
***k**$_3$**	0.00268	0.00057	0.00014	166 (8)	114 (15)

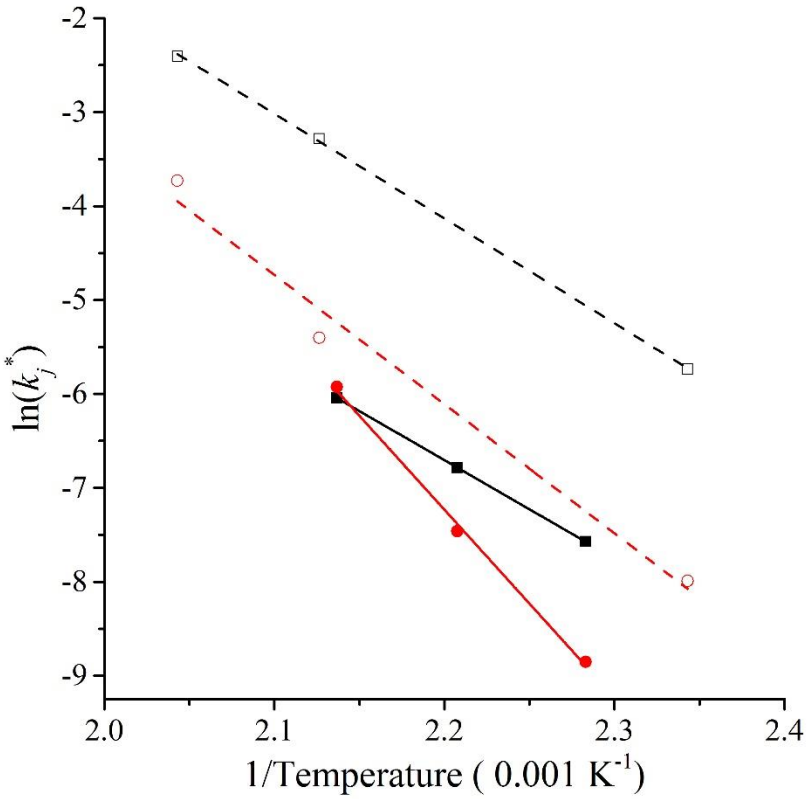

Figure 6.9: Arrhenius plot to determine the activation energies of PAN and PAN_2 degradation and formation as shown in **Table 6.1**. The black squares and red circles represent the rate constants k_1^* and k_3^*, respectively. The solid and hollow symbols denote the data presented in this work and that of Omrani et al., respectively.[49] The difference is due to that, different batches were used and so the concentration of radicals formed is potentially different. Furthermore, in the experiment run by Omrani et al. a condenser was not used and thus the volatile compounds would escape and not be detected.

6.3.5 Comparison of the antioxidant concentration measurements obtained by LSV and EEMS

To determine whether fluorescence can be used as a technique to determine the RUL of lubrication oil it needs to be compared with an ASTM standard such as RULER or LSV. Both components (PAN and PAN_2) obtained using PARAFAC analysis on the EEM spectra are added since in RULER all the aromatic amine groups are oxidised concurrently at the same voltage (**Figure 6.3**). The relative remaining antioxidant concentration for EEMS was calculated using equation (6.19) and is shown in **Figure 6.10**,

$$\%\ \text{relative remaining antioxidant} = \frac{\left([\text{PAN}]+[\text{PAN}_2]\right)_t}{\left([\text{PAN}]+[\text{PAN}_2]\right)_0} \times 100\ \%. \quad \textbf{(6.19)}$$

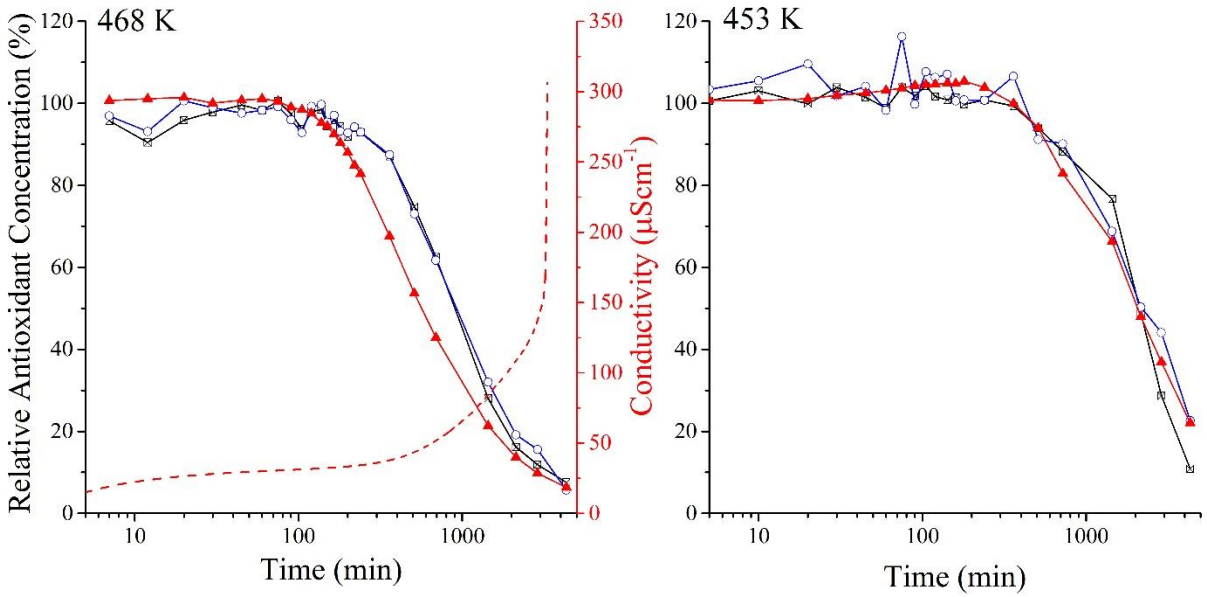

Figure 6.10: Relative remaining antioxidant concentration in jet turbine oil samples using both RULER and EEMS. The same degraded lubrication oil samples were used for both RULER and EEMS and heated to 468 K and 453 K and fresh oil is when t = 0 min. This figure is similar to that of **Figure 6.4** but has the sum of both PARAFAC component scores overlaid as solid red triangles. To compare with RULER, the hollow blue circles and crossed black squares represent the LSV data obtained using the Gaussian integral and cursor method, respectively. The Rancimat data obtained by Omrani et al. is further added to the left figure for comparison as a dashed red line.[49]

Figure 6.10 shows that the relative remaining antioxidant concentration obtained using both RULER and EEMS agree especially at the lower temperature of 453 K. On the other hand, the LSV results recorded when the lubricant was oxidised at 468 K indicate the presence of antioxidants even when the combined component scores of the PARAFAC analysis have already declined. At high temperatures compounds such as the PAN oligomer may be formed, which also acts as an antioxidant before decomposing. If these compounds were weakly or non-fluorescing, they would contribute to the LSV signal but not to the EEM spectra. It is also possible that the intensity of the fluorescence decreased at long times due to the presence

of absorbing oil degradation products. While the redesigned fibre probe has been equipped with a window to reduce the distance of reabsorption, it is perceivable that degradation products nevertheless reduce the fluorescence intensity near the end of the lubricants lifetime (Chapter 5).

In **Figure 6.11** the correlation between LSV data and the PARAFAC component scores are shown. In the range of low antioxidant concentrations, the data are linearly correlated, whereas at high concentrations the LSV method yields concentrations that vary over a somewhat larger range compared to the fluorescence data. Many of these high concentration measurements correspond to samples obtained at oil change intervals from a military helicopter, and it may be expected (and hoped!) that the antioxidant concentration levels in these samples were near 100%. In addition, **Figure 6.11** shows that the remaining antioxidant concentration can reach over 100%, — an unusual response. However, these are likely caused by the field samples using oil with a slightly greater antioxidant concentration. It is possible that the variability of the peak amplitude in the LSV measurements is a consequence of the sensitivity of the electrochemical method to the sample preparation. It is also conceivable, of course, that the LSV measurements reflect the antioxidant concentration more accurately and show the additional decay of the PAN oligomer that can be extracted into the acetone electrolyte phase. The fluorescence EEM method does not observe the PAN oligomers, since the PAN and PAN_2 components dominate the spectra. We also note that other non-fluorescent antioxidants and corrosion inhibitors such as ZDDP, would not be detectable using fluorescence EEM and would also not contribute to the LSV feature at 900 mV. In any case from **Figure 6.11** it may be concluded that fluorescence EEM measurements provide a viable alternative to LSV measurements over the whole range of antioxidant concentrations.

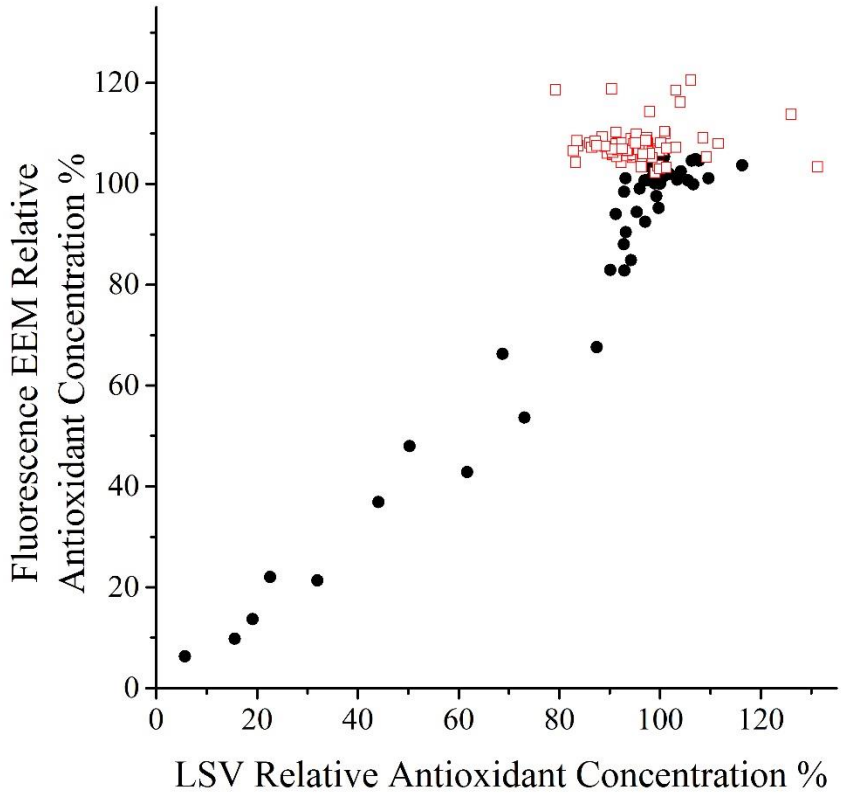

Figure 6.11: Correlation of the relative remaining antioxidant concentrations in jet turbine oil, obtained using RULER / LSV and fluorescence-EEM. The data includes, both, lab batches heated at 468 K and 453 K (shown as black circles, and reproduced from **Figure 6.10**) and 79 field samples taken from the main rotor (*BCE* turbo shaft T58-GE) engines used in *Sikorsky* Sea King helicopters (shown as hollow red squares).

6.4 Concluding remarks

In this chapter it is shown that fluorescence EEMS can be used to determine the remaining antioxidant concentration in lubrication oil.[25] The comparative analysis of the LSV by RULER and fluorescence EEM indicates that the total antioxidant concentrations obtained by both methods correlate very well. At the same time, EEM has two noticeable advantages. First, it provides information on the chemical identity of the lubricants. Thus a more thorough understanding of the kinetics of the chemical reactions as the oil degrades is possible as compared to RULER. Second, without the need for sample preparation, fluorescence EEMS is amenable for real-time, on-line measurements.

As the remaining antioxidant concentration determines the RUL of oil, EEMS can be used as a technique to determine and consequently predict when lubrication oil will become unsafe to use. In the case of PAN antioxidants, the accuracy of this prediction is further enhanced by the fact that the EEMS analysis method is able to extract rate constants on multiple antioxidants within the oil, i.e. PAN transforms into the dimer before both antioxidants decompose. A potential lubricant oil sensor can then be envisioned, whereby an alarm would go off when the ratio of PAN to PAN-dimer falls below a certain threshold. In addition, by knowing the kinetics of the reaction, a reliable RUL of the oil can be calculated as the engine is operating and can be updated accordingly.

As was shown in this chapter, our fluorescence EEMS analysis method can be used as a tool to determine the oil quality in real-time and on-line. However, the commercial fluorescence EEM instrument (Cary Eclipse *Varian*) and other commercial instruments tend to be expensive and bulky. They also take over 30 mins to acquire each EEM spectrum. The existing instruments are therefore not suitable as real-time lubricant quality sensors. Fortunately, as discussed in Chapter 9, we invented a novel technique of multiplexing the excitation light, thereby allowing EEM spectra to be obtained rapidly. We then have the capability of monitoring reactions that occur in a matter of minutes. Such a multiplexed fluorescence-EEM spectrometer, will make it possible to determine the RUL of oil as it degrades — on-line and in real-time.

6.5 Bibliography

1. R. M. Mortier, M. F. Fox and S. T. Orszulik, *Chemistry and technology of lubricants*, Springer Netherlands, Dordrecht, 2010.
2. R. E. Kauffman, Remaining useful life measurements of diesel engine oils, automotive engine oils, hydraulic fluids, and greases using cyclic voltammetric methods. *Lubrication engineering* **1995,** *51* (3), 223-229.
3. J. Dong and C. A. Migdal, in *Lubricant Additives: Chemistry and Applications, Second Edition*, ed. L. R. Rudnick, CRC Press, 2nd Edition edn., 2009, pp. 4-41.
4. P. C. Hamblin, U. Kristen and D. Chasan, Ashless antioxidants, copper deactivators and corrosion inhibitors: Their use in lubricating oils. *Lubrication Science* **1990,** *2*, 287-318.
5. H. H. Zuidema, Oxidation of lubricating oils. *Chemical Reviews* **1946,** *38*, 197-226.
6. T. Colclough, Role of additives and transition metals in lubricating oil oxidation. *Industrial & Engineering Chemistry Research* **1987,** *26*, 1888-1895.

7. P. Rohrbach, P. C. Hamblin and M. Ribeaud, Benefits of antioxidants in lubricants and greases assessed by pressurised differential scanning calorimetry. *Tribotest* **2005,** *11*, 233-246.
8. H. Spikes, The history and mechanisms of ZDDP. *Tribology Letters* **2004,** *17*, 469-489.
9. H. Fujita and H. A. Spikes, Study of zinc dialkyldithiophosphate antiwear film formation and removal processes, part II: Kinetic model. *Tribology Transactions* **2005,** *48*, 567-575.
10. J. M. Martin, Antiwear mechanisms of zinc dithiophosphate: A chemical hardness approach. *Tribology Letters* **1999,** *6*, 1-8.
11. M. Becchi, F. Perret, B. Carraze, J. F. Beziau and J. P. Michel, Structural determination of zinc dithiophosphates in lubricating oils by gas chromatography–mass spectrometry with electron impact and electron-capture negative ion chemical ionization. *Journal of Chromatography A* **2001,** *905*, 207-222.
12. R. A. McDonald, in *Lubricant Additives: Chemistry and Applications, Second Edition*, ed. L. R. Rudnick, CRC Press, 2nd Edition edn., 2009, pp. 51-61.
13. R. E. Kauffman,*United States Pat.*, US4744870 A, 1988.
14. P. R. D. Silva, M. Priest, P. M. Lee, R. C. Coy and R. I. Taylor, Tribometer investigation of the frictional response of piston rings with lubricant contaminated with the gasoline engine biofuel ethanol and water. *Proceedings of the Institution of Mechanical Engineers, Part J: Journal of Engineering Tribology* **2011,** *225*, 347-358.
15. E. D. Silva, 20040169858, 2004.
16. A. Borin and R. J. Poppi, Multivariate quality control of lubricating oils using Fourier transform infrared spectroscopy. *Journal of the Brazilian Chemical Society* **2004,** *15*, 570-576.
17. N. L. P. Andrews, A. G. MacLean, J. E. Saunders, J. A. Barnes, H.-P. Loock, M. Saad, C. Jia, K. Ramaswamy and L. R. Chen, Quantification of different water species in acetone using a NIR-triple-wavelength fiber laser. *Optics Express* **2014,** *22*, 19337.
18. Y. Maréchal, The molecular structure of liquid water delivered by absorption spectroscopy in the whole IR region completed with thermodynamics data. *Journal of Molecular Structure* **2011,** *1004*, 146-155.
19. L. A. Toms and A. M. Toms, *Machinery oil analysis: Methods, automation & benefits: A guide for maintenance managers & supervisors*, 3 edn., Society of Tribologists and Lubrication Engineers, 2008.
20. M. J. Adams, M. J. Romeo and P. Rawson, FTIR analysis and monitoring of synthetic aviation engine oils. *Talanta* **2007,** *73*, 629-634.
21. A. G. Mignani, L. Ciaccheri, A. A. Mencaglia, G. Adriani, A. Paccagnini, M. Campatelli, H. Ottevaere and H. Thienpont, Proc. SPIE 9141, Optical Sensing and Detection III, 91411U, 2014.
22. A. G. Mignani, L. Ciaccheri, A. A. Mencaglia, G. Adriani, A. Paccagnini, M. Campatelli, H. Ottevaere and H. Thienpont, 2014 Fotonica AEIT Italian Conference on Photonics Technologies, 2014.
23. A. G. Mignani, L. Ciaccheri, N. Díaz-Herrera, A. A. Mencaglia, H. Ottevaere, H. Thienpont, S. Francalanci, A. Paccagnini and F. S. Pavone, Optical fiber spectroscopy for measuring quality indicators of lubricant oils. *Measurement Science and Technology* **2009,** *20*, 034011.
24. C. Lenauer, C. Tomastik, T. Wopelka and M. Jech, Piston ring wear and cylinder liner tribofilm in tribotests with lubricants artificially altered with ethanol combustion products. *Tribology International* **2015,** *82, Part B*, 415-422.
25. N. L. P. Andrews, J. Z. Fan, H. Omrani, A. Dudelzak and H.-P. Loock, Comparison of lubricant oil antioxidant analysis by fluorescence spectroscopy and linear sweep voltammetry. *Tribology International* **2016,** *94*, 279-287.
26. *ASTM standard D445 - 15a, standard test method for kinematic viscosity of transparent and opaque liquids (and calculation of dynamic viscosity)*, ASTM International, West Conshohocken, PA, 2015.

27. *ASTM standard D2983 - 15, standard test method for low-temperature viscosity of lubricants measured by Brookfeild viscometer*, ASTM International, West Conshohocken, PA, 2015.
28. C. Besser, K. Steinschütz, N. Dörr, F. Novotny-Farkas and G. Allmaier, Impact of engine oil degradation on wear and corrosion caused by acetic acid evaluated by chassis dynamometer bench tests. *Wear* **2014,** *317*, 64-76.
29. R. E. Kauffman and J. Ameye, in *COMADEM '97; 10th International congress and exhibition on condition monitoring and diagnostic engineering management*, Valtion Teknillinen Tutkimuskeskus, Espoo, Finland, 1997, vol. 171, pp. 183-192.
30. *ASTM standard D4739 - 11, standard test method for base number determination by potentiometric hydrochloric acid titration*, ASTM International, West Conshohocken, PA, 2011.
31. *ASTM standard D974 - 14e2, standard test method for acid and base number by color-indicator titration*, ASTM International, West Conshohocken, PA, 2014.
32. *ASTM standard D664 - 11a, standard test method for acid number of petroleum products by potentiometric titration*, ASTM International, West Conshohocken, PA, 2011.
33. Y. Felkel, N. Dörr, F. Glatz and K. Varmuza, Determination of the total acid number (TAN) of used gas engine oils by IR and chemometrics applying a combined strategy for variable selection. *Chemometrics and Intelligent Laboratory Systems* **2010,** *101*, 14-22.
34. S. S. Wang and H.-S. Lee, The development of in situ electrochemical oil-condition sensors. *Sensors and Actuators B: Chemical* **1994,** *17*, 179-185.
35. E. C. f. Standardization, in *BS EN 14112:2003*, Brussels, 2003.
36. J. Zhu, J. M. Yoon, D. He and E. Bechhoefer, Online particle-contaminated lubrication oil condition monitoring and remaining useful life prediction for wind turbines. *Wind Energy* **2015,** *18*, 1131-1149.
37. G. E. Newell, Oil analysis cost-effective machine condition monitoring technique. *Industrial Lubrication and Tribology* **1999,** *51*, 119-124.
38. R. F. Lara, S. M. Azcarate, M. Á. Cantarelli, I. M. Orozco, M. E. Caroprese, M. Savio and J. M. Camiña, Lubricant quality control: A chemometric approach to assess wear engine in heavy machines. *Tribology International* **2015,** *86*, 36-41.
39. http://www.gastops.com/, 2016.
40. G. R. Humphrey, R. Whitlock, D. Little and R. Godin, *Energy dispersive X-ray fluorescence evaluation of debris from F-18 engine oil filters*, Joint Oil Analysis Program Technical Support Center, JOAP-TSC-TR-96-02, 1998.
41. *ASTM standard D7590, guide for measurement of remaining primary antioxidant content in in-service industrial lubricating oils by linear sweep voltammetry*, ASTM International, West Conshohocken, PA, 2014.
42. N. Gracia, Combination of mid-infrared spectroscopy and curve resolution method to follow the antioxidant action of alkylated diphenylamines. *Chemometrics and Intelligent Laboratory Systems* **2011,** *106*, 210-215.
43. N. Gracia, Combination of mid-infrared spectroscopy and chemometric factorization tools to study the oxidation of lubricating base oils. *Catalysis Today* **2010,** *155*, 255-260.
44. T. K. Liang, M. Friedrich, D. Lala and K. B. Ozanyan, Proceedings of IEEE Sensors, 2004.
45. X. Yi, C. Chen, Z. Wang, K. Ozanvan and D. Jones, 22nd International Conference and Exhibition on Electricity Distribution (CIRED 2013), 2013.
46. D. D. Dorigo, B. R. Wiesent, Ö. Simsek, A. Pérez Grassi and A. W. Koch, 2012.
47. J. Dennis, J. Briant and J. C. Hipeaux, Lubricant properties analysis and testing. *Industrial Lubrication and Tribology* **2000,** *52* (5), 248-248.
48. C. Besser, C. Schneidhofer, N. Dörr, F. Novotny-Farkas and G. Allmaier, Investigation of long-term engine oil performance using lab-based artificial ageing illustrated by the impact of ethanol as fuel component. *Tribology International* **2012,** *46*, 174-182.

49. H. Omrani, A. E. Dudelzak, B. P. Hollebone and H.-P. Loock, Assessment of the oxidative stability of lubricant oil using fiber-coupled fluorescence excitation–emission matrix spectroscopy. *Analytica Chimica Acta* **2014,** *811*, 1-12.
50. R. K. Jensen, S. Korcek, M. Zinbo and J. L. Gerlock, Regeneration of amine in catalytic inhibition of oxidation. *The Journal of Organic Chemistry* **1995,** *60*, 5396-5400.
51. G. E. Totten, S. R. Westbrook and R. J. Shah, *Fuels and lubricants handbook technology, properties, performance, and testing*, ASTM International, West Conshohocken, PA, 2003.
52. *ASTM standard D7527, test method for measurement of antioxidant content in lubricating greases by linear sweep voltammetry* D7527-10, ASTM International, West Conshohocken, PA, 2010.
53. *ASTM standard D6971, test method for measurement of hindered phenolic and aromatic amine antioxidant content in non-zinc turbine oils by linear sweep voltammetry*, ASTM International, West Conshohocken, PA, 2014.
54. *ASTM standard D6810, test method for measurement of hindered phenolic antioxidant content in non-zinc turbine oils by linear sweep voltammetry*, ASTM International, West Conshohocken, PA, 2013.
55. A. M. Farrington and J. M. Slater, Monitoring of engine oil degradation by voltammetric methods utilizing disposable solid wire microelectrodes. *Analyst* **1997,** *122*, 593-596.
56. R. J. Price and L. J. Clarke, Chemical sensing of amine antioxidants in turbine lubricants. *Analyst* **1991,** *116*, 1121-1123.
57. H. Omrani, J. A. Barnes, A. E. Dudelzak, H.-P. Loock and H. Waechter, Fluorescence excitation–emission matrix (EEM) spectroscopy and cavity ring-down (CRD) absorption spectroscopy of oil-contaminated jet fuel using fiber-optic probes. *The Analyst* **2012,** *137*, 2782.
58. H. Omrani, Ph.D. Thesis, Queen's University, 2014.
59. N. S. Foster, J. E. Amonette, T. Autrey and J. T. Ho, Detection of trace levels of water in oil by photoacoustic spectroscopy. *Sensors and Actuators B: Chemical* **2001,** *77*, 620-624.
60. R. M. B. O. Duarte, C. A. Pio and A. C. Duarte, Synchronous scan and excitation-emission matrix fluorescence spectroscopy of water-soluble organic compounds in atmospheric aerosols. *Journal of Atmospheric Chemistry* **2004,** *48*, 157-171.
61. M. M. Schachter and E. O. Haenni, Automatic triparametric recording in fluorometry of polynuclear hydrocarbons. *Analytical Chemistry* **1964,** *36*, 2045-2047.
62. R. Bro, PARAFAC. Tutorial and applications. *Chemometrics and Intelligent Laboratory Systems* **1997,** *38*, 149-171.
63. D. Munzke, J. Saunders, H. Omrani, O. Reich and H.-P. Loock, Modeling of fiber-optic fluorescence probes for strongly absorbing samples. *Applied Optics* **2012,** *51*, 6343-6351.
64. K. R. Murphy, C. A. Stedmon, D. Graeber and R. Bro, Fluorescence spectroscopy and multi-way techniques. PARAFAC. *Analytical Methods* **2013,** *5*, 6557-6566.
65. C. A. Stedmon, S. Markager and R. Bro, Tracing dissolved organic matter in aquatic environments using a new approach to fluorescence spectroscopy. *Marine Chemistry* **2003,** *82*, 239-254.
66. R. Bro and H. A. L. Kiers, A new efficient method for determining the number of components in PARAFAC models. *Journal of Chemometrics* **2003,** *17*, 274-286.

Chapter 7

Scintillator solution analysis

This chapter is based on the article entitled "Determination of the thermal oxidative and photochemical degradation rates of the scintillator liquid by fluorescence EEM spectroscopy" is published as a front cover article in the 100th anniversary edition for the Canadian Society for Chemistry for publication in Physical Chemistry Chemical Physics, N. L. P. Andrews, J. Z. Fan, R. L. Forward, M. Chen, H.-P Loock, 2017. The material presented below has been added according to the RSC's fair use policy. Under supervision, James Fan and Rebecka Forward helped in ageing the liquid scintillator samples and collected some of the EEM spectra. Mark Chen is the principal investigator at SNOLAB and generously donated samples and provided useful consultation. With these exceptions all work presented below is that of the author.

7.1 Introduction

The Sudbury Neutrino Observatory (SNO) was built at the 6800-foot level in the Vale Creighton mine near Sudbury, Ontario.[1] It's successor, the upcoming SNO+ project, has a liquid scintillator (replacing the heavy water that was in SNO) as the detection medium for neutrinos and will study solar neutrinos, reactor and geo antineutrinos, supernova neutrinos, and especially neutrinoless double beta decay ($0\nu\beta\beta$).[2, 3] If neutrinos are Majorana particles (as opposed to Dirac particles), and thereby their own antiparticles, double beta decay events may occur without neutrino emission.[4] To observe neutrinoless double beta decay ($0\nu\beta\beta$) experimentally, a double-beta decaying isotope, ^{130}Te, will be monitored for several years. If neutrinos are Dirac particles, the decay of the ^{130}Te, would exclusively proceed as,

$$^{130}_{52}\mathrm{Te} \longrightarrow {}^{130}_{54}\mathrm{Xe} + 2e^- + 2\bar{\nu}_e , \qquad \textbf{(R 7.1)}$$

with the emission of two beta particles, e^-, and two electron anti-neutrinos, $\bar{\nu}_e$.[5, 6] However, if neutrinos are Majorana particles it is possible that the co-produced neutrinos will annihilate and one observes,

$$^{130}_{52}\mathrm{Te} \longrightarrow {}^{130}_{54}\mathrm{Xe} + 2e^- . \qquad \textbf{(R 7.2)}$$

As the neutrinos annihilate, their energy leads to a higher kinetic energy of the two emitted electrons.

The double beta decay process can be monitored by detecting the light emission generated by the produced e^- from decaying ^{130}Te nuclei as they interact with the scintillator solution. The scintillator is an organic solvent mixture which also contains the dissolved or emulsified tellurium. Several thousand photomultiplier tubes (PMT)s are dedicated to detecting the emission in the visible region of the spectrum and the liquid scintillator solution therefore contains several fluorescence shifters — dyes that absorb the primary ultraviolet (UV) emission and fluoresce at longer wavelengths. In addition to the primary fluorophore, which also acts as a solvent, the scintillator solution contains strongly fluorescent compounds that through absorption of the primary fluorescence and subsequent fluorescence emission at longer wavelength, shift the emission to the optimum wavelength for light detection. Specifically, for the SNO+ experiment, the scintillator solution under consideration comprises of a mixture of the primary fluorophore, linear alkylbenzene (LAB), a secondary fluorophore, 2,5-diphenyloxazole (PPO), and a tertiary fluorophore, 1,4-bis(2-methylstyryl)benzene (bis-MSB). The structures of the scintillator probes, LAB, PPO and bis-MSB are given in **Figure 7.1**.

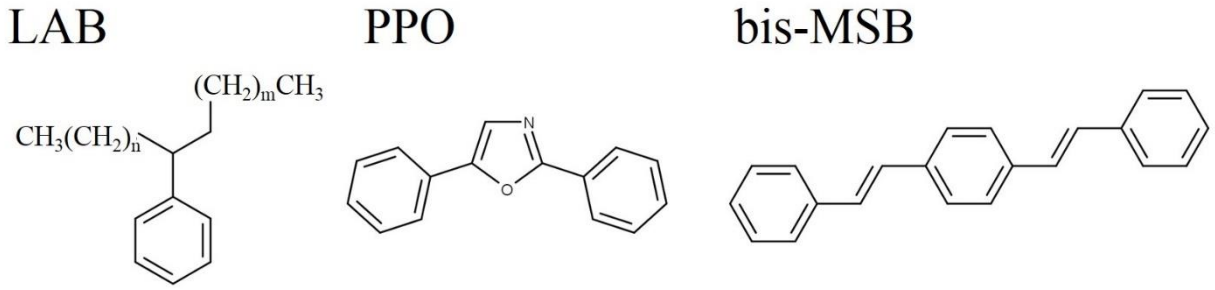

Figure 7.1: Chemical structures of LAB, PPO and bis-MSB, where n + m = 6 - 12.

Telluric acid, $Te(OH)_6$, may be encapsulated by micelles of dodecylbenzenesulfonic acid 2-propylamine, a surfactant. The scintillator compounds are selected such that the emission by LAB is absorbed by PPO and

the PPO emission is absorbed by bis-MSB. The emission of PPO and bis-MSB falls into a window of high optical transparency of the primary fluorophore and solvent LAB as well as into a sensitive region of the photodetector response spectrum. Similar mixtures of fluorophores are also used in other neutrino detectors such as the Daya Bay Reactor Neutrino Experiment and the Reactor Experiment for Neutrino Oscillations (RENO).[7, 8] The acrylic vessel for the SNO+ experiment will hold approximately 780 tonnes of liquid scintillator loaded with around 3.9 tonnes of tellurium. Over 9000 PMTs surround the SNO+ vessel to detect the light emission from the fluorescing species in solution.

It is anticipated that a $0\nu\beta\beta$ event is, at best, an extremely rare process producing only a few events per year, and the SNO+ experiment will have to be conducted for around seven years in a largely inert atmosphere at around 12°C.[6] During this period, the scintillator solution may start to decompose, thereby reducing the overall quantum yield of the scintillator. This would be detrimental to the SNO+ experiment, since the stability of the detector light yield is important for determining the energy of detected neutrinos and especially critical for the double beta decay search.[6] Also, the production of coloured degradation products may reduce the transparency of the cocktail and thereby reduce the intensity of the detectable emission.

In this chapter, the same fluorescence excitation emission matrix (EEM) spectroscopy method described in Chapter 5 and utilised to determine the degradation of lubrication oil (Chapter 6) is used to independently evaluate the thermal decomposition, oxidative destruction and photochemical degradation of the SNO+ scintillator solution. For these three processes rate constants and associated activation energies are obtained to predict the lifetime of the solution. This allows us to estimate the tolerances that are acceptable to maintain a functioning scintillator liquid.

This study is intended to guide the scintillator composition of the SNO+ project, and allow us to specify the conditions that permit the scintillator to function throughout the several year duration of the SNO+

experiment. It also serves as an additional example on the application of fluorescence EEM in determining chemical decay kinetics.

7.2 Experimental

7.2.1 Sample preparation

Samples contained 2 g/L PPO (Top Grade, *PerkinElmer*), 15 mg/L bis-MSB (*Aldrich*, Milwaukee, WI) all dissolved in LAB (*Petresa* Canada).[6, 9] The modified replicate cocktail was identical to that proposed for SNO+ with the exception of the tellurium-containing micelles consisting of $Te(OH)_6$ and surfactant. These compounds do not contribute or alter the fluorescence of the scintillator (**Figure 7.2**).

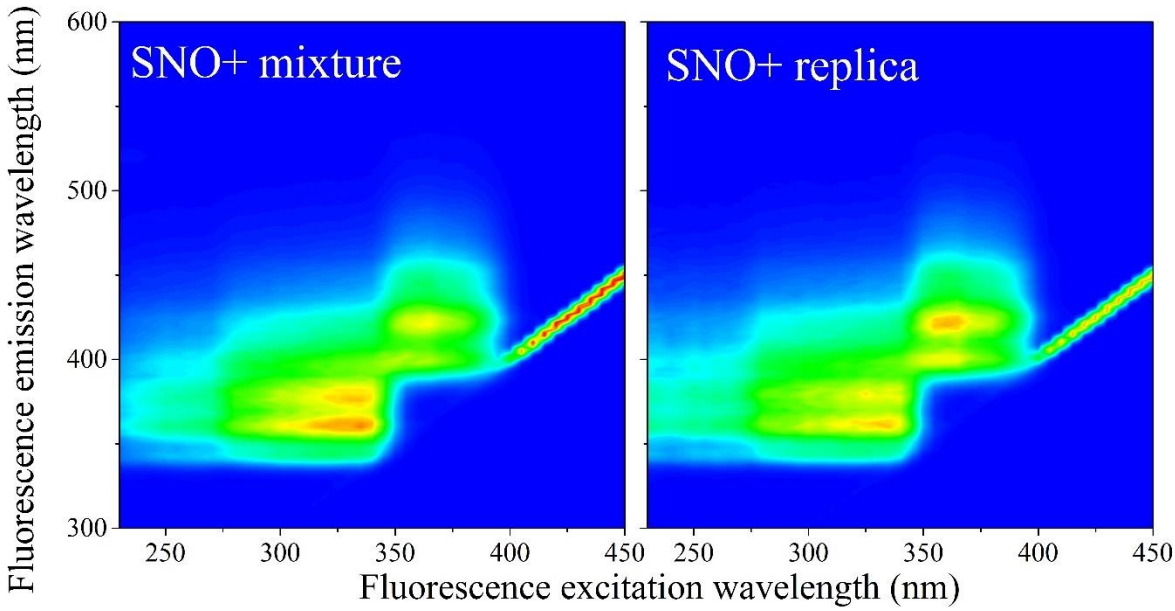

Figure 7.2: Normalised EEM spectra of the original SNO+ and replica scintillator solutions. The replica solution is comprised of 15 mg/l bis-MSB, and 2 g/l PPO, dissolved in LAB. The original solution also contains micelles of $Te(OH)_6$ and surfactant. The colours from blue to red represent the normalised intensity of 0 to 1, respectively.

7.2.2 Ageing experiments

7.2.2.1 Oxidative ageing

The replica SNO+ cocktail (200 mL) was heated under reflux under a constant stream of breathing grade air (*Praxair*) for one to three days. The samples were heated to 397, 426, 444, 455, 466 K and the temperature was maintained for the entire duration of the experiment. 5 mL aliquots were withdrawn at logarithmic time intervals over the course of up to three days.

7.2.2.2 Thermal ageing under nitrogen

In order to thermally degrade samples under inert atmosphere, the replica SNO+ solution was degassed by bubbling nitrogen gas (4.8 nitrogen, *Praxair*) for 24 hours.[10, 11] The solution was then placed in a nitrogen glove bag where 4 mL of SNO+ solution was added to ampules and temporarily capped. The ampules were subsequently evacuated using a vacuum pump and refilled with nitrogen. Evacuation and backfilling was repeated twice. The ampules were then sealed using a propane torch. To age the samples, the ampules were placed in a recrystallization oven which held a steady temperature of 513 ± 1 K. The ampules were removed on a semi-logarithmic time scale, and, once cooled, they were used for subsequent analysis.

7.2.2.3 Photochemical ageing

To remove oxygen, the replica SNO+ cocktail and a PPO solution (2 g/L PPO dissolved in LAB) were both degassed using a constant flow of high purity nitrogen gas (4.8 nitrogen, *Praxair*) for over 48 hours prior to the UV ageing experiment. The SNO+ cocktail was then exposed to UV light (Bondwand 365 nm UV curing lamp, *Electrolite*, USA), at room temperature (298 K). The luminous flux through the sample was determined as 8.49 ± 0.35 photonmol s^{-1} with a ferrioxalate actinometer using an established method by Hatchard et al. (See section 7.2.4).[12] The power density of the lamp 350 nm is 10 $mWcm^{-2}$ and decreases to 1.19 ± 0.05 $mWcm^{-2}$ when it passes through the sample vessel.[13] The UV lamp was placed under the sample vessel, and the sample was continuously exposed to UV light for a period of 60 minute intervals and remained in the dark for 30 minute intervals. The periodic irradiation ensured that the UV lamp would

not overheat or burn out. The SNO+ cocktail was exposed to UV light for approximately 1 week. The entire setup was contained in a black box to minimise degradation due to stray light.

7.2.3 Measurement techniques

7.2.3.1 Absorption

Absorption spectra were acquired for 91 of the 101 degraded scintillation solutions using an *Ocean Optics* USB4000 spectrometer coupled to an *Ocean Optics* USB-ISS-UV-Vis light source. Since thermal ageing under an inert atmosphere had no measurable effect, not all samples from this experiment were analysed. For each sample 10 spectra were averaged with an integration time of 60 ms. The oxidised samples were placed in a 1 mm cuvette and were diluted with LAB as to not saturate the detector.

7.2.3.2 Fluorescence excitation emission matrix spectroscopy

A double-grating fluorescence spectrometer (*Varian*, Cary Eclipse) was used to collect EEM spectra of all 101 aged sample solutions. Approximately 3.5 mL of each sample was placed into a 10×10×45 mm fused silica cuvette. The spectral acquisition was performed in the dark to ensure minimal stray light. A custom-built bifurcated fibre-optic cable bundle was coupled directly to the spectrometer. The design of the fibre probe is discussed in detail in Chapter 5. The custom probe was used instead of a typical right angle fluorescence collection, since it is less affected by the secondary absorption by the fluorophores,[14, 15] which is inherent in scintillation solutions.

All EEM spectra were collected in an excitation range of 200-450 nm with an emission range of 300-600 nm. The excitation and emission wavelengths had step increments of 5 nm and 2 nm, respectively. Both of the excitation and emission monochromator slits were set to 5 nm and auto-filters were used to remove second-order diffraction light from exciting the sample. A scan rate of 1200 nm/minute was used for the fluorescence collection and each of the 101 spectra took approximately 28 minutes to collect.

7.2.3.3 Parallel factor analysis

All 101 EEM spectra were analysed together using multivariate analysis. Parallel factor (PARAFAC) analysis was performed using the drEEM toolbox in Matlab to identify specific fluorescent compounds in the SNO+ scintillation solution.[16, 17] In contrast to most other multivariate methods PARAFAC can sometimes help identify specific fluorophores or classes of fluorophores. In our case of initially well-characterised samples, whose composition evolves with time, PARAFAC is a particularly useful technique. The PARAFAC analysis algorithm was applied 10 times to the data set, with random initialisation, non-negativity constraints, and a convergence criterion of 1×10^{-10}. The spectra were also normalised before analysis to give equal weights to those samples having weak fluorescence.

The analysis of the complete data set of 101 EEM spectra gave an excellent fit to only three distinct components, as shown in **Figure 7.3**, with a % explained of 96.0% and a core consistency of 96.7%. Two of the components — F1 and F2 — clearly relate to the two scintillation shifters — PPO and bis-MSB, respectively.[16-18] The spectra of PPO and bis-MSB were recorded independently in the solvent LAB and were very similar to those of the two components in **Figure 7.3**. There is a slight difference in the spectra which is attributed to inner filter effects. The third component F3, which is red-shifted from F1 and F2 is most likely attributable to dimers and oligomers formed as the SNO+ scintillation solution is aged.

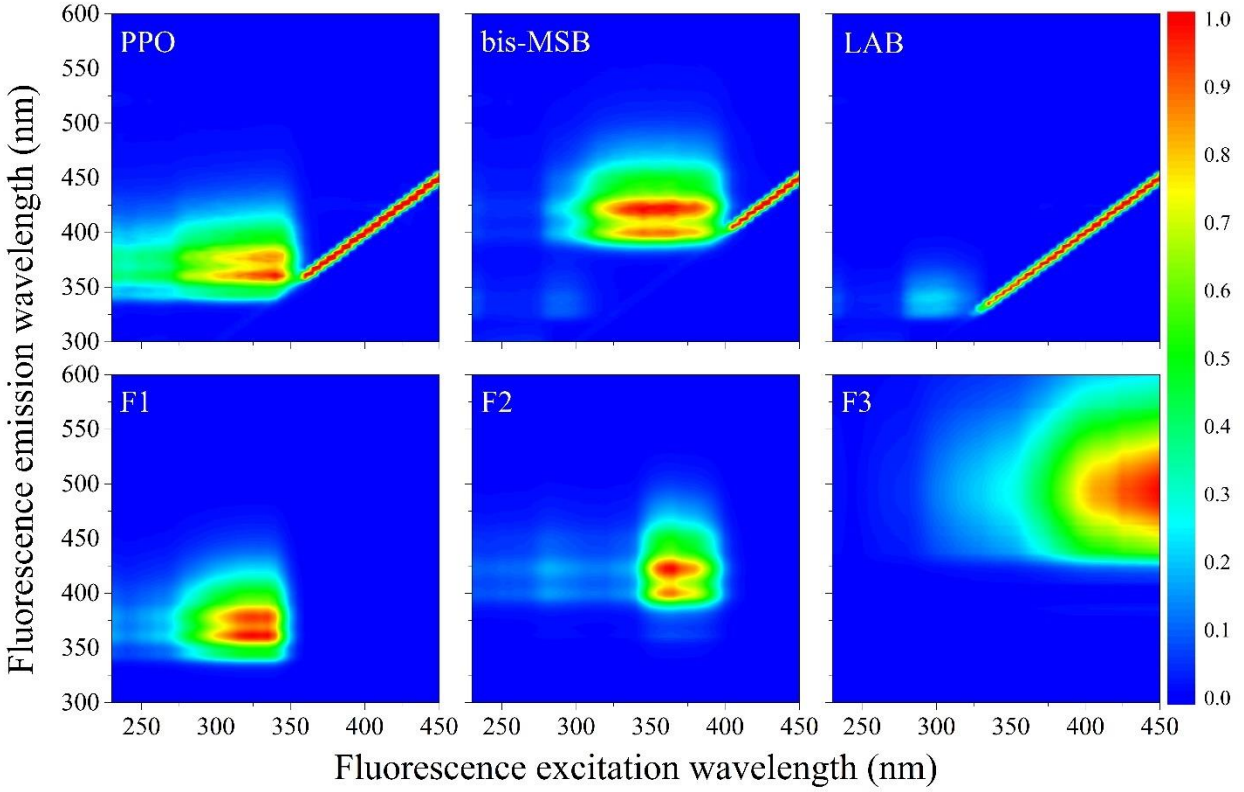

Figure 7.3: EEM spectra of PPO, bis-MSB and LAB with the three components found using PARAFAC on the 101 degraded SNO+ scintillation solutions. The top row represents the normalised EEM spectra of 2 g/L PPO in LAB, 15 mg/L bis-MSB in LAB and LAB separately. The bottom row shows the normalised EEM signatures of the three components (F1, F2, and F3) produced by PARAFAC on all 101 EEM spectra on the aged scintillation solutions. The colours from blue to red represent the normalised intensity from 0 to 1, respectively.

Notably, fluorescence of LAB is *not* directly observed in the EEM spectrum of the scintillator replica (**Figure 7.2**) and is *not* observed as one of the components determined with PARAFAC. LAB exhibits an excitation maximum near 300 nm and emission at around 330 nm (**Figure 7.3**). The emission from LAB is not observed in the presence of PPO, since PPO absorbs the fluorescence of LAB, as indeed it is meant to do in the scintillator solution. This is evident by the increased excitation window of PPO caused by the reabsorption of the LAB fluorescence. The LAB peak is faintly observed in the bis-MSB sample, however.

In addition, the absorption spectra (67 oxidised and 7 thermally aged in inert conditions) were analysed using PARAFAC analysis to determine any increased absorption due to the formation of products from the degradation of the scintillator solution. The 17 absorption spectra of the photo-degraded samples underwent a separate PARAFAC analysis. Since the drEEM toolbox requires a 3-dimensional data cube, the square roots of the 2-D absorption spectra were multiplied by the square roots of their transpose (decimated by 10) to generate a mock-EEM spectrum that could be analysed (**Figure 7.4**).[19] This ensured that the same number of components was present in both dimensions and that the magnitude of absorption matched that of the sample.

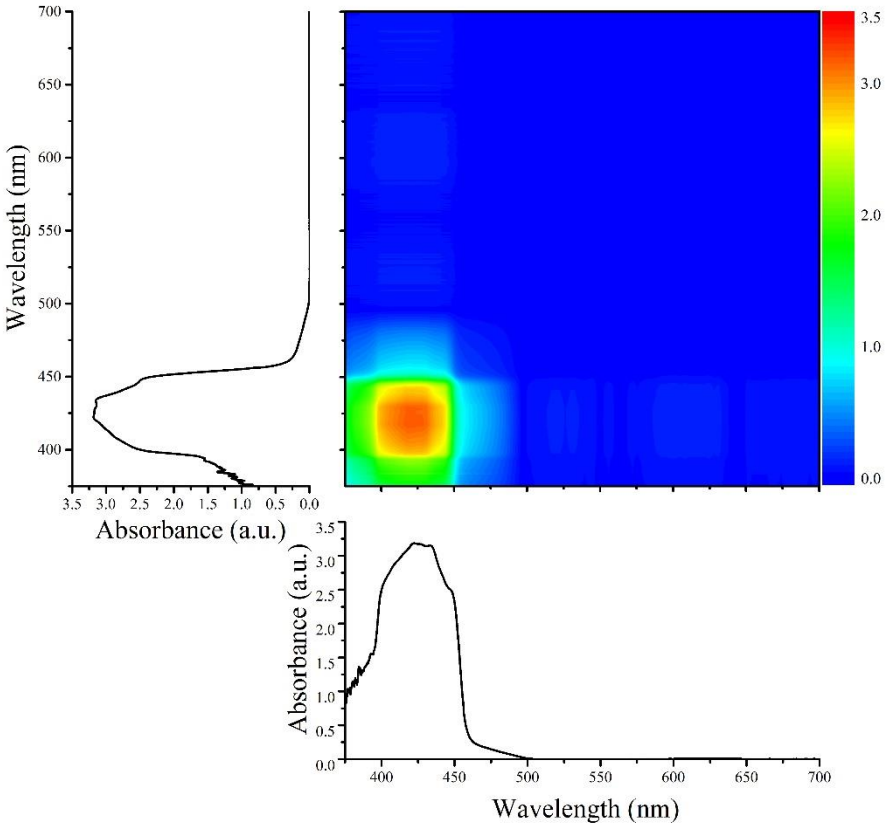

Figure 7.4: Mirrored EEM spectrum of the absorption data ready for PARAFAC analysis. Both the excitation and emission wavelengths are identical so the PARAFAC algorithm can determine a suitable model.

7.2.4 The actinometer

A potassium ferrioxalate actinometer was used to determine the photon flux and photon concentration of the UV light source (Bondwand 365 nm UV curing lamp, *Electrolite*, USA) used to degrade the SNO+ scintillation solution.[12, 20] All the actinometer experiments were carried out using red "darkroom" lighting to minimise any light contamination. The photochemical reaction of ferrioxalate is as follows,

$$2\left[\mathrm{Fe}\left(\mathrm{C_2O_4}\right)_3\right]^{3-} + h\nu \longrightarrow 2\mathrm{Fe}\left(\mathrm{C_2O_4}\right) + 3\left[\mathrm{C_2O_4}\right]^{2-} + \mathrm{CO_2}. \qquad \textbf{(R 7.3)}$$

This reaction is well characterised with a known quantum yield at 509 nm of 0.86.[12] The ferrous ion product species reacts with 1,10-phenanthroline to form ferroin — a red complex, which has a distinct absorbance peak at 510 nm **(R 7.4)**,[21, 22]

$$\mathrm{Fe^{2+}} + 3\mathrm{phen} \longrightarrow \left[\mathrm{Fe}\left(\mathrm{phen}\right)_3\right]^{2+}. \qquad \textbf{(R 7.4)}$$

To calibrate the actinometer study and thus determine the molar extinction coefficient of ferroin at 509 nm, 10 calibration solutions using varying aliquots of $FeSO_4$ were made in a sodium acetate buffer to maintain a pH of 3.5. 2 ml of 0.1% (w/v) of 1,10-phenanthroline monohydrate in water was added to all calibration solutions to form the ferroin complex. Absorption spectra were obtained for all samples using a pathlength of 1 cm and measured using an *Ocean Optics* USB4000 spectrometer coupled to a visible only light source (*Stellarnet Inc* SL1). The absorption at 509 nm is shown as a function of the molarity of ferrous ions in **Figure 7.5(a)**.

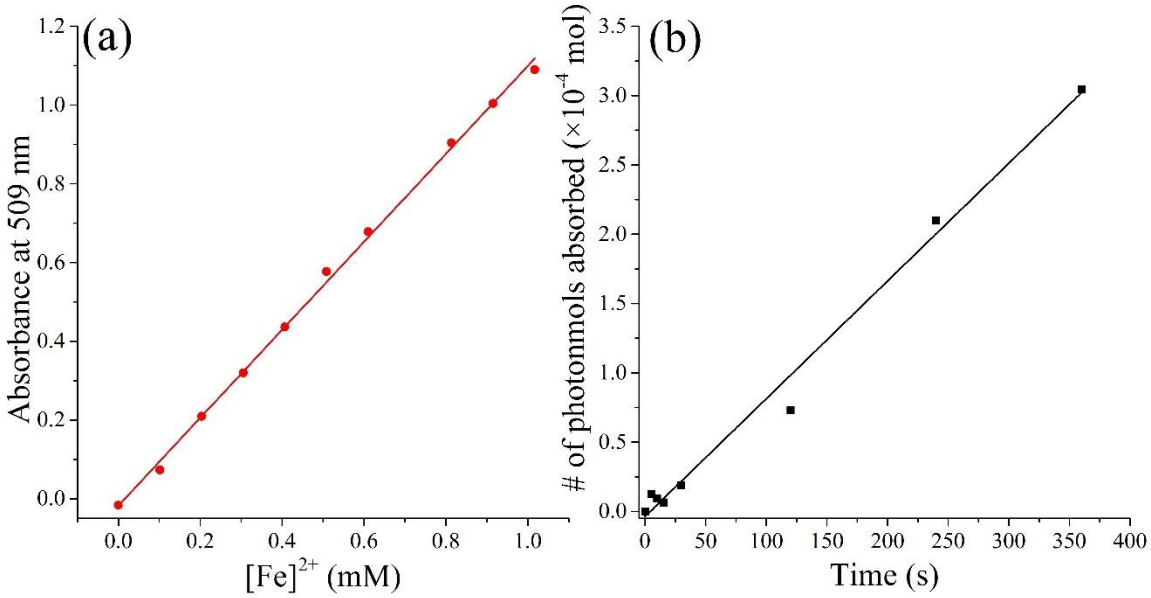

Figure 7.5: Results using the ferrioxalate actinometer solution to characterise the UV light source used to degrade the SNO+ scintillator solution. **(a)** Calibration run using known concentrations of Fe^{2+} giving an extinction coefficient of the ferroin complex at 509 nm to be 11170 ± 170 $M^{-1}cm^{-1}$. **(b)** number of photons in mols absorbed by the actinometer solution as it reacts with the UV source. The slope gives the flux of photons to be 3.34 ± 0.14 × 10^{-8} photonmol s^{-1}.

Using the Beer-Lambert law (equation (7.1)), the slope of **Figure 7.5(a)** gives the extinction coefficient of ferroin at 509 nm to be 11170 ± 170 $M^{-1}cm^{-1}$. This agrees with the literature value of ε = 11100 $M^{-1}cm^{-1}$ at 510 nm.[23] The 0.15 M ferrioxalate solution was prepared with a sodium acetate buffer to maintain a pH of 3.5 and placed in the same vessel used to photodegrade the SNO+ scintillation solution. As with the photodegradation experiments, the UV light source (Bondwand 365 nm) irradiated the ferrioxalate solution from below and samples were removed in increasing time steps. The samples were mixed with 2 ml of (0.1% w/v) 1,10-phenanthroline solution and allowed to stabilise to form the ferroin complex. The samples were subsequently analysed using absorption spectroscopy as with the calibration run,

$$\varepsilon = \frac{A}{cl}. \qquad \textbf{(7.1)}$$

Knowing the extinction coefficient of ferroin allows the concentration of remaining Fe^{2+} in the solution to be calculated from the absorption at 509 nm using equation (7.1). The number of photons absorbed is then calculated using equation (7.2) where V is the volume of the system (200 ml) and Φ is the quantum yield (0.86),

$$\text{photons absorbed} = \frac{[\text{Fe}]^{2+} V}{\Phi}. \quad \textbf{(7.2)}$$

The amount of photons absorbed as the actinometer solution is illuminated is plotted in **Figure 7.5(b)**, where the slope gives the flux of photons to be $8.49 \pm 0.35 \times 10^{-8}$ photonmol s^{-1}. The photon concentration in the reaction flask, $[h\nu]$, is then calculated using equation (7.3) to be $4.25 \pm 0.17 \times 10^{-7}$ photonmol L^{-1},

$$[h\nu] = \frac{\text{flux} \times t}{V}, \quad \textbf{(7.3)}$$

where t is the time at 1 s. The power density, Pd, of the light source at 365 nm can be calculated using equation (7.4),

$$Pd = \frac{\text{flux} \times N_A hc}{\lambda a}, \quad \textbf{(7.4)}$$

where N_A is Avogadro's constant, h is Planck's constant, c is the speed of light in a vacuum, λ is the wavelength, and a is the surface area of the vessel (23.4 cm^2). This gives the power density of photons in the vessel to be 1.19 ± 0.05 $mWcm^{-2}$. This value is expected to be lower than the nominal power density of the lamp, given as 10 $mWcm^{-2}$ by the manufacturer, as many photons will be absorbed by the glass wall of the vessel.[13]

7.3 Kinetic model

The concentration of both fluorophores, bis-MSB and PPO, may be described with a simple kinetic model based on pseudo-first order reactions. As the scintillation solution is heated either with or without oxygen, or degraded using UV radiation, the fluorophore, X, degrades into one or more products, such as an oxidation product, a dimer or higher oligomer. Also, when heated or photochemically excited, bis-MSB isomerises from its trans- to cis-form

(R 7.5.1). In the cis-configuration a reversible pericyclic reaction can occur where the cis-conjugated triene forms a cyclohexadiene, which in this case is a dihydrophenanthrene (R 7.5.2).[24] With the addition of an oxidiser such as O_2, the dihydrophenanthrene intermediate can form phenanthrene (R 7.5).[25, 26]

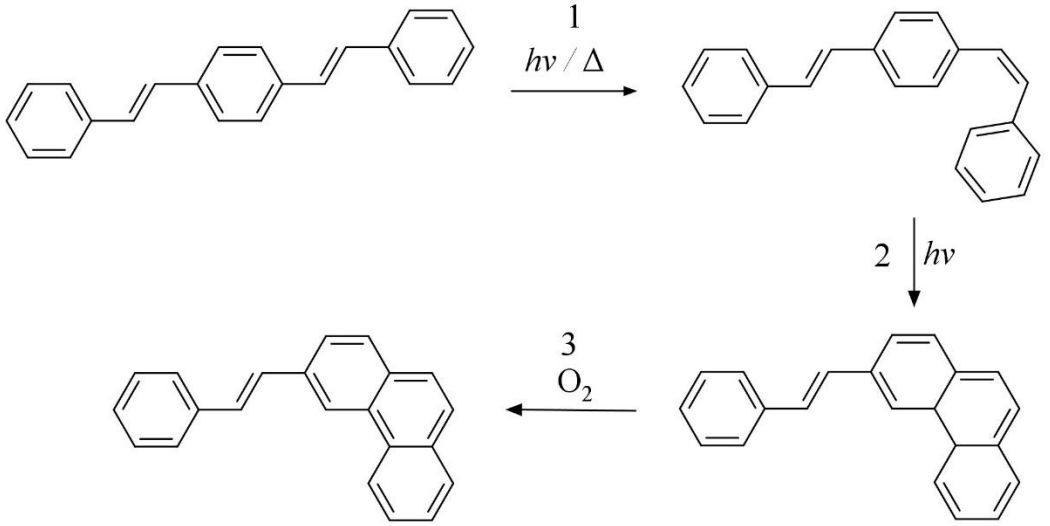

(R 7.5)

However, the reader must be aware however, that this process is likely only possible at high photon concentrations and thus is not going to be very dominant in the conditions present for the SNO+ experiment. PPO when heated in the presence of oxygen will form an ozonide (R 7.6.1).[27] This will break the conjugation and thus reduce the fluorescence in the visible region. The ozonide can then further react with alcohols to form ketones and aldehydes (R 7.6.2-3).[28] In the presence of UV radiation PPO can undergo a photochemical rearrangement to form 3,5-diphenylisoxazole with 2,4-diphenyloxazole (R 7.7).[29]

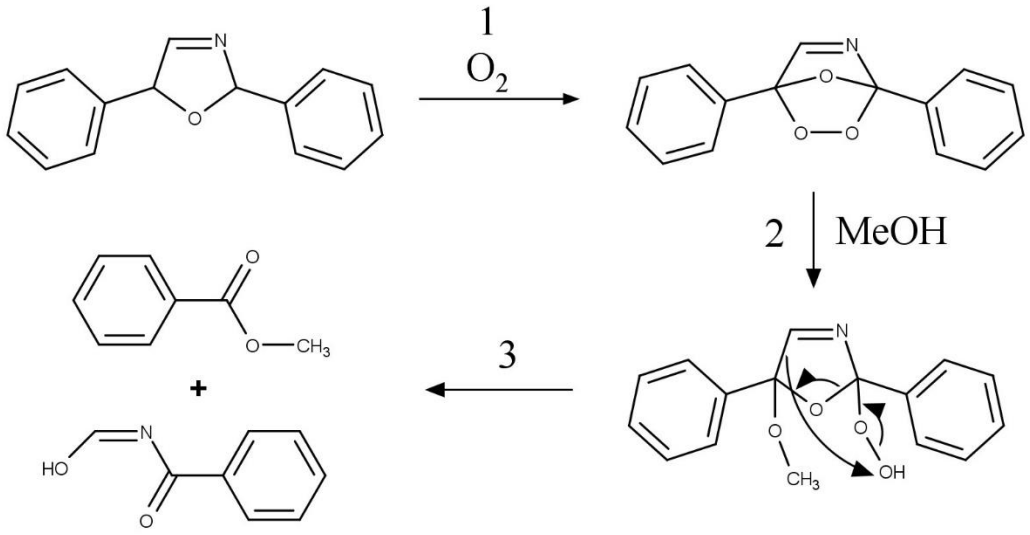

(R 7.6)

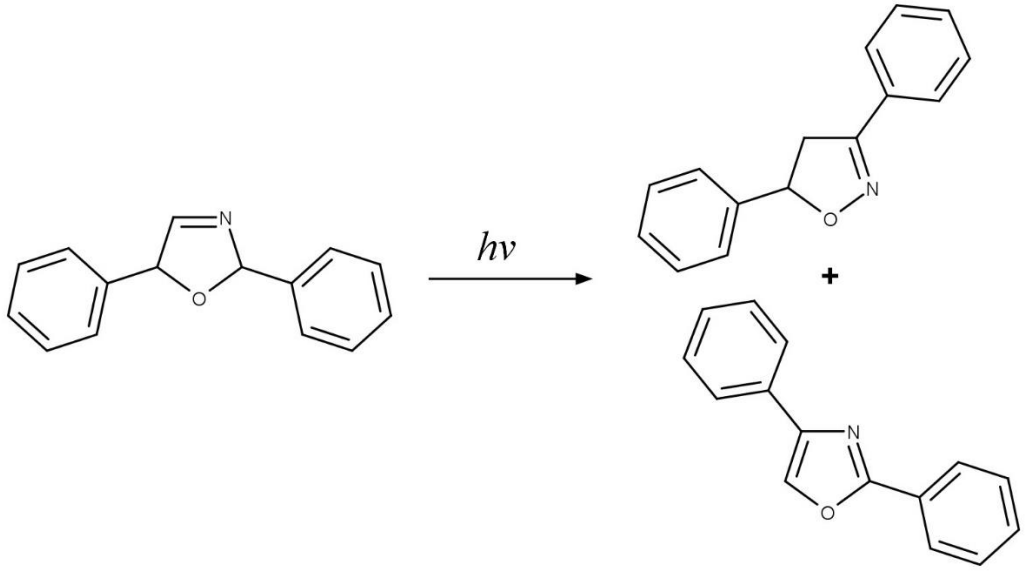

(R 7.7)

The identity of the products is not of great relevance to this study, but their collective fluorescence and absorption properties are important. We model a generic decomposition of fluorophore X using the following reactions:

$$X + O_2 \xrightarrow[\Delta]{k_{O_2}} P_{O_2}, \qquad \textbf{(R 7.8)}$$

$$X \xrightarrow[\Delta]{k_T} P_T, \qquad \textbf{(R 7.9)}$$

$$X + h\nu \xrightarrow{k_P} P_P, \qquad \textbf{(R 7.10)}$$

and if the product degrades further,

$$P_{O_2}, P_T, P_P \xrightarrow{k_{Product}} P_F. \qquad \textbf{(R 7.11)}$$

The concentrations of the fluorophore, X, are therefore governed by the rate equations:

$$-\frac{d[X]}{dt} = k_{O_2}[O_2][X] = k^*_{O_2}[X], \qquad \textbf{(7.5)}$$

$$-\frac{d[X]}{dt} = k_T[X], \qquad \textbf{(7.6)}$$

$$-\frac{d[X]}{dt} = k_P[h\nu][X] = k^*_P[X]. \qquad \textbf{(7.7)}$$

Equations (7.5) and (7.7) involve constant concentrations of oxygen and light, respectively, and are therefore pseudo-first order reactions, with effective rate constants, $k^*_{O_2} = k_{O_2}[O_2]$ and $k^*_P = k_P[h\nu]$. With these assumptions we can integrate the three independent reactions (R 7.8)-(R 7.10) to give:

$$[X] = [X]_0 \exp\left(-k^*_{O_2} t\right), \qquad \textbf{(7.8)}$$

$$[X] = [X]_0 \exp\left(-k_T t\right), \qquad \textbf{(7.9)}$$

$$[X] = [X]_0 \exp\left(-k^*_P t\right). \qquad \textbf{(7.10)}$$

Below we will obtain [X] as a function of time and fit to equations (7.8)-(7.10) to obtain rate constants and activation energies for these reactions. The concentration of the product formation is governed by the rate equation,

$$\frac{d\left[P_{O_2}, P_{O_2}, P_{O_2}\right]}{dt} = k^*_{O_2, T, P}[X] - k_{Product}[X]. \qquad \textbf{(7.11)}$$

This can be readily solved assuming that the initial concentration of the product is zero using the same derivation as shown in Chapter 6,

$$\left[\mathrm{P_{O_2}},\ \mathrm{P_{O_2}},\ \mathrm{P_{O_2}}\right] = \frac{k^{*}_{\mathrm{O_2},\,T,\,P}\left[\mathrm{X}\right]_0}{k_{\mathrm{Product}} - k^{*}_{\mathrm{O_2},\,T,\,P}}\left(\exp\left(-k^{*}_{\mathrm{O_2},\,T,\,P}t\right) - \exp\left(-k_{\mathrm{Product}}t\right)\right). \quad \textbf{(7.12)}$$

If the product does not degrade further, then $k_{\mathrm{Product}} = 0$ and equation (7.12) is simply,

$$\left[\mathrm{P_{O_2}},\ \mathrm{P_{O_2}},\ \mathrm{P_{O_2}}\right] = \left[\mathrm{X}\right]_0\left(1 - \exp\left(-k^{*}_{\mathrm{O_2},\,T,\,P}t\right)\right). \quad \textbf{(7.13)}$$

7.4 Results and discussion

7.4.1 Oxidative ageing

7.4.1.1 Fluorescence

As the SNO+ scintillation solution replica was heated while being exposed to a constant stream of breathing grade air, the solution transformed from a colourless transparent liquid to a black viscous solution containing solid particulates (**Figure 7.6**). As the sample was oxidised, its fluorescence also decreased substantially within 2 days (**Figure 7.7**).

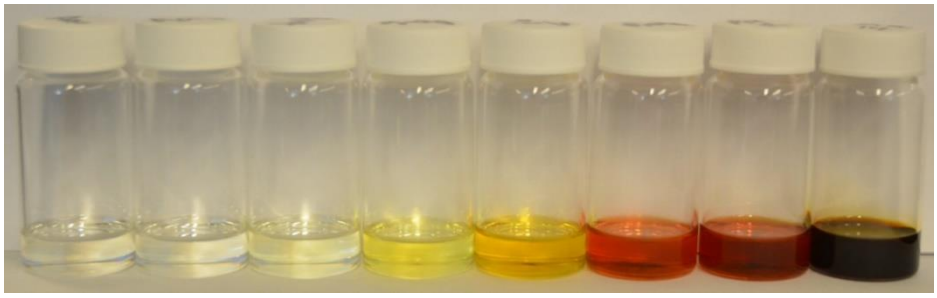

Figure 7.6: A photo of the aged SNO+ cocktail under a constant stream of breathing grade air at 426 K. From left to right are degradation times of 0, 10, 67, 249, 549, 1320, 1567, 2880 mins.

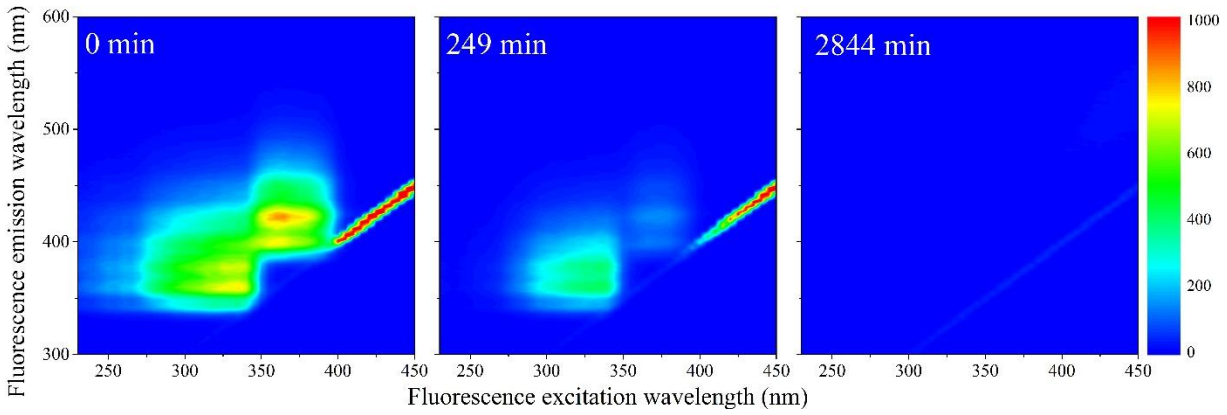

Figure 7.7: EEM spectra of the aged SNO+ cocktail under constant steam of breathing grade air at 426 K. As observed the fluorescence diminishes in 2844 min. The colours from blue to red represent the intensity from 0 to 1000 counts, respectively.

In **Figure 7.8** we show the normalised scores of the three components F1, F2 and F3, which correlate to the concentration of the fluorophores PPO, bis-MSB and what appears to be a product of bis-MSB degradation. As expected, at higher temperatures the sample degrades more quickly. F3 is likely a dimer or oligomer of bis-MSB due to its red shifted spectra. The scores of F3 increase and then subsequently decay as the scintillation solution is aged, indicating that this primary oxidation product further decomposes.

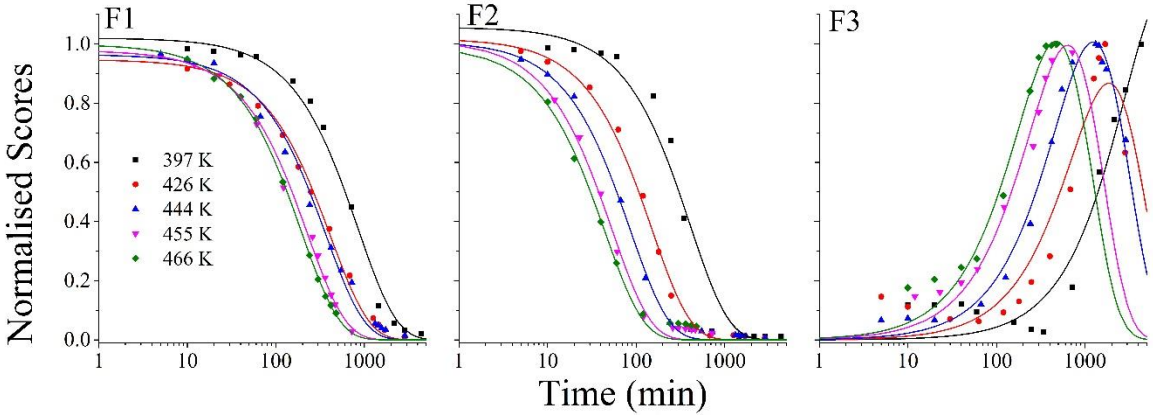

Figure 7.8: Normalised scores for the three components obtained using PARAFAC on the oxidised samples at temperatures from 397 – 466 K. The scores were obtained using PARAFAC analysis on all 101 aged samples. The solid coloured lines for F1 and F2 represent single exponential decay fits through the scores, which correspond to pseudo-first-order kinetics using equation (7.8). The solid lines through the F3 data represent an exponential rise and subsequent decay using equation (7.12).

The rate constants $k^{*}_{O_2}(X)$ were obtained by fitting to equations (7.8) and (7.12), and are given in (**Table 7.1**). Activation energies associated with the pseudo-first-order rate constants are obtained from an Arrhenius plot using,

$$\ln\left(k^{*}_{O_2,\,T,\,P}\right) = \ln(A) - \frac{E_a}{RT}. \qquad \textbf{(7.14)}$$

For the thermal degradation of F1 (PPO) and F2 (bis-MSB) in the presence of oxygen, the activation energies are found to be 32.5 ± 3.7 kJmol^{-1} and 48.0 ± 2.7 kJmol^{-1}, respectively (**Figure 7.9**). With these activation energies, the rate constants, $k^{*}_{O_2}(X)$, at room temperature (298 K) and the temperature of the SNO+ experiment (285 K) can be determined by extrapolation (**Table 7.1**).

Table 7.1: Rate constants for the decay of F1 (PPO) and F2 (bis-MSB) and the rise of F3 (bis-MSB product) in the SNO+ replica scintillation solution obtained by fitting the data shown in **Figure 7.8** to equation (7.8) and (7.12). The temperatures marked with a * are predicted rates obtained by using the activation energies determined from the linear fit (equation (7.14)) in **Figure 7.9**.

$k^{*}_{O_2}$ / ×10^{-3} min^{-1}	Temperature / K							E_a / kJmol^{-1}	Pre exponential / min^{-1}
	285*	298*	397	426	444	455	466		
F1	0.0248	0.0446	1.18	2.40	2.72	4.40	5.17	32.4 (3.5)	20 (20)
F2	0.00593	0.0149	2.46	6.64	11.6	18.7	22.5	50.5 (1.9)	10800 (5700)
F3	0.000457	0.00118	0.259	0.574	1.10	1.82	2.73	52.4 (4.4)	2000 (2000)

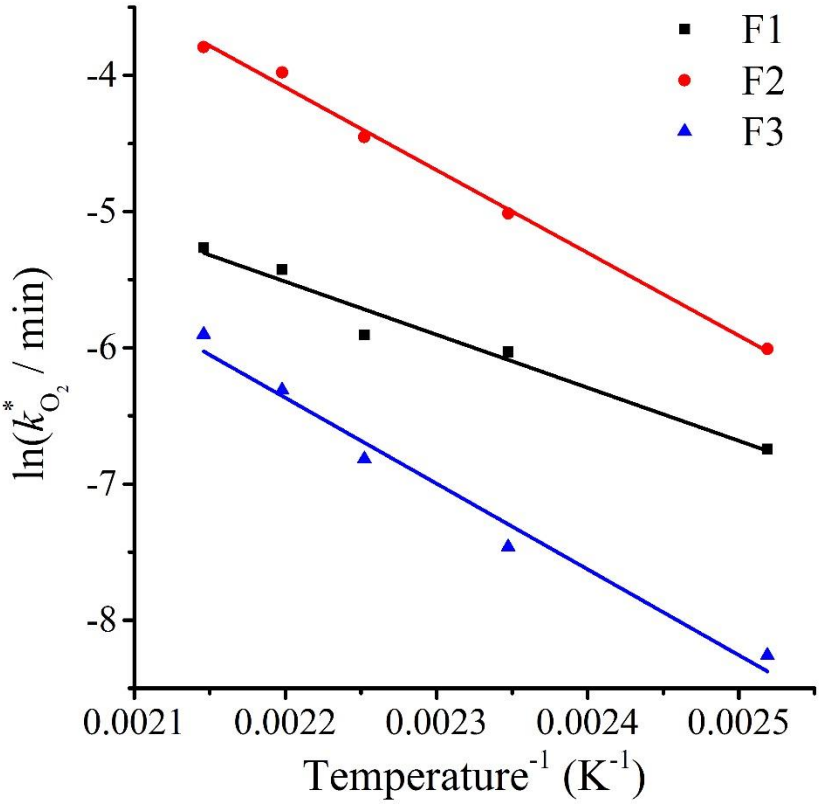

Figure 7.9: Arrhenius plot of the oxidised SNO+ scintillator solution using the rate constants, $k^*_{O_2}(X)$, obtained from the fits in **Figure 7.8** and equation (7.14). The slopes give the activation energy of F1 (PPO) and F2 (bis-MSB) as 32.4 ± 3.5 kJmol^{-1} and 50.5 ± 1.9 kJ mol^{-1} respectively. The slope of F3 gives an activation energy of 52.4 ± 4.4 kJ mol^{-1} and matches bis-MSB.

These rates were then used to determine the fraction of F1 (PPO) and F2 (bis-MSB) remaining (equation (7.15)). **Figure 7.10** shows that in the presence of oxygen, PPO in the SNO+ scintillation replica drops to 90% (99%) of the original concentration in only about 3 (0.3) days at 285 K. Once bis-MSB and PPO are degraded to less than 99% of their original concentration the scintillator function is affected,

$$\text{Fraction remaining} = \frac{[X]}{[X]_0} = \exp\left(-k^*_{O_2}(298/285\ \text{K})t\right). \qquad \textbf{(7.15)}$$

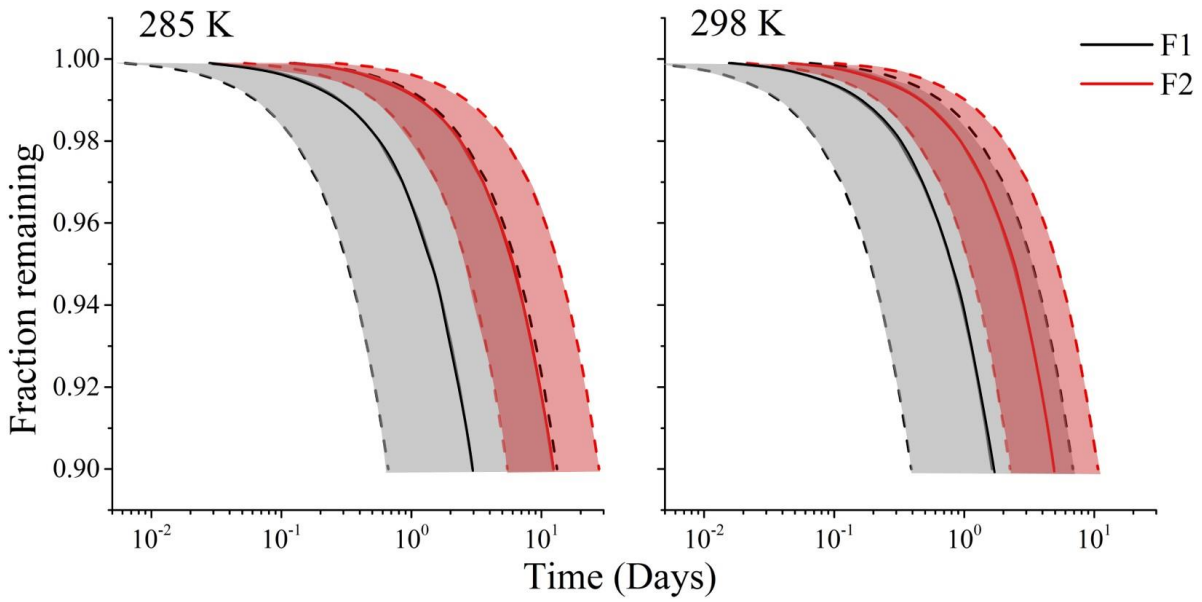

Figure 7.10: The fraction remaining of F1 (PPO) (black) and F2 (bis-MSB) (red) in oxidised samples at 285 K and 298 K. The shaded area between the dashed lines represent the upper and lower boundary using one standard deviation of the activation energy. Using the obtained activation energies, rate constants were obtained at room temperature (298 K) and the temperature of the SNO+ experiment (285 K), as shown in (**Table 7.1**).

Oxygen at ambient concentration ($[O_2]_{air} = 22\%$) will degrade the scintillator liquid within a few days and must therefore be removed to ensure its longevity. By reducing the oxygen concentration, the first order rate constant, $k^*_{O_2} = k_{O_2}[O_2]$, is correspondingly reduced and the lifetime can be extended. An oxygen partial pressure in the headspace never exceeding 24 ppm_v would allow the scintillator fluorescence to remain within 99% of its initial value over the anticipated 7-year lifespan, as calculated using equation (7.18). The pseudo first order rate constant required for the scintillator solution to remain for the 7 years with a concentration of O_2 in air is calculated using equation (7.16),

$$\frac{[X]}{[X]_0} = \exp\left(-k^*_{O_2} t\right)$$
$$k^*_{O_2} = -\frac{\ln\left([X]/[X]_0\right)}{t}. \quad \textbf{(7.16)}$$

Knowing the pseudo first order rate required using a concentration 0.22% O_2, the concentration of O_2 required for the scintillation solution to last 7 years can be calculated using a ratio of the pseudo rate constants in equation (7.17),

$$k^*_{O_2\,7yr} = k_{O_2}\left[O_2\right]_{7yr}$$
$$k^*_{O_2\,air} = k_{O_2}\left[O_2\right]_{air}\ . \qquad \textbf{(7.17)}$$

Dividing $k^*_{O_2\,7yr}$ by $k^*_{O_2\,air}$ then the concentration of O_2 required for the solution to last 7 years is,

$$\frac{k^*_{O_2\,7yr}}{k^*_{O_2\,air}} = \frac{k_{O_2}\left[O_2\right]_{7yr}}{k_{O_2}\left[O_2\right]_{air}}$$
$$\left[O_2\right]_{7yr} = \left[O_2\right]_{air}\frac{k^*_{O_2\,7yr}}{k^*_{O_2\,air}}\ . \qquad \textbf{(7.18)}$$

The solubility of O_2 in LAB is not given in the literature. However, Battino et al. have performed a comprehensive investigation of the solubility of O_2 in a number of related solvents.[30, 31] The solubility of oxygen in LAB may be approximated with that of long chain hydrocarbons such n-decane to hexadecane and the solubility in aromatic hydrocarbons such as butylbenzene. The dissolved mole fraction of O_2 in n-decane, hexadecane and butylbenzene are 22×10^{-4}, 24×10^{-4} and 15×10^{-4}, respectively, at an oxygen pressure of 101.35 kPa.[30, 31] Thus it is expected that in our experiment using a partial O_2 pressure of 0.22 × 101.35 kPa O_2 the mole fraction of O_2 in LAB is estimated to be $3.2\text{-}5.3\times10^{-4}$. To protect the scintillator liquid against oxidation the headspace oxygen concentration should not exceed a partial pressure of 2.4 Pa (24 ppm_v) which corresponds to an estimated dissolved O_2 molefraction of $3.5\text{-}5.8\times10^{-8}$ (4.3-7.1 ppb_w) if the gas in the headspace was completely equilibrated with the liquid.

In fact, the formation of coloured oxidation products poses even more stringent limits on the oxygen concentration as is shown in the following section.

7.4.1.2 Absorption

The scintillator liquid not only has to remain fluorescent but it also has to be transparent over a length of at least 12 m.[9] As observed in **Figure 7.6**, the scintillator replica when heated and exposed to breathing grade air quickly transforms from a transparent to an opaque black solution. **Figure 7.11(a)** shows the absorption spectra for the oxidised solution at 466 K and, as expected, the absorption increases as the solution is aged. The absorption peak also shifts to longer wavelengths as it degrades. The absorption spectra of neat PPO and bis-MSB in LAB (**Figure 7.11(b)**) agree well with the integrated fluorescence excitation spectra of the corresponding PARAFAC components (**Figure 7.11(d)**). PARAFAC analysis on the 74 absorption spectra of the heated samples (67 oxidised, 7 inert) yields spectra of two distinct components, AO1 and AO2 (**Figure 7.11(b)**). Component AO2 can be unambiguously associated with the PPO absorption spectrum. Bis-MSB, on the other hand could not be identified in the absorption spectra, likely because it is far less concentrated than PPO — 15 mg/L (0.048 mmol/L) as opposed to 2 g/L (9 mmol/L). The absorption component AO1 rises as the sample is oxidised and shows a peak located at 280 nm (**Figure 7.11(c)**), which matches the small peak in the F2 (bis-MSB) excitation spectrum in **Figure 7.11(d)**. Absorption around 280 nm is frequently caused by phenyl groups.[32] The red-shifted absorption likely corresponds to more conjugated oxidation products such as dimers or oligomers as mentioned in section 3. These products may include the bis-MSB product apparent in the fluorescence excitation spectrum of **Figure 7.11(d)** or products of PPO degradation.

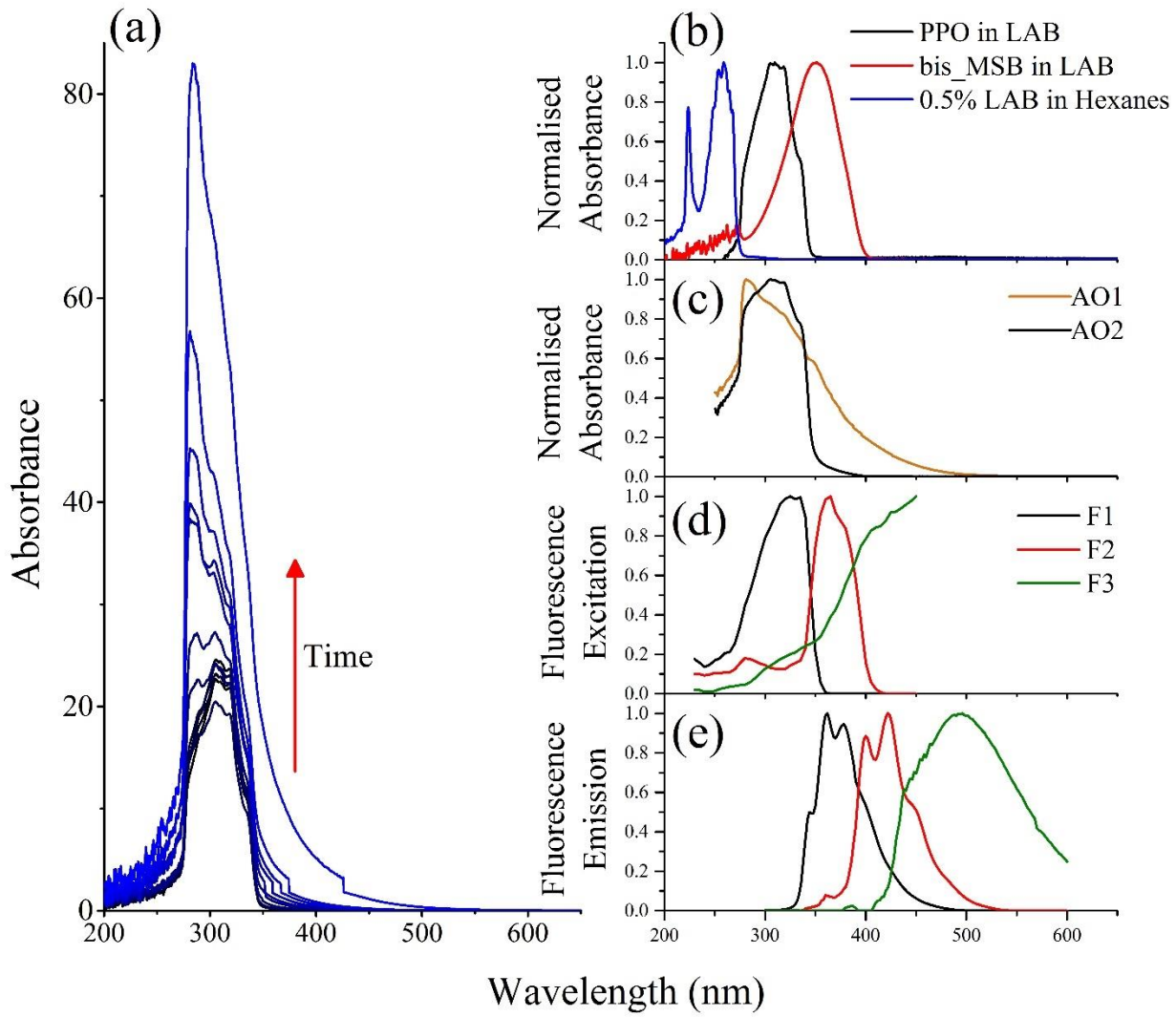

Figure 7.11: Spectra of the degraded SNO+ scintillation solution at 455 K with the components determined using PARAFAC analysis. **(a)** Absorption spectra for the 455 K heated with air series using a 1 mm cuvette. As expected from **Figure 7.6**, as the sample is aged the absorption increases. Note these spectra were obtained by diluting in hexanes and multiplying the spectra accordingly. **(b)** Normalised absorption spectra of PPO in LAB, bis-MSB in LAB and 0.5% LAB diluted in hexanes **(c)** Normalised absorption spectra of the 2 components (AO1, AO2) found using PARAFAC analysis on the 74 heated samples (67 oxidised, 7 inert) are given. **(d)** Normalised fluorescence excitation and **(e)** fluorescence emission spectra of F1 (PPO), F2 (bis-MSB) and F3 (bis-MSB product) as shown in **Figure 7.3**.

The absorption scores obtained by PARAFAC analysis of the 67 oxidised samples are given in **Figure 7.12**. Note the scores for the 7 thermally aged samples under inert atmosphere were excluded as they showed no

degradation. Component AO1 increases and decays as the SNO+ replica reacts with O_2 and the scores of this PARAFAC component fit quite well to equation (7.12). For most temperatures, there were not enough data on the decreasing slope and only the rate constant associated with the rise was found (equation (7.13)). Component AO2 shows a single exponential decay and fits well to equation (7.8). Both components AO1 and AO2 were fit simultaneously to the same rate constants given in **Table 7.2**.

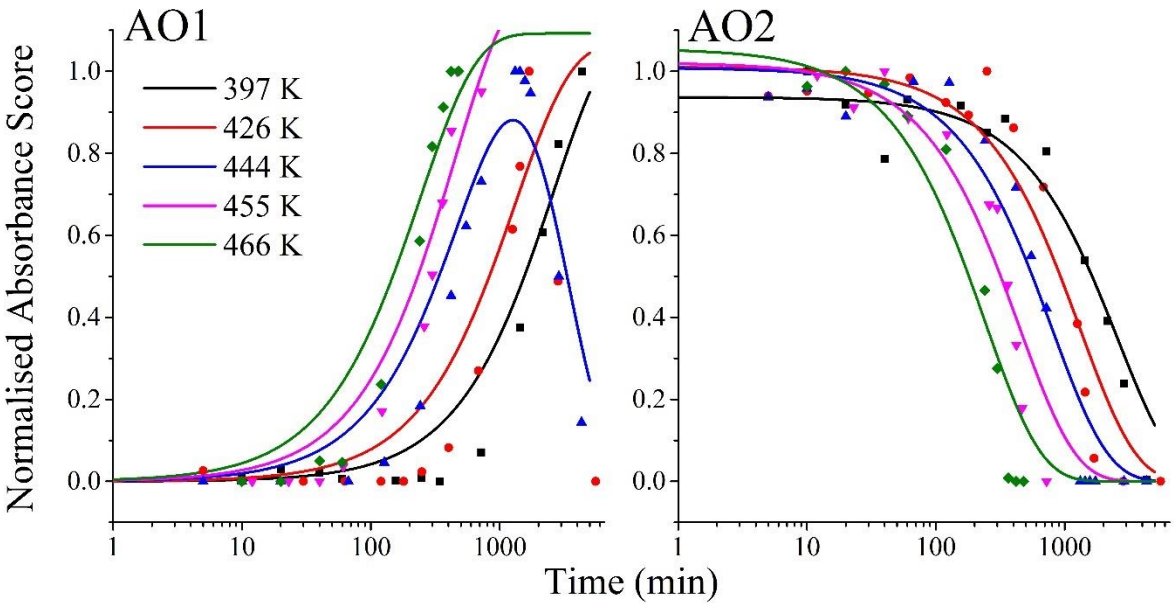

Figure 7.12: Normalised scores for the two components obtained using PARAFAC on the absorption spectra of the oxidised samples at temperatures from 397 – 466 K. The data points resemble normalised absorption scores of the two components obtained using PARAFAC on the absorption spectra of the 74 heated samples (67 oxidised, 7 inert). The solid coloured lines represent fits through the data. For component AO1, equations (7.12) and (7.13) were used depending whether enough data was collected for the downward. For component AO2, equation (7.8) was used for the fit.

Table 7.2: Rate constants for the decay and rise of absorption components AO1 and AO2 in **Figure 7.12**. The temperatures marked with a ***** are predicted rates obtained by using the activation energy determined at lower temperatures from the linear fit in **Figure 7.13**.

$k^*_{O_2}$ / $\times 10^{-3}$ min^{-1}	Temperature / K							E_a < 444 K / kJmol^{-1}	E_a > 444 K / kJmol^{-1}	Pre exp. < 444 K / min^{-1}	Pre exp. > 444 K / min^{-1}
	285*	298*	397	426	444	455	466				
AO1, AO2	0.00509	0.00985	0.385	0.760	1.25	1.25	4.14	36.2 (2.7)	93.7 (2.5)	22.2 (5.5)	1.298 (0.047) $\times 10^8$

As with the fluorescence data, the rates determined by the fits of the scores can serve to obtain activation energies (**Figure 7.13**). Using the Arrhenius plot the activation energy for the decay of AO2 and formation of AO1 was found to be 36.2 ± 2.7 kJmol^{-1} at lower temperatures. This matches the activation energy of PPO as obtained by the fluorescence. Thus AO1 is likely the absorption of the PPO product. At higher temperatures the activation energy is 93.7 ± 2.5 kJmol^{-1}. This appearance of a kink in the Arrhenius plot is unusual. However, components AO1 and AO2 are related to absorption and it is likely that at higher temperatures, LAB itself degrades in the presence of oxygen. In addition, further products from the degradation of PPO and bis-MSB in addition to further sequential product formation will contribute to this increase in absorption. Components AO2 and, especially, AO1, also incorporate these breakdown products at higher temperatures and deviate further from describing solely the degradation of PPO and the formation of one of its product. This explains why the fits to the data in **Figure 7.12** are less than ideal.

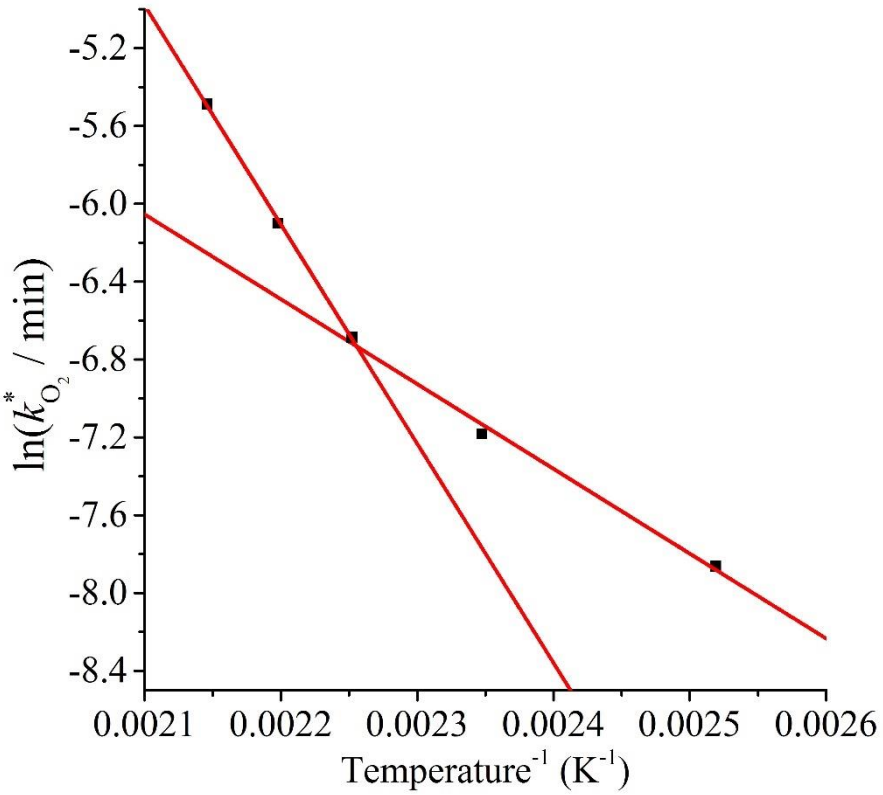

Figure 7.13: Arrhenius plot using the rate constants, $k^*_{O_2}$, obtained from the exponential rise and decay fits in **Figure 7.12**. The slope at lower temperatures gives the activation energy of Component AO1 and AO2, as 36.2 ± 2.7 kJmol^{-1}, which matches the activation energy of F1 (PPO). The slope at hotter temperatures gives an activation energy of 93.7 ± 2.7 kJmol^{-1}.

Figure 7.15 shows the predicted transmission of light through the SNO+ flask at the emission maximum of bis-MSB at 422 nm. The emission maximum of bis-MSB was chosen as it is these photons that are required to be detected by the PMTs during a $0\nu\beta\beta$ event. In the following we describe the steps to estimate how long it takes the scintillation solution to reduce its transmission to 90% of the original transmission.

First, the absorption, *A*, is calculated at the specified transmission,

$$A = -\log\left(\frac{I}{I_0}\right). \qquad \textbf{(7.19)}$$

Therefore, for $I/I_0 = 0.9$ we calculate $A = 0.045$. The SNO+ lab scintillation chamber has a diameter of 12 m whereas in our experiment a 1 mm cuvette was used. Therefore, the absorption at 1 mm to require an absorption of 0.045 over 12 m is calculated using,

$$A_{1\text{ mm}} = \frac{A_{12\text{ m}}}{12000}. \quad \textbf{(7.20)}$$

The scores obtained using PARAFAC analysis on the absorption data are proportional to the concentration, which is, in turn, proportional to absorption using the Beer-Lambert law. The fluorescence maximum of bis-MSB lies at 422 nm (**Figure 7.11(e)**). Thus this is the chosen wavelength as the SNO+ experiment aims to detect the emission from bis-MSB. Using "Solver" in *Microsoft*'s Excel to convert the normalised score to the true absorption at 422 nm we need to divide by a scaling factor of 2.47 (See **Figure 7.14**). This scaling factor includes values such as the normalisation factor, extinction coefficient of the degraded samples in addition to the proportionality constant of converting the score to the concentration of the sample,

$$A_{1\text{ mm}} = \frac{Score}{2.47}. \quad \textbf{(7.21)}$$

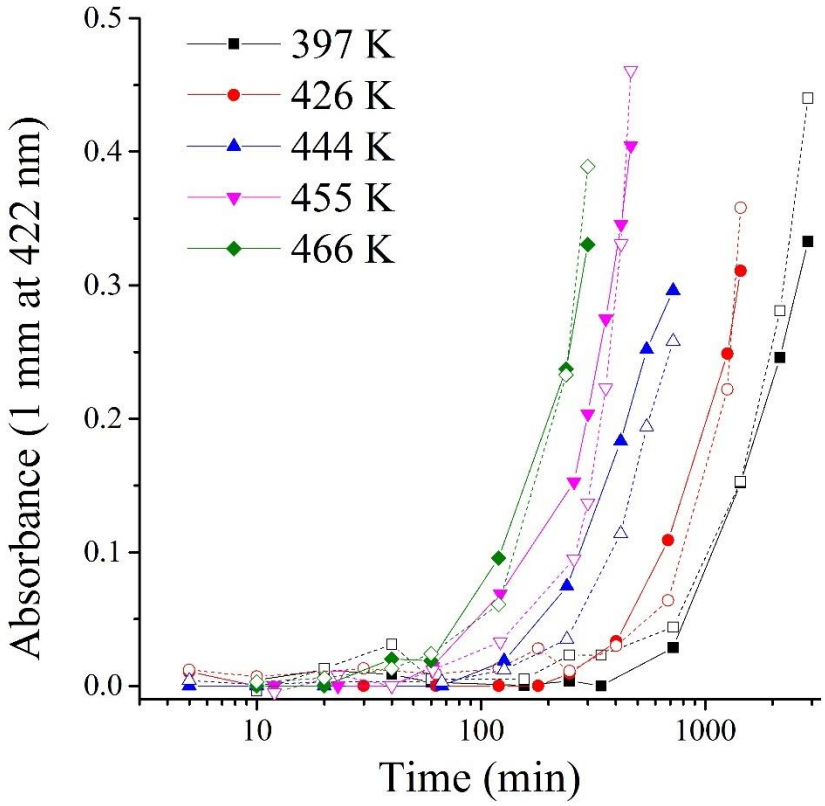

Figure 7.14: Conversion of the normalised scores to the absorption of the aged scintillator solutions at 422 nm over a pathlength of 1 mm. The solid data points (with solid lines) resemble the converted normalised scores divided by the factor of 2.47 (equation (7.21)), whereas the hollow data points (with dashed lines) resemble the true absorption of the aged samples at 422 nm. The lines are only meant as a means to help guide the eye.

To calculate the time at which the sample degrades to 90%, the PARAFAC score relates to the time using the first order rate as with equation (7.13),

$$Score = 1 - \exp(-kt)$$
$$t = -\frac{\ln(1 - Score)}{k^*_{O_2}} \quad . \qquad \textbf{(7.22)}$$

Using equations (7.19) to (7.22) and a rate, $k^*_{O_2}$ = 0.00509 min^{-1} for AO1 and AO2, the transmission of light through the SNO+ flask will fall to 90% (99%) in 140 min (13 min) at 285 K in the presence of oxygen (mole fraction of 3.2-5.3×10^{-4}) as shown in **Figure 7.15**.

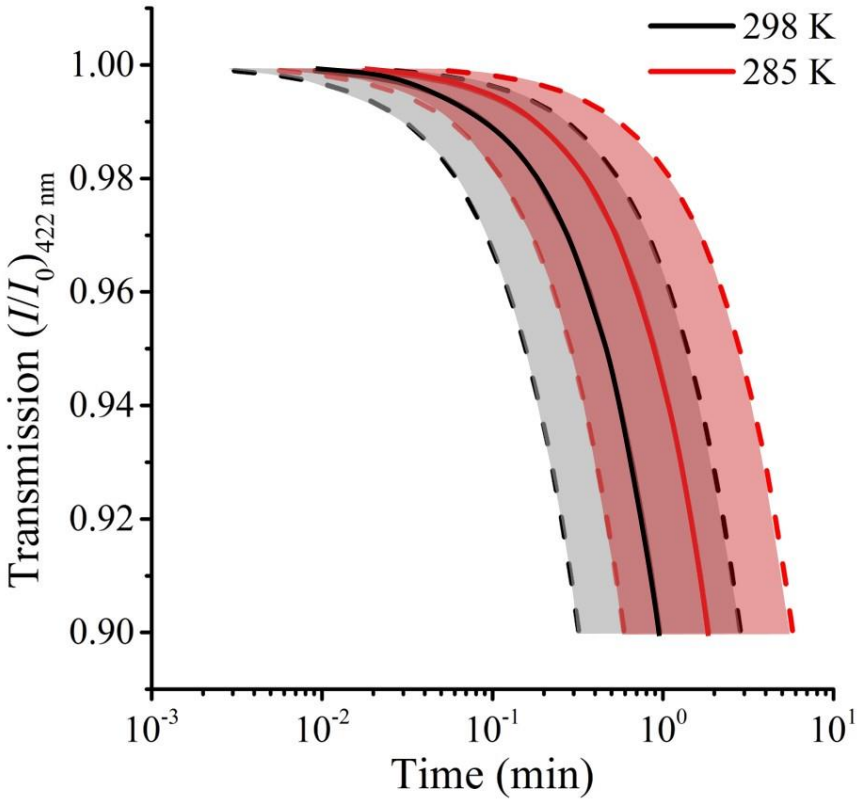

Figure 7.15: The predicted transmission I/I_0 at 422 nm as the solution degrades in oxidised samples at 298 and 285 K using the predicted rates obtained using the activation energies obtained in **Figure 7.13** and a maximum pathlength in the SNO+ vial of 12 m. The shaded area between the dashed lines represent the upper and lower boundary using one standard deviation of the activation energy.

As with the fluorescence data, reducing the concentration of oxygen in the scintillation solution increases its lifetime. Using equations (7.16) to (7.18), reducing the partial pressure of O_2 in the headspace to 4.2×10^{-3} Pa (41 ppb$_v$), which is a dissolved mole fraction of O_2 to 1.13-1.9×10^{-10} (14-23 ppt$_w$) will ensure the solution will remain 90% transmissive over 7 years. However, this is an extremely small amount of

dissolved O_2, and is very unlikely to occur in practice. It has been observed that scintillator solutions stay stable at room temperature and in ambient air — thus a simple extrapolation to room temperature might not be as straightforward. Our accelerated ageing process may be due to other processes such as degradation of LAB occur at higher temperatures, which do not relate to the degradation mechanisms at lower temperatures. In addition, the components AO1 and AO2 may not singly relate to PPO and contain compounds of LAB by-products and bis-MSB.

7.4.2 Thermal ageing under inert conditions

The fluorescence EEM spectra of the thermally aged scintillation replica in inert conditions at 513 K are given in **Figure 7.16**. Even at the highest temperature of 513 K, the sample remains highly fluorescent for nearly two months. This is in stark contrast to the oxidised samples that degraded within two days.

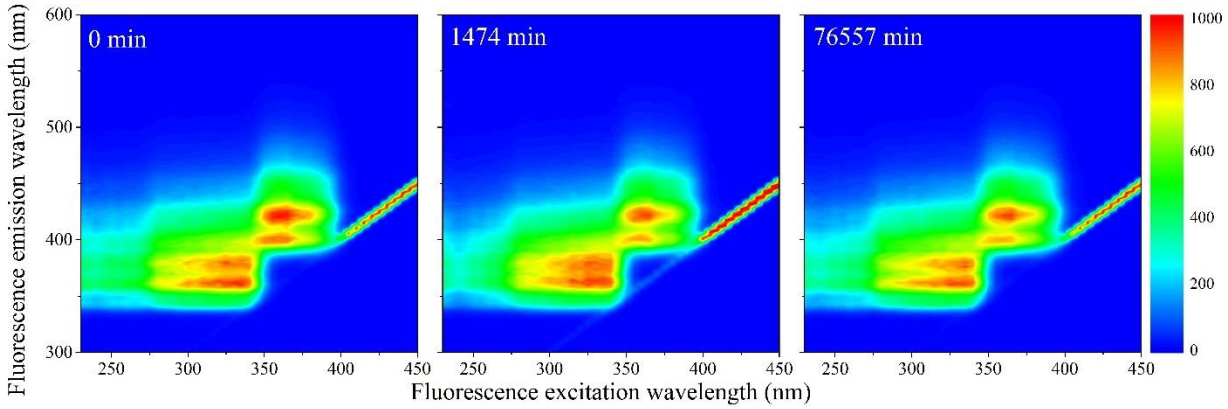

Figure 7.16: Three EEM spectra of the samples obtained after heating to 513 K in inert conditions at increasing time steps. As observed the fluorescence remains strong even after ageing for nearly 2 months. The colours from blue to red represent the intensity from 0 to 1000 counts, respectively.

The normalised scores obtained by PARAFAC analysis are given in **Figure 7.17** and are fit to an exponential decay function, to resemble a first order kinetic reaction, equation (7.9). As the scores do not decrease enough to generate a reliable exponential decay, a worst case scenario was implemented by adding an extra data point located at 50% of the normalised score at the next, future, time interval (200 days).

Obviously, this does not produce a reliable fit but does help in predicting a worst case lifetime of the SNO+ scintillator solution under inert conditions.

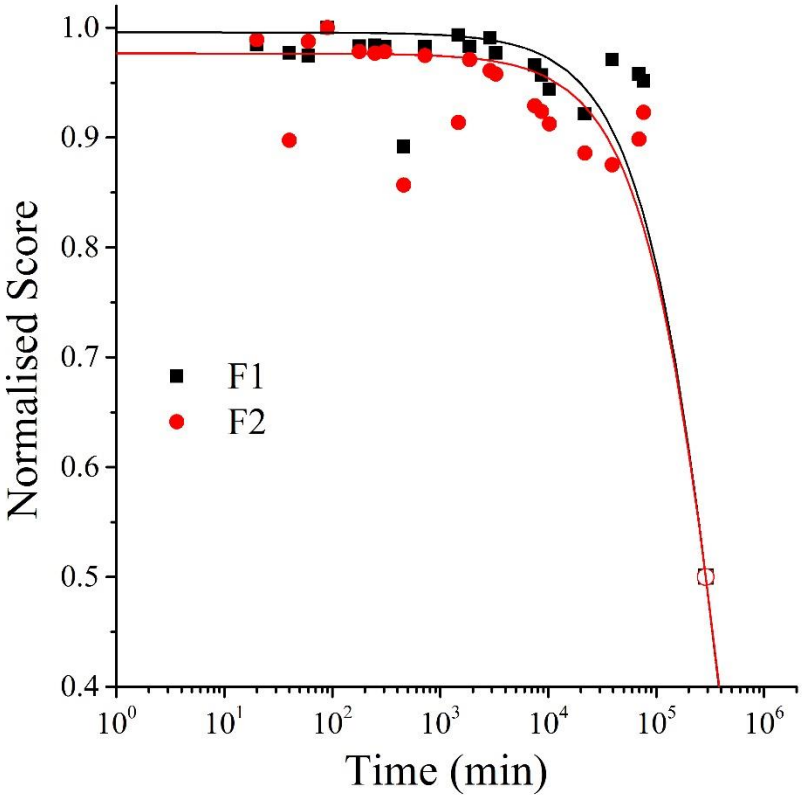

Figure 7.17: Normalised scores of the inert aged samples heated to 513 K. The data points resemble normalised scores of F1 (PPO) and F2 (bis-MSB) of the inert aged samples obtained using PARAFAC on all 101 samples. Component F3 was excluded as it was negligible for the inert samples. The solid coloured lines represent single exponential decay fits through the scores. The hollow data points at 50% were added to help the exponential fit and are used as a worst case scenario.

The rate constants obtained in the fit of **Figure 7.17** are given in **Table 7.3**. The Gibbs free energies of activation, $\Delta G^{\ddagger}$, were obtained using the Eyring-Polanyi equation below and are also given in **Table 7.3**,

$$k_{\mathrm{T}} = \frac{k_B T}{h} \exp\left(-\frac{\Delta G^{\ddagger}}{RT}\right). \qquad \textbf{(7.23)}$$

The rate at 285 K — the temperature of the SNO+ experiment — could then be determined by extrapolation. Using equation (7.23), the fraction of F1 (PPO) and F2 (bis-MSB) remaining in the SNO+ scintillation replica was determined and is shown in **Figure 7.18**. As observed, even in a worst case scenario, the SNO+ scintillation replica is extremely stable when kept under inert conditions. It will take at least an approximately 3.42×10^{15} (3.20×10^{14}) years for the bis-MSB concentration to degrade to 90% (99%) of its original concentration.

Table 7.3: Rate constants for the decay of F1 (PPO) and F2 (bis-MSB) in the SNO+ replica scintillation solution obtained by fitting the data shown in **Figure 7.17** to equation (7.9).

k_T / **s^{-1}**	**Temperature / K**		**$\Delta G^{\ddagger}$ / kJmol^{-1}**
	285*	**513**	
F1	1.03 (0.03) $\times10^{-24}$	2.39 (0.04) $\times10^{-6}$	200.7 (0.1)
F2	0.98 (0.03) $\times10^{-24}$	2.32 (0.04) $\times10^{-6}$	200.8 (0.1)

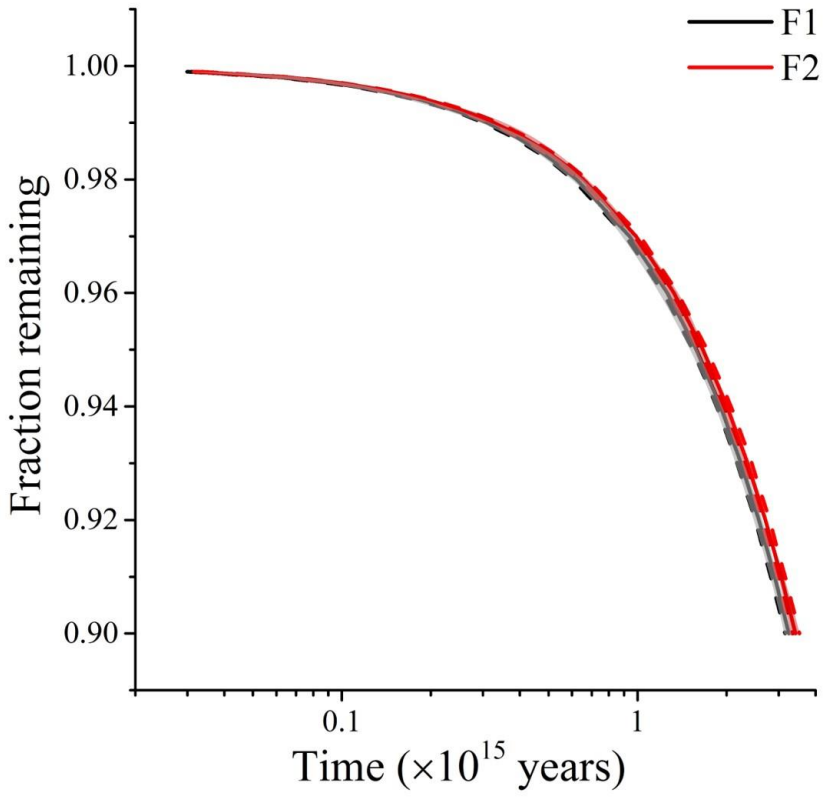

Figure 7.18: Fraction remaining of F1 (black) and F2 (red) at 285 K if the sample is kept in inert conditions. These were obtained by calculating the Gibbs free energy of activation, $\Delta G^{\ddagger}$, obtained from the rates in **Figure 7.17** with equation (7.23). The shaded area between the dashed lines represent one standard deviation of the rate at 285 K.

In addition as expected, the absorption does not noticably change as the sample is aged under inert conditions and, similar to the EEM spectrum, the absorption spectra at 0 and 76557 min are nearly identical**.**

7.4.3 Photochemical ageing

7.4.3.1 Fluorescence

When exposed to UV light, the fluorescence of the SNO+ scintillation solution replica rapidly diminishes as shown in **Figure 7.19**. This is clearly visible as the blue fluorescence decreases after samples were illuminated by UV radiation. The resultant EEM spectra of the photodegraded samples are given in **Figure 7.20**.

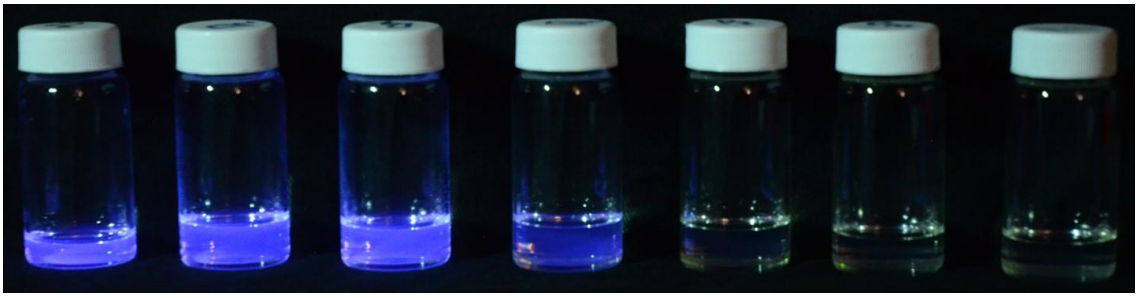

Figure 7.19: A photo of the photo degraded SNO+ scintillator replica illuminated by a UV source. From left to right show samples taken at 0, 20, 123, 449, 1329, 2759, 7049 min. As shown the blue fluorescence decreases as the samples were aged.

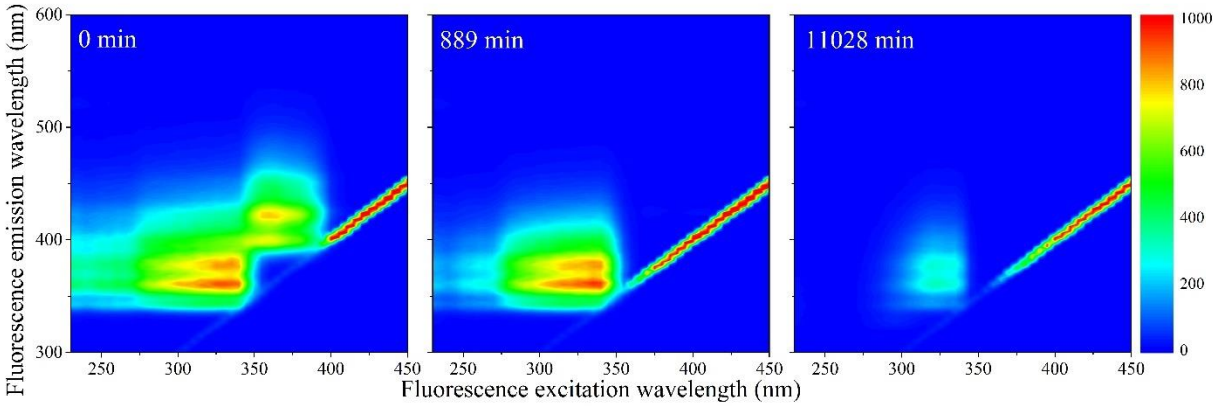

Figure 7.20: Three EEM spectra of the photo degraded samples at increasing time steps. As observed the fluorescence diminishes as the sample is exposed to UV light.

The normalised scores obtained by PARAFAC analysis on the photo degraded samples on all the 101 samples are given in **Figure 7.21** and are fit to an exponential decay (equation (7.10)). Inner filter effects are apparent in the initial increase of the PPO signal once the bis-MSB has degraded. Thus to fit the PPO scores, only the scores after the maximum were used.

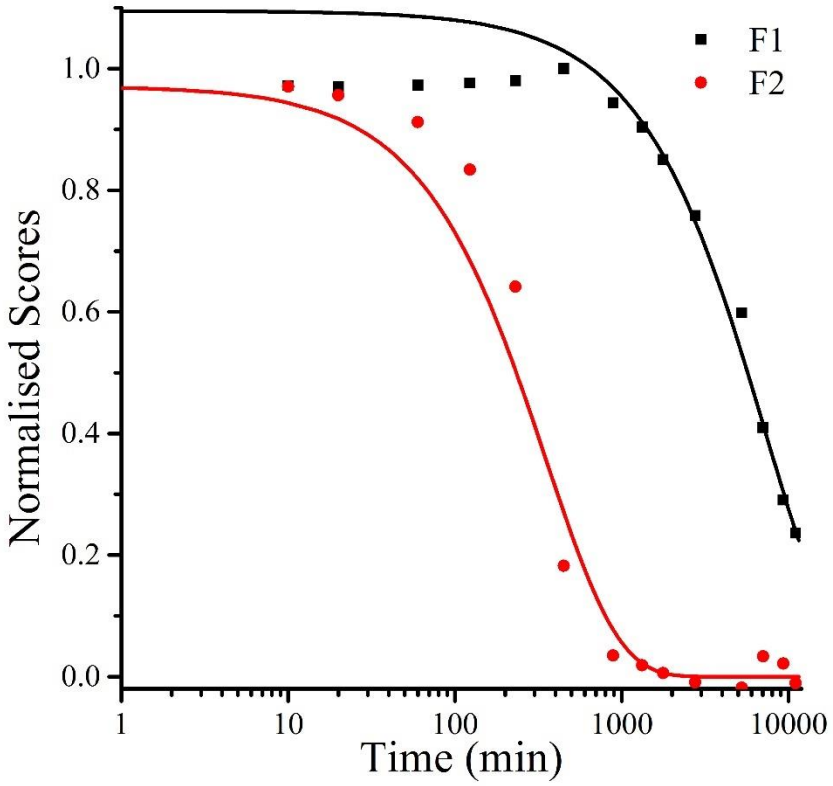

Figure 7.21: Kinetic plot of the scores obtained using PARAFAC on the photodegraded samples. The data points resemble normalised scores of F1 (PPO) and F2 (bis-MSB) of the photo degraded samples obtained using PARAFAC on all 101 samples. The solid coloured lines represent single exponential decay fits through the scores. The fit for F1 was only conducted on the decreasing portion of the data, due to inner filter effects. Component F3 was excluded as it shows no change in the scores.

Multiplying the pseudo-first order rate constants by the photon concentration of $4.25 \pm 0.17 \times 10^{-7}$ photonmol L^{-1} allows us to obtain the second order rate constant, k_p, (**Table 7.4**). As with the thermally aged samples, the Gibbs free energies of activation, $\Delta G^{\ddagger}$, of the photoreaction was obtained using equation (7.23). Knowing $\Delta G^{\ddagger}$, the rate of degradation at the SNO+ experiment conditions, was determined by extrapolation. The photon concentrations required to degrade the SNO+ scintillation solution replica to 99% and 90% of the fluorophores original concentration are given in **Figure 7.22**. **Figure 7.21** shows that bis-MSB is much more sensitive than PPO to photochemical decomposition under UV-radiation. The

maximum concentration of UV photons at 365 nm that can be exposed to the scintillation solution to remain 90% (99%) effective over 7 years was determined to be $0.138 \pm 0.009 \times 10^{-11}$ photonmol L^{-1} ($0.132 \pm 0.008 \times 10^{-12}$ photonmol L^{-1}).

Table 7.4: Rate constants for the decay of F1 (PPO), F2 (bis-MSB), and AP1 and the rise of AP2 in the SNO+ replica scintillation solution obtained by fitting the data shown in **Figure 7.21** and **Figure 7.24** to equations (7.10) and (7.13). The second order rate constant, k_P, was obtained by dividing the pseudo first order rate constant with the concentration of photons emitted by the light source $[h\nu] = 4.25 \pm 0.17 \times 10^{-7}$ photonmol L^{-1} using $k_P = k_P^* / [h\nu]$. The column marked with * gives the predicted rate constants obtained using the listed value for $\Delta G^{\ddagger}$. The values for $[h\nu]_{max}$ represent the maximum concentration of UV photons allowed to ensure the solution remains 90% and 99% fluorescent over the 7 years. These are shown graphically in **Figure 7.22** for F2.

k_p / **L photonmol^{-1}**	**Temperature / K**		$\Delta G^{\ddagger}$ /	$[h\nu]_{max}$ / $\times 10^{-10}$ **photonmol L^{-1}**	
M^{-1}s^{-1}	285*	298	**kJmol^{-1}**	90% remaining	99% remaining
F1	1.458 (0.052)	5.41 (0.18)	68.84 (0.08)	3.27 (0.11)	0.312 (0.011)
F2	34.6 (2.3)	111.7 (7.0)	61.33 (0.16)	0.138 (0.009)	0.0132 (0.0008)
AP1	5.58 (0.32)	19.5 (1.1)	65.66 (0.13)		
AP2	1.58 (0.34)	5.8 (1.2)	68.65 (0.51)		

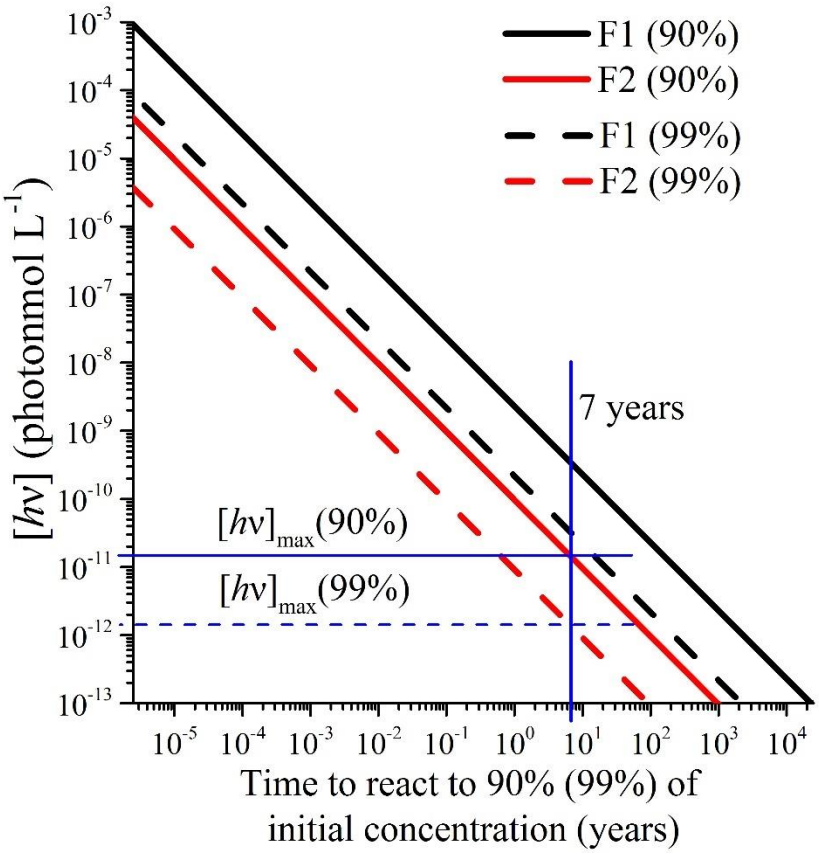

Figure 7.22: Concentration of photons to degrade the SNO+ scintillation replica to 90% (Solid lines) or 99% (dashed lines) of its original concentration at 285 K. The solid blue line represents the 7 years of the SNO+ experiment and the horizontal blue lines show the maximum number of allowed photons that the solution can be exposed to in order to ensure a 90% or 99% effective solution. These were obtained by calculating the Gibbs free energy of activation, $\Delta G^{\ddagger}$, obtained from the rates in **Figure 7.21** with equation (7.23).

7.4.3.2 Absorption

Absorption spectra of the UV aged samples, **Figure 7.23(a)**, show that the absorption also decreases with increased exposure. PARAFAC analysis of the 17 photo degraded sample absorption spectra led to a two component fit which is given in **Figure 7.23(b)**.

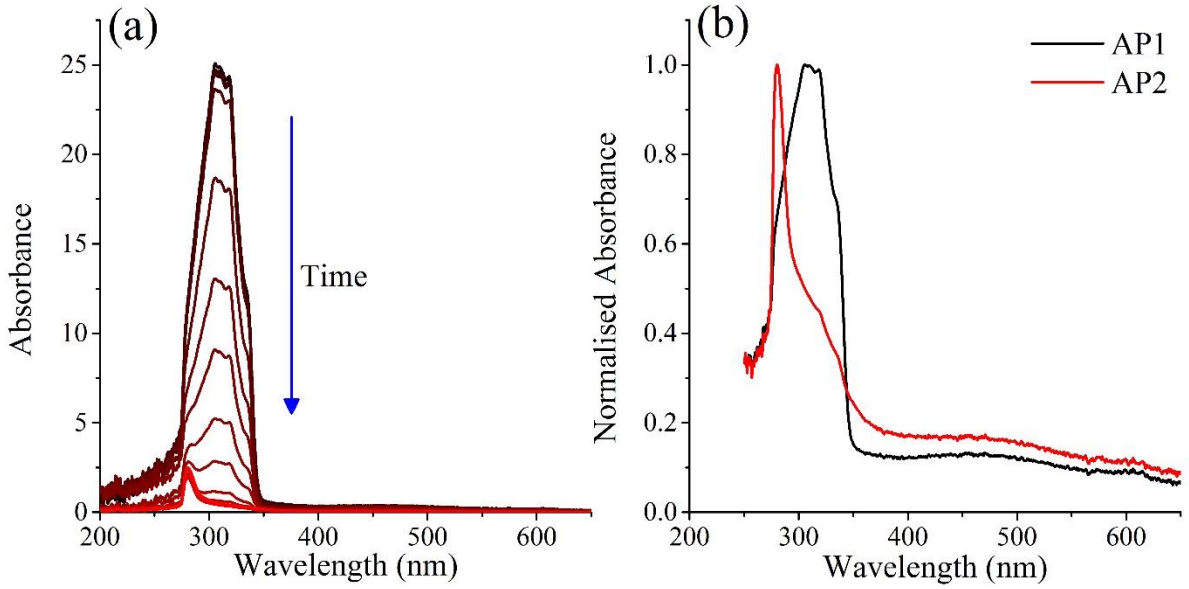

Figure 7.23: Absorption spectra of the photo degraded samples. **(a)** Shows the absorption spectra of the samples when exposed to UV light resulting in the absorption decreasing. Note these spectra were obtained by diluting in hexanes and multiplying the spectra accordingly. **(b)** Represents the two components determined using PARAFAC (AP1, AP2) on the 17 absorption spectra shown in **(a)**.

Component AP1 matches the absorption spectrum of PPO, **Figure 7.11(b)**, and decreases with a first order decay and with the concentration of [*hv*], gives a k_P(AP1) = 19.5 (1.1) L photonmol^{-1} M^{-1}s^{-1} at 298 K (**Figure 7.24**). Although the absorption spectrum matches that of PPO this decay rate does not match the decay constant of the fluorescence component F1, k_P(F1) = 5.41 (0.18) L photonmol^{-1} M^{-1}s^{-1}. AP1 must then be attributed to both the degradation of PPO and another process that occurs much faster — the degradation of bis-MSB as a possible example. The second component, AP2, which has $\lambda_{max} \approx 280$ nm increases as the sample is degraded and follows an exponential rise giving a k_P(AP2) = 5.8 (1.2) L photonmol^{-1} M^{-1}s^{-1} (**Figure 7.24**). This matches rate of the degradation of F1 (PPO) from the fluorescence data (**Table 7.4**) and it is likely that component AP2 is a PPO photoproduct. Given that the absorption peak of AP2 at 280 nm (**Figure 7.23(b)**) is similar to those of phenyl groups it is plausible that PPO photochemically degrades by breaking its conjugation.

In addition, comparing the Gibbs free energies of activation, the formation of AP2 matches the degradation of F1 (PPO) (**Table 7.4**). F2 (bis-MSB) degrades at a slightly lower Gibbs free energy of activation and thus is more sensitive to the presence of UV photons. The Gibbs free energy of activation of the degradation of AP1 rises lies in-between the energies of the degradation of F1 (PPO) and F2 (bis-MSB). Therefore, it is possible that AP1 contains both degradation profiles of both bis-MSB and PPO, which agrees with the second order rates of degradation.

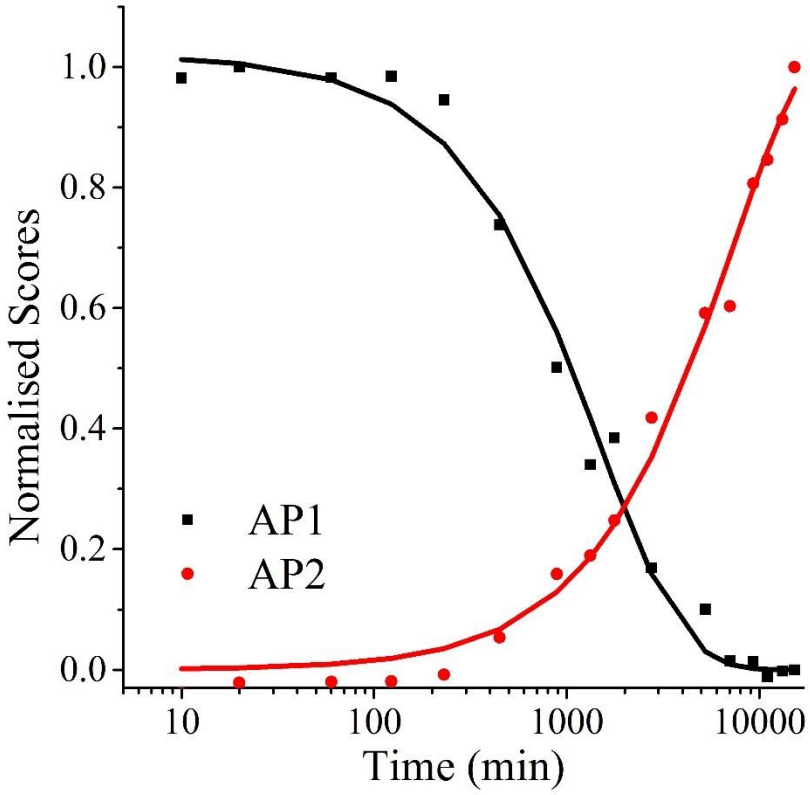

Figure 7.24: Kinetic plot of the normalised absorption scores of both the photodegraded components shown in **Figure 7.23(b)**. The data points represent the scores whereas the lines represent the exponential fits to the data using equations (7.10) and (7.13) for AP1 and AP2 respectively.

7.5 Concluding remarks

The EEM method was used to determine the stability of the SNO+ scintillation solution under oxidative, thermal, and photochemical conditions and to specify the necessary conditions needed to ensure its function

for the duration of the SNO+ experiment (e.g. 7 years). In the presence of an infinitely large headspace with a constant concentration of O_2, the level of O_2 must be kept below 24 ppm_v (or a dissolved amount of 4.3-7.1 ppb_w) to ensure the solution remains 90% fluorescent after 7 years. An even more stringent condition was found for the transparency of the solution. Degradation products produced at high temperatures are absorbing and suggest that the partial pressure in the headspace must be kept below 4.2×10^{-3} Pa (41 ppb_v) corresponding to an approximate dissolved mole fraction of 1.13×10^{-10} to 1.9×10^{-10} (14-23 ppt_w) for the SNO+ scintillator to remain 90% transmissive after 7 years. We note that the latter condition was established from experimental results at high temperature at which cracking of the LAB molecules is known to occur in the presence of oxygen.

We note that oxygen can be removed quite effectively from water and other solvents by bubbling purified nitrogen gas through solution. It was shown previously that no more than 500 ppb_w of O_2 (mole fraction of 4.1×10^{-6}) remain dissolved in water after purging with nitrogen. This concentration would be equilibrated to a concentration of 2700 ppm_v in the headspace. Simple purging of the scintillator liquid with N_2 may therefore not be sufficient if the scintillator was allowed to equilibrate with an infinitely large headspace. In the SNO+ experiment, however, the headspace volume is very small compared to the volume of the liquid and the supply of O_2 is very limited. The SNO+ detector will be airtight, the headspace very small, and all SNO+ scintillator process lines will be under nitrogen. The SNO+ scintillator will have any oxygen content efficiently depleted in a very efficient counter-current nitrogen and steam stripping column. In the worst case, any residual oxygen in the SNO+ scintillator will result in some oxidation that would terminate as soon as the O_2 supply is depleted; for example, the depletion reaction will stop after all O_2 has reacted with the large amount of PPO.

The experimental results also established that after purging the scintillator with purified N_2, and keeping the SNO+ scintillation solution under inert gas, that the solution is expected to remain useable for much

longer than 7 years. When handling the SNO+ scintillator liquid, e.g. when filling tanker trucks, storage vessels, pipes, and of course the SNO+ detector, it is therefore important to first purge the empty container with N_2 before filling it will scintillator. These steps have been adopted in the liquid handling strategy and procedures for the SNO+ experiment.

In addition, adding a singlet oxygen quencher such as 1,4-diazabicyclo[2.2.2]octane (DABCO) may improve the lifetime of the fluorescent dyes and increase the SNO+ scintillation solutions lifetime.[33] However, there are inherent risks in adding even more compounds to the scintillator mixture, as they may also contaminate the liquid.

We also show that UV radiation degrades the SNO+ scintillation solution and measures must be taken to ensure that the concentration of photons in the flask remains lower than $0.138 \pm 0.009 \times 10^{-11}$ photonmol L^{-1}. As a comparison the photon flux of a UV curing lamp is about $4.25 \pm 0.17 \times 10^{-7}$ photonmol L^{-1}. While the SNO+ scintillator will be kept in the dark during the experiment, precautions are also needed when preparing the solution.

The main advantage of combining EEM fluorescence spectra with PARAFAC analysis is its ability in extracting kinetic information. Here, we show EEM and PARAFAC's applicability to quantify the stability of the SNO+ solution. As shown in Chapter 6 this method is also very suitable in studying other mixtures such as lubrication oil and this method has the potential of analysing other mixtures of fluorescent species, such as the degradation of foodstuff and environmental samples, lubricants, and other industrial liquids.[14]

7.6 Bibliography

1. J. Boger, R. L. Hahn and J. K. Rowley et al. (SNO Collaboration), The Sudbury Neutrino Observatory. *Nuclear Instruments and Methods in Physics Research Section A: Accelerators, Spectrometers, Detectors and Associated Equipment* **2000,** *449*, 172-207.
2. M. C. Chen, The SNO liquid scintillator project. *Nuclear Physics B - Proceedings Supplements* **2005,** *145*, 65-68.

3. http://snoplus.phy.queensu.ca/About.html, 2016.
4. S. Dell'Oro, S. Marcocci, M. Viel and F. Vissani, Neutrinoless double beta decay: 2015 review. *Advances in High Energy Physics* **2016,** *2016*, 1-37.
5. S. Biller, 13th Int. Conf. on Topics in Astroparticle and Underground Physics, 2014.
6. S. Andringa, E. Arushanova and S. Asahi et al., Current status and future prospects of the SNO, current status and future prospects of the SNO. *Advances in High Energy Physics* **2016,** *2016*, e6194250.
7. F. P. An, Q. An and J. Z. Bai et al. (Daya Bay Collaboration), A side-by-side comparison of Daya Bay antineutrino detectors. *Nuclear Instruments and Methods in Physics Research Section A: Accelerators, Spectrometers, Detectors and Associated Equipment* **2012,** *685*, 78-97.
8. J. S. Park, J. Lee and I. S. Yeo et al. (RENO Collaboration), Production and optical properties of Gd-loaded liquid scintillator for the RENO neutrino detector. *Nuclear Instruments and Methods in Physics Research Section A: Accelerators, Spectrometers, Detectors and Associated Equipment* **2013,** *707*, 45-53.
9. H. M. O'Keeffe, E. O'Sullivan and M. C. Chen, Scintillation decay time and pulse shape discrimination in oxygenated and deoxygenated solutions of linear alkylbenzene for the SNO+ experiment. *Nuclear Instruments and Methods in Physics Research Section A: Accelerators, Spectrometers, Detectors and Associated Equipment* **2011,** *640*, 119-122.
10. D. T. Mahin, A new way to reduce oxygen quenching in liquid scintillation samples. *The International Journal of Applied Radiation and Isotopes* **1966,** *17*, 185-191.
11. R. W. Pringle, L. D. Black, B. L. Funt and S. Sobering, A new quenching effect in liquid scintillators. *Physical Review* **1953,** *92*, 1582-1583.
12. C. G. Hatchard and C. A. Parker, A new sensitive chemical actinometer. II. Potassium ferrioxalate as a standard chemical actinometer. *Proceedings of the Royal Society of London A: Mathematical, Physical and Engineering Sciences* **1956,** *235*, 518-536.
13. http://www.electro-lite.com/PDFs/BW.pdf, 2016.
14. N. L. P. Andrews, J. Z. Fan, H. Omrani, A. Dudelzak and H.-P. Loock, Comparison of lubricant oil antioxidant analysis by fluorescence spectroscopy and linear sweep voltammetry. *Tribology International* **2016,** *94*, 279-287.
15. D. Munzke, J. Saunders, H. Omrani, O. Reich and H.-P. Loock, Modeling of fiber-optic fluorescence probes for strongly absorbing samples. *Applied Optics* **2012,** *51*, 6343-6351.
16. K. R. Murphy, C. A. Stedmon, D. Graeber and R. Bro, Fluorescence spectroscopy and multi-way techniques. PARAFAC. *Analytical Methods* **2013,** *5*, 6557-6566.
17. R. Bro and H. A. L. Kiers, A new efficient method for determining the number of components in PARAFAC models. *Journal of Chemometrics* **2003,** *17*, 274-286.
18. H.-L. Xiao, X.-B. Li, D. Zheng, J. Cao, L.-J. Wen and N.-Y. Wang, Study of absorption and re-emission processes in a ternary liquid scintillation system. *Chinese Physics C* **2010,** *34*, 1724.
19. N. L. P. Andrews, A. G. MacLean, J. E. Saunders, J. A. Barnes, H. P. Loock, M. Saad, C. L. Jia, K. Ramaswamy and L. R. Chen, Quantification of different water species in acetone using a NIR-triple-wavelength fiber laser. *Optics Express* **2014,** *22* (16), 19337.
20. J. N. Demas, W. D. Bowman, E. F. Zalewski and R. A. Velapoldi, Determination of the quantum yield of the ferrioxalate actinometer with electrically calibrated radiometers. *The Journal of Physical Chemistry* **1981,** *85*, 2766-2771.
21. F. Rossi, R. Lombardo, L. Sciascia, C. Sbriziolo and M. L. T. Liveri, Spatio-temporal perturbation of the dynamics of the ferroin catalyzed Belousov−Zhabotinsky reaction in a batch reactor caused by sodium dodecyl sulfate micelles. *The Journal of Physical Chemistry B* **2008,** *112*, 7244-7250.
22. J. O. Edwards, K. Edwards and J. Palma, The reactions of ferroin complexes. A color-to-colorless freshman kinetic experiment. *Journal of Chemical Education* **1975,** *52*, 408.

23. J. L. Bitter, J. Yang, S. B. Milani, C. T. Jafvert and D. H. Fairbrother, Transformations of oxidized multiwalled carbon nanotubes exposed to UVC (254 nm) irradiation. *Environmental Science: Nano* **2014,** *1*, 324-337.
24. J. McMurry, in *Organic Chemistry*, Brooks/Cole Publishing Company, Cornell University, 4th Edition edn., 2012, pp. 1215 - 1219.
25. T. J. H. M. Cuppen and W. H. Laarhoven, Photodehydrocyclizations of stilbene-like compounds. VI. Chemical evidence of an excited state mechanism. *Journal of the American Chemical Society* **1972,** *94*, 5914-5915.
26. F. B. Mallory and C. W. Mallory, in *Organic Reactions*, John Wiley & Sons, Inc., 2004.
27. M. E. Ackerman, G. H. Daub, F. N. Hayes and H. A. Mackay, in *Organic Scintillators and Scintillation Counting*, ed. D. Horrocks, Elsevier, 2012, pp. 315 - 325.
28. C. Geletneky and S. Berger, The mechanism of ozonolysis revisited by ^{17}O-NMR spectroscopy. *European Journal of Organic Chemistry* **1998,** *1998*, 1625-1627.
29. D. a. Maurizio, in *Advances in Heterocyclic Chemistry*, Elsevier, 2001, vol. 79, pp. 41-88.
30. H. L. Clever, R. Battino, H. Miyamoto, Y. Yampolski and C. L. Young, IUPAC-NIST solubility data series. 103. Oxygen and ozone in water, aqueous solutions, and organic liquids (supplement to solubility data series volume 7). *Journal of Physical and Chemical Reference Data* **2014,** *43* (3), 033102.
31. R. Battino, T. R. Rettich and T. Tominaga, The solubility of oxygen and ozone in liquids. *Journal of Physical and Chemical Reference Data* **1983,** *12*, 163-178.
32. M. Martynoff, Note de laboratoire: Spectres d'absorption de quelques p-quinones. *Bulletin de la Société Chimique de France* **1949,** *16*, 258-261.
33. C. Schweitzer and R. Schmidt, Physical mechanisms of generation and deactivation of singlet oxygen. *Chemical Reviews* **2003,** *103*, 1685-1758.

Chapter 8

Detection of Different Water Solvation Species Mixed with Acetone

This chapter is based on the paper entitled "Quantification of different water species in acetone using a NIR-triple-wavelength fiber laser" Optics Express, Vol. 22, Iss. 16 (2014) P. 19337, N. L. P. Andrews, A. G. MacLean, J. E. Saunders, J. A. Barnes, H.-P. Loock, M. Saad, C. Jia, K. Ramaswamy and L. R. Chen. Permission to reproduce the material from this article for this chapter from OSA has been acquired. Lawrence Chen's group at McGill University (Saad, Jia, Ramaswamy and Chen) designed and built the triple wavelength laser used to detect water in acetone. Amy Maclean obtained the NIR spectra of the water acetone mixtures at Queen's and also calculated the nonlinear fractional absorption effects for this system. With these exceptions all work presented below is that of the author.

8.1 Introduction

In Chapter 6, the monitoring of the quality of lubrication oil is shown to be an important factor in ensuring the good health of an engine. Contamination of the lubricant with water severely reduces its remaining useful life, and forms emulsions affecting the lubricity of the oil.[1-4] Water contamination also leads to premature corrosion and wear of the engine.[5] Therefore the detection of water in engine fluids is of high priority. Water has been detected using infrared spectroscopy at the H_2O absorption lines at 3400 cm^{-1} (2930 nm) and overtones at 6760 cm^{-1} (1480 nm) and 5200 cm^{-1} (1920 nm).[6-13] The near-infrared (NIR) region is particularly well suited for chemical detection, as most analytes show well resolved and structured overtone or combination bands which are comparable to bands in the mid-infrared (MIR) spectrum. Light sources and detectors are much less expensive in the NIR region of the spectrum compared to mid-IR components. Even though the transitions are weaker, the development of brighter and sometimes tuneable laser sources can lead to a similar spectral response.

The detection of water as with other compounds, can be improved through the use of dual- and multi-wavelength fibre lasers. By simultaneously measuring the optical attenuation at several wavelengths, it is possible to generate a "response pattern" that can improve the specificity and sensitivity of the chemical detection.

Thulium ions (Tm^{3+}) provide a very effective means for developing fibre lasers operating at a wide range of wavelengths, including the NIR region. The $^3H_4 \rightarrow {}^3F_4$ and $^3F_4 \rightarrow {}^3H_6$ transitions can provide lasing around 1480 nm and 1900 nm, respectively. The 1480 nm wavelength lies near an overtone absorption peak of liquid water and can provide a convenient means for water detection in various liquids. When thulium is doped in ZBLAN (a fluoride glass host), the lifetime of its excited $^3H_4$ state is almost hundred-fold longer (1350 μs) than in silica (14.2 μs),[14] due to the lower phonon energy of ZBLAN glass.

In this chapter, we demonstrate the use of a fibre laser that emits at three NIR wavelengths to quantify the water content in a simple miscible solvent such as liquid acetone. Detection is accomplished through the $\nu_2+\nu_3$ combination band near 1930 nm (5180 cm^{-1}) and the first overtone of the ν_1 symmetric stretch vibration near 1450 nm (7000 cm^{-1}). This chemical system was selected as a case study for several reasons: the partial molar volume corrections of acetone/water mixtures are well understood, the related MIR bands have been extensively studied and interpreted using multivariate analysis methods, and acetone itself has a well-defined and sparse background spectrum in this region. As a similar understanding of other matrices becomes available, we envision that the water content of other liquids, such as lubrication oils and fuels, can similarly be determined.

Of particular interest in this study is the system's deviation from the Beer-Lambert absorption law. While these deviations are well documented,[15, 16] it is often overlooked that the centre frequencies of vibrational

absorption spectra — including overtone and combination band spectra — of small molecules can change dramatically depending on their solvent environments or the first solvation cage structure. Here, we explicitly consider the spectral signatures of three distinct water solvation "species" known to exist in acetone at concentrations ranging from 0.55-11.4 M (approx. 1.0 vol % - 20 vol %) of water.

8.2 Distinct water solvation species

The deviation from the Beer-Lambert law is due to the emergence and decline of distinct water species as the mole fraction of water increases in a solvent such as acetone. One can envision the presence of multiple species of water as the first solvation cage structure changes from predominantly consisting of other water molecules to predominantly consisting of only acetone molecules.

Previously, Max and Chapados (MC) used factor analysis to distinguish between the bonding environments in water and acetone over the entire miscibility regime.[15, 16] They recorded and analysed MIR spectra of the O-H and C-H stretch regions, as well as strong overtone and combination bands. Nine water environments were identified, correlating to five factors (W1–W5), as factor analysis cannot distinguish between species that evolve concurrently.[15, 16] The factor W1 represented a water species that is surrounded by acetone and so has zero hydrogen bonds to other water molecules. Factors W2-W4 correspond to water species that form 1 to 3 hydrogen bonds to other water molecules. Factor W5 relates to a completely water-solvated species and forms 4 hydrogen bonds to the surrounding water molecules.

The presence of distinct water species was also discussed by Koga et al.[17] and by Czarnik-Matusewicz and co-workers,[18, 19] who analysed water at different temperatures using multivariate analysis to rationalise the peak shifts. To our knowledge, MC provides the only previous characterisation of mixtures using factor analysis.[15, 16] These workers provided a persuasive model that describes the emergence and decline of each species as a function of water mole fraction. From their factor analysis, MC derived equilibrium constants

that were used as parameters to fit their data, in addition to a comprehensive model describing each species' concentration as a function of water mole fraction.

8.3 Experimental

8.3.1 Triple-wavelength laser

A schematic drawing of the laser system built by the group at McGill University is shown in **Figure 8.1**. The system contains two independent branches, which generate lasing at 1461/1505 nm and 1874 nm, respectively. These branches are coupled to complete the laser cavity provide a single output of the laser light. The gain medium for operation at 1461 nm and 1503 nm (top branch) is a 52 cm segment of Tm^{3+} doped ZBLAN fibre (*IRphotonics/Thorlabs*), while the gain medium for operation at 1874 nm (bottom branch) is an 85 cm segment of the same Tm^{3+}:ZBLAN fibre. The double-cladding ZBLAN fibre is doped with 8,000 ppm Tm^{3+}, has an 8 µm core diameter, a 125 µm cladding diameter and is coated with 15 µm of mixed fluoroacrylate and acrylate polymer.

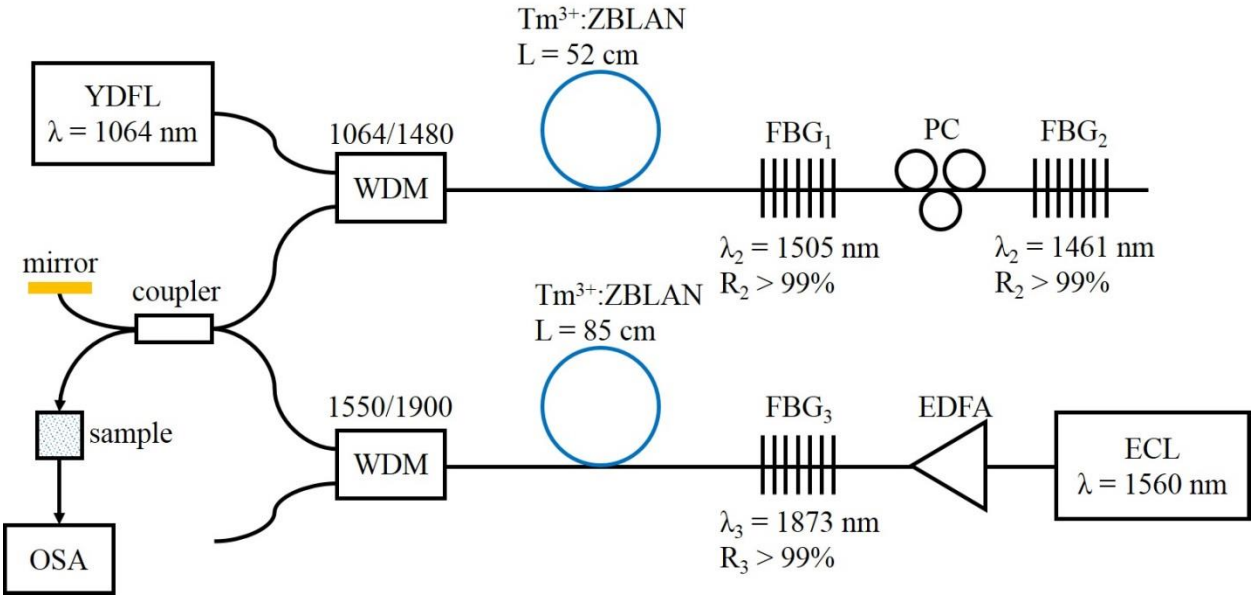

Figure 8.1: Schematic of the triple-wavelength fibre laser. Two Tm^{3+}:ZBLAN fibres are incorporated into fibre cavities that are defined by three different FBGs and a shared gold mirror.

The top branch cavity is constructed using two fibre Bragg gratings (FBGs) on one end and a gold-tipped fibre mirror on the other. The FBGs define the lasing wavelengths, and FBG_1 and FBG_2 have centre wavelengths of λ_1 = 1505 nm and λ_2 = 1461 nm. The 52 cm gain fibre is pumped by up-conversion pumping from a 1064 nm ytterbium-doped fibre laser (YDFL) through a 1064/1480 wavelength division multiplexer (WDM). In the bottom branch, the cavity is formed on one end by FBG_3, which has a centre wavelength λ_3 = 1874 nm and completed with the shared gold-tipped fibre mirror. The 85 cm gain fibre is pumped directly by a 1560 nm pump consisting of an external cavity laser (ECL) and an erbium-doped fibre amplifier (EDFA). All three FBGs are written in single mode fibre (SMF-28) and have a peak reflectivity > 99%. The two branches are connected to a coupler so that they can share a common gold-tipped fibre mirror, which completes the laser cavities. The coupler also serves as an output for all three wavelengths. The output is collimated through a 1 cm sample cuvette using two GRIN lenses and the transmitted light is detected using an optical spectrum analyser (OSA, *Yokogawa*, AQ6375). The coupler itself has a 50/50 splitting ratio at 1461/1505 nm and an 87/13 splitting ratio at 1874 nm (87% towards the mirror). A polarisation controller (PC) is placed between FBG_1 and FBG_2 to equalise the power generated at λ_1 and λ_2.

Figure 8.2 shows the output spectrum of the three lasing lines at λ_1, λ_2 and λ_3. Note that the peak at 2128 nm is an artefact of the OSA due to higher-order diffraction from the λ = 1064 nm pump light, P_{1064}.

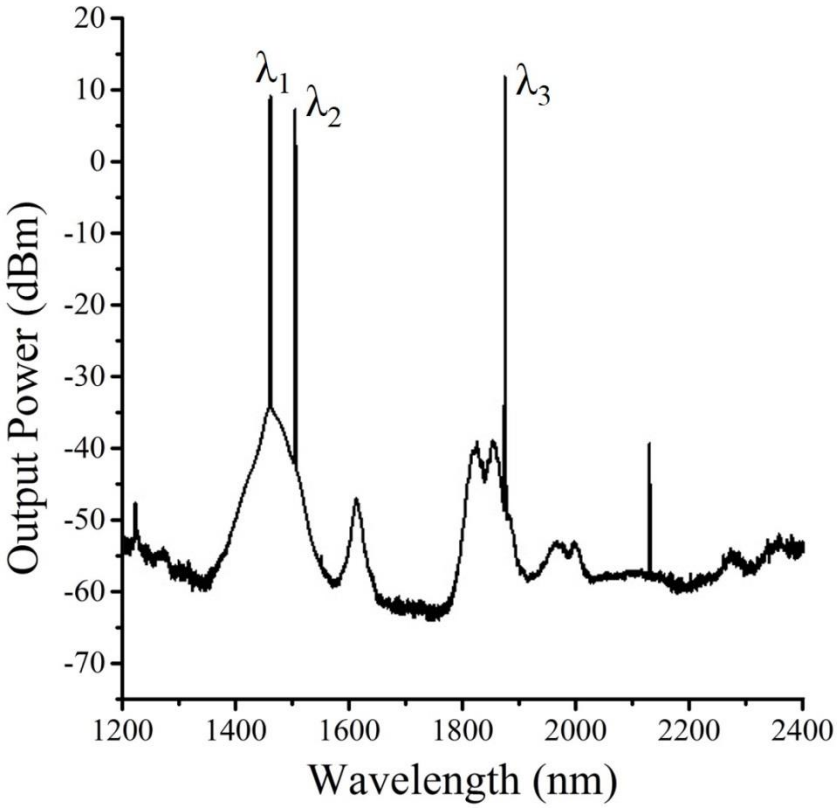

Figure 8.2: Emission spectrum for the triple wavelength laser with the output power for the YDFL is P_{1064} = 1520 mW and ECL is P_{1560} = 480 mW.

8.3.2 Sample preparation

Acetone (*ACP Chemicals*, ≥ 99.9%, reagent grade) and deionised water (*Thermo Scientific*, Type 1 reagent grade) were used to create solution samples without additional purification. Twelve mixtures of water in acetone between 0.55 M and 11.4 M were prepared using Eppendorf micropipettes to measure volumes of both neat components. As the solution volume differs from the sum of component volumes, molar concentrations were calculated using an average of the values for the concentration-dependent density provided in the literature.[20-22]

8.3.3 Absorption spectroscopy

The absorption spectra of water-acetone samples were obtained using both the triple-wavelength Tm^{3+}:ZBLAN fibre laser and a conventional Fourier-transform near-infrared (FT-NIR) absorption

spectrometer (*Perkin-Elmer*, Spectrum 400). FT-NIR spectra over the 1.0-2.5 μm (10,000 – 4000 cm^{-1}) spectral range were obtained at 1 cm^{-1} increments and 4 cm^{-1} resolution, using a 2 mm/s mirror scan rate and a triglycine sulfate pyroelectric detector. Samples were placed in a 1.0 mm quartz cuvette and each transmittance spectrum was taken from an average of 8 scans. Background measurements were taken without a cuvette between spectra, with pure acetone serving as a blank.

NIR transmittance measurements on the same samples were also obtained using the triple-wavelength Tm^{3+}:ZBLAN fibre laser. GRIN lenses were used to couple the fibre laser output to a 1 cm quartz cuvette containing the samples. Sample transmittance was detected using an OSA with a 55 dB dynamic range and 0.5 nm bandwidth from 1450 nm to 1900 nm. Each transmittance measurement was taken from an average of 30 sequential OSA scans. Background measurements were taken using neat acetone before and after each sample measurement. The reference spectrum was obtained from the average of the two background measurements.

8.3.4 Factor analysis

To obtain the components present in the NIR spectra, factor analysis was used to extract the components in the NIR spectra. Factor analysis was conducted on all the 20 absorption spectra for the water acetone mixtures using the drEEM toolbox in MATLAB.[23] The drEEM toolbox provides a parallel factor (PARAFAC) analysis method but requires a 3-dimensional data cube. The square roots of the 2-D absorption spectra were therefore multiplied by the square roots of their transpose (decimated by 10) to generate a mock-3D spectrum that could be analysed. The same technique was used for the absorption spectra of scintillator solutions and are presented in Chapter 7. Generating a mock 3D spectrum from the absorption spectra using this method, ensures that the same number of components are present for both dimensions allowing the parallel factor algorithm to be used for factor analysis to find appropriate 2D components. The drEEM program was run 10 times using random initialisation, a non-negativity constraint, and a convergence criterion of 10^{-8}. The spectra were fitted to 2 to 5 components, and it was found that 3

components provided the best explanation for the data when considering both core consistency and "percentage-explained" — these concepts are described in more detail in Chapter 5.

8.4 Results and discussion

8.4.1 Interpretation of the absorption spectra

The NIR spectra of the 20 samples plus one acetone blank are given in **Figure 8.3**. Linear offset corrections were first applied to all spectra to compensate for stray light contributions at regions with no absorption features, i.e. at 1250-1300 nm, 1660-1670 nm, 1820 nm and 2190 nm. Then a second common linear offset was applied to align the baseline with the spectrum for neat water as had been done by Bertie et al. for ease of comparison.[24] In all spectral regions, the peaks attributed to water absorption show a clear bathochromic shift as the water concentration increases. The absorption spectrum of neat water as reported by Bertie et al. is also included in **Figure 8.3**.[24] For water mole fractions above 0.6, the spectra are saturated in the 1900-2000 nm region.

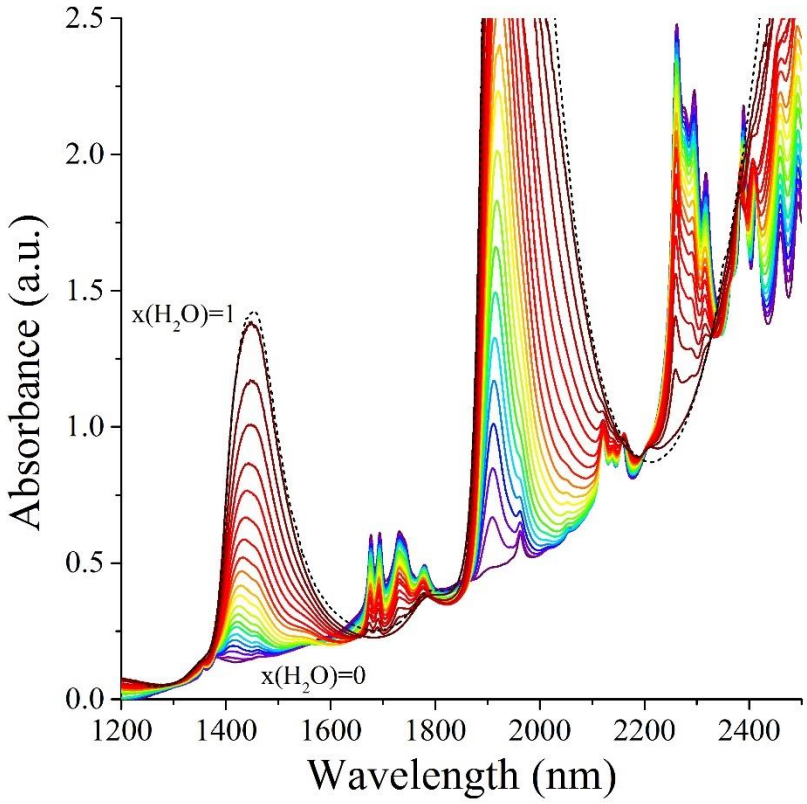

Figure 8.3: NIR spectra of water in acetone with 21 different concentrations. The dashed black line shows the spectrum of neat water from Bertie et al., whereas the solid lines show water acetone solutions with mole fractions between 1.0 and 0.0 in intervals of 0.05.[24]

The peak shifts in **Figure 8.3** are attributed to the emergence and decline of water species that interact with their solvent environments in different ways, depending on the number of hydrogen bonds formed with either surrounding water molecules or with acetone. The average hydrogen-bonding network around any water molecule is predicted to change with water concentration; several solvation species with distinct MIR spectral features have been reported.[15-17, 25] Assuming solution homogeneity, we expect to find water in 3-4 distinct hydrogen bonding environments in the concentration range of 0.0 - 11.4 M, and at least five distinct water species in the complete concentration range of 0.0 - 55.6 M. These solvation species can be interpreted in a first approximation as: water molecules surrounded exclusively by acetone (W1); water forming a hydrogen bond to one adjacent water molecule (W2); to two adjacent water molecules (W3); to

three adjacent water molecules (W4); and four adjacent water molecules (W5). Since these solvation species cannot be isolated from one another, deconvolution of the spectrum is difficult. Therefore, factor analysis is used to identify the number of components, their absorption spectra, and their relative contributions to the triple-wavelength laser spectra.

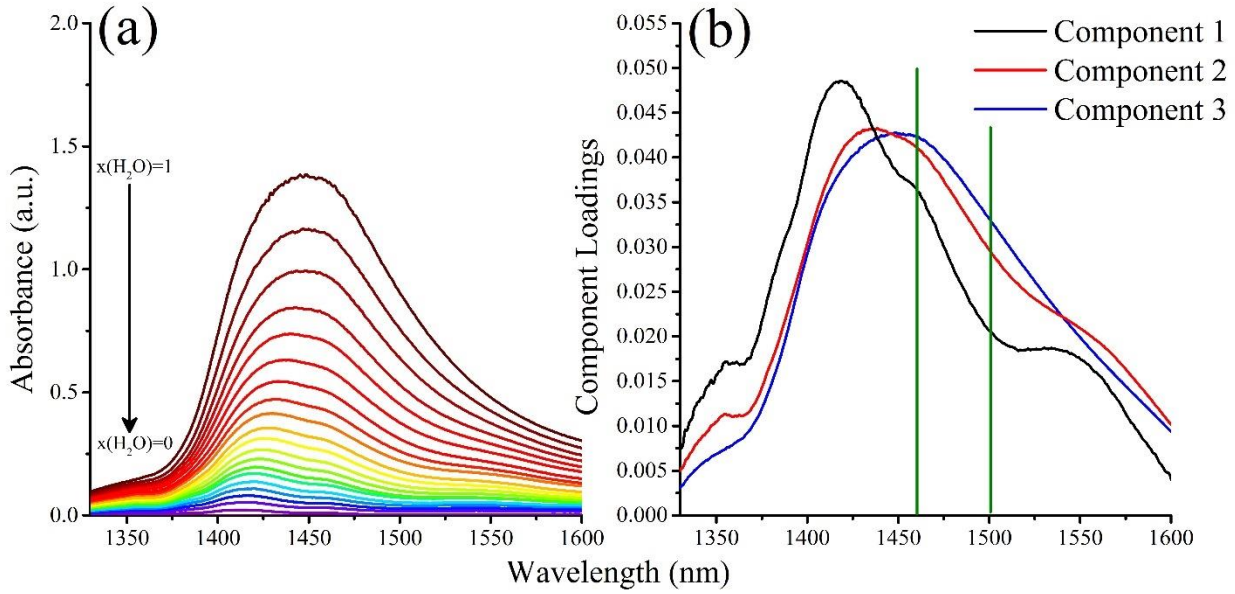

Figure 8.4: Spectral region used for factor analysis on the water in acetone mixtures. **(a)** Near-infrared spectra of water in acetone with 20 different concentrations as in **Figure 8.3** after a weighted contribution of the acetone absorption spectrum had been subtracted from all spectra in **Figure 8.3**. **(b)** The spectra of the three PARAFAC components obtained by decomposition of **(a)** show an isosbestic point near 1440 nm. The 1461 and 1505 nm laser wavelengths are included as vertical green lines.

Since our data set was not large enough to analyse the different acetone solvation species, we assumed that the acetone spectra are very similar and subtracted from the spectra in **Figure 8.3** the contribution of neat acetone absorption weighted by its mole fraction (**Figure 8.4(a)**). PARAFAC analysis on the processed NIR spectra was performed using drEEM software,[23] and determined that three components best described the data. The component loadings for these three components are shown in **Figure 8.4(b)**.

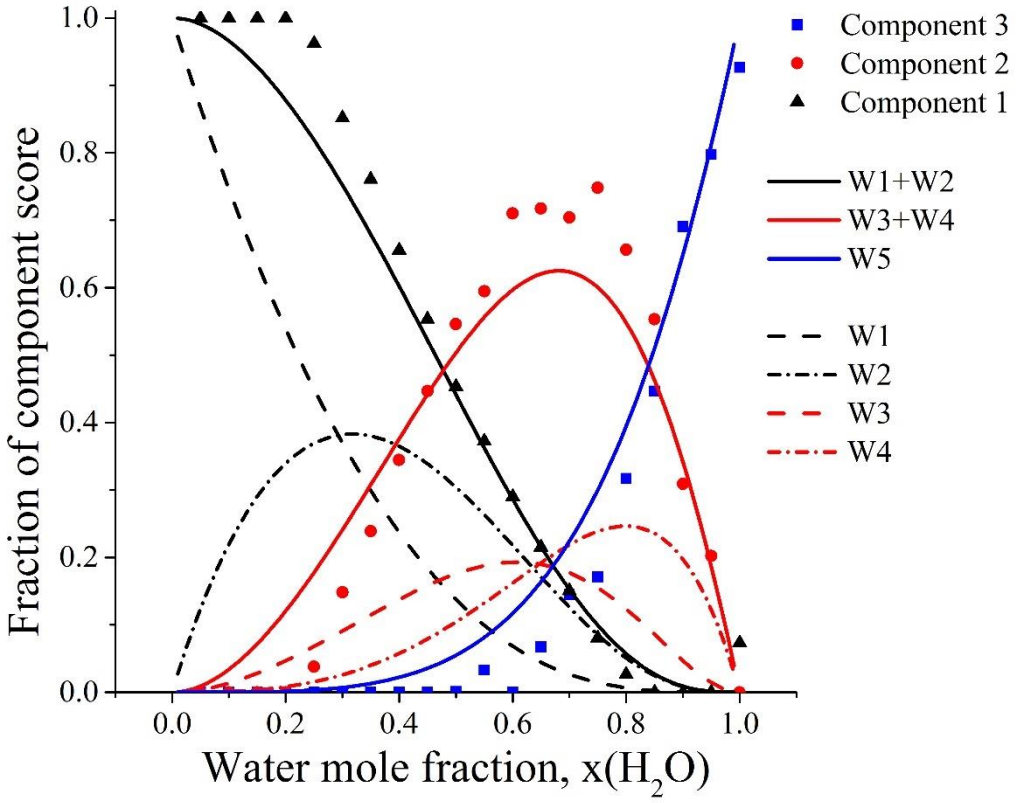

Figure 8.5: The fractions of the three PARAFAC components as with the water solvation species W1-W5. The symbols show the fraction that each of the three PARFAC components contributes to the absorption spectrum. The contribution of component 1 (black triangles) is compared to the sum of water species W1+W2 as calculated from MC (solid black line), whereas component 2 (red circles) qualitatively agrees with the sum of species W3+W4 (solid red line) and component 3 (blue squares) rises akin to W5 (blue line). The contributions of each of the five water species according to MC is given with dashed lines.

Figure 8.5 shows the relative contribution of each component to the overall water absorption spectrum, compared to the theoretical curves calculated by MC.[15, 16] The completeness of the spectral analysis is supported by the observation of an isosbestic point around 1440 nm (**Figure 8.4(b)**), which is consistent with the three components being stoichiometrically related. Component 3 is related to the completely water-solvated species (W5 in MC), and thus its score increases as water is added (**Figure 8.5**). Component 1 falls as the water concentration increases, and the data follows the sum of W1+W2 described by MC, i.e., water species that form either zero or one hydrogen bond(s) with other water molecules. Similarly,

component 2 rises and falls as water concentration increases and follows closely the sum of species W3+W4, corresponding to water molecules surrounded predominantly by other water molecules. Given a larger number of samples and a stronger absorption feature, it is conceivable that components 1 and 2 could be further separated into the water species described by MC. In any case, it is apparent that with the addition of water, more hydrogen bonds are formed and the O-H bond weakens, resulting in the observed red shift.[15, 16]

In our analysis, we were guided by this previous work, but our spectra were much weaker and we did not desiccate the supplied acetone. Despite these sources of error, our analysis is nevertheless adequate to guide the chemical analysis performed with the triple-wavelength laser.

8.4.2 Quantification of water content in acetone using multi-wavelength laser absorption

The absorption measurements of water in acetone, which are taken with the triple-wavelength fibre laser, show approximately linear trends (**Figure 8.6**). The detection limits are lowest (about 2.8 M) when absorption was measured at the 1461 nm laser line, presumably due to higher laser stability and a larger absorption cross-section. The molar absorptivity, ε, is calculated from the slope of each linear fit, and the detection limit at each wavelength is calculated from the 99% confidence interval as described previously (**Table 8.1**).[26] The difference between experimental and literature ε_{H_2O} values is due to variations in sample composition. There is little reason to assume that the hydrogen-bonded water species in tetrahedrally coordinated bulk water have the same absorption spectra compared to water species surrounded largely by acetone. Although a better comparison can be made using pure water, this spectrum was not obtained due to total attenuation of the laser light through a 1 cm cuvette. The discrepancy between our measured ε_{H_2O} at low water concentrations and the literature ε_{H_2O} for pure water is therefore understandable.

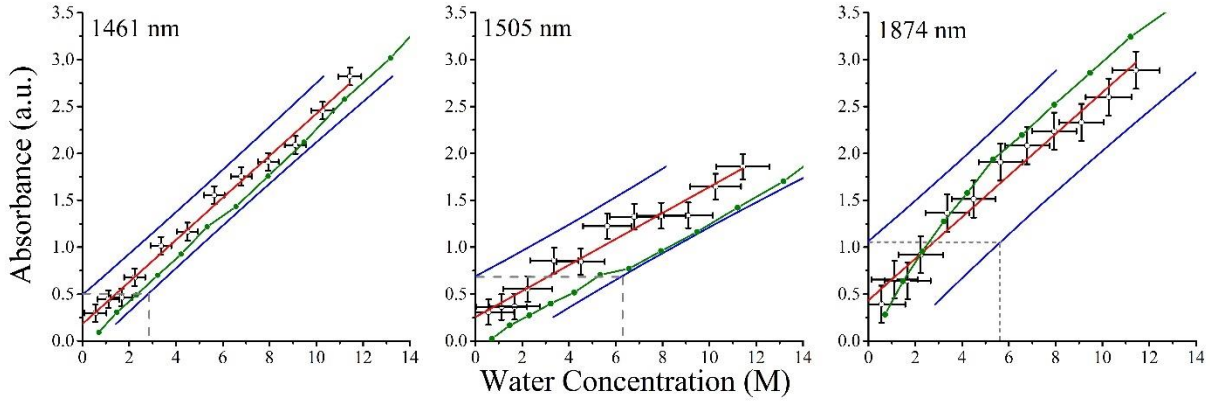

Figure 8.6: Absorption of solutions of water in acetone measured using the triple wavelength fibre laser at 1461 nm, 1505 nm and 1874 nm. The 99% confidence intervals are shown as two blue lines and used to calculate the limit of detection (dashed line). The molar absorptivity at each wavelength was calculated from the slope of the linear fit (red line). The data were analysed as in reference 26. The solid green symbols are absorption values extracted from **Figure 8.3** and are connected to guide the eye.

Consider that both the transition dipole moment of the overtone absorption and its resonance wavelength are related to the anharmonicity of the O-H stretching vibration, which increases with the strength and number of hydrogen bonds. This explains both the shift to longer wavelength and the increased overtone absorption cross-section of bulk water. A similar argument for the bathochromic shift was made by Dickens and Dickens and later quantified by MC.[15, 16, 25]

Table 8.1: Absorption coefficients of water in [L mol^{-1} m^{-1}] calculated using the laser absorption at low concentrations in acetone compared to the literature values for bulk water.

Wavelength	**This work**	**Ref.[24]**
1461 nm	22.4 ± 0.8	25.4
1505 nm	13.9 ± 1.1	16.2
1874 nm	22.2 ± 1.6	18.2

8.5 Concluding remarks

The detection of water in a simple solvent such as acetone has been shown to deviate from the Beer-Lambert law due to concentration dependent composition of the first solvation cage surrounding each water molecule. This solvation effect on the spectra must be taken into account when detecting water in other solvents such as lubrication oil. Despite this entanglement and bathochromic shift of the spectra, PARAFAC analysis was able to deconvolute the spectra into its respective water:acetone solvation species. The fraction of each water component agreed with their respective probabilities as calculated by MC.[15, 16] Now with a better understanding of the solvation effects in a simple system such as water in acetone, this technique can be easily extended to the detection of water in other solvents such as lubrication oil or hydrocarbon fuels as a better understanding of each of these solvent matrices becomes available.

In addition, a triple-wavelength Tm^{3+}:ZBLAN fibre laser emitting simultaneously at 1461, 1505, and 1874 nm, was utilised for water detection in acetone. Using the knowledge obtained from the chemometric analyses of water in acetone NIR spectra the optimisation of this laser for chemical sensing can be realised. To maximise the sensitivity, it may seem preferable to measure at a water NIR absorption maximum (1480 nm and/or 1920 nm), though both peaks exhibit a pronounced red shift and nonlinear absorption with increasing water concentration. It is, then conceivable to measure at the isosbestic point around 1440 nm, where all water species have an identical absorption cross section. At this wavelength, the absorption signal scales linearly with concentration making it far more suitable to detect water. Therefore, after characterising the solvation effects of water in lubrication oil, a distinct isosbestic point should be determined and a laser built to probe this exact wavelength for use to detect water contamination.

8.6 Bibliography

1. P. R. D. Silva, M. Priest, P. M. Lee, R. C. Coy and R. I. Taylor, Tribometer investigation of the frictional response of piston rings with lubricant contaminated with the gasoline engine biofuel ethanol and water. *Proceedings of the Institution of Mechanical Engineers, Part J: Journal of Engineering Tribology* **2011,** *225*, 347-358.
2. P. R. D. Silva, M. Priest, P. M. Lee, R. C. Coy and R. I. Taylor, Tribometer investigation of the frictional response of piston rings when lubricated with the separated phases of lubricant

contaminated with the gasoline engine biofuel ethanol and water. *Tribology Letters* **2011,** *43*, 107-120.
3. R. M. Mortier, M. F. Fox and S. T. Orszulik, *Chemistry and technology of lubricants*, Springer Netherlands, Dordrecht, 2010.
4. C. Lenauer, C. Tomastik, T. Wopelka and M. Jech, Piston ring wear and cylinder liner tribofilm in tribotests with lubricants artificially altered with ethanol combustion products. *Tribology International* **2015,** *82, Part B*, 415-422.
5. *ASTM standard D6304, test method for determination of water in petroleum products, lubricating oils, and additives by coulometric Karl Fischer titration*, ASTM International, West Conshohocken, PA, 2016.
6. A. Borin and R. J. Poppi, Multivariate quality control of lubricating oils using Fourier transform infrared spectroscopy. *Journal of the Brazilian Chemical Society* **2004,** *15*, 570-576.
7. N. L. P. Andrews, A. G. MacLean, J. E. Saunders, J. A. Barnes, H.-P. Loock, M. Saad, C. Jia, K. Ramaswamy and L. R. Chen, Quantification of different water species in acetone using a NIR-triple-wavelength fiber laser. *Optics Express* **2014,** *22*, 19337.
8. Y. Maréchal, The molecular structure of liquid water delivered by absorption spectroscopy in the whole IR region completed with thermodynamics data. *Journal of Molecular Structure* **2011,** *1004*, 146-155.
9. L. A. Toms and A. M. Toms, *Machinery oil analysis: Methods, automation & benefits: A guide for maintenance managers & supervisors*, 3 edn., Society of Tribologists and Lubrication Engineers, 2008.
10. M. J. Adams, M. J. Romeo and P. Rawson, FTIR analysis and monitoring of synthetic aviation engine oils. *Talanta* **2007,** *73*, 629-634.
11. A. G. Mignani, L. Ciaccheri, A. A. Mencaglia, G. Adriani, A. Paccagnini, M. Campatelli, H. Ottevaere and H. Thienpont, Proc. SPIE 9141, Optical Sensing and Detection III, 91411U, 2014.
12. A. G. Mignani, L. Ciaccheri, A. A. Mencaglia, G. Adriani, A. Paccagnini, M. Campatelli, H. Ottevaere and H. Thienpont, 2014 Fotonica AEIT Italian Conference on Photonics Technologies, 2014.
13. A. G. Mignani, L. Ciaccheri, N. Díaz-Herrera, A. A. Mencaglia, H. Ottevaere, H. Thienpont, S. Francalanci, A. Paccagnini and F. S. Pavone, Optical fiber spectroscopy for measuring quality indicators of lubricant oils. *Measurement Science and Technology* **2009,** *20*, 034011.
14. P. Peterka, I. Kasik, A. Dhar, B. Dussardier and W. Blanc, Theoretical modeling of fiber laser at 810 nm based on thulium-doped silica fibers with enhanced $^{3}H_{4}$ level lifetime. *Optics Express* **2011,** *19*, 2773.
15. J.-J. Max and C. Chapados, Infrared spectroscopy of acetone–water liquid mixtures. I. Factor analysis. *The Journal of Chemical Physics* **2003,** *119*, 5632-5643.
16. J.-J. Max and C. Chapados, Infrared spectroscopy of acetone–water liquid mixtures. II. Molecular model. *The Journal of Chemical Physics* **2004,** *120*, 6625-6641.
17. Y. Koga, F. Sebe, T. Minami, K. Otake, K.-i. Saitow and K. Nishikawa, Spectrum of excess partial molar absorptivity. I. Near infrared spectroscopic study of aqueous acetonitrile and acetone. *The Journal of Physical Chemistry B* **2009,** *113*, 11928-11935.
18. B. Czarnik-Matusewicz and S. Pilorz, Study of the temperature-dependent near-infrared spectra of water by two-dimensional correlation spectroscopy and principal components analysis. *Vibrational Spectroscopy* **2006,** *40*, 235-245.
19. B. Czarnik-Matusewicz, S. Pilorz and J. P. Hawranek, Temperature-dependent water structural transitions examined by near-IR and mid-IR spectra analyzed by multivariate curve resolution and two-dimensional correlation spectroscopy. *Analytica Chimica Acta* **2005,** *544*, 15-25.
20. A. Estrada-Baltazar, A. De León-Rodríguez, K. R. Hall, M. Ramos-Estrada and G. A. Iglesias-Silva, Experimental densities and excess volumes for binary mixtures containing propionic acid,

acetone, and water from 283.15 K to 323.15 K at atmospheric pressure. *Journal of Chemical & Engineering Data* **2003,** *48*, 1425-1431.
21. K. Noda, M. Ohashi and K. Ishida, Viscosities and densities at 298.15 K for mixtures of methanol, acetone, and water. *Journal of Chemical & Engineering Data* **1982,** *27*, 326-328.
22. L. Bøje and A. Hvidt, Densities of aqueous mixtures of non-electrolytes. *The Journal of Chemical Thermodynamics* **1971,** *3*, 663-673.
23. K. R. Murphy, C. A. Stedmon, D. Graeber and R. Bro, Fluorescence spectroscopy and multi-way techniques. PARAFAC. *Analytical Methods* **2013,** *5*, 6557-6566.
24. J. E. Bertie and Z. Lan, Infrared intensities of liquids XX: The intensity of the OH stretching band of liquid water revisited, and the best current values of the optical constants of H_2O(l) at 25°C between 15,000 and 1 cm^{-1}. *Applied Spectroscopy* **1996,** *50*, 1047-1057.
25. B. Dickens and S. H. Dickens, Estimation of concentration and bonding environment of water dissolved in common solvents using near infrared absorptivity. *Journal of Research of the National Institute of Standards and Technology* **1999,** *104*, 173.
26. H.-P. Loock and P. D. Wentzell, Detection limits of chemical sensors: Applications and misapplications. *Sensors and Actuators B: Chemical* **2012,** *173*, 157-163.

Chapter 9

Construction of a Hadamard Fluorescence Spectrometer

This chapter is based on the technique developed leading to a US and Canadian patent application No. 15/216,296 filed 21 July 2016, with the inventors N. L. P. Andrews, O. Reich, and H.-P. Loock. In addition, the technique in this chapter forms the basis of the paper entitled "Hadamard fluorescence excitation emission matrix spectrometer", N. L. P. Andrews, A. M. Rangaswamy, T. G. Ferguson, A. R. Bernicky, N. Henning, O. Reich, A. Dudelzak, and H.-P. Loock, which is in preparation. Under direct supervision, Alana Rangaswamy, Adam Bernicky, and Niklas Henning helped with alignment and collection of data. Travis Ferguson is continuing the project and is currently improving the spectrometer. Alex Dudelzak works at GasTOPS and has provided useful consultation towards the project. Peter Loock and Oli Reich both invented the concept of the project to utilise wave division multiplexing to enhance the rate at which fluorescence excitation emission matrix spectra were obtained.

9.1 Introduction

Excitation emission matrix (EEM) spectroscopy has been shown as an effective method for determining the quality of lubrication oil and scintillator solutions in Chapter 6 and Chapter 7. However, a major obstacle for EEM spectroscopy as a tool for online real-time analysis, is that it can take ≥30 mins to acquire a single spectrum. This prevents it for being used to monitor fast reactions and as a real-time "remaining useful lifetime" monitor for lubricants and other machinery liquids that rely on stabilisation by antioxidants.[1] Many other processes exist in which fluorescence of multiple compounds changes over the course of seconds or minutes, due to oxidation, quenching, reabsorption, fluorescence transfer or other physical or chemical modification. Examples are oxidation of foodstuff such as fruit juices and wine,[2-4] dissolution of fluorescing compounds such as dissolved organic matter in environmental water samples,[5-7] and the fluorescence of oxygenated and deoxygenated blood.[8-10] In addition, commercial instruments such as the

fluorescence EEM spectrometer used in this study (*Varian* Cary Eclipse) are bulky and thus not suitable for use in the field. To realise the fluorescence EEM technique for commercial applications as a real-time sensor, EEM spectra must be collected in a fraction of the time — by a much more compact and ideally, less expensive instrument.

In this chapter we introduce a new technique that may be compared to wave division multiplexing (WDM) through modulation of the excitation light — a technique commonly used in the telecom industry to increase the density of information while retaining low error rates. Compared to sequential transmission, in WDM a signal generates a higher signal-to-noise ratio (SNR) leading to faster transmission rates.[11, 12] Transferred to fluorescence spectroscopy we use the Hadamard transform (HT), which may be called a binary Fourier transform (FT), to give each excitation wavelength a "Hadamard barcode" (on/off) frequency. Several of these wavelengths are then allowed to excite the sample simultaneously. The temporally encoded excitation light produces a correspondingly encoded fluorescence signal that then is demodulated using the respective inverse Hadamard transform (iHT) to produce the EEM spectrum in a matter of seconds and without loss of spectral resolution. Although concept of using HTs or WDM to enhance the SNR and allow for faster spectral acquisition is not new, applying it to second order techniques such as fluorescence EEM has not been done previously and amplifies the multiplex advantages making it an innovative area for research.

This chapter, details the theoretical foundation of Hadamard transform fluorescence EEM (HT-FEEM) spectroscopy, the design and construction of the HT fluorescence EEM spectrometer and then evaluates its performance in comparison with the commercial *Varian* Cary Eclipse spectrometer. The HT fluorescence EEM spectrometer is controlled using a custom-designed graphical user interface (GUI) using MATLAB. This code connects the devices, collects spectra and demodulates the encoded fluorescence automatically and it is briefly described herein.

9.2 Wavelength division multiplexing

9.2.1 Advantages over dispersive techniques

Obtaining EEM spectra from the commercial *Varian* Cary Eclipse spectrometer, a dispersive instrument, is both slow and wasteful of light. The acquisition of EEM spectra can be made more rapidly by WDM — a method that generates a higher SNR leading to faster acquisition rates.[11-14] As in the related FT method (e.g. infrared spectroscopy, nuclear magnetic resonance (NMR)) HT-spectroscopy has the multiplex or Fellgett advantage, meaning that at each point in time the collected data contain information from all the wavelengths of the input light, as opposed to dispersive techniques which sample each wavelength only once. This generates an improved SNR of the multiplexed spectrum compared to the dispersed spectrum of the order of the square root of the number of sample points comprising the spectrum.[15, 16] In addition, if all acquired data points contain information of all (excitation) wavelengths, HT spectroscopy is considerably more robust against temporal fluctuations.[17, 18] A second, related advantage is the "throughput advantage" (Jacquinot advantage): since no slits are used when multiplexing the excitation wavelengths, more energy reaches the detector producing a larger SNR.[19, 20] Third, is the wavelength accuracy or Connes advantage, which arises because the multiplexed instrument can be calibrated very accurately using a known laser frequency.[11, 13] Using these advantages, techniques using WDM such as FT and HT-spectroscopies are able to acquire high quality spectra in a fraction of the time as opposed to dispersive instruments.

9.2.2 Fourier transforms

9.2.2.1 Theory

The Fourier transform (FT) is a mathematical formula that decomposes a function of time, t, into its comprised sinusoidal frequencies, ω. Because of this, a FT allows measurements in the time domain to be interconverted with the frequency domain:[21-23]

$$F(\omega) = \frac{1}{\sqrt{2\pi}} \int_{-\infty}^{\infty} f(t) e^{-i\omega t}\, dt$$
$$f(t) = \frac{1}{\sqrt{2\pi}} \int_{-\infty}^{\infty} F(\omega) e^{i\omega t}\, d\omega \quad . \qquad \textbf{(9.1)}$$

FTs are especially useful in spectroscopy, as signals measured in the time domain can be converted into a frequency spectrum for ease of analysis. Every signal is represented as a combination of sine waves with different frequency, amplitude and phase. For example, a box function can be described by a weighted sum of the odd harmonics of a fundamental sine wave. A FT of a signal serves to decompose the signal into its constituent sine waves. (**Figure 9.1**)

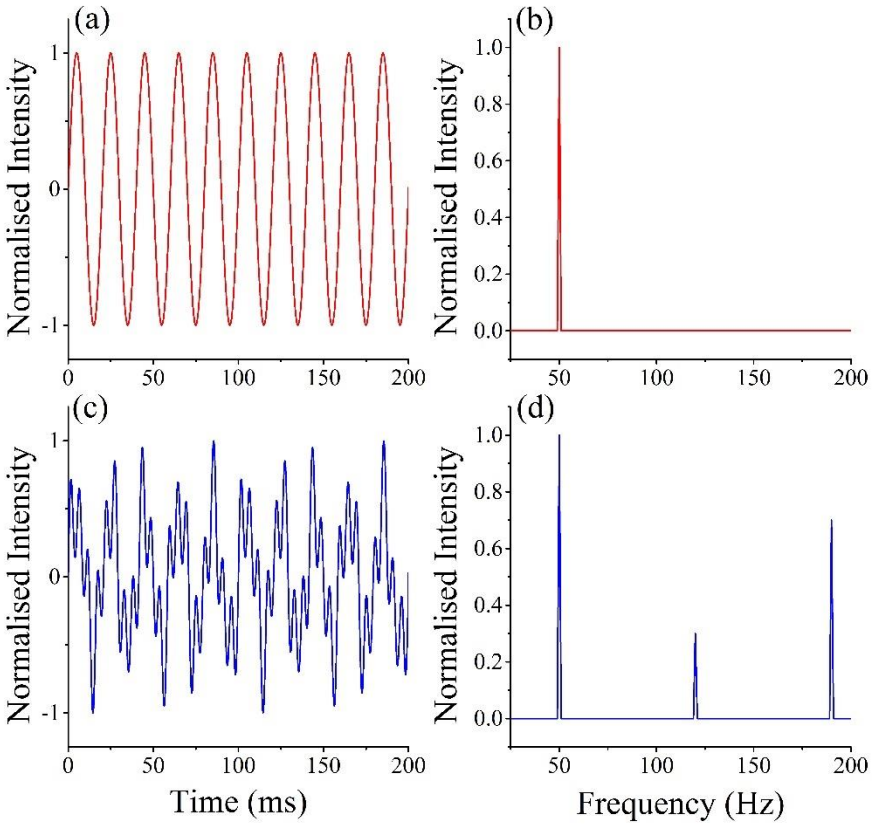

Figure 9.1: Fourier transforms of different sine waves. **(a)** and **(b)** show the time signal and FT frequency spectrum, respectively of a single 50 Hz signal. **(c)** and **(d)** show the time signal and FT frequency spectrum of a beating signal comprised of multiple frequencies at 50, 120 and 190 Hz.

By our above definition, FT related techniques are multiplex approaches to spectroscopy, as each measurement in the time (or spatial) domain will contain information on all wavelengths in the spectrum. Therefore, FT spectroscopic techniques have all the advantages of multiplexing, such as enhanced SNR as discussed in section 9.2.1.[24] The apparent advantages of FT techniques have given rise to a multitude of applications (Chapter 2) and spectral information is collected over a given frequency range simultaneously.[25, 26]

At radio frequencies, time-domain recordings of FT signals is practical and have been widely used in NMR and magnetic resonance imaging (MRI).[27-29] The FT is able to extract the frequency domain spectrum from the measured time domain free induction decay of the excited nuclei. However, at the high frequencies of visible and IR light it is not practical to record spectroscopic information in the time domain, since one requires an ultrafast laser and/or a very rapid detector to obtain an accurate and resolvable signal, although these experiments have been performed.[30, 31] To overcome this challenge, the signal can be measured in the distance (instead of time) domain by measuring an interferogram of two or more standing waves. These interference techniques have been developed primarily to utilise the multiplexing advantage for IR and UV-Vis applications.[18, 32, 33]

9.2.2.2 Fourier transform fluorescence EEM spectroscopy

The multiplex advantage has previously been applied for collection of EEM spectra using FTs, where a full EEM spectrum (excitation range = 425-550 nm and emission range = 580-750 nm) can be obtained within 40 s with a resolution of 82 cm^{-1}.[34] The FT EEM spectrometer is fabricated using two Michelson interferometers. The first interferometer modulates the excitation light which is coupled to a sample cuvette. The emission light is then coupled to the second Michelson interferometer and detected using a PMT. The adjustable mirror positions in both interferometers are monitored using separate lasers — a HeNe for the excitation and a green diode laser for the emission. Two additional PMT detectors were further used to determine when the differential delay of both interferometers were zero. The FT EEM spectrometer was

used to detect fluorescent dyes such as rhodamine 6G in DMSO in 40 s.[34] The same group then went onto detecting Förster resonance energy transfer (FRET) using a similar setup.[35] However, to enhance the rate of acquisition so that the FRET process can be measured, the system was modified to only include one double pass interferometer. Although this made the spectral acquisition faster (~1.5 ms), it only was able to collect the excitation and emission spectra and the diagonal projection and not a true EEM spectrum.

9.2.3 Hadamard transforms

9.2.3.1 Theory

The HT is a binary equivalent of the analogue FT. Instead of using sine functions as in FTs, the HT uses a set of Walsh functions, which are binary with values 1 and -1.[36] The Walsh functions are mutually orthogonal and the Hadamard matrix is constructed as a square symmetric matrix from rows and columns of Walsh functions. The HT involves multiplying a signal, **S**, (dimension of 2^m) with the Hadamard matrix, $\mathbf{H}_m$, where m is the number of bits,

$$\boldsymbol{\eta} = \mathbf{H} \times \mathbf{S}, \tag{9.2}$$

where $\boldsymbol{\eta}$ is the series of data that is encoded. The signal is obtained from the encoded data by simply multiplying by the inverse matrix of the Hadamard matrix, $\mathbf{H}^{-1}$,

$$\mathbf{S} = \mathbf{H}^{-1} \times \boldsymbol{\eta}. \tag{9.3}$$

The elements of the Hadamard matrix may be obtained from,[37-39]

$$(\mathbf{H}_m)_{i,j} = \frac{1}{2^{m/2}} (-1)^{i \cdot j}, \tag{9.4}$$

where i and j represent the indices within the Hadamard matrix and $i \cdot j$ represents the binary dot product of i and j. For example, a 2-bit Hadamard matrix, $\mathbf{H}_2$, is:

$$\mathbf{H}_2 = \frac{1}{2} \begin{pmatrix} 1 & 1 & 1 & 1 \\ 1 & -1 & 1 & -1 \\ 1 & 1 & -1 & -1 \\ 1 & -1 & -1 & 1 \end{pmatrix}. \tag{9.5}$$

The orthogonality of the Walsh functions implies that $\mathbf{H}^2 = \boldsymbol{I}$, where $\boldsymbol{I}$ is the identity matrix, and ideally the noise-free intensities (or spectra) recorded at differing wavelengths (or times) will not affect one another; similar to the basis functions forming a Fourier Series.[39, 40]

In previous work, HT spectroscopic techniques are typically based on a Hadamard encoding mask (**Figure 9.2**). The mask is generated by each row of the Hadamard matrix. Light is dispersed onto the mask and the wavelengths that pass through the mask are detected. A stepper motor may be used to step between each subsequent mask. The signal from each mask is recorded and the resultant array is decoded using the inverse of the Hadamard matrix.[14, 41, 42] Decker used this method to obtain the spectrum of the light source.[42] Using the same stepping setup, HT spectroscopy has been used to measure the absorption spectrum of hexane in the near-infrared (NIR),[43] and the atomic fluorescence spectrum of Zn and Cd in the UV.[44] In addition to the horizontal stepping motor, a rotating wheel has been used to apply the Hadamard mask. With this setup, absorption spectra of pyrene derivatives have been collected in the UV and used to determine their concentrations.[45]

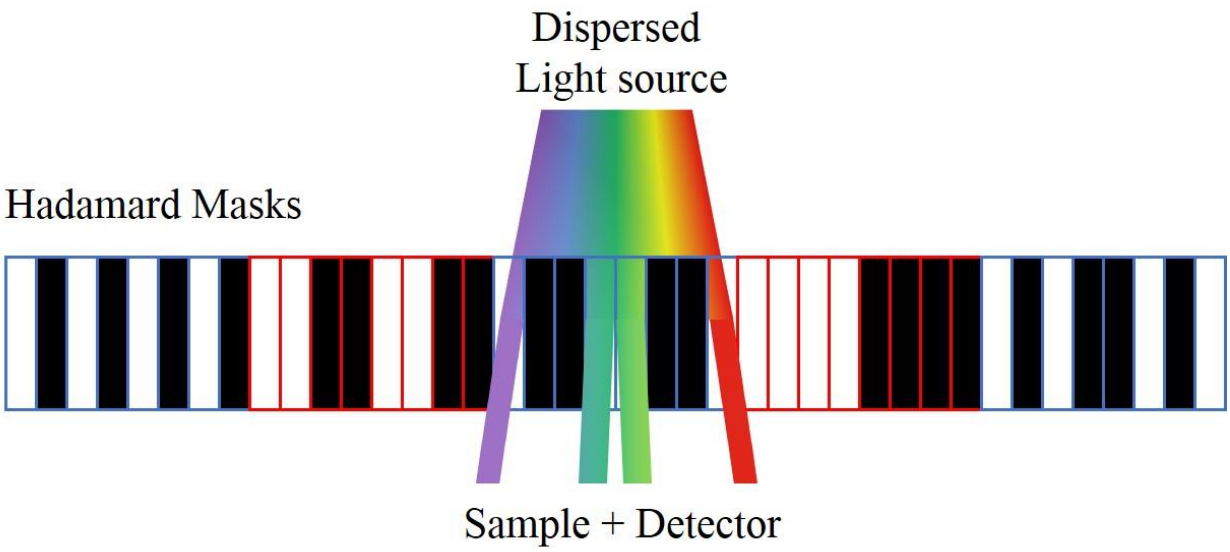

Figure 9.2: Modulation of light using a Hadamard encoding mask. The mask is of order m = 3 (8-masks) and the alternating blue and red borders represent each mask. Once the spectrum of each mask is obtained a motor moves the mask such that the next mask lines up with the dispersed light. In this example the white

sections of the mask allow the loght to pass and be used to excite the sample, whereas the black sections block the light. By running through each image in turn, this will modulate each excitation wavelength with a binary barcode.

9.2.3.2 Digital micromirror array

Another method of modulating light with a Hadamard mask is to use a digital micromirror array (DMA) — also known as a digital micromirror device (DMD). Developed in 1987 by Hornbeck at *Texas Instruments*, a DMA is a rectangular array of hinge-mounted microscopic mirrors that are able to be individually switched to an "on" or "off" state (**Figure 9.3**).[46, 47] The DMA is fabricated over a complementary metal oxide semiconductor (CMOS) memory layer. For each mirror, a voltage can be implanted into the memory layer. After a trigger signal, the mirror is then free to rotate through electrostatic attraction between the mirror and memory cell.[47]

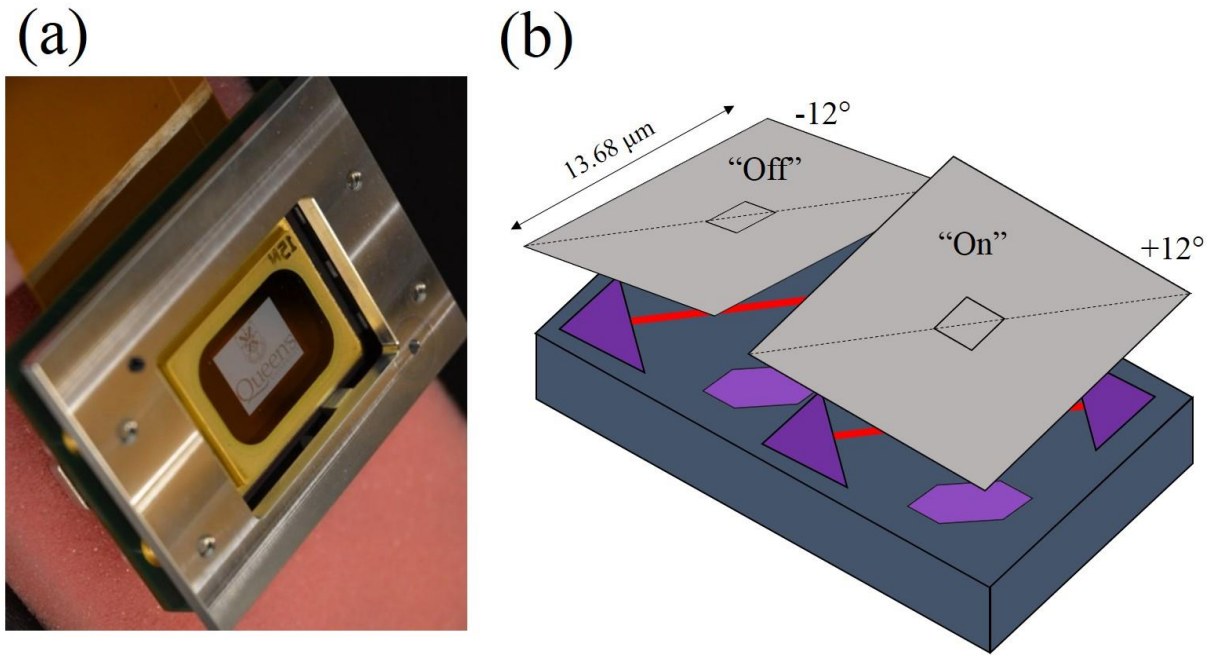

Figure 9.3: Digital micromirror array used to modulate the light. **(a)** a photo of the DMA showing the queen's university logo. **(b)** Schematic of the DMA showing both the "on" and "off" states at +12° and -12°, respectively.

DMAs are widely commercialised for digital light processing, for high resolution and high brightness applications and have also been utilised in spectrometers. DMAs have been used in conjunction with photomultiplier tubes (PMT)s to replace charged coupled device (CCD) array detectors,[48, 49] as PMTs are much more sensitive, cheaper and faster at data collection. Wagner *et al.* dispersed a white light source onto the DMA, where the DMA was only a 1D array of mirrors so each column of mirrors represented a different wavelength.[48] Each mirror was switched so that only the light from one column and hence one wavelength at a time was detected using the PMT. This is in comparison to the CCD that detects each wavelength that is dispersed along the array. DMAs have also been used to make FTIR spectrometers more compact by replacing the traditional moving mirror arrangement.[50]

DMAs have also been exploited to make use of the multiplex advantage. Spudich *et al.* modulated columns of the DMA with separate square wave frequencies;[51] an inverse FT was used to demodulate the signal and obtain the resultant spectra. Although the instrument was not tested using a real sample, they showed the potential for DMAs as a tool for multiplexing. Instead of simply scanning along the columns of mirrors for detection of light using a PMT, each column (C1-C8 in **Figure 9.4**) can be separately modulated on the DMA using a Hadamard mask. The Hadamard mask is generated as the mirrors flip to the "on" and "off" positions (**Figure 9.4**). The "on" light is collected and detected whereas the "off" light is blocked and discarded. The group of Fateley *et al.* at Kansas State University have published a number of articles using a DMA to multiplex signals with a Hadamard mask.[52-57] They disperse and focus light onto the DMA so that each column represents a different wavelength. The DMA was then programmed to either conventional raster scan (CRS) through the spectrum or to use a Hadamard mask and demodulate the resultant signal. The CRS and HT methods where compared and the HT method showed an improved SNR of ≈13 for four peaks from 1000-1600 nm when using a Hg-Ar lamp. They then used the same setup for Raman spectroscopy and obtained spectra of naphthalene.[56]

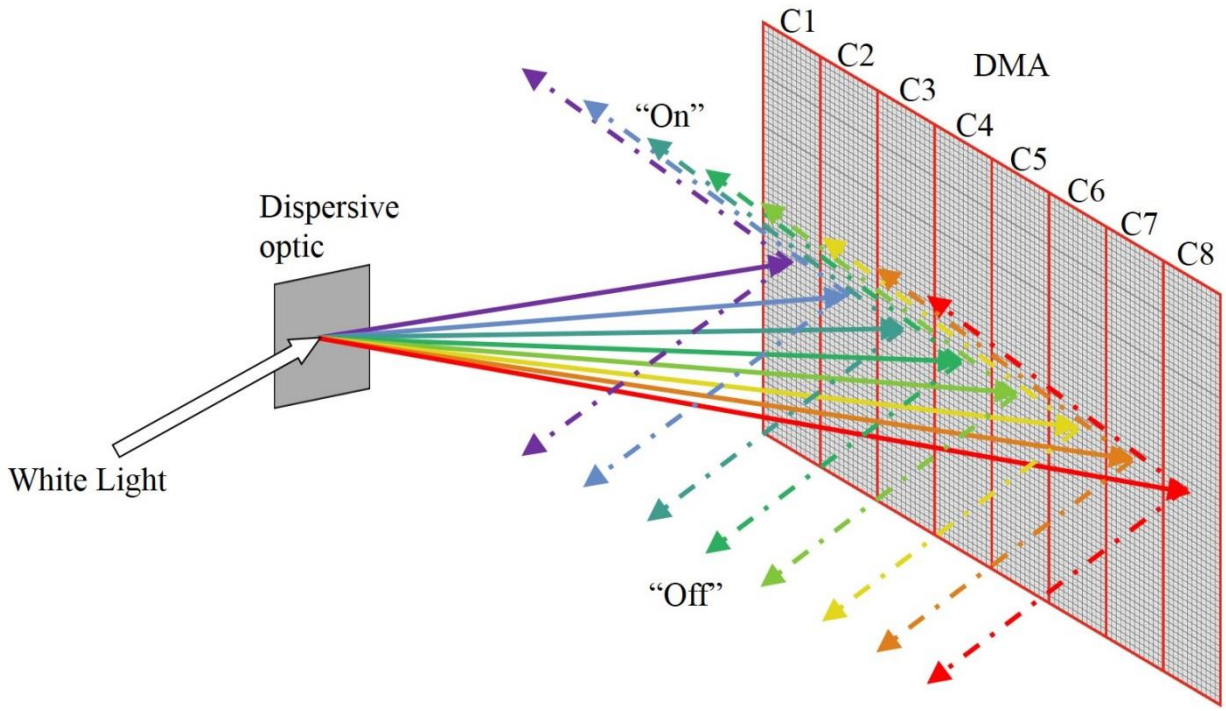

Figure 9.4: Schematic of a DMA being used to modulate white light. The white light is dispersed onto the DMA so that each mirror column represents a separate wavelength. Here, there are 8 columns labelled C1 – C8 and represent purple – red light respectively. Each column of mirrors is given a distinct Hadamard pattern and by flipping the mirrors "on" and "off" in the Hadamard sequence so each wavelength of light is separately encoded. Note the DMA is not limited for use with visible light and can be applied in the UV or IR depending on the reflectivity of the mirrors.

HT Raman imaging was also developed using the DMA. The DMA modulates the light along the columns as before (**Figure 9.4**), but now the additional dimension along the rows, were used as a spatial component. The second spatial dimension was obtained by translating the sample using a micro-meter translation stage.[53, 55, 56, 58] Additionally, the DMA system has been used by a number of researchers for HT hyperspectral imaging.[59-66]

9.2.3.3 Applications of Hadamard transforms

HT techniques are not limited to being used for spectral resolution as in absorption spectroscopy. HTs have also seen applications in time-of-flight mass spectrometry and chromatography techniques such as gas

chromatography / mass spectrometry (GC/MS) and liquid chromatography / mass spectrometry (LC/MS).[67-70] Here the injection of the analyte is modulated using the Hadamard sequence.[71, 72] The encoded chromatogram is then decoded by multiplying it with the inverse of the Hadamard matrix. This resulted in an enhanced SNR for example in the detection of drugs in urine — 3,4-Methylenedioxy-N-methylamphetamine (MDMA / ecstasy) with GC/MS and N,N-dimethyltryptamine (DMT) with LC/MS.[69]

Additionally, HTs have also been used for optical fluorescence microscopy.[73-75] A Hadamard mask, similar to one shown in **Figure 9.2**, was used to spatially encode the light in the horizontal dimension. The vertical dimension information was obtained by using the dimension of the CCD array used to detect the light. The spectral resolution was determined using a monochromator. It was reported that the Hadamard system improved the SNR such that images of weak fluorescence signals can be obtained.

Furthermore, the HT multiplex advantage has been utilised for ion mobility spectroscopy.[76, 77] The ion gate is controlled using the Hadamard sequence with a 50% duty cycle. The mobility spectrum is obtained from the multiplexed ion signal through multiplication of the inverse of the Hadamard matrix. Using the multiplex advantage of the HT, demonstrated a SNR improvement by a factor of 2-10 for drugs such as amphetamine.

HT techniques have also been applied to NMR and MRI.[39, 78-81] Selective irradiation is achieved by a repetitive Hadamard sequence of radiofrequency pulses. The NMR signal is acquired for all frequency channels and decoded with an inverse Hadamard transformation. This direct irradiation method is useful for monitoring a chosen component in a complex mixture as is the case when studying human metabolites *in vitro*. Two dimensional NMR spectroscopy has also been achieved through Hadamard multiplexing over one frequency dimension while using Fourier transformation in the second detection frequency dimension.[78]

9.2.4 Hadamard transform fluorescence EEM spectroscopy

9.2.4.1 Introduction

The slightly faster acquisition rates due to the multiplex advantages with HT spectroscopy became dwarfed with the rise of dispersive array detectors such as the CCD in the late 80's and early 90's.[82, 83] This likely reduced the interest in using and developing Hadamard spectrometers for spectral multiplexing in recent years.[84-86]

With second or higher order techniques such as fluorescence EEM spectroscopy — or two-dimensional NMR [81] — the multiplex advantages of Hadamard transforms become apparent. This is due to the increased acquisition time and SNR with the removal of a scanning slit. Fluorescence EEM spectrometers generally involve the use of two monochromators in a step by step collection of excitation and emission pairs (**Figure 9.5**).[87] This is both wasteful of light and very time consuming, which prevents the applicability of EEM to be used for real-time measurements. Additionally, one can imagine replacing one of the monochromator slits with a dispersive array detector. Although this will enhance the rate of acquisition, it still needs to scan along one dimension and thus using multiplexing techniques for fluorescence EEM becomes apparent.

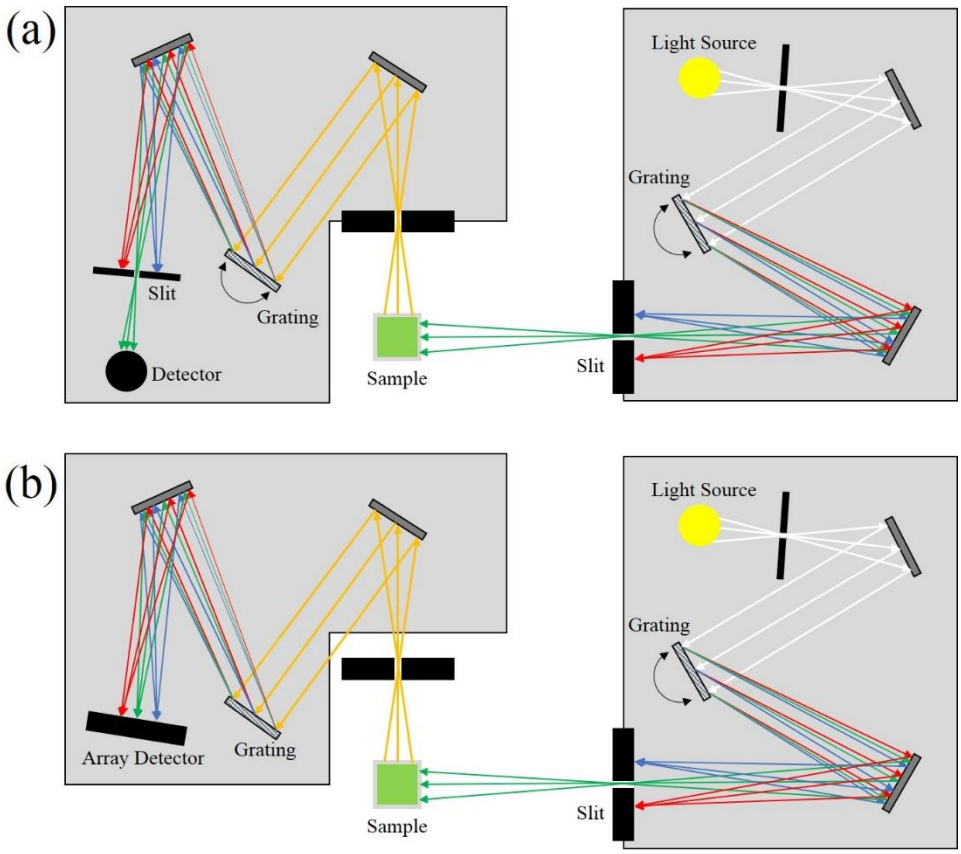

Figure 9.5: Schematics of typical fluorescence spectrometers. **(a)** represents a fluorescence spectrometer with two stepping monochromators used for excitation and emission wavelengths as with the *Varian* Cary Eclipse spectrometer. **(b)** represents a fluorescence spectrometer with a stationary emission monochromator used with an array detector as with an *Ocean Optics* USB4000 spectrometer.

Although there are some disagreements in the literature for which is the better method, HT and FT spectroscopy yield results that are nearly identical.[88, 89] Therefore there is no inherent advantage to using either technique. However, it can be envisioned that the optical design to create a Hadamard mask is much easier than modulating the light with sine waves. In addition, to modulate the light, our technique makes use of the DMA. The DMA is an array of mirrors that can be separately switched to the "on" or "off" position.[46, 47] This binary mirror switching lends itself to the ease of using the Hadamard system, and this is why the HT was chosen as the method for this technique.

9.2.4.2 Hadamard fluorescence theory

In our Hadamard fluorescence EEM spectrometer, a binary HT is used corresponding to the "on" and "off" states of the mirrors in a DMA. To do this, the values of -1 in the Hadamard matrix (equation (9.5)) are replaced with zeros,

$$\mathbf{H}_2 = \frac{1}{2}\begin{pmatrix} 1 & 1 & 1 & 1 \\ 1 & 0 & 1 & 0 \\ 1 & 1 & 0 & 0 \\ 1 & 0 & 0 & 1 \end{pmatrix}. \tag{9.6}$$

Computers are able to decode HT encoded signals much faster than their FT equivalents and decoding can frequently be done in real-time.[23, 42]

For example, to encode the emission spectrum of a light source — here represented as rows in a matrix $[\mathbf{S}]$ where all rows are identical — each wavelength is modulated separately by an individual row of the Hadamard matrix. The resulting sequence of spectra is represented by the Hadamard product giving matrix $[\mathbf{HS}]$ in which each row represents a spectrum,

$$[\mathbf{H}] \circ [\mathbf{S}] = [\mathbf{HS}]$$

$$[\mathbf{H}_{ij}] \circ \begin{bmatrix} S_{11} & S_{12} & \cdots & S_{1j} \\ \vdots & & & \vdots \\ S_{j1} & S_{j2} & \cdots & S_{jj} \end{bmatrix} = \begin{bmatrix} H_{11}S_{11} & H_{12}S_{12} & \cdots & H_{1j}S_{1j} \\ \vdots & & & \vdots \\ H_{i1}S_{j1} & S_{j2} & \cdots & H_{ij}S_{jj} \end{bmatrix}. \tag{9.7}$$

If only the integrated intensity of each spectrum is measured, then the intensity for each mirror configuration can be represented by the column vector,

$$[\mathbf{E}] = \begin{bmatrix} \sum_{k=1}^{j} H_{1k}S_k \\ \vdots \\ \sum_{k=1}^{j} H_{ik}S_k \end{bmatrix} = \mathbf{H}_{ij} \times \begin{bmatrix} S_1 \\ \vdots \\ S_j \end{bmatrix}. \tag{9.8}$$

The spectrum of the light source, $\begin{pmatrix} S_1 & \cdots & S_j \end{pmatrix}$, can be obtained by multiplying $[\mathbf{E}]$ with the inverse of the binary Hadamard matrix,

$$\begin{bmatrix} S_1 \\ \vdots \\ S_j \end{bmatrix} = \mathbf{H}_{ij}^{-1} \times \begin{bmatrix} \sum_{k=1}^{j} H_{1k} S_k \\ \vdots \\ \sum_{k=1}^{j} H_{ik} S_k \end{bmatrix}. \tag{9.9}$$

When the encoded excitation light, $[\mathbf{HS}]$, is used to excite fluorescence in a sample, the resulting fluorescence matrix, $[\mathbf{F}]$, is given by,

$$\begin{bmatrix} H_{11}S_{11} & H_{12}S_{12} & \cdots & H_{1j}S_{1j} \\ \vdots & & & \vdots \\ H_{i1}S_{j1} & S_{j2} & \cdots & H_{ij}S_{jj} \end{bmatrix} \times \mathbf{M}_{ij} = \begin{bmatrix} f_{11} & f_{12} & \cdots & f_{1j} \\ \vdots & & & \vdots \\ f_{j1} & f_{j2} & \cdots & f_{jj} \end{bmatrix}, \tag{9.10}$$

$$[\mathbf{HS}] \times [\mathbf{M}] = [\mathbf{F}]$$

where $\mathbf{M}_{ij}$ is the fluorescence intensity at the wavelength *j* with normalised excitation at wavelength *i*, i.e. the desired EEM spectrum. Each row of matrix $[\mathbf{F}]$, represents the fluorescence spectrum for a given mirror configuration. To demodulate $[\mathbf{F}]$ into the EEM spectrum, $[\mathbf{M}]^{\mathrm{T}}$, the transpose of $[\mathbf{F}]$, i.e. $[\mathbf{F}]^{\mathrm{T}}$ is multiplied with the transpose inverse of the source-weighted Hadamard matrix, $\left[[\mathbf{HS}]^{-1}\right]^{\mathrm{T}}$,

$$[\mathbf{M}]^{\mathrm{T}} = [\mathbf{F}]\left[[\mathbf{HS}]^{-1}\right]^{\mathbf{T}}. \tag{9.11}$$

A program was written using Matlab to generate Hadamard matrices using equation (9.4), and to decode the fluorescence signal $[\mathbf{F}]$ thereby generating the EEM spectrum, $[\mathbf{M}]$, according to equation (9.11).

9.3 Experimental

9.3.1 Modulation using digital micromirror array

HTs are binary and therefore binary switches are required to modulate the excitation light. DMAs are one such system and consist of an array of mirrors (in our case 1024 × 768 mirrors) that can be individually switched to an "on" or "off" state.[46] White light is dispersed along the DMA so that each mirror column represents a separate wavelength of light (**Figure 9.4**). Each excitation wavelength is then independently modulated with its own distinct Hadamard pattern by flipping the mirrors of the DMA. Each row in the binary Hadamard matrix of equation (9.6) is used to generate a separate Walsh mask, where the value in each column of the Hadamard matrix is applied to all rows, i.e. to 768 mirrors on our DMA (**Figure 9.6**). Each mask is played in sequence by loading the corresponding "image" into the memory of the DMA. As a consequence, at each instant in time the wavelengths are modulated by the binary Walsh function, and each of the wavelengths are modulated in the time domain by the same Walsh function.

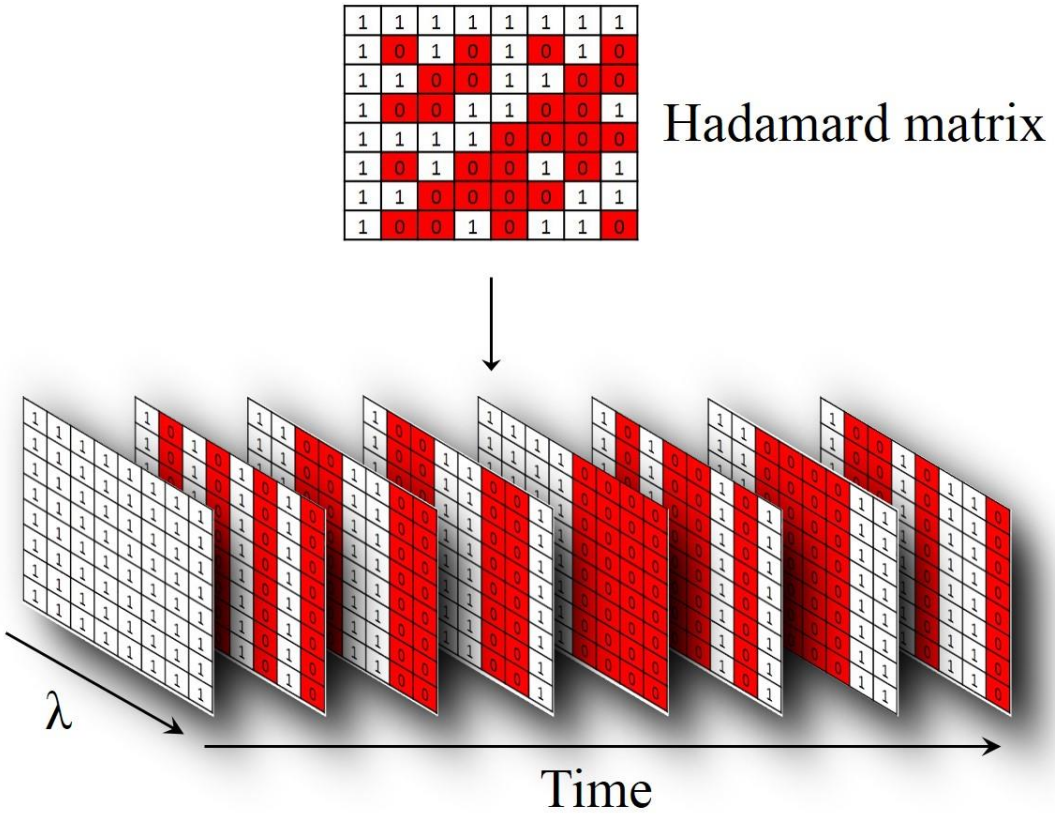

Figure 9.6: Method of the Hadamard mask generation. Each row in this 8×8 Hadamard matrix (m = 3) generates a mask that is displayed onto the DMA as an image. The columns are distributed along the 1024 pixels, while all the rows have the same value. As the columns on the DMA represent a different wavelength of light, only the "on" (1) values will be detected for each image, creating a mask.

Figure 9.7 shows how the emission spectrum of a light source may be encoded and subsequently decoded using an 8×8 Hadamard mask. The emission spectrum is projected onto the DMA which displays all 8 masks sequentially. Since only those wavelengths are collected that are reflected by mirrors in the "on" state, the emission spectrum is modified. Its total (wavelength-integrated) intensity may be collected with a broadband photodetector. We create the vector **E** (see equation (9.8)) by integrating each of the eight recorded spectra where each integrated intensity corresponds to one entry. The emission spectrum of the light source, **S**, is obtained by multiplying **E** with the inverse of the loading matrix, **H** (equation (9.9)).

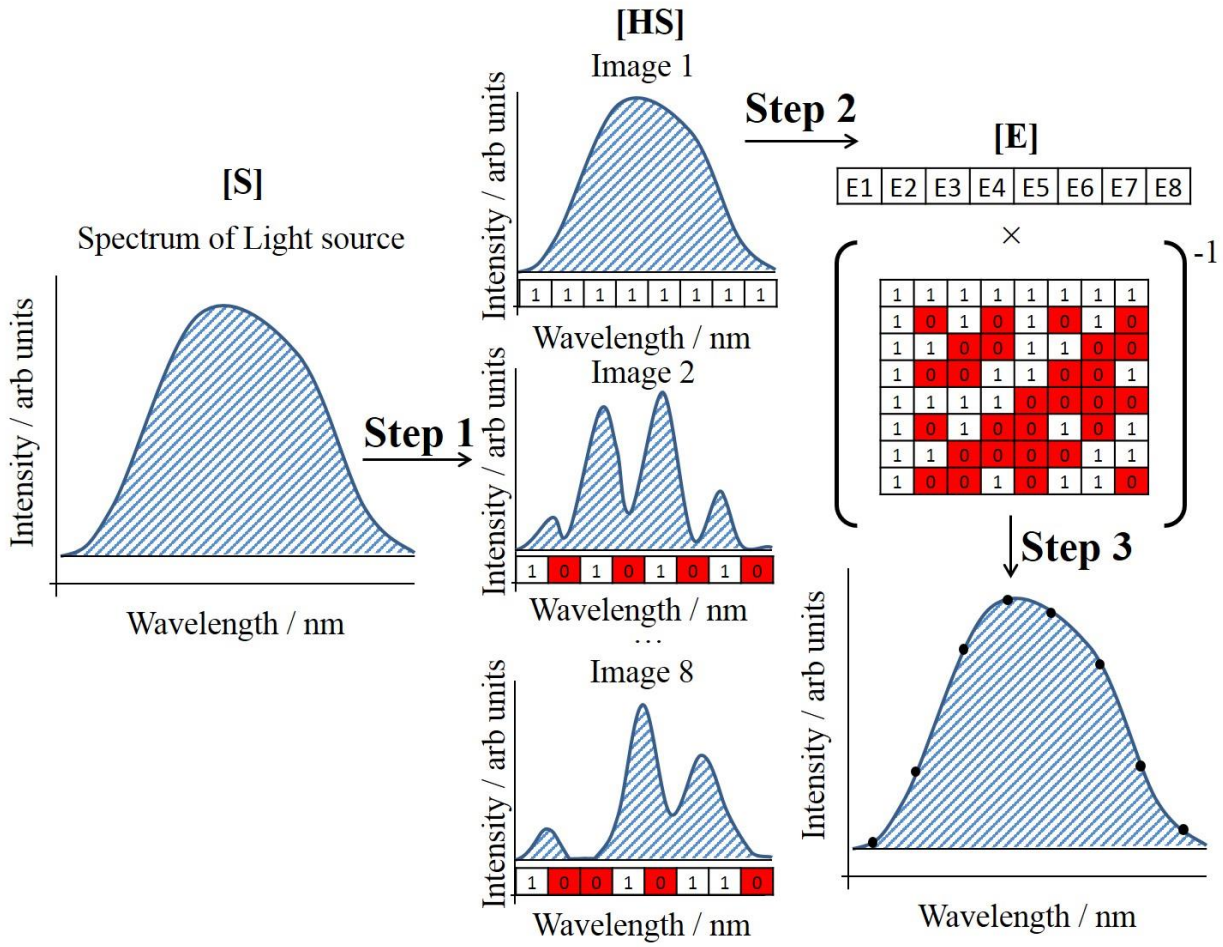

Figure 9.7: Modulation and demodulation of the light source. Step 1: Modulate the light source with each of the Hadamard masks and collect the resulting spectrum. Step 2: Integrate the spectrum obtained for each mask and create a 1D array where the index of the array matches the image / spectrum number. Step 3: Recover the source spectrum by multiplication of the array with the inverse of the loading matrix.

Figure 9.8 shows how an EEM spectrum, $[\mathbf{M}]$, may be produced using the Hadamard transform technique. Each Hadamard mask displayed by the DMA generates an excitation spectrum, $[\mathbf{HS}]$, which in turn produces a characteristic fluorescence spectrum after interaction with a fluorescing sample. After having displayed all Hadamard masks on the DMA the resulting 3D array of spectral data, $[\mathbf{F}]$, contains the fluorescence intensities as a function of Hadamard mask index and emission wavelength. To demodulate

$[\mathbf{F}]$ into an EEM spectrum, $[\mathbf{M}]$ the Hadamard index is converted to excitation wavelength through multiplication of the transpose of $[\mathbf{F}]$, with the transpose inverse of the weighted Hadamard matrix, $\left[[\mathbf{HS}]^{-1}\right]^{T}$ (equation (9.11)). This operation may be executed using MATLAB or other suitable software so that the EEM can be generated from the modulated fluorescence rapidly, e.g., typically within 1.5 s or less for a 6-bit matrix and non-optimised code.

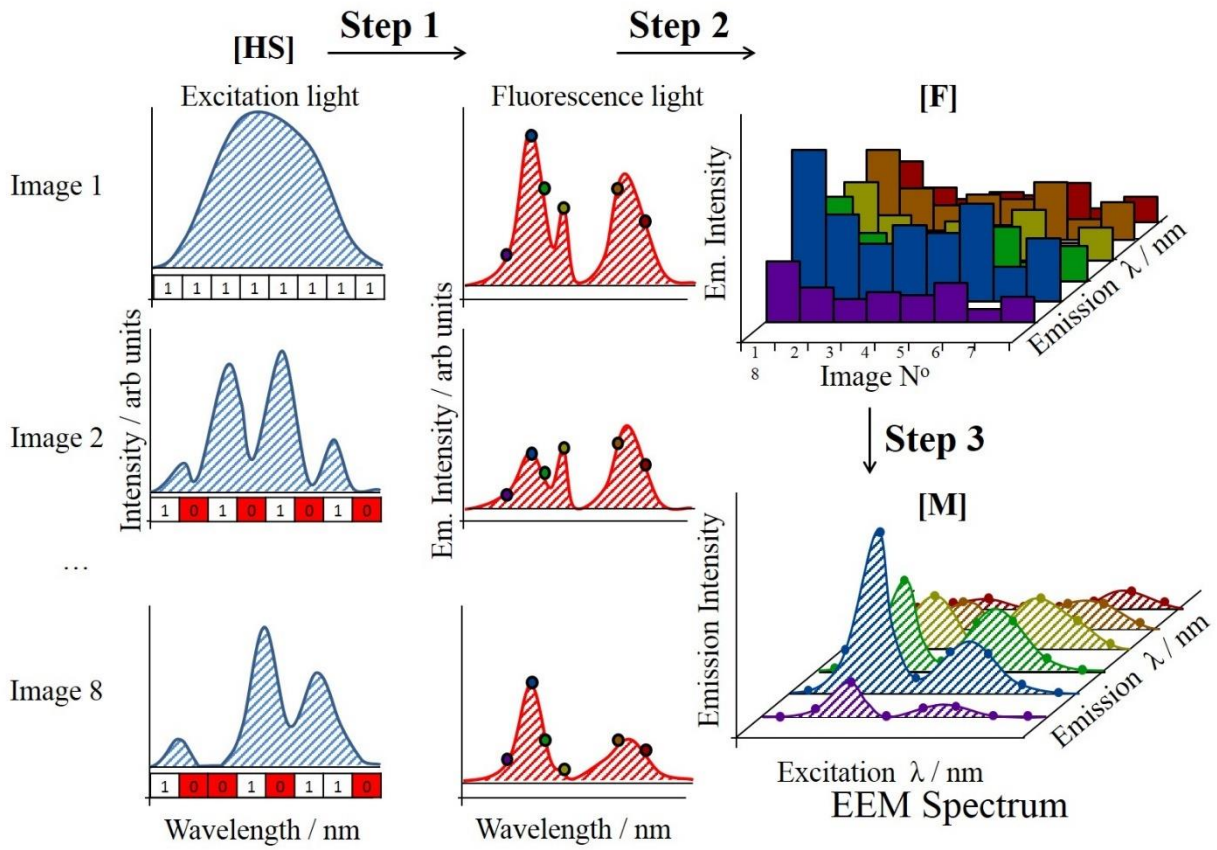

Figure 9.8: The generation of an EEM spectrum through Hadamard modulation. Step 1: The sequence of modulated excitation light spectra which is generated as in **Figure 9.7** by modulation of a broad band source with a DMA, is used to excite a luminescent (fluorescing or scattering sample) which generates a corresponding emission spectrum. Step 2: the intensities at each of the 2^m emission spectra are placed into the 3D data set. Step 3: The EEM spectrum, $[\mathbf{M}]$, is generated by converting the image number into

excitation wavelength, i.e. by multiplying the transpose of the Hadamard encoded 3D data set, $\left[\mathbf{F}\right]$, by the inverse of the binary Hadamard matrix (**Figure 9.6**) that is weighted by the excitation source, $\left[\mathbf{HS}\right]$.

9.3.2 Optical layout

An overall schematic drawing of the HT-EEM spectrometer is shown in **Figure 9.9**. White light from a light emitting diode (*Cree* CXB1830, ~3000 lm, Ø14 mm, bandwidth ≈ 400-800 nm (**Figure 9.10(b)**)) [90] is coupled into a custom-built fibre bundle comprised of 11 multimode fibres (core Ø400 µm, cladding Ø440 µm) (**Figure 9.10(d)**). The fibre bundle guides the light to the dispersive element, which is based on a miniature spectrometer from which the detector array has been removed (*Ocean Optics*, USBCUT) (**Figure 9.10(a)**). At the USBCUT the fibres from the LED fibre bundle are arranged in a row to allow a large amount of light to enter the dispersive element while maintaining a good spectral resolution. The white light is dispersed using the grating and focused onto the DMA (**Figure 9.10(c)**). A translation stage was added to the dispersion unit to ensure that the dispersed light is focused on the DMA to achieve maximal spectral resolution. The DMA modulates the light (**Figure 9.4**) so that each column section and hence each wavelength is associated with a different Walsh function. This modulated light is collimated and refocused using two off-axis parabolic mirrors and coupled into the excitation fibre of a bifurcated fibre probe (**Figure 9.11**) — similar to the one described in Chapter 5, but with 22 excitation and 15 collection fibres.[1] The pattern of the excitation and collection fibres for the probe end in **Figure 9.11(c)** was selected to maximise the amount of excitation fibres surrounding each collection fibre and thus the acceptance cone overlap.. The light is directed into the sample, which then fluoresces and scatters light. The consequent encoded emission is captured by the collection fibres and spectrally dispersed and detected using the *Ocean Optics* USB4000 spectrometer. The DMA is addressed using custom written software in MATLAB — elaborated in section 9.3.5 — that permits binning of groups of mirror rows such that Hadamard matrices with different dimensions from 1-bit (2×2) to 10-bit (1024×1024) can be used.

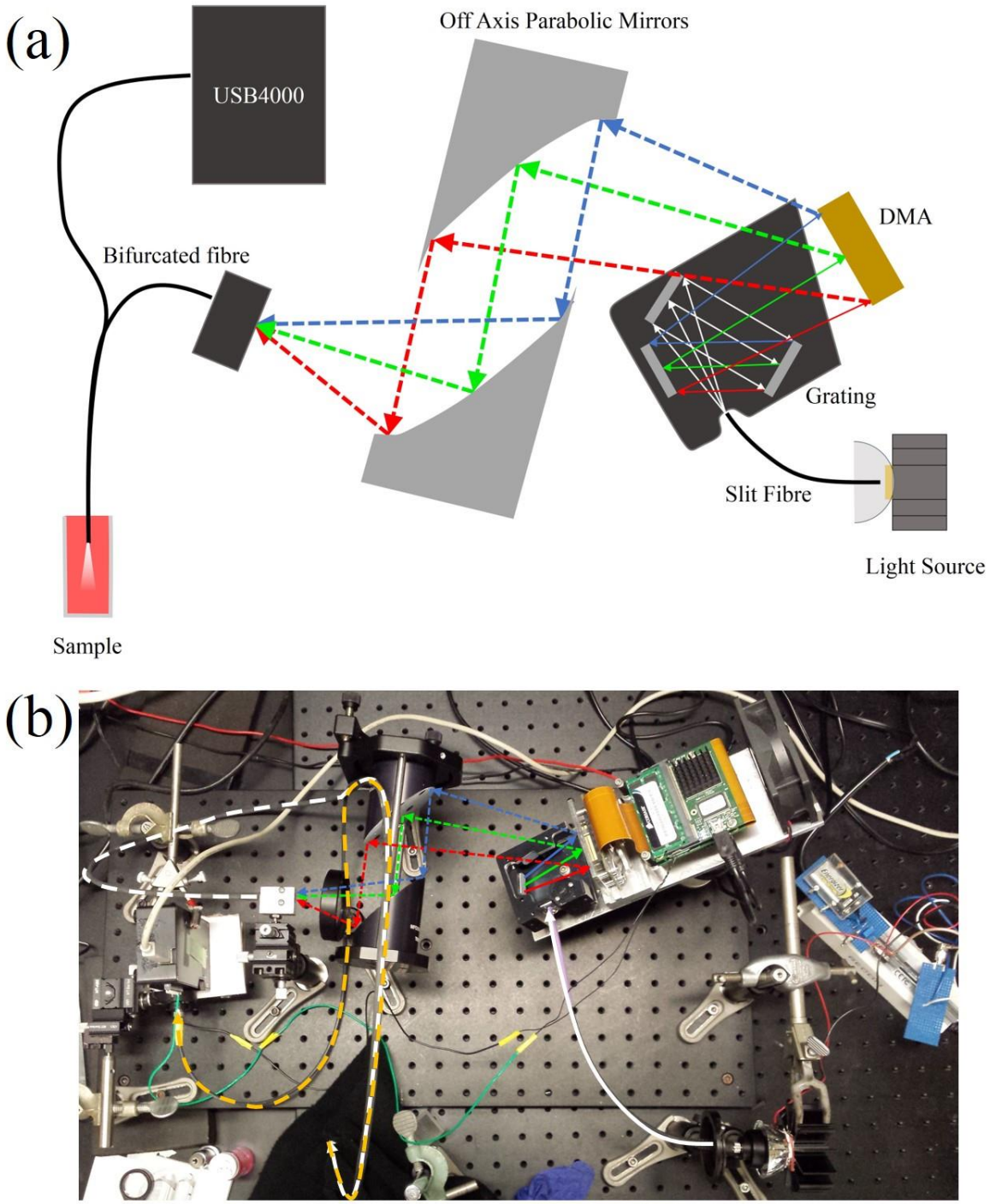

Figure 9.9: Optical layout of the HT fluorescence EEM spectrometer. **(a)** shows a schematic with all the components, where "USB4000" refers to the dispersive fluorescence spectrometer used to collect the modulated emission spectra, $[\mathbf{F}]$. The solid and dashed coloured arrows represent unmodulated light and encoded light respectively. **(b)** shows a photo of the HT fluorescence spectrometer. The dashed orange line represents the modulated fluorescence.

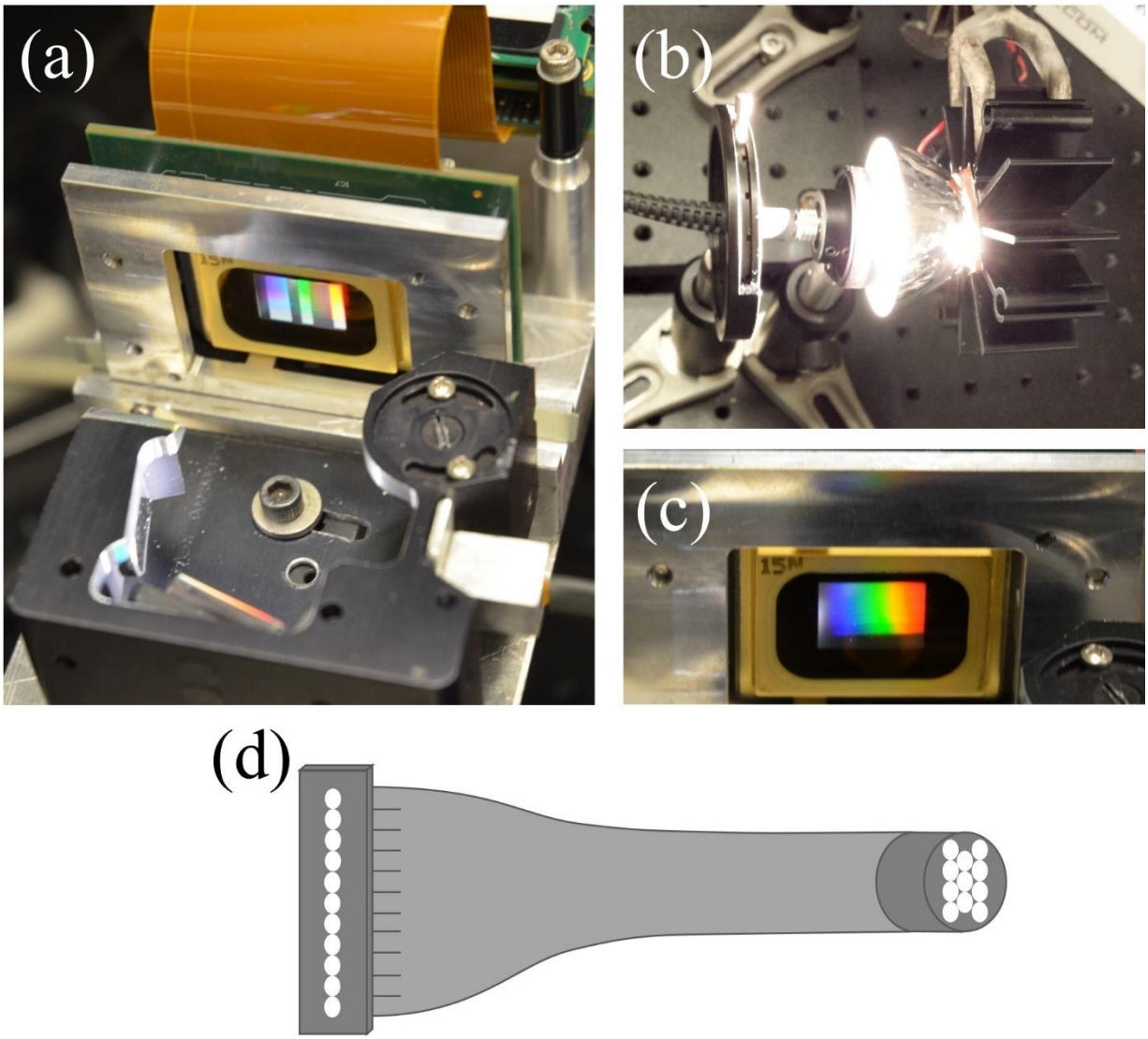

Figure 9.10: Dispersion of the white light source onto the DMA. **(a)** Photo of the *Ocean Optics* USBCUT used to disperse the white light onto the DMA which is used to encode the light. Note due to the angle that the photo is taken the dark bands are those that are in the "on" position. **(b)** Photo of the *Cree* CXB1830 white light LED used as the white light source. The LED is attached to a heat sink to keep it cool and functional. **(c)** Photo of the dispersed white light on the DMA. **(d)** Schematic of the fibre bundle used to couple the white LED light to the *Ocean Optics* USBCUT.

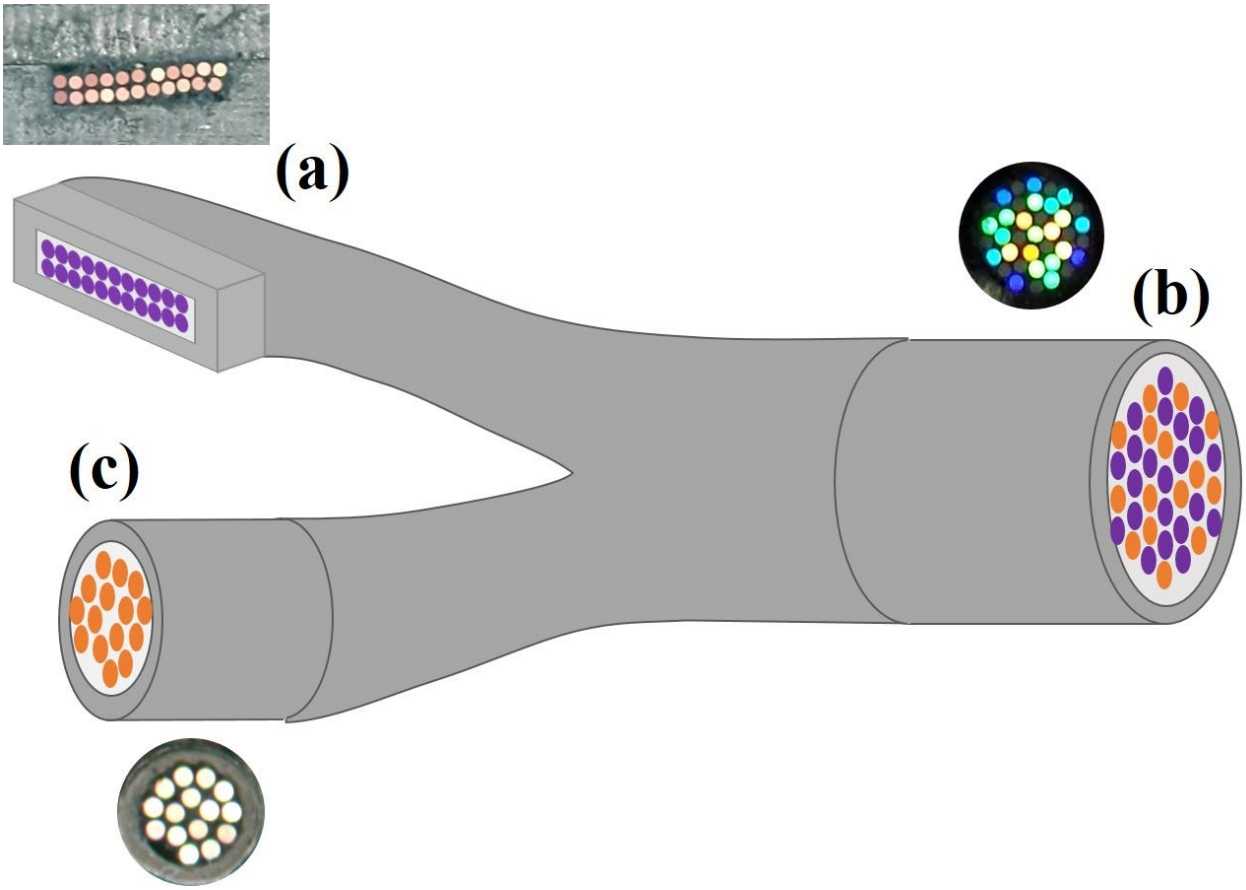

Figure 9.11: Bifurcated fibre probe used to couple the modulated white light to the sample. The encoded excitation light is focused and coupled into the 22 multimode fibres located at **(a)**, shown as purple circles. The light is coupled to the probe end at **(b)** where the light excites a sample. The sample fluoresces and the emitted light is collected by the 15 collection fibres shown as orange circles. The encoded fluorescence is sent to the detector located at the emission end **(c)**. The pattern was chosen to maximise the amount of excitation fibres surrounding each collection fibre and thus maximise the potential acceptance cone overlap. Colour photographs are shown as inserts.

9.3.3 Calibration

To calibrate the Hadamard fluorescence spectrometer such that the excitation wavelength for each segment column of mirrors is known, a column segment scan is conducted (**Figure 9.12**). Here, each column segment is switched "on" sequentially so that a spectrum is acquired for all separate mirror sections. Placing a scattering medium such as a white reflector (lens paper) at the sample end of the bifurcated fibre probe (**Figure 9.11(b)**) allows for an excitation spectrum to be collected and detected by the *Ocean Optics*

USB4000 detector. Each spectrum will contain a peak with all the wavelengths in the mirror segment. The wavelength gives the excitation wavelength of the segment and is determined with the centre of a Gaussian fit to the peak (**Figure 9.13**). To validate the method used to calibrate the excitation wavelength, a plot of the determined excitation wavelength of each segment against the directly recorded spectrum should yield a straight line where both wavelengths are equal. **Figure 9.14** shows that this is indeed the case.

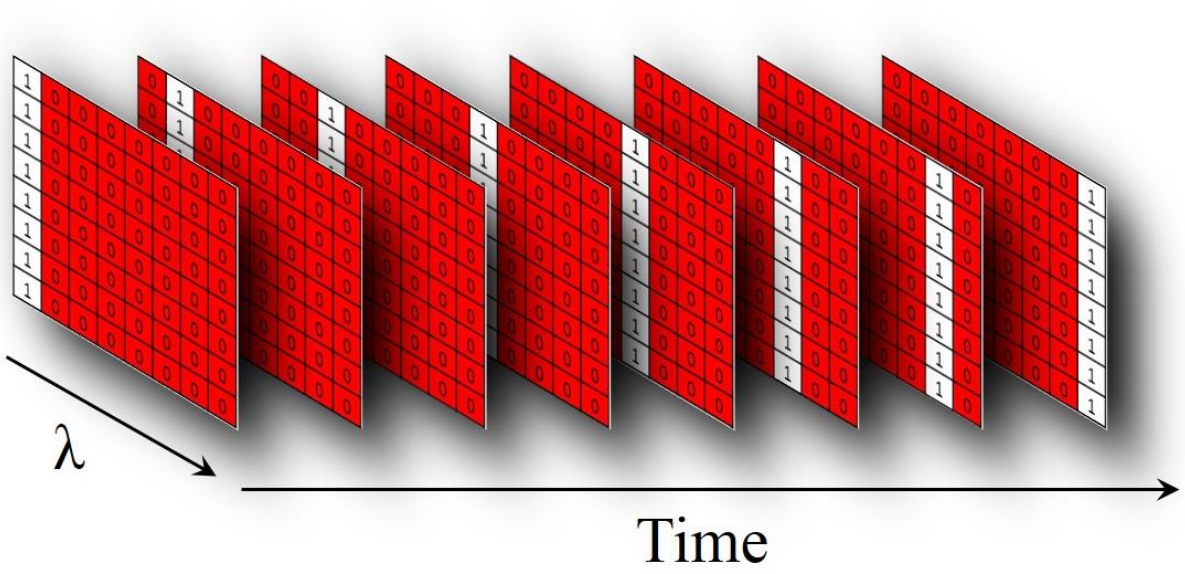

Figure 9.12: Method used to calibrate the excitation wavelength for each mirror column. Each mirror column segment is switched "on" sequentially and a spectrum is recorded. This produces a peak, where the centre is used as the wavelength of that column.

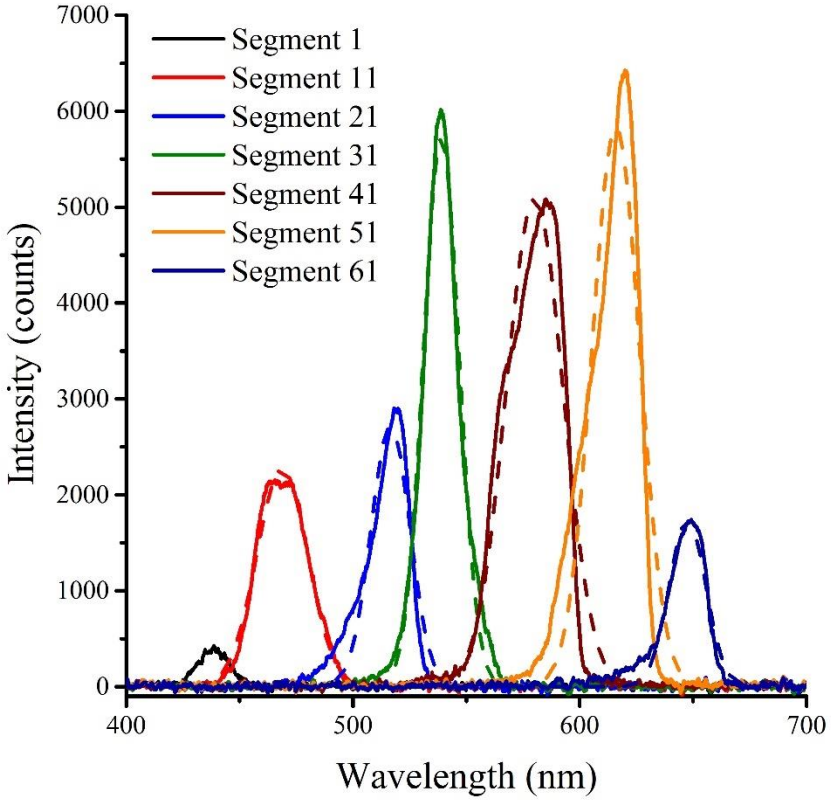

Figure 9.13: White LED Spectra of a 6-bit (64 image) segment scan. Note that only 7 spectra of the total 64 are shown to reduce clutter. The dashed lines represent the Gaussian fits through the data, the centre of which is used for the wavelength of that mirror column section.

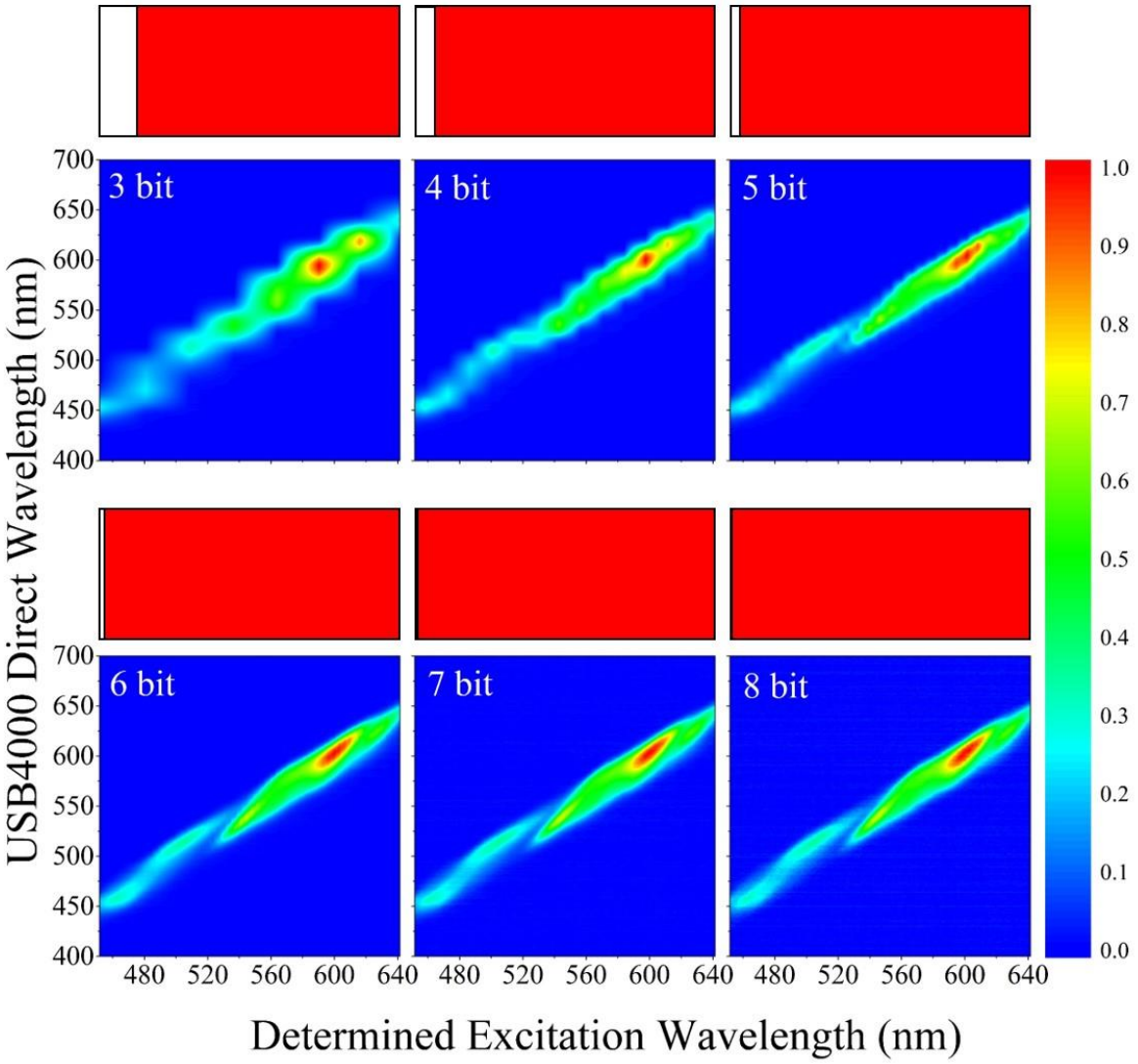

Figure 9.14: Normalised 2D calibration spectra showing linear correlation between the determined excitation wavelength from the Gaussian fit with the direct wavelength obtained using the Ocean Optics USB4000 spectrometer. The colours from blue to red represent the normalised intensity from 0 to 1, respectively. The boxes above the spectra correspond to the DMA where the white represents the "on" mirrors in each segment while the red represents the other mirrors that are "off".

The spectral resolution for each mirror segment is obtained from the full width half maximum (FWHM) of the same Gaussian fit in **Figure 9.13** and is given in **Figure 9.15(a)**. The average resolution over the whole DMA was determined and is limited by the DMA to $\delta\lambda = 23$ nm. Consequently, for the current setup, there is no resolution advantage in increasing the modulation to over 6-bit (64×64 Hadamard matrix). After

calibration, the wavelength of the light that is incident on the white reflector corresponds wavelength of the scattered light.

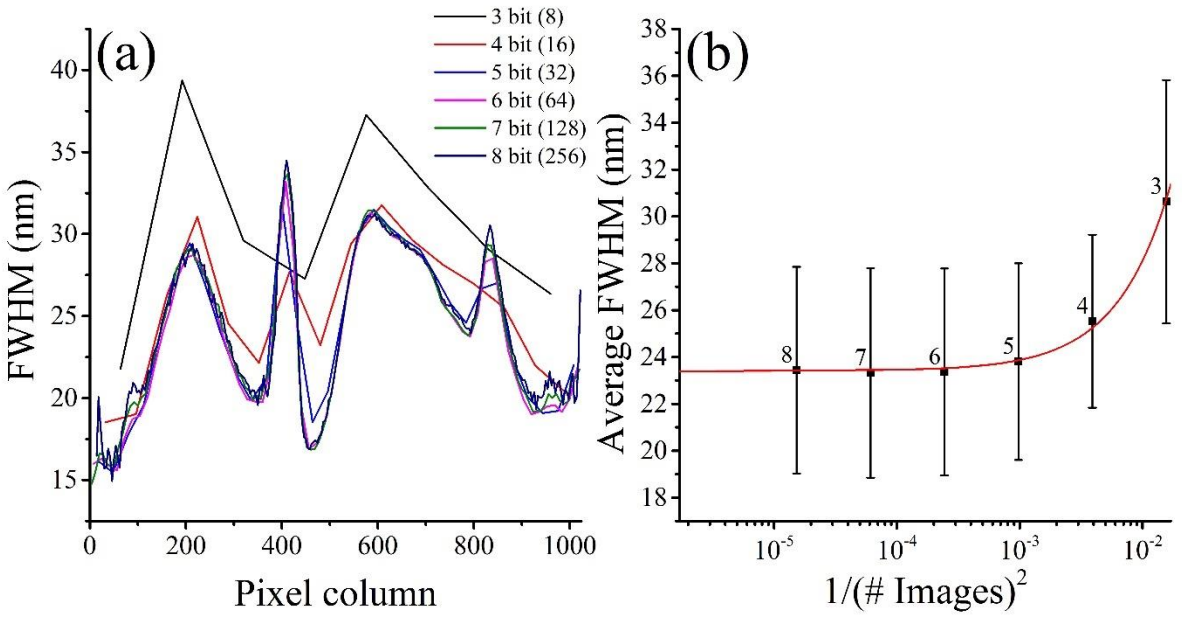

Figure 9.15: Full width half max values obtained from the Gaussian fits on the column segment scan peaks. **(a)** Shows the FWHM value across the DMA for each mirror pixel column. **(b)** Shows the average FWHM over the whole DMA as function of the number of images for each Hadamard *m* value. The error bars represent one standard deviation of the FWHM. Note that the average FWHM converges to 23 nm and thus there is no resolution advantage in increasing the modulation to over 6-bit.

9.3.4 Trigger settings

For a correct spectrum acquisition for each Hadamard mask, the spectrometer must be triggered with each successive mirror flip. This would ensure that all the collected fluorescence in each spectrum corresponds to the correct Hadamard image. In the ideal case the DMA would be used as the "master clock", whereby, when the mirrors flip, a transistor-transistor logic (TTL) pulse will be sent to the spectrometer to start the acquisition. The *Ocean Optics* USB4000 spectrometer requires a hardware edge trigger setting to run as a "slave" in this case. However, in this setting, the *Toshiba* TCD1304AP CCD used in the *Ocean Optics* USB4000 spectrometer enters a shutter mode.[91] In shutter mode, the integration time is reduced to ensure enough time to read out all the data, freeing the detector for the next trigger pulse. The reduced integration

time decreased the resulting signal intensity considerably, which is problematic when the aim of the spectrometer is to achieve as high of a SNR as possible. A further problem with the shutter mode setting is that there was a substantial memory effect between sequential spectra. This error in the CCD is detrimental as the Hadamard transformation requires that each spectrum for every image is completely independent from any other one. Using the *Ocean Optics* USB4000 spectrometer as the "master clock" prevented these problems caused by the CCD shutter mode. For this, the spectrometer was run in "normal" mode. At the start of every integration time, the spectrometer sends a TTL pulse to the DMA commanding the mirrors to flip. Although this is imperfect as some signal acquisition occurs during the mirror flip (~44 us) and required idle period of 1 ms, this was considered negligible for integration times in the order of 0.9 s and is preferential compared to the shutter mode. The idle period for the DMA was required to free the device for the subsequent spectrum. **Figure 9.16** shows the triggering settings used for the current setup of the Hadamard fluorescence spectrometer.

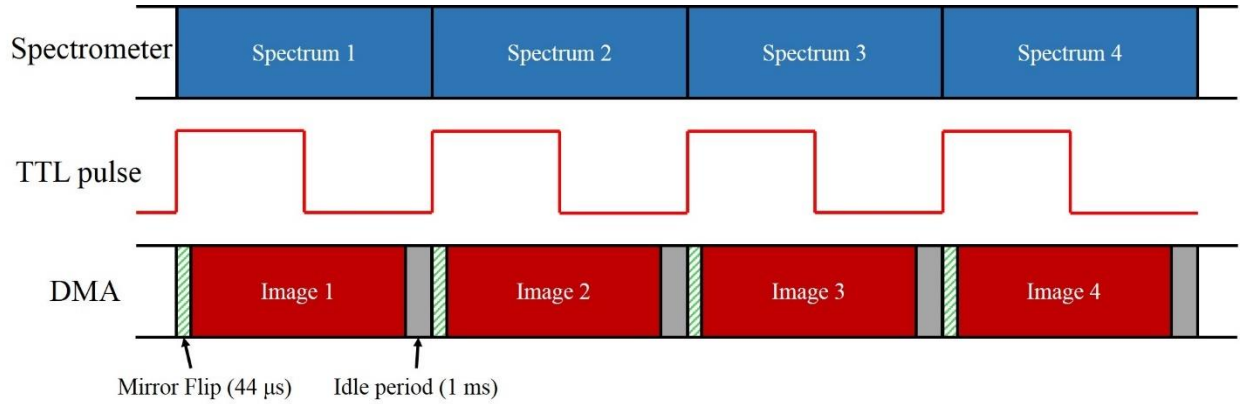

Figure 9.16: Triggering setting used for the Hadamard fluorescence spectrometer. The top row represents the integration time for the Ocean Optics USB4000 spectrometer. The middle row represents the 50% duty cycle TTL pulse produced by the spectrometer at the start of the integration time. The bottom row represents the DMA images. When the rising edge of the TTL pulse is received, the mirrors flip (44 µs) to one of the Hadamard images (**Figure 9.6**). The image is then displayed for the remainder of the integration time minus 1 ms. The 1 ms is used as an idle period so that the DMA is ready to receive the successive TTL pulse for the subsequent spectrum.

A further unexpected problem in the triggering configuration is that the first two spectra do not correlate to the first two images. The third spectrum corresponds, in fact, to the first image. To overcome this offset with the spectrum and image acquisition, two blank images were added to the end of the Hadamard sequence to ensure that all spectra had been acquired.

9.3.5 Custom built code

A custom built MATLAB code was written to control the devices used in the Hadamard fluoresce spectrometer. This code, allows automatic acquisition of spectra for each Hadamard image. In addition, the code allows for multiple EEM spectra to be acquired automatically for real time analysis of samples. **Figure 9.17** shows the graphic user interface (GUI) of the code. In addition, **Figure 9.18** shows a flow diagram of the steps the code uses to acquire fluorescence EEM spectra.

The first step of the code is to connect both the DMA and spectrometer to the PC. This is done by pressing the green box titled "Connect" in the GUI. If the devices are correctly connected, then their information appears in the three boxes below. The second step is to load the Hadamard images (**Figure 9.6**) onto the DMA's integrated random access memory (RAM), which allows for quick loading and displaying of the images. To do this the user presses the button titled "Choose Image Sequence" and selects the appropriate image folder in the folder selection pop up. Then the user types the appropriate resolution i.e. the value of *m* they require and press the button titled "Load_images". If the user wants to save the data, the save folder is selected using the "Choose Save Location" button and the save file name can be entered to the appropriate white box directly. The integration time can be selected by writing the value in μs in the appropriate box and then pressing the button titled "Set_Timing". Upon this button press all the necessary triggering and timing commands are calculated and inputted onto the devices. For accurate selection of the corresponding excitation wavelength for each mirror segment column, a prior calibration run must be conducted and the appropriate folder containing their spectra is selected using the button titled "Choose Blank Location". For more information regarding the calibration of the light source please refer to section 9.3.3.

If the user only wants to run a single EEM spectrum, then the button titled “Run_images” is pressed. The Hadamard fluorescence spectrometer will consequently collect spectra for all the *m* Hadamard images in the sequence and save the raw encoded fluorescence spectra in the chosen folder. To demodulate the encoded fluorescence data to the EEM spectrum, the user presses the button titled “Demodulate”. This will run a command that demodulates the signal as with the theory in section 9.2.4.2 and saves a raw and normalised EEM spectrum in the same folder.

If the user wants to run a multiple of *n* EEM spectra i.e. for real time degradation or kinetic studies, the user types in the value of *n* they require and presses the button titled “Run_Spectra”. This will run multiple versions of the single run command *n* times and automatically save the raw fluorescence spectra. The time at which the spectrum is acquired is also saved in the same folder. Once all raw encoded sequences are collected, the spectra are demodulated automatically and saved as raw and normalised EEM spectra.

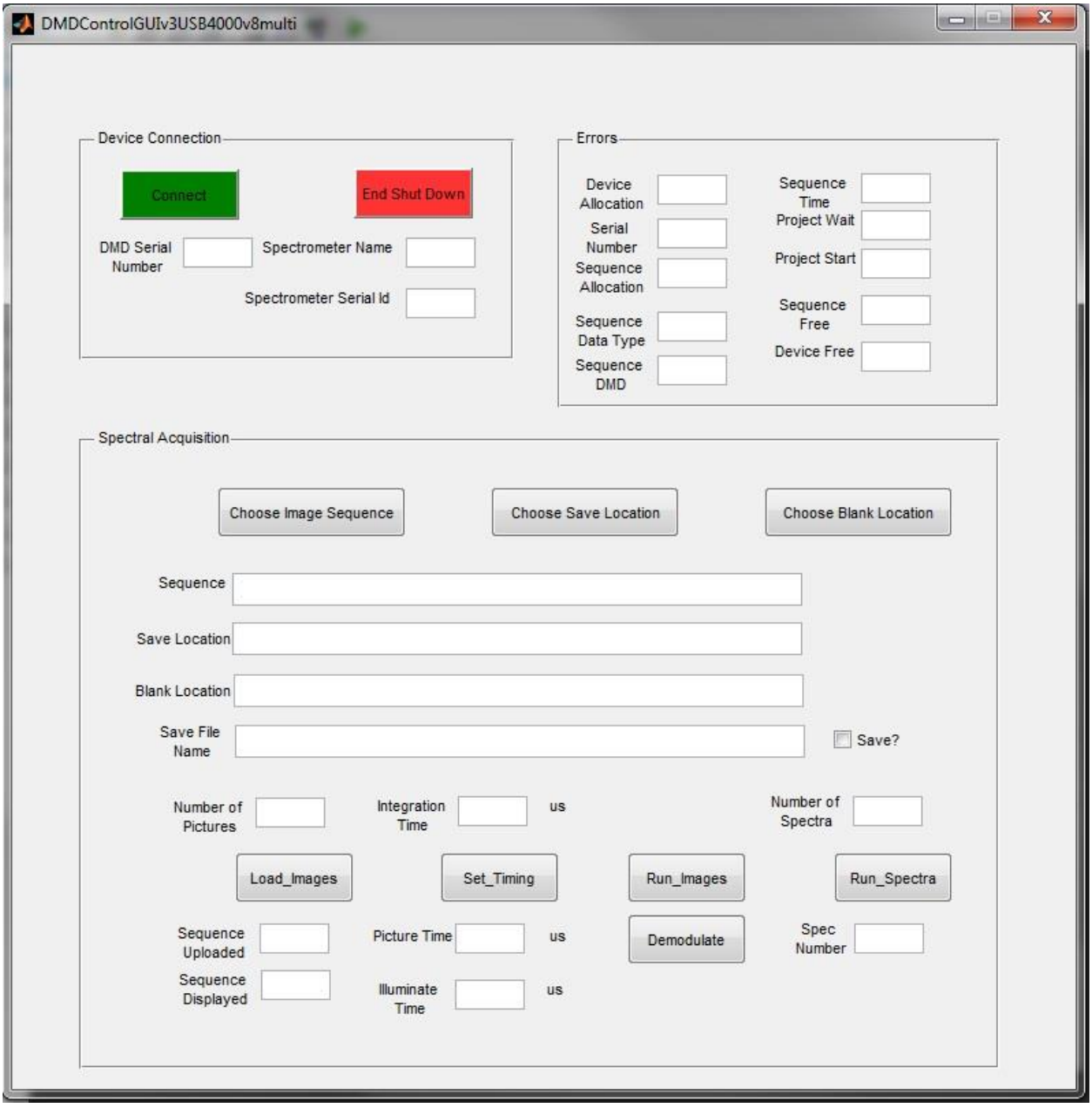

Figure 9.17: GUI of the code used to control the Hadamard fluorescence spectrometer and acquire EEM spectra.

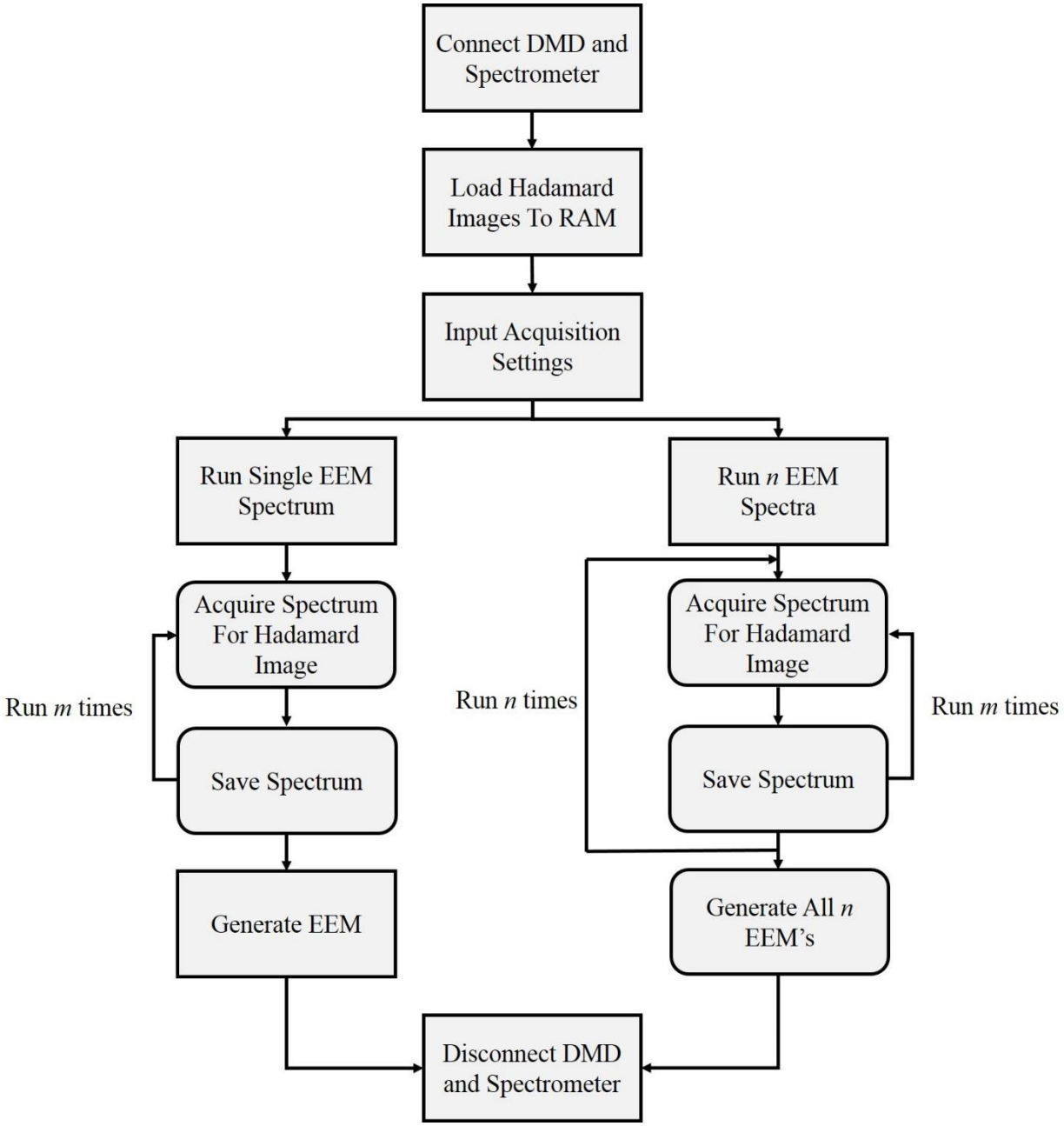

Figure 9.18: Flow diagram for the steps used to acquire EEM spectra using the Hadamard fluorescence spectrometer. The square edge boxes represent manual user buttons where the rounded edge boxes occur automatically.

9.4 Results and discussion

9.4.1 Characterisation of light source

As described in equations (9.7) to (9.9) the Hadamard modulation can be used to reobtain the spectrum of the light source (see **Figure 9.7**). Similar to the calibration of the excitation wavelength, a scattering white reflective medium (lens paper) is placed at the end of the fibre probe (**Figure 9.11(b)**) so that the excitation light can be collected and detected. With all the mirrors on the DMA set to the "on" position, the emission profile of the light source can be recorded as shown in **Figure 9.19** using an integration time of 900 ms. The light source can then be modulated by running the sequence of Hadamard images (**Figure 9.6**). **Figure 9.19** shows that the demodulated spectrum agrees with the spectrum of the light source.

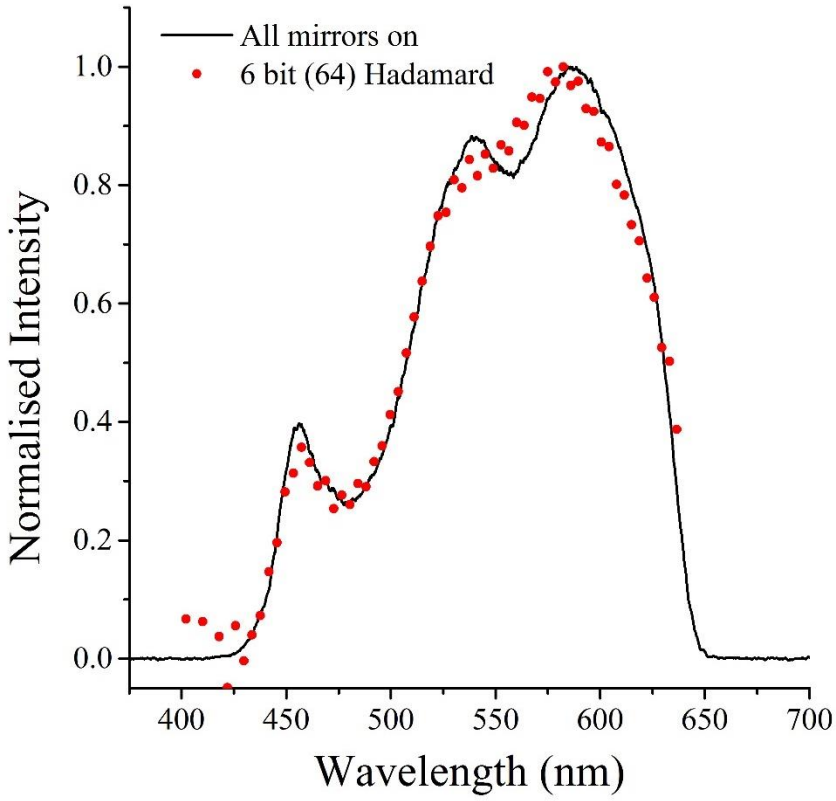

Figure 9.19: Spectrum of the white LED excitation source obtained by a 6-bit HT showing the normalised emission spectrum with all the mirrors switched to the "on" position using an integration time of 900 ms (solid line). The points represent the HT demodulated excitation light using a 6-bit (64 image) Hadamard matrix.

9.4.2 Hadamard-transform fluorescence EEM

Sulforhodamine 640 (50 μM in anhydrous ethanol) was used as a test dye to validate the proposed HT-Fluorescence EEM method (**Figure 9.20**). As a reference, the spectrum of sulforhodamine 640 in ethanol was obtained using the standard EEM scanning technique with the *Varian* Cary Eclipse spectrometer (**Figure 9.21**). The Hadamard fluorescence spectra of the same solutions of sulforhodamine 640 were obtained using an integration time of 900 ms for each Hadamard mask. The acquisition time for each EEM spectrum is the product of integration time and number of images, (2^m) and it therefore takes 7.2 s to acquire a 3-bit (8 image) spectrum, and 57.6 s for a 6-bit (64 image) spectrum. The latter gives the maximal resolution whilst maintaining a high data acquisition rate (**Figure 9.15(b)**). **Figure 9.22** shows that the Hadamard spectra match those of the conventional spectrometer while taking only a fraction of the time to complete (1 minute compared to 1 hour). Note that we observe a dip in the fluorescence intensity at an excitation wavelength of 520 nm. This is caused by the lower intensity of the light source in that range (**Figure 9.19**).

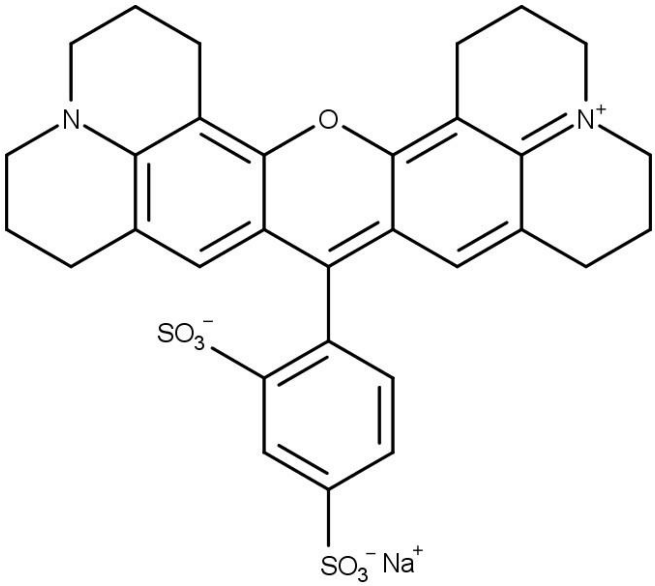

Figure 9.20: Chemical structure of sulforhodamine 640**.**

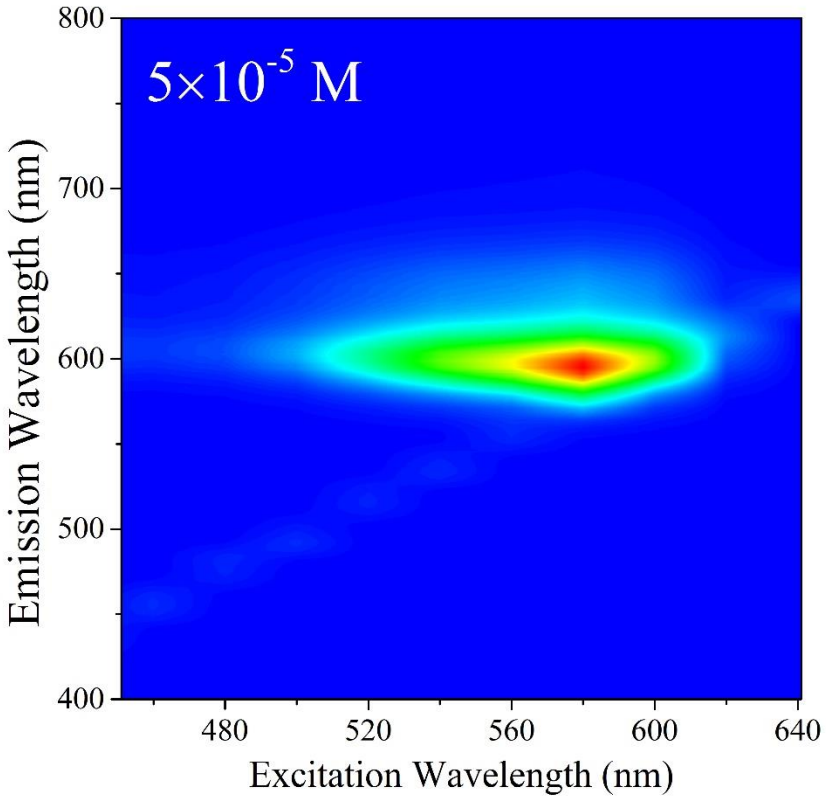

Figure 9.21: EEM spectrum of sulforhodamine 640 in anhydrous ethanol as obtained by the *Varian* Cary Eclipse spectrometer, using an excitation step and slit size of 20 nm, an emission step size of 10 nm, and a scan rate of 120 nm/min. These parameters were chosen to match that of the Hadamard spectra shown in **Figure 9.22**. This spectrum took approximately 1 hour to obtain. The colours from blue to red represent the normalised intensity from 0 to 1, respectively.

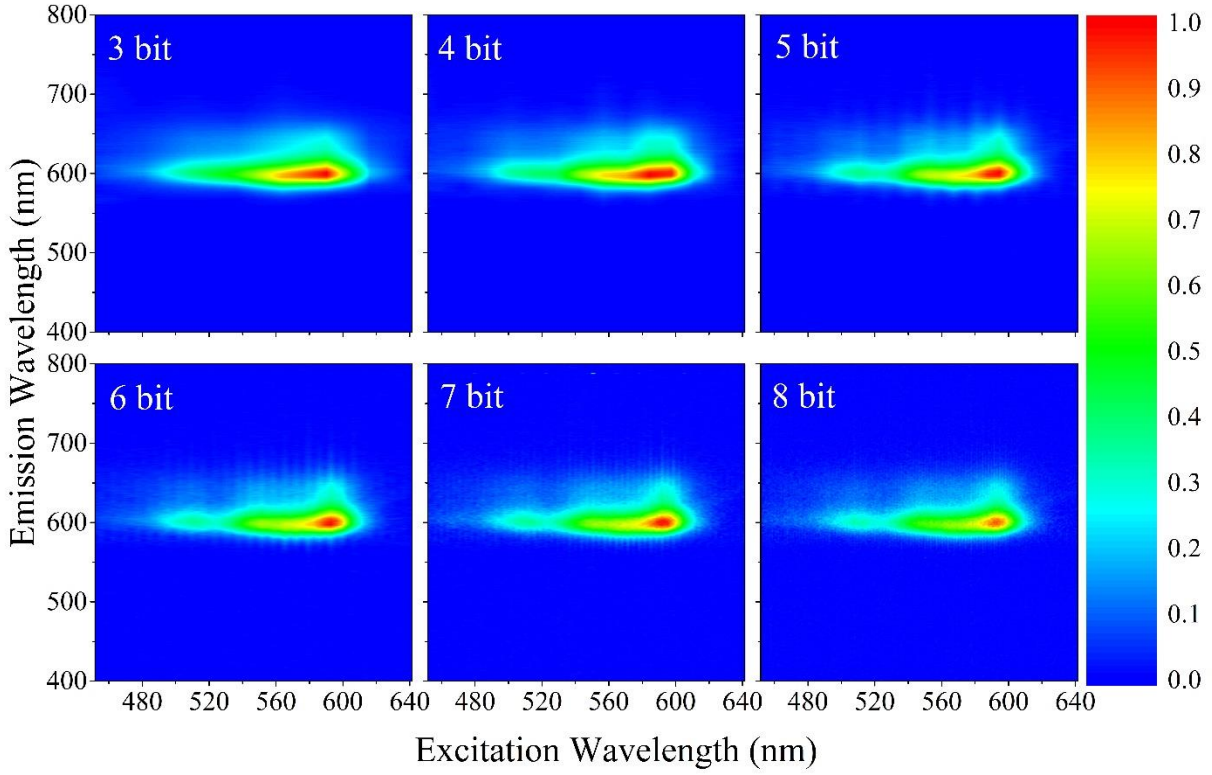

Figure 9.22: Hadamard fluorescence spectra of 5×10^{-5} M sulforhodamine 640 in anhydrous ethanol using an integration time of 900 ms. The time that it takes for each spectrum is 900 ms × 2^m where m is the number of bits. Therefore, a 6 bit (64 image) spectrum took 56.7 s to acquire. The colours from blue to red represent the normalised intensity from 0 to 1, respectively.

To better compare and show the advantages of the Hadamard technique, conventional line scans using the same bit rates were obtained (**Figure 9.23**). These line scan spectra were acquired with the same DMA based setup, but the columns of mirrors are turned on sequentially — the same way that the calibration scans were performed. This simulates a conventional scanning light source, similar to the technique employed by the conventional spectrometer. As before, the total data acquisition time per EEM is 900 ms × 2^m. While the line scan spectra match those obtained using the Hadamard method they have far lower intensity and lower SNR. This is due to the difference in the amount of light directed into the sample between each method. For the line scan method, a higher bit number corresponds to a smaller column width, and a smaller fraction of light reflected.

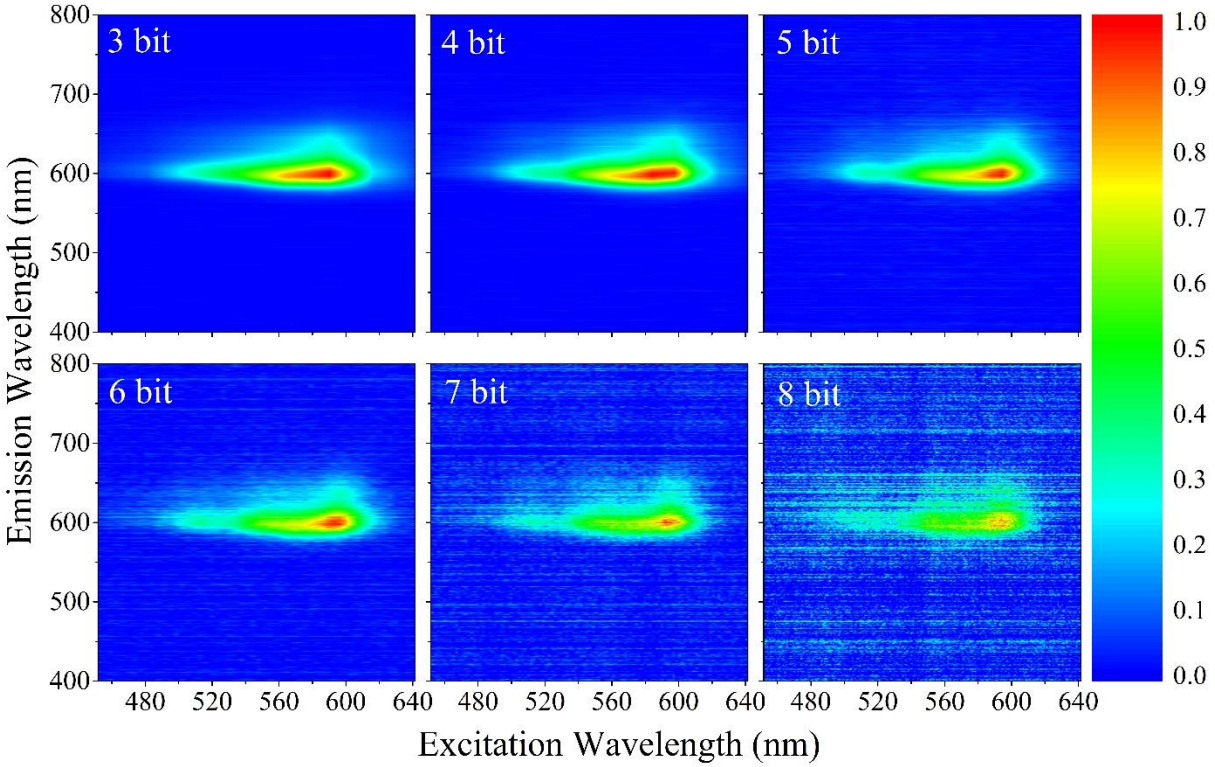

Figure 9.23: Conventional line scan fluorescence spectra of 5×10^{-5} M sulforhodamine 640 in anhydrous ethanol using an integration time of 900 ms. The time that it takes for each spectrum is 900 ms × 2^m where m is the number of bits. Therefore, a 6 bit (64 image) spectrum took 56.7 s to acquire. The colours from blue to red represent the normalised intensity from 0 to 1, respectively.

To further highlight the advantages of the Hadamard technique, the integration time was reduced to 90 ms (**Figure 9.24**). This means it only takes 5.76 s to obtain a 6-bit (64 image) spectrum. This highlights the technique's ability for real-time fluorescence analysis of samples. A series of line scan spectra were also recorded (**Figure 9.25**), but fluorescence could not be observed apart from a very weak signal at the lowest 8 channel resolution.

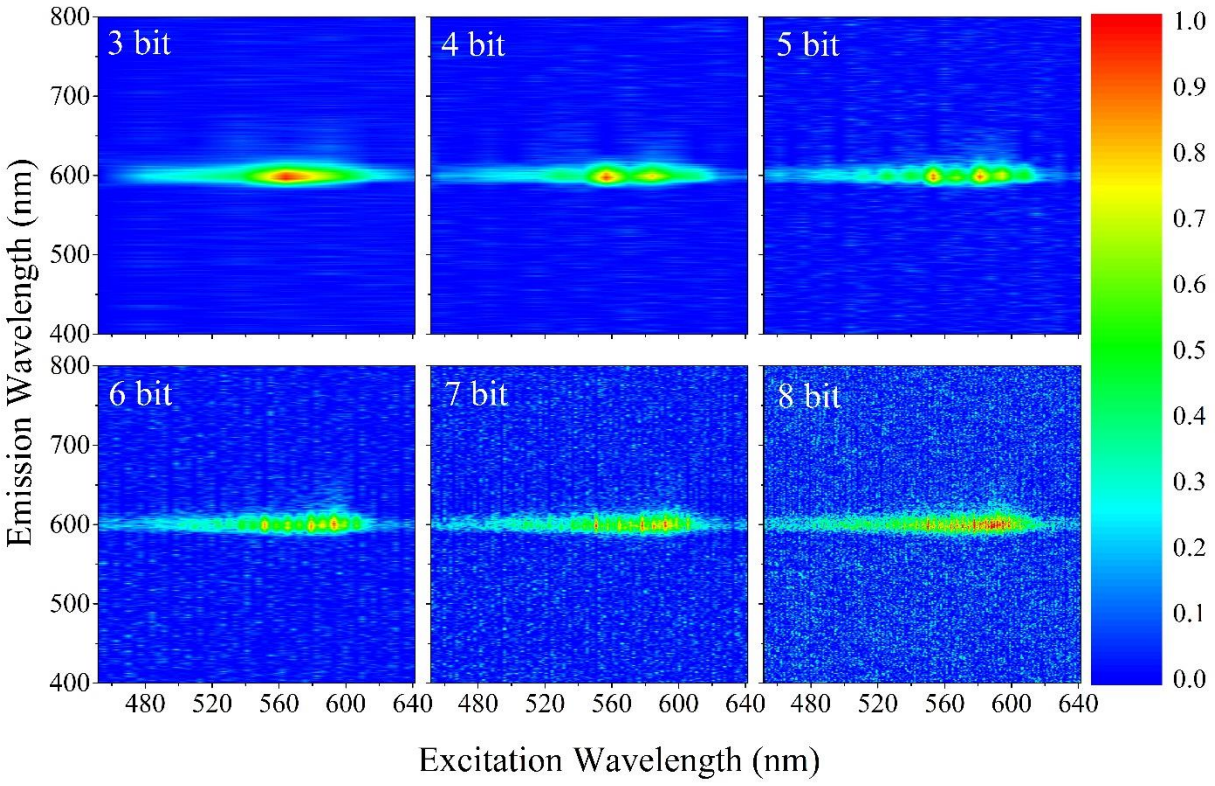

Figure 9.24: Hadamard fluorescence spectra of 5×10^{-5} M sulforhodamine 640 in anhydrous ethanol using an integration time of 90 ms. The time that it takes for each spectrum is 90 ms × 2^m where *m* is the number of bits. Therefore, a 6 bit (64 image) spectrum took 5.67 s to acquire. The colours from blue to red represent the normalised intensity from 0 to 1, respectively.

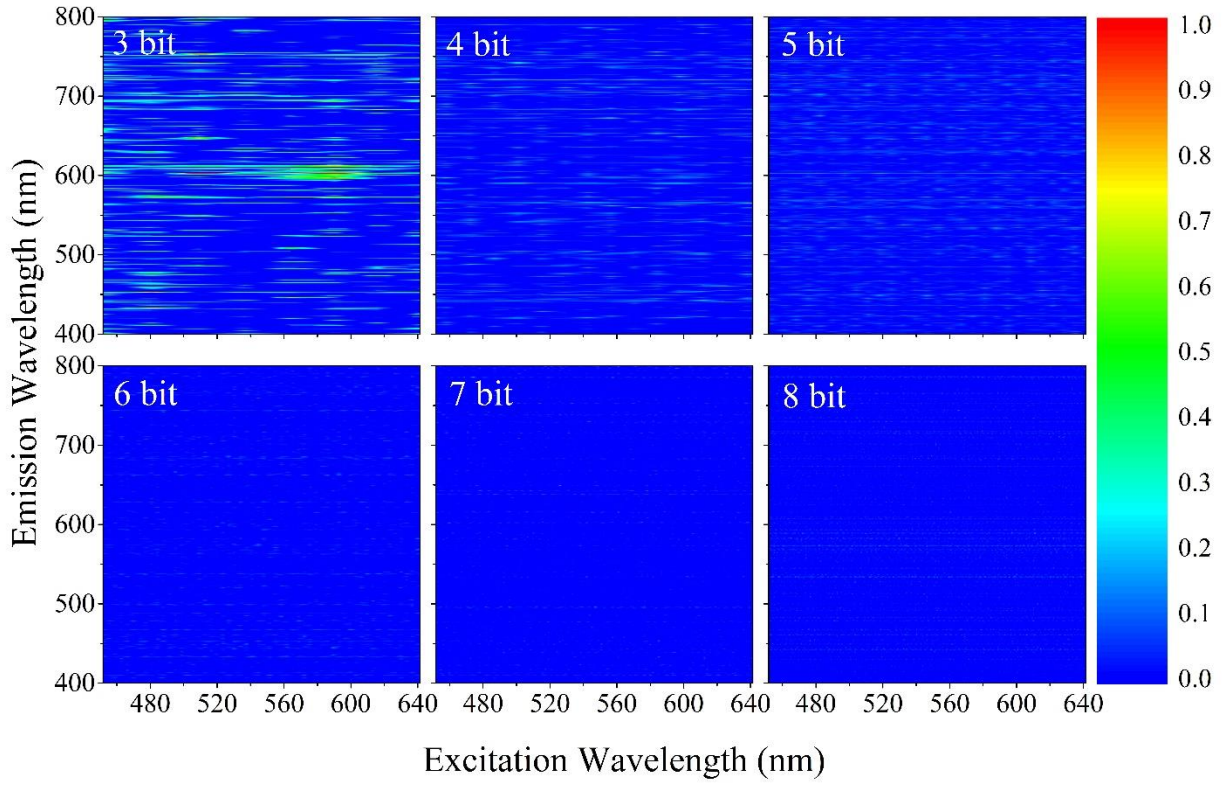

Figure 9.25: Conventional line scan fluorescence spectra of 5×10^{-5} M sulforhodamine 640 in anhydrous ethanol using an integration time of 90 ms. The time that it takes for each spectrum is 90 ms × 2^m where *m* is the number of bits. Therefore, a 6 bit (64 image) spectrum took 5.67 s to acquire. The colours from blue to red represent the normalised intensity from 0 to 1, respectively.

Due to the nature of the Walsh functions, in the Hadamard sequence — irrespective of the bit rate — exactly half of the total light directed to the DMA is reflected per image. Of course, reflection losses as well as coupling losses at the optical elements reduce the efficiency considerably. Nevertheless, the multiplex advantage is largely retained, as is apparent from the shorter data acquisition time. In conventional fluorescence EEM spectroscopy each pair of excitation and emission wavelengths is excited by a fraction of light corresponding to 2^{-2m} — for example by $1/64^{th}$ of the excitation light and $1/64^{th}$ of the dispersed fluorescence spectrum for a 64×64 EEM spectrum. In this example it would take 4096 s to collect the fluorescence intensity at each wavelength pair with an integration time of one second. In the Hadamard configuration, $^1/_2$ of the light incident on the DMA is used to generate the fluorescence spectrum, which in

our configuration is recorded in its entirety. Each EEM wavelength pair then collects a fraction of $^1/_2$ of the fluorescence. The multiplex advantage therefore scales with 2^{2m-1}. Unfortunately, this advantage could not be fully realised given the lower optical coupling efficiencies of the many components, the lower sensitivity of the fluorescence array detector compared to a photomultiplier tube, the DMA mirror reflectivity of at most 80%, and a lower reflectivity at shorter wavelength.

9.5 Concluding remarks

This chapter discussed the construction of a HT fluorescence EEM spectrometer and highlighted its main advantage as compared to a conventional scanning instrument that a high-resolution spectrum (6-bit, or 64 images) can be acquired in a matter of seconds. For that reason, this spectrometer is optimal for real-time kinetic studies and online measurements. The fibre probe can be inserted directly into a reaction flask, allowing the continuous acquisition of fluorescence spectra while a reaction is occurring. The reaction rate can be determined as the intensity of a given fluorescence peak increases or decreases, and with this method, even relatively fast processes can be studied with a high degree of accuracy. This is realised in the following Chapter 10 through the diffusion of tea — a reaction that occurs in a matter of minutes.

The data acquired by the HT spectrometer constructed in this chapter provides a proof-of-principle that the Hadamard system works and is much faster than that of a conventional dispersive spectrometer. It is optimised to the best of our current ability. However, the amount of light coupled into the fibres to the sample and detector are inefficient leading to low SNRs. Further improvements to the optical layout will be required to enhance the sensitivity and SNR that can be achieved. Additionally, the *Ocean Optics* USB4000 spectrometer used as a detector is both insensitive and has various problems with triggering, which hinders the optimisation of the current setup. Obviously these problems must be addressed to be able to use the HT-FEEM spectrometer on a wide variety of analytes.

The spectrometer was designed to operate in the visible region of the spectrum (440-660 nm). As most fluorescent compounds are excited in the range of 200-300 nm future designs will attempt to shift the excitation range into the UV. This requires that the light source be replaced with a UV source such as a Xenon flash lamp and that the window protecting the DMA be replaced with a UV-transparent window.

9.6 Bibliography

1. N. L. P. Andrews, J. Z. Fan, H. Omrani, A. Dudelzak and H.-P. Loock, Comparison of lubricant oil antioxidant analysis by fluorescence spectroscopy and linear sweep voltammetry. *Tribology International* **2016,** *94*, 279-287.
2. A. Dávalos, B. Bartolomé and C. Gómez-Cordovés, Antioxidant properties of commercial grape juices and vinegars. *Food Chemistry* **2005,** *93*, 325-330.
3. A. Zulueta, M. J. Esteve and A. Frígola, ORAC and TEAC assays comparison to measure the antioxidant capacity of food products. *Food Chemistry* **2009,** *114*, 310-316.
4. G. Agati, P. Matteini, J. Oliveira, V. de Freitas and N. Mateus, Fluorescence approach for measuring anthocyanins and derived pigments in red wine. *Journal of Agricultural and Food Chemistry* **2013,** *61*, 10156-10162.
5. D. N. Kothawala, C. A. Stedmon, R. A. Müller, G. A. Weyhenmeyer, S. J. Köhler and L. J. Tranvik, Controls of dissolved organic matter quality: Evidence from a large-scale boreal lake survey. *Global Change Biology* **2014,** *20*, 1101-1114.
6. X. Zhang, X. Zhao and M. Zhang, Characterization of persistent dissolved organic matter in municipal effluents after ozonation and soil aquifer treatment. *Environmental Earth Sciences* **2014,** *73*, 7789-7794.
7. H. Ma, H. E. Allen and Y. Yin, Characterization of isolated fractions of dissolved organic matter from natural waters and a wastewater effluent. *Water Research* **2001,** *35*, 985-996.
8. W. Zheng, D. Li, Y. Zeng, Y. Luo and J. Y. Qu, Two-photon excited hemoglobin fluorescence. *Biomedical Optics Express* **2010,** *2*, 71-79.
9. L. De-jia, L. Hai-cheng and Z. Guo-lin, Fluorescence spectra and enzymatic property of hemoglobin as mimetic peroxidase. *Wuhan University Journal of Natural Sciences* **2003,** *8*, 875-879.
10. K. Sudhakar, S. Loe, T. Yonetani and J. M. Vanderkooi, Fluorescent derivatives of human hemoglobin. Differences in interaction of the porphyrin with the protein between the alpha and beta subunits. *The Journal of Biological Chemistry* **1994,** *269*, 23095-23101.
11. A. Oriana, J. Réhault, F. Preda, D. Polli and G. Cerullo, Scanning Fourier transform spectrometer in the visible range based on birefringent wedges. *Journal of the Optical Society of America A* **2016,** *33*, 1415.
12. K. W. Busch and L. D. Benton, Multiplex methods in atomic spectroscopy. *Analytical Chemistry* **1983,** *55*, 445A-460A.
13. R. Kellner and G. Gidály, Fourier-transform infrared versus conventional grating-infrared-attenuated total reflectance spectroscopic investigation of the adsorption of blood proteins on polymer surfaces. *Microchimica Acta* **1981,** *75*, 119-129.
14. J. A. Decker, Experimental realization of the multiplex advantage with a Hadamard-transform spectrometer. *Applied Optics* **1971,** *10* (3), 510-514.
15. P. B. Fellgett, On the ultimate sensitivity and practical performance of radiation detectors. *Journal of the Optical Society of America* **1949,** *39*, 970.

16. R. H. Brown and R. Q. Twiss, Interferometry of the intensity fluctuations in light. I. Basic theory: The correlation between photons in coherent beams of radiation. *Proceedings of the Royal Society of London A: Mathematical, Physical and Engineering Sciences* **1957,** *242*, 300-324.
17. F. K. Fotiou and M. D. Morris, Performance of a Hadamard transform photothermal deflection imager with continuous wave laser illumination. *Analytical Chemistry* **1987,** *59*, 185-189.
18. R. Engeln and G. Meijer, A Fourier transform cavity ring down spectrometer. *Review of Scientific Instruments* **1996,** *67*, 2708-2713.
19. P. Jacquinot, New developments in interference spectroscopy. *Reports on Progress in Physics* **1960,** *23*, 267.
20. P. G. Lucey, K. A. Horton and T. Williams, Performance of a long-wave infrared hyperspectral imager using a Sagnac interferometer and an uncooled microbolometer array. *Applied Optics* **2008,** *47*, F107.
21. G. Kaiser, *A friendly guide to wavelets*, Springer Science & Business Media, 2010.
22. M. Rahman, *Applications of Fourier transforms to generalized functions*, WIT Press, 2011.
23. P. Griffiths, *Transform techniques in chemistry*, Springer Science & Business Media, 2012.
24. T. L. Chester, J. J. Fitzgerald and J. D. Winefordner, Theoretical comparison of signal-to-noise ratios of Fourier-transform spectrometry with single slit linear and slewed scan spectrometric methods for photon noise limited situation. *Analytical Chemistry* **1976,** *48*, 779-783.
25. W. Yuen and G. Horlick, Atomic spectrochemical measurements with a Fourier-transform spectrometer. *Analytical Chemistry* **1977,** *49*, 1446-1448.
26. G. Horlick and W. Yuen, Modular Michelson interferometer for Fourier-transform spectrochemical measurements from mid-infrared to ultraviolet. *Applied Spectroscopy* **1978,** *32*, 38-46.
27. R. Freeman and H. D. W. Hill, Fourier transform study of NMR spin–lattice relaxation by "progressive saturation". *The Journal of Chemical Physics* **2003,** *54*, 3367-3377.
28. K. P. Pruessmann, M. Weiger, M. B. Scheidegger and P. Boesiger, SENSE: Sensitivity encoding for fast MRI. *Magnetic Resonance in Medicine* **1999,** *42*, 952–962.
29. R. R. Ernst and W. A. Anderson, Application of Fourier transform spectroscopy to magnetic resonance. *Review of Scientific Instruments* **2004,** *37*, 93-102.
30. M. J. J. Vrakking, D. M. Villeneuve and A. Stolow, Nonadiabatic wave packet dynamics: Predissociation of IBr. *The Journal of Chemical Physics* **1996,** *105*, 5647-5650.
31. M. Shapiro, M. J. J. Vrakking and A. Stolow, Nonadiabatic wave packet dynamics: Experiment and theory in IBr. *The Journal of Chemical Physics* **1999,** *110*, 2465-2473.
32. D. A. Skoog, F. J. Holler and T. A. Nieman, in *Principles of Instrumental Analysis*, Saunders College Pub., 1998, pp. 182-189.
33. D. C. Harris, in *Quantitative Chemical Analysis, Sixth Edition*, W. H. Freeman, 2003, pp. 481-487.
34. L. Peng, J. A. Gardecki, B. E. Bouma and G. J. Tearney, Fourier fluorescence spectrometer for excitation emission matrix measurement. *Optics Express* **2008,** *16*, 10493.
35. J. Yuan, L. Peng, B. E. Bouma and G. J. Tearney, Quantitative FRET measurement by high-speed fluorescence excitation and emission spectrometer. *Optics Express* **2010,** *18*, 18839.
36. K. W. Henderson, Some notes on the walsh functions. *IEEE Transactions on Electronic Computers* **1964,** *EC-13*, 50-52.
37. W. Pratt, J. Kane and H. C. Andrews, Hadamard transform image coding. *Proceedings of the IEEE* **1969,** *57*, 58-68.
38. E. E. Sutter, The fast m-transform: A fast computation of cross-correlations with binary m-sequences. *SIAM Journal on Computing* **1991,** *20*, 9.
39. E. Kupče, T. Nishida and R. Freeman, Hadamard NMR spectroscopy. *Progress in Nuclear Magnetic Resonance Spectroscopy* **2003,** *42*, 95-122.

40. K. Balasubramanian, Computational strategies for the generation of equivalence classes of Hadamard matrices. *Journal of Chemical Information and Modeling* **1995,** *35*, 581-589.
41. J. A. Decker and M. Harwit, Experimental operation of a Hadamard spectrometer. *Applied Optics* **1969,** *8*, 2552-2554.
42. J. A. Decker, Hadamard-Transform spectrometry: A new analytical technique. *Analytical Chemistry* **1972,** *44*, 127A-134A.
43. H. E. B. d. Silva and C. Pasquini, Dual-beam near-infrared Hadamard spectrophotometer. *Applied Spectroscopy* **2001,** *55*, 715-721.
44. F. W. Plankey, T. H. Glenn, L. P. Hart and J. D. Winefordner, Hadamard spectrometer for ultraviolet-visible spectrometry. *Analytical Chemistry* **1974,** *46*, 1000-1005.
45. J. G. Brayan, D. J. Malcolmelawes, C. D. Mew and S. Xie, A Hadamard-transform UV absorption detection for high-performance liquid-chromatography. 1. Preliminary experiments. *Journal of Automatic Chemistry* **1995,** *17*, 77-82.
46. L. J. Hornbeck, US4662746 A, 1987.
47. L. J. Hornbeck, Society of Photo-Optical Instrumentation Engineers (SPIE) Conference Series, 1997.
48. E. P. Wagner, B. W. Smith, S. Madden, J. D. Winefordner and M. Mignardi, Construction and evaluation of a visible spectrometer using digital micromirror spatial light modulation. *Applied Spectroscopy* **1995,** *49*, 1715-1719.
49. J. D. Batchelor and B. T. Jones, Development of a digital micromirror spectrometer for analytical atomic spectrometry. *Analytical Chemistry* **1998,** *70*, 4907-4914.
50. J.-j. Chen, Y. Zhu, B. Liu, W. Wei, J. Zhang and N. Wang, The principle and Analysis of micro-Fourier transform spectrometer based on MEMS micro-mirror. *Spectroscopy and Spectral Analysis* **2012,** *32*, 3151-3154.
51. T. M. Spudich, C. K. Utz, J. M. Kuntz, R. A. Deverse, R. M. Hammaker and D. L. McCurdy, Potential for using a digital micromirror device as a signal multiplexer in visible spectroscopy. *Applied spectroscopy* **2003,** *57*, 733-736.
52. R. A. DeVerse, R. M. Hammaker and W. G. Fateley, Realization of the Hadamard multiplex advantage using a programmable optical mask in a dispersive flat-field near-infrared spectrometer. *Applied Spectroscopy* **2000,** *54*, 1751-1758.
53. W. G. Fateley, R. M. Hammaker, R. A. DeVerse, R. R. Coifman and F. B. Geshwind, The other spectroscopy: Demonstration of a new de-dispersion imaging spectrograph. *Vibrational Spectroscopy* **2002,** *29*, 163-170.
54. W. G. Fateley, R. M. Hammaker and R. A. DeVerse, Modulations used to transmit information in spectrometry and imaging. *Journal of Molecular Structure* **2000,** *550–551*, 117-122.
55. R. A. DeVerse, R. M. Hammaker, W. G. Fateley, J. A. Graham and J. D. Tate, Spectrometry and imaging using a digital micromirror array. *American Laboratory* **1998,** *30*, 112S-+.
56. R. A. DeVerse, R. M. Hammaker and W. G. Fateley, An improved Hadamard encoding mask for multiplexed Raman imaging using single channel detection. *Journal of Molecular Structure* **2000,** *521*, 77-88.
57. R. A. DeVerse, R. M. Hammaker and W. G. Fateley, Hadamard transform Raman imagery with a digital micro-mirror array. *Vibrational Spectroscopy* **1999,** *19*, 177-186.
58. W. G. Fateley, 6128078, 2000.
59. C. M. Wehlburg, J. C. Wehlburg, S. M. Gentry and J. Smith, in *Algorithms for Multispectral, Hyperspectral and Ultraspectral Imagery Vii*, eds. S. S. Shen and M. R. Descour, Spie-Int Soc Optical Engineering, Bellingham, 2001, vol. 4381, pp. 506-515.
60. M. W. Smith, J. L. Smith, G. K. Torrington, C. M. Wehlburg and J. C. Wehlburg, in *Imaging Spectrometry Viii*, ed. S. S. Shen, Spie-Int Soc Optical Engineering, Bellingham, 2002, vol. 4816, pp. 372-380.

61. S. P. Love and D. L. Graff, Full-frame programmable spectral filters based on micro-mirror arrays. *Proceedings of SPIE* **2013,** *8618*, 86180C-86180C.
62. S. P. Love, Programmable matched filter and Hadamard transform hyperspectral imagers based on micromirror arrays. *Proceedings of SPIE* **2009,** *7210*, 721007-721007.
63. L. Streeter, G. R. Burling-Claridge, M. J. Cree and R. Künnemeyer, 2008.
64. L. Streeter, G. R. Burling-Claridge, M. J. Cree and R. Künnemeyer, Optical full Hadamard matrix multiplexing and noise effects. *Applied Optics* **2009,** *48*, 2078-2085.
65. L. Streeter, G. Buling-Claridge, M. Cree and R. Künnemeyer, Short communication: Visible/near infrared hyperspectral imaging via spatial illumination source modulation. *Journal of Near Infrared Spectroscopy* **2007,** *15*, 395.
66. N. Goldstein, P. Vujkovic-Cvijin, M. Fox, B. Gregor, J. Lee, J. Cline and S. Adler-Golden, 2009.
67. A. Brock, N. Rodriguez and R. N. Zare, Hadamard transform time of flight mass spectrometry. *Analytical Chemistry* **1998,** *70*, 3735-3741.
68. O. Trapp, J. R. Kimmel, O. K. Yoon, I. A. Zuleta, F. M. Fernandez and R. N. Zare, Continuous two-channel time-of-flight mass spectrometric detection of electrosprayed ions. *Angewandte Chemie International Edition* **2004,** *43*, 6541-6544.
69. C.-H. Lin, T. Kaneta, H.-M. Chen, W.-X. Chen, H.-W. Chang and J.-T. Liu, Applications of Hadamard transform to gas chromatography/mass spectrometry and liquid chromatography/mass spectrometry. *Analytical Chemistry* **2008,** *80*, 5755-5759.
70. G.-T. Fan, C.-L. Yang, C.-H. Lin, C.-C. Chen and C.-H. Shih, Applications of Hadamard transform-gas chromatography/mass spectrometry to the detection of acetone in healthy human and diabetes mellitus patient breath. *Talanta* **2014,** *120*, 386-390.
71. O. Trapp, Boosting the throughput of separation techniques by "multiplexing". *Angewandte Chemie International Edition* **2007,** *46*, 5609-5613.
72. M. Kaljurand and H. C. Smit, Application of random and regular input in analytical separation methods: A critical insight. *Chemometrics and Intelligent Laboratory Systems* **2005,** *79*, 65-72.
73. G. Chen, E. Mei, W. Gu, X. Zeng and Y. e. Zeng, Instrument for Hadamard transform three-dimensional fluorescence microscope image analysis. *Analytica Chimica Acta* **1995,** *300*, 261-267.
74. E. W. Mei, G. Q. Chen and Y. E. Zeng, Hadamard transform microscope fluorescence image. *Microchemical Journal* **1996,** *53*, 316-325.
75. H. Tang, G. Chen, J. Zhou and Q. Wu, Hadamard transform fluorescence image microscopy using one-dimensional movable mask. *Analytica Chimica Acta* **2002,** *468*, 27-34.
76. B. H. Clowers, W. F. Siems, H. H. Hill and S. M. Massick, Hadamard transform ion mobility spectrometry. *Analytical Chemistry* **2006,** *78*, 44-51.
77. A. W. Szumlas, S. J. Ray and G. M. Hieftje, Hadamard transform ion mobility spectrometry. *Analytical Chemistry* **2006,** *78*, 4474-4481.
78. Ē. Kupče and R. Freeman, Two-dimensional Hadamard spectroscopy. *Journal of Magnetic Resonance* **2003,** *162*, 300-310.
79. G. Goelman, G. Walter and J. S. Leigh, Hadamard spectroscopic imaging technique as applied to study human calf muscles. *Magnetic Resonance in Medicine* **1992,** *25*, 349-354.
80. A. Kubo, A. Yogo, F. Imashiro and T. Terao, Deuterium NMR study of the glassy crystal pentachlorotoluene. Hadamard quadrupole-order exchange NMR. *Journal of Physical Chemistry* **1996,** *100*, 15933-15941.
81. M. Feliz, J. Garcia, E. Aragon and M. Pons, Fast 2D NMR ligand screening using Hadamard spectroscopy. *Journal of the American Chemical Society* **2006,** *128*, 7146-7147.
82. J. D. T. Kruschwitz, *From small fish to oceans of opportunity: The story of Ocean Optics Inc.*, OSA OPN, 2006.
83. http://www.avantes.com/company, 2016.

84. R. B. Bilhorn, J. V. Sweedler, P. M. Epperson and M. B. Denton, Charge transfer device detectors for analytical optical spectroscopy — operation and characteristics. *Applied Spectroscopy* **1987,** *41*, 1114-1125.
85. P. M. Epperson and M. B. Denton, Binning spectral images in a charge-coupled device. *Analytical Chemistry* **1989,** *61*, 1513-1519.
86. R. E. Santini, M. J. Milano and H. L. Pardue, Rapid scanning spectroscopy. Prelude to a new era in analytical spectroscopy. *Analytical Chemistry* **1973,** *45*, 915A-927a.
87. http://www.agilent.com/en-us/products/fluorescence/fluorescence-systems/cary-eclipse-fluorescence-spectrophotometer, 2016.
88. T. Hirschfeld and G. Wyntjes, Fourier transform vs Hadamard transform spectroscopy. *Applied Optics* **1973,** *12*, 2876.
89. J. A. Decker, Comments on: Fourier transform vs Hadamard transform spectrometry. *Applied Optics* **1974,** *13*, 1296.
90. http://www.cree.com/Xlamp, 2016.
91. USB4000 data sheet. *Ocean Optics Inc.* **2016**.

Chapter 10

Real-Time Analysis of Tea Diffusion with the Hadamard Fluorescence EEM Spectrometer

This chapter is based on the technique discussed in the previous Chapter 9. In addition, this chapter is based on the paper entitled "Hadamard fluorescence excitation emission matrix spectrometer", N. L. P. Andrews, A. M. Rangaswamy, T. G. Ferguson, A. R. Bernicky, N. Henning, O. Reich, A. Dudelzak, and H.-P. Loock, which is in preparation. Under direct supervision, Alana Rangaswamy and Adam Bernicky collected and ran tea samples. Travis Ferguson is continuing the work on the Hadamard spectrometer and Niklas Henning helped with some coding and alignment.

10.1 Introduction

The Hadamard transform (HT) excitation emission matrix (EEM) spectrometer, described in Chapter 9, is able to produce EEM spectra in a fraction of the time it takes compared to a conventional dispersive EEM spectrometer. As shown in Chapter 6 and Chapter 7, EEM spectroscopy when combined with parallel factor (PARAFAC) analysis is a very powerful technique in determining degradation kinetics. Now that a faster EEM spectrometer has been built, faster chemical processes can be monitored and to showcase the spectrometer to be useful for kinetics a system needs to be analysed in real-time. One such process is the brewing of tea in water, which occurs within about 5 mins.[1]

For thousands of years, leaves of the plant species *Camellia sinesis*, otherwise known as tea, have been harvested, processed and packaged. These leaves are used to make a beverage that has fundamental roots in many societies and cultures.[2] Indeed, being a British citizen, the idea of sipping on a perfect cup of tea lies very close to my heart. Tea leaves are steeped in hot water, which infuses their flavours and properties into the drink. Tea is the most consumed beverage in the world besides water and in many places safer to

drink being that water has to be boiled prior to consumption.[2-5] Tea is widely valued for its health benefits and potential anticancer properties due to its formation of antioxidants that are readily digested *in vivo*.[6] These include compounds such as polyphenols, including flavonoids such as flavanol and catechin.[2, 6-8] In addition, tea is widely treasured due to its caffeine content, which is an important central nervous stimulant.[2, 9]

There are two major varieties of *Camellia sinensis* which are recognised — *var. sinensis* and *var. assamica*. These vary in leaf size depending on the cultivation climates.[8] The *sinensis* variety has smaller leaves (5-12 cm) and is primarily cultivated in China due to its temperate climate, whereas the *assamica* variety has larger leaves up to 20 cm in length and is cultivated primarily in Southeast Asia. These varieties have been hybridised, generating thousands of crossbreeds for their taste and growing properties. In addition, tea leaves have been manufactured in several ways to produce green, black, oolong, and white tea. Green tea is rolled and steamed immediately after picking to prevent oxidation of the green leaf polyphenols.[8, 10] In contrast, black tea is allowed to oxidise for 90-120 mins after being rolled.[2, 10] During this oxidation process, catechins are converted into complex condensation products such as theaflavins, which gives black tea its characteristic flavour and colour. Oolong tea is only partially oxidised producing an intermediate composition between green and black tea.[8, 10, 11] White tea is prepared from very young tea leaves or buds, which are covered in silver hairs. Similar to green tea, white tea is steamed and dried immediately after picking to prevent oxidation.[10]

The aromatic polyphenols in tea are luminescent due to their highly conjugated structure.[12] Therefore, tea can be analysed using fluorescence spectroscopy. Furthermore, EEM fluorescence spectroscopy is advantageous in analysing complex solutions such as steeped tea, which contains multiple fluorescence compounds. Previously, EEM spectroscopy has been used to determine the quality and origin of various teas.[3, 13] Therefore, EEM spectroscopy using the HT spectrometer is a perfect system to investigate the

diffusion of tea into water. However, the fluorescence of tea following excitation at wavelengths longer than 450 nm is very weak.[14-16] Therefore, our HT spectrometer — which does not yet allow for excitation at $\lambda < 450$ nm — is currently unable to observe its fluorescence directly.

As an alternative method to measure the diffusion of tea the associated pH change can be tracked through use of a fluorescent dye such as fluorescein. As the tea brews, the solution becomes more acidic,[17, 18] which affects the fluorescence intensity of fluorescein.[19] Since fluorescein has a high quantum yield, this process can be monitored using the HT fluorescence EEM spectrometer. As with the degradation studies shown in Chapter 6 and Chapter 7, rate constants and activation energies of the diffusion of tea can be obtained by brewing the teas at differing temperatures.

10.2 Rate determination of tea diffusion through pH change

10.2.1 Effect of tea brewing on pH

Since the setup described in Chapter 9 is not sensitive enough to detect a fluorescent signal from tea itself, a method of indirect detection by means of a fluorescent dye of tea has been devised. This fluorescence excitation must also occur in the visible range of 450 – 650 nm so it can be detected using the HT fluorescence spectrometer. As tea diffuses into water, the solution becomes more acidic due to the presence of oxalic and citric acid in the tea.[17, 18] A simple reaction of tea brewing into water with a rate of *k* may be described as follows,

$$\mathrm{TeaH}(s) \xrightarrow[\mathrm{H_2O}]{k} \mathrm{Tea^-}(aq) + \mathrm{H^+}. \qquad \textbf{(R 10.1)}$$

The corresponding differential equation governing the formation of H^+ ions can be solved as a first order rate equation,

$$\left[\mathrm{H^+}\right] = \left[\mathrm{H^+}\right]_0 \left(1 - \exp\left(-kt\right)\right). \qquad \textbf{(10.1)}$$

The increase of H^+ ions (decrease of pH) is shown in **Figure 10.1**. Earl grey (*Twinings*) and green (*Our Finest*) tea were brewed at 70°C and samples were extracted at pseudo logarithmic time points. The pH was

measured using a Accumet AB15 pH meter (*Fisher Scientific*). The pH can be converted to the concentration of H^+ ions using equation (10.2),

$$[H]^+ = 10^{-pH}. \quad \textbf{(10.2)}$$

Using equation (10.1) the rate constant, *k*, was found to be 0.002 s^{-1} and 0.008 s^{-1} for earl grey and green tea, respectively.

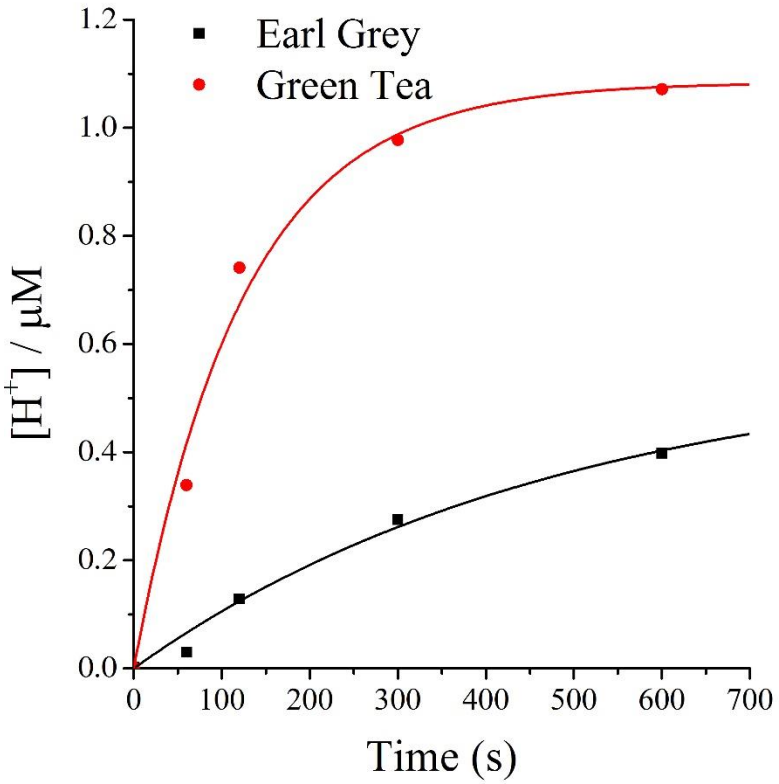

Figure 10.1: Concentration of H^+ ions as earl grey and green tea are brewed at 70°C as obtained from the pH measurement. The solid lines are an exponential rise through the data using equation (10.1). For both the black Earl Grey and Green tea, as tea brews it becomes acidic.

10.2.2 pH dependence of fluorescein

The pH decrease associated with the dissolution of acidic compounds in the tea leaves can also be monitored using a pH-dependent fluorescent dye. Fluorescein is one such compound, having a high quantum yield of

0.97 in basic conditions, in addition to its excitation maximum at ~499 nm.[19] The quantum yield decreases to 0.25-0.35 in acidic conditions. This change of quantum yield is detectable with the HT fluorescence spectrometer and PARAFAC analysis.

The fluorescence change of fluorescein due to pH depends on the pK_a of the hydroxyl groups on the xanthene group.[20] As the pH increases from acidic to basic conditions, fluorescein reacts from its cationic form to its neutral, monoanionic, and subsequently dianionic form (**Figure 10.2**).[20] The neutral and monoanion of fluorescein both exhibit an excitation maximum near 437 nm with an emission at around 515 nm. These states are expected to have a very similar fluorescence emission, as the carboxyl group does not affect the conjugation of the xanthene part of the molecule.[20] By contrast the dianion is excited at a longer wavelength of 490 nm with a similar emission at 515 nm because the ionisation of the hydroxyl group will affect the conjugation of the xanthene group. This generates further conjugation and a bathochromic shift of the spectra.[21, 22] This change of excitation of fluorescein's fluorescence between its monoanionic and dianionic states is observable using fluorescence EEM spectroscopy. The quantum yield decrease of fluorescein in acidic conditions is due to internal conversion ($S_0 \leftarrow S_1$) or intersystem crossing ($T_1 \leftarrow S_1$) processes of the neutral fluorescein molecule.[20, 23-26]

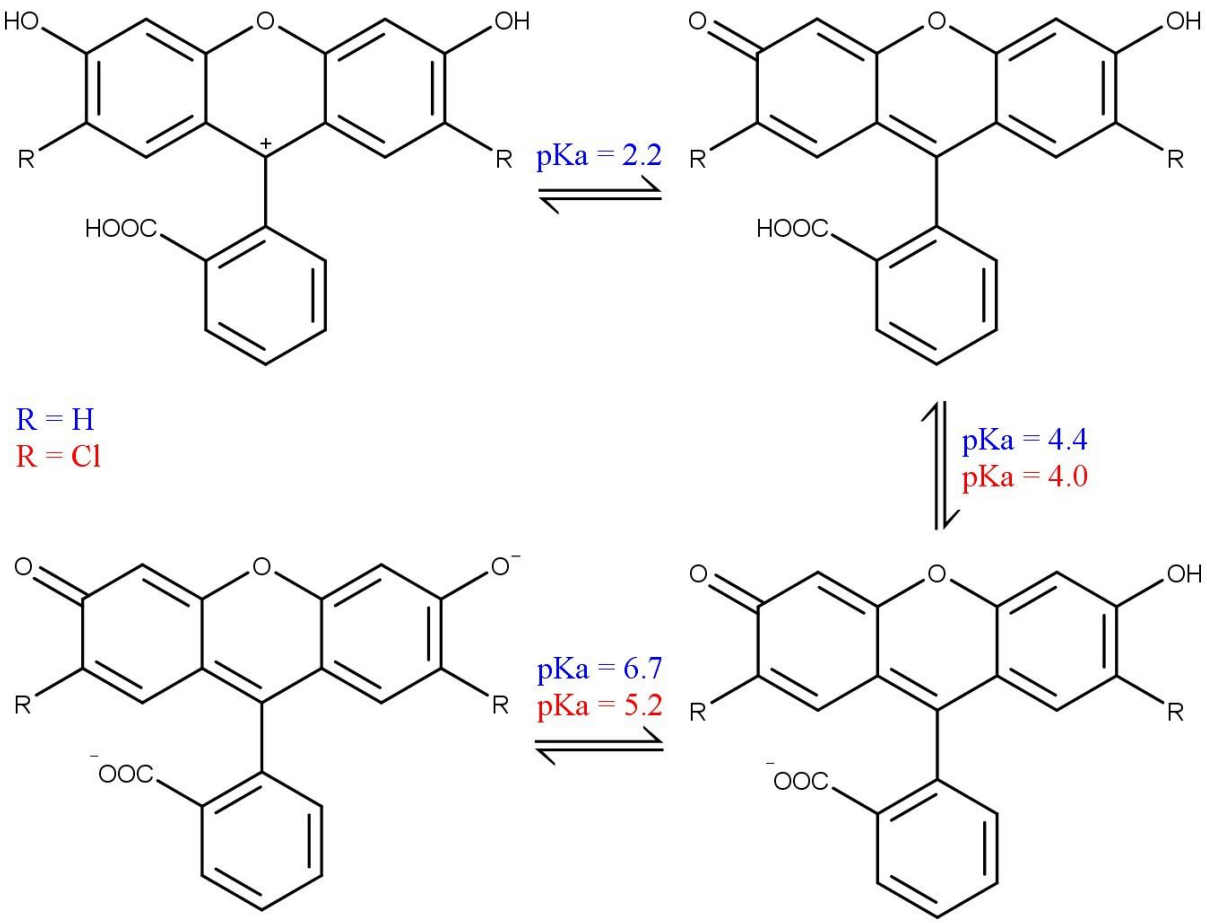

Figure 10.2: Structure of two fluorescein derivatives at different pH. The top left structure shows the fluorescein cation which exists in acidic conditions. As the solution becomes basic, fluorescein reacts to its neutral, monoanion, and lastly the dianion form. The red and blue values for the pKa represent fluorescein and dichlorofluorescein respectively.[23, 27]

10.3 Experimental

10.3.1 Fluorescein pH

Solutions of different pH values were made using a 0.28 M phosphate buffer at pH values ranging from 1.8 to 9.1. The phosphate buffer solutions were made with differing ratios of ≥85 w/w % phosphoric acid (*Fisher Scientific*), potassium phosphate monobasic, KH_2PO_4 (*Sigma Aldrich*, ≥99.0%), and potassium phosphate dibasic, K_2HPO_4 (*Sigma Aldrich*, ≥99.0%). 16 mL of phosphate buffer were added to 4 mL of

1×10^{-4} M fluorescein (*Sigma Aldrich*) or 2',7'-dichlorofluoroscein (*Sigma Aldrich*, ~90%) to a total of 20 mL.

The fluorescent samples were all analysed using the both the commercial *Varian* Cary Eclipse spectrometer and HT fluorescence EEM spectrometer. For the commercial instrument, the excitation and emission step and slit sizes were set to 10 nm with a scan rate of 600 nm/min and a photomultiplier tube (PMT) voltage of 530 V. For samples containing dichlorofluorescein, a higher PMT voltage of 540 V was used as it had a slightly weaker fluorescence. For the HT fluorescence spectrometer, an integration time of 0.9 s was used with a Hadamard bit size of 5 (32 images) corresponding to a 28.8 s acquisition time per spectrum.

For the four sets of data, a separate PARAFAC analysis was conducted using the drEEM toolbox in MATLAB.[28, 29] This included the 9 fluorescein samples that ranged from a pH of 3.9 to 9.1 using both the conventional and HT fluorescence spectrometers. In addition, 11 dichlorofluorescein samples were analysed in a pH range of 1.82 to 9.08 using both spectrometers as it has a slightly lower pK_a of 5.2.[27] For all samples the same PARAFAC settings were used which include non-negativity constraints, random initialisation (ten times), and a convergence criterion of 10^{-10}.

10.3.2 Tea brewing

250 ml of a 2×10^{-5} M fluorescein and 2×10^{-5} M dichlorofluorescein solution were used for the brewing of tea. The solution was placed in a 500 ml round bottom flask and submerged in a water bath. A Heidolph MR Hei-Standard hot plate used with a feedback loop to keep the solution at constant temperatures of 50, to 85 °C in steps of 5 degrees. A Teflon stirrer was added at 250 rpm to ensure complete diffusion of tea. The tea bag, ~2.23 g, was added to the fluorophore-spiked solution after it achieved temperature equilibration.

The bifurcated fibre probe was submerged in the tea solution to measure spectra without the need for sample withdrawal. The HT spectrometer was used to acquire 5-bit (32 image) EEM spectra for the duration ~10 mins (20-30 spectra) while the tea compounds diffused into the fluorescein solution. In addition, an initial spectrum of the fluorophore-spiked solution at temperature, *T*, was acquired. PARAFAC analysis was used on all 180 EEM spectra.

10.4 Results and discussion

10.4.1 Fluorescein pH dependence

The EEM spectra of fluorescein and dichlorofluorescein at differing pH values using both the Hadamard and conventional EEM spectrometers are given in **Figure 10.3** and **Figure 10.4**, respectively. As observed, the fluorescence decreases as the pH of the solution decreases, due to the formation of the neutral compound in acidic conditions (**Figure 10.2**). Both the Hadamard and conventional fluorescence EEM spectrometers are able to determine the fluorescence features in the EEM spectrum. However, the Hadamard spectra are noticeably noisier. This is due to the less than optimal coupling of light into the fibre probe in addition to the inferior array detector used in the Ocean Optics spectrometer. Note that the Hadamard spectra only took approximately 30 s to acquire whereas the conventional setup took 30 minutes.

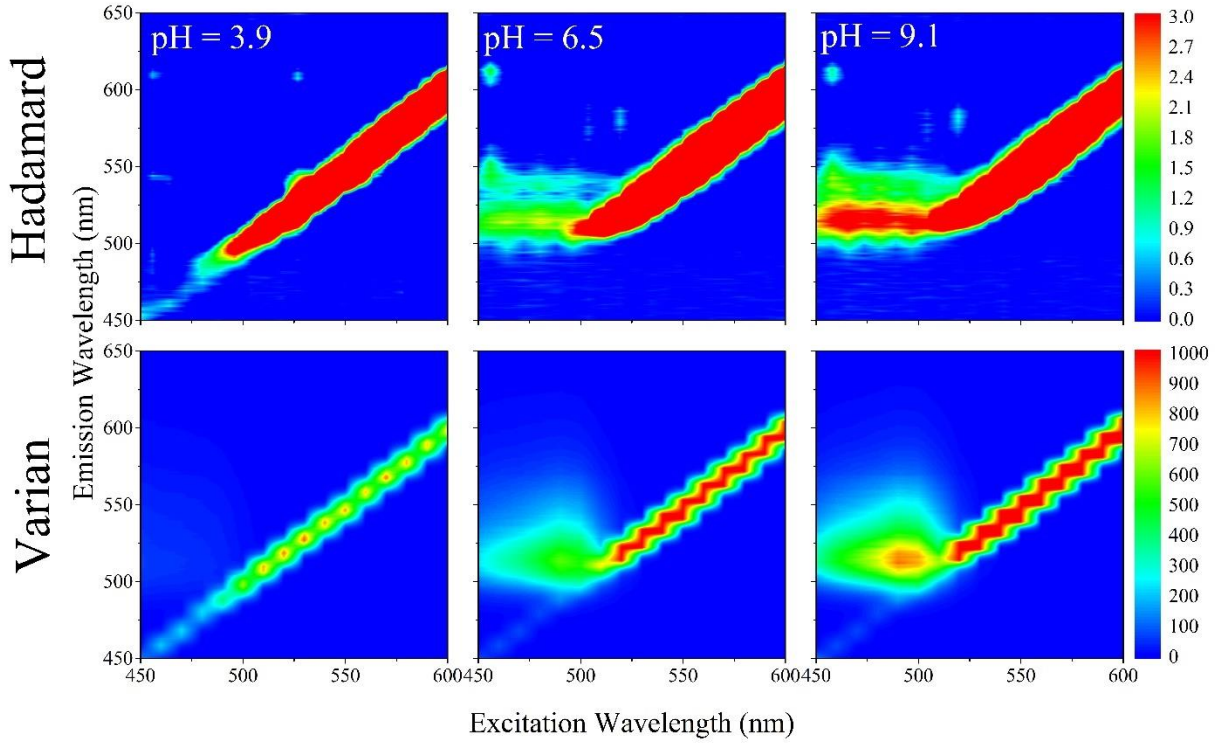

Figure 10.3: EEM spectra of fluorescein at a series of pH values using both the HT fluorescence spectrometer and the conventional *Varian* Cary Eclipse spectrometer. The colours from blue to red represent the intensity of the EEM spectra.

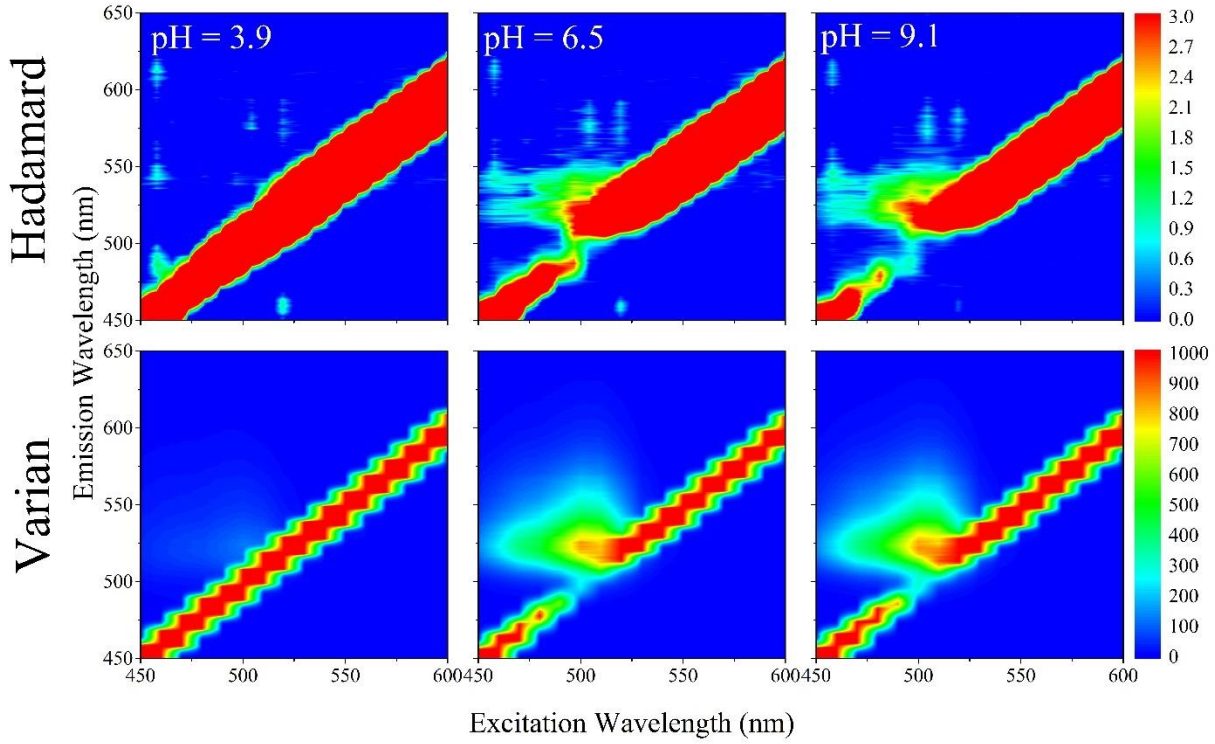

Figure 10.4: EEM spectra of dichlorofluorescein at a series of pH values using both the HT fluorescence spectrometer and the conventional *Varian* Cary Eclipse spectrometer. The colours from blue to red represent the intensity of the EEM spectra.

PARAFAC analysis was conducted on the four series of data, and the normalised component signatures are shown in **Figure 10.5**. From PARAFAC analysis it was determined that two components provided the best fit to all the data series. When analysing the HT-EEM spectra in most cases, only one of the components provided logical information representing the fluorescence of the dianion states of fluorescein and dichlorofluorescein. In most cases the second component only fit to spectral noise or artefacts. However, when the conventional *Varian* Cary Eclipse spectrometer was used, the second component corresponded to the fluorescence of the monoanion form of fluorescein, i.e. it had chemical significance.

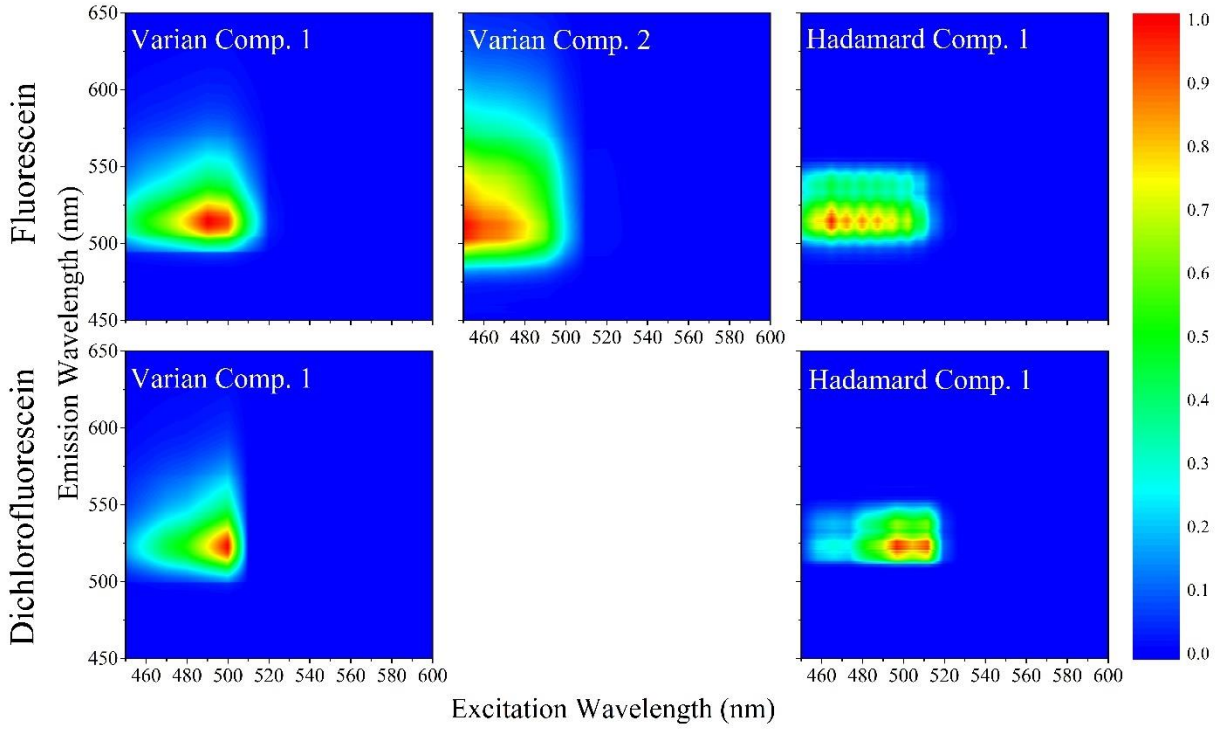

Figure 10.5: Normalised EEM signatures for the components determined using PARAFAC on the EEM spectra of fluorescein and dichlorofluorescein using both the HT EEM and the *Varian* Cary Eclipse spectrometers. Note that only the conventional *Varian* run on fluorescein obtained a reasonable second component whereas the other three series only obtained a single chemically meaningful component and a second one containing spectroscopic noise. The colours from blue to red represent the normalised intensity from 0 to 1, respectively.

The normalised scores of the fluorescein and dichlorofluorescein are given in **Figure 10.6**. As shown, all scores associated with component 1 (dianion state) show a decrease of fluorescence intensity as the solution becomes more acidic. In addition, both scans using the conventional and HT spectrometer show similar curves where the turning point marks the pKa value. The fluorescein fluorescence as a function of pH can be determined using,

$$F_{\mathrm{pH}} = F_{\max} - \left(\frac{F_{\max} - F_{\min}}{1 + 10^{(\mathrm{pH} - \mathrm{pKa})}} \right), \qquad \textbf{(10.3)}$$

where F_{max} and F_{min} are the maximum and minimum fluorescence intensities.[30, 31] A fit of the fluorescence scores from PARAFAC analysis to this equation will yield the pK_a of fluorescein and dichlorofluorescein, which are given in **Table 10.1**. As expected the pK_a's determined using the HT and conventional EEM methods agree with one another and with literature values.

Component 2 (monoanion state) for the conventional spectra on fluorescein shows a decrease of fluorescence intensity as the solution becomes more basic. This is due to the monoanionic state reacting to form the dianionic state in basic conditions. The curve can be fit with a rising logistic function similar to equation to (10.3),

$$F_{pH} = F_{min} + \left(\frac{F_{max} - F_{min}}{1+10^{(pH-pKa)}} \right). \qquad \textbf{(10.4)}$$

This equation allows the determination of the pK_a, which is given in **Table 10.1** and also agrees with the pK_a of fluorescein in the literature.

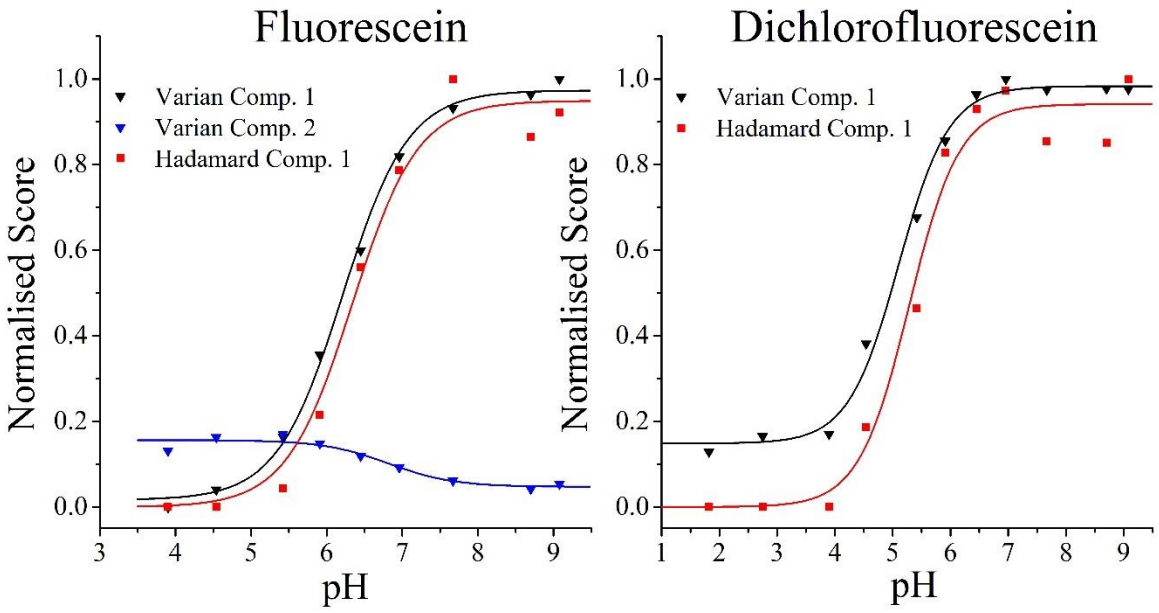

Figure 10.6: Normalised scores of the fluorescein and dichlorofluorescein determined using PARAFAC analysis on the four sets of spectra. The solid lines represent a fit through the data using a logistic fit (equation (10.3)) where the turning point gives the pKa.

Table 10.1: pK_a values of fluorescein and dichlorofluorescein determined by fitting the normalised scores in **Figure 10.6** to equations (10.3) and (10.4).

	Varian component 1	Varian component 2	Hadamard component 1	Literature,[20, 27, 32]
Fluorescein	6.2	6.8	6.3	6.7
Dichlorofluorescein	5.1		5.3	5.2

As shown in **Table 10.1** the Hadamard and Varian EEM methods are both able to produce pK_a values of fluorescein and dichlorofluorescein that match the literature values. As the HT spectrometer is able to track the fluorescence change of fluorescein, it is suitable to monitor the dissolution of acids in tea leaves.

10.4.2 Real-time analysis of tea acids' dissolution

EEM spectra were obtained for English breakfast tea as it diffused into water containing 2×10^{-5} M fluorescein and 2×10^{-5} M dichlorofluorescein. Select spectra of the spiked tea are shown as an example in **Figure 10.7**. As observed, the fluorescence decreases as the tea brews, due to the solution becoming more acidic.

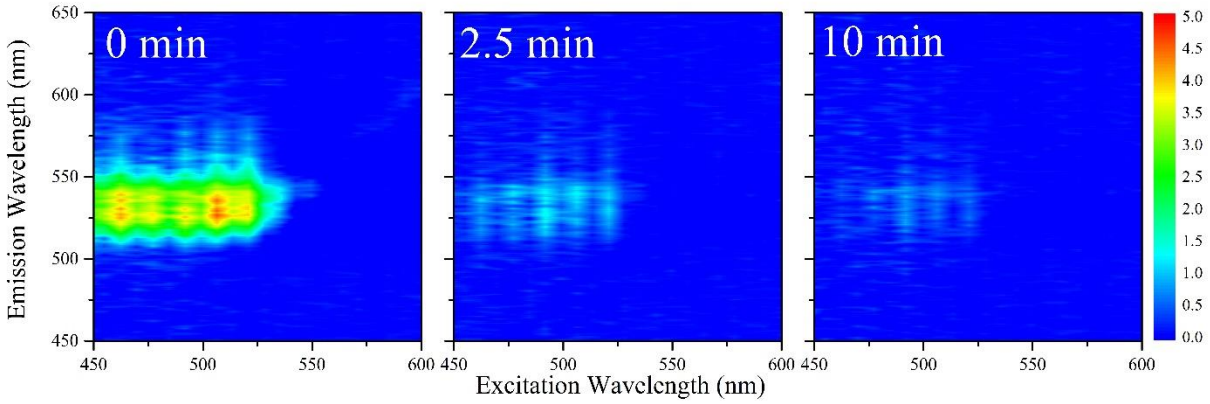

Figure 10.7: EEM spectra obtained using the HT fluorescence spectrometer on the diffusion of English breakfast tea in fluorescein and dichlorofluorescein spiked water at 85°C. The colours from blue to red represent the intensity from 0 to 5, respectively.

PARAFAC analysis on the 180 tea samples determined a two component fit best explained the data, resulting a core consistency and "percent explained" of 92.6% and 84.2%, respectively. Both the components are shown in **Figure 10.8**. Component 1 represents the fluorescence of fluorescein and component 2 represents the fluorescence of dichlorofluorescein (**Figure 10.5**). An odd feature is observed in component 2 as it seems to have peaks and troughs in alternating excitation wavelengths. This is likely caused by inner filter effects between fluorescein and dichlorofluorescein as their peaks lie close to one another. The scores determined using PARAFAC analysis for both components are given in **Figure 10.9(a)** and show that as the temperature increases from 50 to 85 °C the rate at which the dianion becomes the monoanion state also increases. Furthermore, it can be seen that the second component (dichlorofluorescein) has consistently lower scores, which is expected being that it has a lower quantum yield.

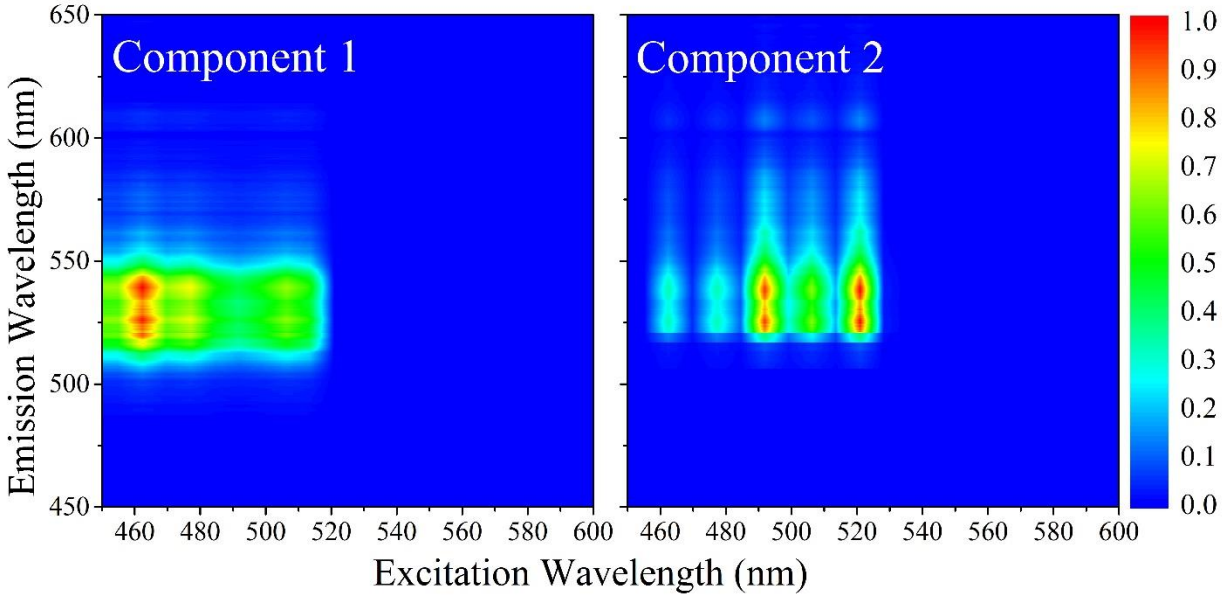

Figure 10.8: Normalised EEM signatures for the two components determined using PARAFAC analysis on the 180 EEM spectra obtained as English breakfast tea diffused into fluorophore-spiked water. The colours from blue to red represent the normalised intensity from 0 to 1, respectively.

Using equation (10.1), it is expected that the associated rate corresponds to the concentration of H^+ ions and not the normalised fluorescence of the tea itself. Therefore, a conversion of the scores to the concentration of H^+ ions using a rearranged version of equation (10.4) is required:

$$\mathrm{pH} = \mathrm{pKa} + \log\left(\frac{F_{\max} - F_{\min}}{F_{\max} - F_{\mathrm{pH}}} - 1\right)$$
$$\left[\mathrm{H}^+\right] = 10^{-\left(\mathrm{pKa}+\log\left(\frac{F_{\max}-F_{\min}}{F_{\max}-F_{\mathrm{pH}}}-1\right)\right)} \quad \textbf{(10.5)}$$

The concentration of H^+ ions determined through conversion of the normalised scores obtained using PARAFAC analysis are shown in **Figure 10.9(b)**. As expected, when the tea diffused into water the acidity of the solution increases. Satisfyingly, the fluorescein and dichlorofluorescein curves give similar values for the H^+ concentration. Therefore, to enhance the accuracy of the fit to the rate constants using equation (10.1), both component curves were fit simultaneously to the same rate law. As expected the rate of $[H^+]$ formation increases as the temperature of the water increases.

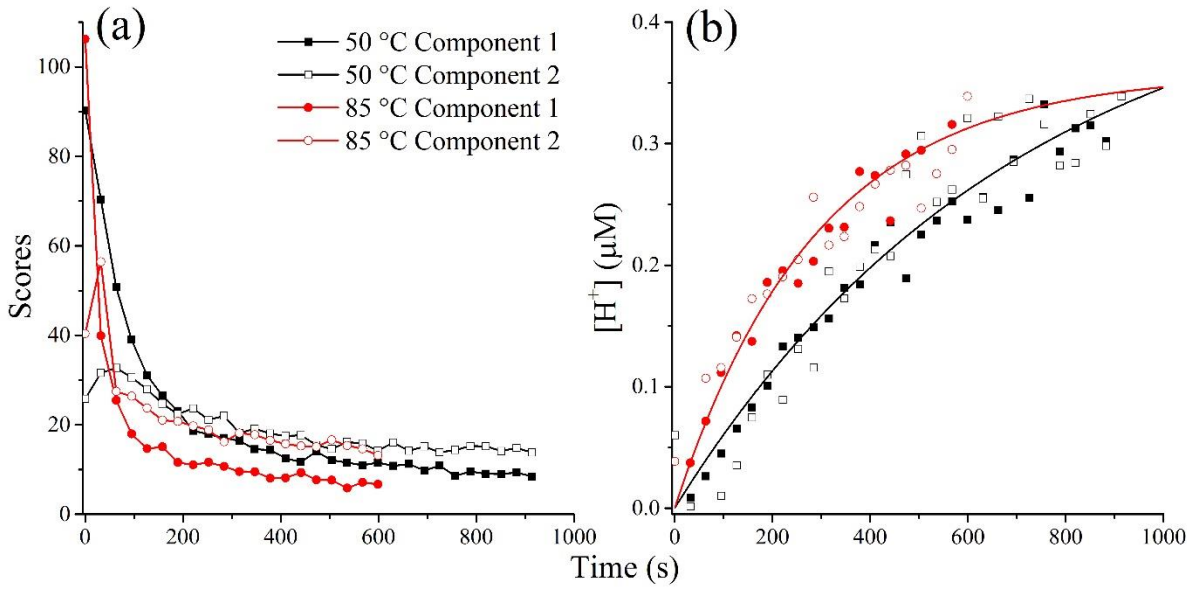

Figure 10.9: Scores of both components determined using PARAFAC analysis on the 180 EEM spectra obtained as English breakfast tea diffused into fluorophore spiked water. **(a)** shows the scores that were directly obtained from PARAFAC analysis. **(b)** gives the concentration of H^+ ions determined from the

normalised scores using equation (10.5). The solid line through the data shows a single exponential fit to both components using equation (10.1). In this figure only temperatures of 50 and 85 °C are given for clarity.

Fitting equation (10.1), to the concentration of H^+ ions gives the rate of the dissolution of acids in tea, *k*. The Arrhenius plot for is shown in **Figure 10.10**. A linear fit as calculated from equation (10.6) determined the activation energy for the dissolution tea acids of English breakfast tea in water to be 24.1 ± 0.2 $kJmol^{-1}$,

$$\ln(k) = \frac{-E_a}{RT} + \ln(A). \qquad \textbf{(10.6)}$$

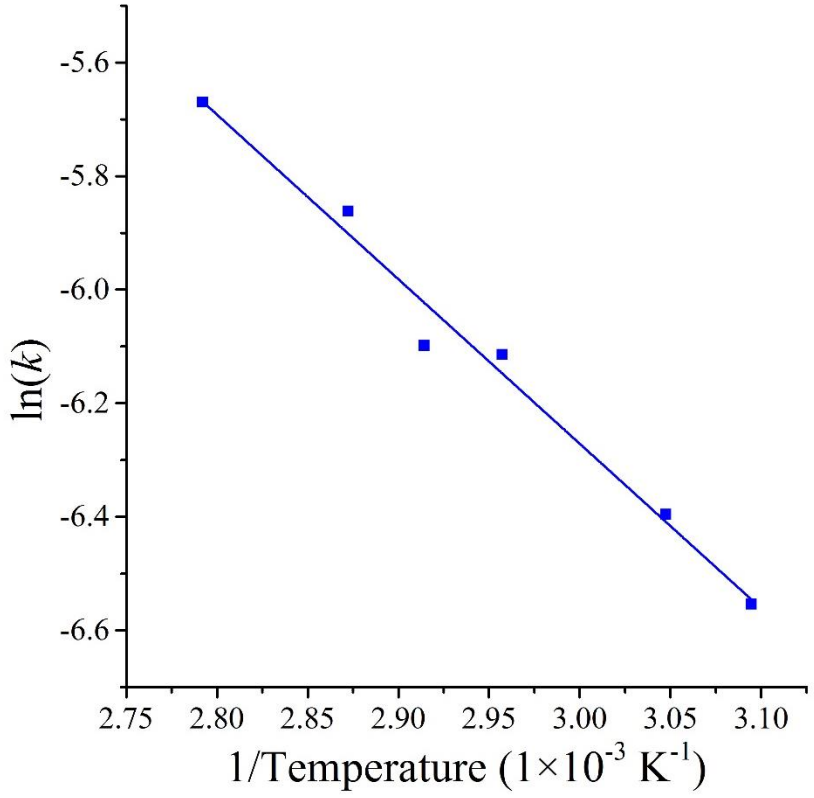

Figure 10.10: Arrhenius plot of English breakfast tea as it diffused into water. The slope of the linear fits gives $-E_a/R$ using equation (10.6). The rates used in this figure were obtained by fitting the both components to the same rate equation as in **Figure 10.9(b)**.

To my knowledge activation energies obtained for the dissolution of acids of tea have not been reported in the literature. However, activation energies for the dissolution of acids have been reported in the range of 14-68 $kJmol^{-1}$.[33-37] The activation energy obtained for the dissolution of English breakfast tea in water obtained using the HT EEM spectrometer with PARAFAC analysis lie in this range. There are also many reports for the infusion of tea compounds in water.[38-42] Jaganyi et al. determined that the activation energy of the infusion of caffeine from black Assam tea to be 43 $kJmol^{-1}$.[39] In addition, Price et al. determined that the activation energy for the infusion of flavanols from Sencha green tea to be 31.2 – 44.9 $kJmol^{-1}$.[40] The activation energy for English breakfast tea in water determined in this report is in fact a measure of the dissolution of compounds in tea — such as citrates and oxalates — that alter the pH. The pH decrease will then occur instantaneously when these molecules enter the solution where the infusion of flavanols and caffeine from tea will be a much slower process.[43]

10.5 Concluding remarks

To my knowledge, the above experiment marks the first time that EEM spectra were obtained *in situ*, and in real-time. Due to the multiplex advantages, the HT EEM fluorescence spectrometer is able to rapidly collect EEM spectra used to monitor the dissolution of tea in water. This is a process that occurs in a matter of minutes and is otherwise impossible to monitor in real time using conventional EEM spectrometers, where a single scan takes ≥30 mins. We showed that with the HT EEM spectrometer it is now possible to measure EEM spectra of a chemical system wherein fluorescence changes as it degrades or reacts. This means that the EEM method — which is advantageous in the analysis of complex mixtures — shown in Chapter 6 and Chapter 7 can be completed in real-time on systems that react much faster without the need for sample withdrawal. Using PARAFAC analysis on the EEM spectra obtained using the HT spectrometer provided activation energies of the dissolution of tea, which are consistent with those in the literature. Furthermore, as EEM spectra can be acquired more rapidly, the quantity of spectra can be increased — using the *Varian* Cary Eclipse to acquire 180 spectra would take 90 continuous hours. Having more spectra enhances the PARAFAC analysis technique's ability of finding the correct components.

Although the spectra obtained using the HT spectrometer are less than ideal, improvements to the spectrometer to enhance the SNR — such as replacing the detector — should greatly improve this method. For example, with an enhanced SNR, the HT EEM fluorescence spectrometer has the potential to analyse the diffusion of tea directly, without the need for a fluorescent dye. In addition, with a wider range of excitation wavelengths we will be able to use the EEM method to monitor other time-sensitive systems such as real-time lifetime evaluation of lubrication oil quality as well as that of other foodstuff such as wine, juices, and spirits. Finally, as the HT spectrometer uses a fibre probe that is simply submerged in the solution of interest, the analytical process is streamlined as it removes the need for sample withdrawal.

10.6 Bibliography

1. https://www.tea.co.uk/make-a-perfect-brew, **2016**.
2. M. E. Harbowy, D. A. Balentine, A. P. Davies and Y. Cai, Tea chemistry. *Critical Reviews in Plant Sciences* **1997,** *16*, 415-480.
3. L. N. Seetohul, M. Islam, W. T. O'Hare and Z. Ali, Discrimination of teas based on total luminescence spectroscopy and pattern recognition. *Journal of the Science of Food and Agriculture* **2006,** *86*, 2092–2098.
4. T. I. Mbata, L. U. Debiao and A. Saikia, Antibacterial activity of the crude extract of Chinese green tea (Camellia sinensis) on Listeria monocytogenes. *African Journal of Biotechnology* **2008,** *7*.
5. R. Curtis, in *The Backpacker's Field Manual*, Random House Publishing, Princeton University, 1999.
6. J. V. Higdon and B. Frei, Tea catechins and polyphenols: Health effects, metabolism, and antioxidant functions. *Critical Reviews in Food Science and Nutrition* **2003,** *43*, 89-143.
7. A. Rietveld and S. Wiseman, Antioxidant effects of tea: Evidence from human clinical trials. *The Journal of Nutrition* **2003,** *133*, 3285S-3292S.
8. H. N. Graham, Green tea composition, consumption, and polyphenol chemistry. *Preventive Medicine* **1992,** *21*, 334-350.
9. A. Nehlig, J.-L. Daval and G. Debry, Caffeine and the central nervous system: mechanisms of action, biochemical, metabolic and psychostimulant effects. *Brain Research Reviews* **1992,** *17*, 139-170.
10. G. Rusak, D. Komes, S. Likić, D. Horžić and M. Kovač, Phenolic content and antioxidative capacity of green and white tea extracts depending on extraction conditions and the solvent used. *Food Chemistry* **2008,** *110*, 852-858.
11. D. Del Rio, A. J. Stewart, W. Mullen, J. Burns, M. E. J. Lean, F. Brighenti and A. Crozier, HPLC-MS analysis of phenolic compounds and purine alkaloids in green and black tea. *Journal of Agricultural and Food Chemistry* **2004,** *52*, 2807-2815.
12. T. Miyazawa and K. Nakagawa, Structure-related emission spectrometric analysis of the chemiluminescence of catechins, theaflavins and anthocyanins. *Bioscience, Biotechnology, and Biochemistry* **1998,** *62*, 829-832.

13. L. N. Seetohul, S. M. Scott, W. T. O'Hare, Z. Ali and M. Islam, Discrimination of Sri Lankan black teas using fluorescence spectroscopy and linear discriminant analysis. *Journal of the Science of Food and Agriculture* **2013,** *93*, 2308–2314.
14. K.-M. Bark, J.-E. Yeom, J.-I. Yang, I.-J. Yang, C.-H. Park and H.-R. Park, Spectroscopic studies on the oxidation of catechin in aqueous solution. *Bulletin of the Korean Chemical Society* **2011,** *32*, 3443-3447.
15. D. Sarkar, S. Das and A. Pramanik, A solution spectroscopy study of tea polyphenol and cellulose: Effect of surfactants. *RSC Advances* **2014,** *4*, 36196.
16. D. Cho, W. L. Mattice, L. J. Porter and R. W. Hemingway, Use of the fluorescence quantum yield for the determination of the number-average molecular weight of polymers of epicatechin with 4β→8 interflavan bonds. *Polymer* **1989,** *30*, 1955-1958.
17. A. Simpson, L. Shaw and A. J. Smith, Tooth erosion: Tooth surface pH during drinking of black tea. *British Dental Journal* **2001,** *190*, 374-376.
18. A. P. Harrison, R. G. Cooper, M. A. Suliman and U. AlAlami, The efficacy of Karkadeh tea in controlling post-prandial blood glucose levels. *American Journal of Pharmacology and Toxicology* **2009,** *4*, 151-157.
19. P. G. Seybold, M. Gouterman and J. Callis, Calorimetric, photometric and lifetime determinations of fluorescence yields of fluorescein dyes. *Photochemistry and Photobiology* **1969,** *9*, 229-242.
20. M. M. Martin and L. Lindqvist, The pH dependence of fluorescein fluorescence. *Journal of Luminescence* **1975,** *10*, 381-390.
21. H. Meier, R. Petermann and J. Gerold, Bathochromic or hypsochromic effects via the extension of conjugation: a study of stilbenoid squaraines. *Chemical Communications* **1999**, 977-978.
22. M. Sauer, J. Hofkens and J. Enderlein, in *Handbook of Fluorescence Spectroscopy and Imaging*, Wiley-VCH Verlag GmbH & Co. KGaA, 2011, pp. 1-30.
23. M. M. Martin, Hydrogen-bond effects on radiationless electronic-transitions in xanthene dyes. *Chemical Physics Letters* **1975,** *35*, 105-111.
24. D. Magde, R. Wong and P. G. Seybold, Fluorescence quantum yields and their relation to lifetimes of rhodamine. *Photochemistry and Photobiology* **2002,** *75*, 327-334.
25. D. Magde, G. E. Rojas and P. G. Seybold, Solvent dependence of the fluorescence lifetimes of xanthene dyes. *Photochemistry and Photobiology* **1999,** *70*, 737-744.
26. L. Lindqvist and G. W. Lundeen, Radiationless transitions in xanthene dyes. *Journal of Chemical Physics* **1966,** *44*, 1711-&.
27. N. O. Mchedlov-Petrossyan, N. V. Salamanova, N. A. Vodolazkaya, Y. A. Gurina and V. I. Borodenko, A dibasic acid with reversed order of the stepwise ionization constants: 2,7-dichlorofluorescein in the ternary solvent mixture benzene–ethanol–water. *Journal of Physical Organic Chemistry* **2006,** *19*, 365-375.
28. R. Bro and H. A. L. Kiers, A new efficient method for determining the number of components in PARAFAC models. *Journal of Chemometrics* **2003,** *17*, 274-286.
29. K. R. Murphy, C. A. Stedmon, D. Graeber and R. Bro, Fluorescence spectroscopy and multi-way techniques. PARAFAC. *Analytical Methods* **2013,** *5*, 6557-6566.
30. B. Fu, J. Huang, D. Bai, Y. Xie, Y. Wang, S. Wang and X. Zhou, Label-free detection of pH based on the i-motif using an aggregation-caused quenching strategy. *Chemical Communications* **2015,** *51*, 16960-16963.
31. L.-N. Liu, H.-N. Su, S.-G. Yan, S.-M. Shao, B.-B. Xie, X.-L. Chen, X.-Y. Zhang, B.-C. Zhou and Y.-Z. Zhang, Probing the pH sensitivity of R-phycoerythrin: Investigations of active conformational and functional variation. *Biochimica et Biophysica Acta (BBA) - Bioenergetics* **2009,** *1787*, 939-946.
32. L. D. Lavis, T. J. Rutkoski and R. T. Raines, Tuning the pK_a of fluorescein to optimize binding assays. *Analytical Chemistry* **2007,** *79*, 6775-6782.

33. O. S. Ayanda, F. A. Adekola, A. A. Baba, O. S. Fatoki and B. J. Ximba, Comparative study of the kinetics of dissolution of laterite in some acidic media. *Journal of Minerals and Materials Characterization and Engineering* **2011,** *10*, 1457-1472.
34. C. E. Calmanovici, B. Gilot and C. Laguérie, Mechanism and kinetics for the dissolution of apatitic materials in acid solutions. *Brazilian Journal of Chemical Engineering* **1997,** *14*.
35. W. E. Kline and H. S. Fogler, Dissolution kinetics: Catalysis by strong acids. *Journal of Colloid and Interface Science* **1981,** *82*, 93-102.
36. K. Lund, H. S. Fogler, C. C. McCune and J. W. Ault, Acidization—II. The dissolution of calcite in hydrochloric acid. *Chemical Engineering Science* **1975,** *30*, 825-835.
37. P. Ptáček, M. Nosková, J. Brandštetr, F. Šoukal and T. Opravil, Mechanism and kinetics of wollastonite fibre dissolution in the aqueous solution of acetic acid. *Powder Technology* **2011,** *206*, 338-344.
38. D. Jaganyi and R. D. Price, Kinetics of tea infusion: The effect of the manufacturing process on the rate of extraction of caffeine. *Food Chemistry* **1999,** *64*, 27-31.
39. D. Jaganyi and S. Mdletshe, Kinetics of tea infusion. Part 2: The effect of tea-bag material on the rate and temperature dependence of caffeine extraction from black Assam tea. *Food Chemistry* **2000,** *70*, 163-165.
40. W. E. Price and J. C. Spitzer, The kinetics of extraction of individual flavanols and caffeine from a Japanese green tea (Sen Cha Uji Tsuyu) as a function of temperature. *Food Chemistry* **1994,** *50*, 19-23.
41. D.-J. Yang, C.-C. Hu and J.-T. Lin, Kinetics of short-time tea infusion using a diffusion model. *Chung Shan Medical Journal* **2014,** *25*, 31-39.
42. Y. Komatsu, S. Suematsu, Y. Hisanobu, H. Saigo, R. Matsuda and K. Hara, Effects of pH and temperature on reaction kinetics of catechins in green tea infusion. *Bioscience, Biotechnology, and Biochemistry* **1993,** *57*, 907-910.
43. M. Boero, T. Ikeshoji and K. Terakura, Density and temperature dependence of proton diffusion in water: A first-principles molecular dynamics study. *ChemPhysChem* **2005,** *6*, 1775-1779.

Chapter 11

Conclusions and Future Directions

This chapter highlights the work presented in this thesis on the development of optical systems for measuring refractive index, absorption, and fluorescence. It includes a summary of each project in this thesis, and provides overall conclusions and possible future directions of the projects involved.

11.1 Thesis summary

In this thesis, multiple optical techniques used for chemical sensing are presented. This included refractive index measurements using an in-fibre hollow-core photonic crystal fibre (HC-PCF) interferometer, absorption analysis using an amplified fibre-loop cavity ring-down (FLCRDS) setup and fluorescence measurements in the form of excitation emission matrix (EEM) spectra. All of the optical chemical sensing platforms described utilise the benefits of optical fibres, which allow for the detection of analytes in small volumes resulting in cheaper smaller instruments that are applicable for on-line field sensing.

The in-fibre HC-PCF interferometer shown in Chapter 3 was used to determine the polarisability of nine gases from the observed phase-shift at different pressures.[1] There have been hundreds of examples of simple in-fibre interferometers published in the literature to determine the change of the refractive index of liquids including mainly sucrose solutions.[2-6] The instrument presented in this thesis was quick to construct, simple to use, and only required a rudimentary interpretation of the interferograms using Fourier transform (FT) phase analysis. HC-PCFs confine light within the hollow core using the photonic band gap effect.[7] As the light propagates in the hollow core, HC-PCFs are an ideal absorption cell to be used for gas sensing as the light-matter interaction is very strong.[8] Additionally, using the HC-PCF as a sample cell allows the setup to be uniquely suited to measure the refractive index of small gas volumes of about a microliter (1.2 μL in our case).

When light is coupled from a single mode fibre (SMF) into the PCF, multiple PCF guiding modes are populated, which act as separate arms of a Mach-Zehnder interferometer. When the light was recombined at the second SMF an interferogram was produced and the fringes shifted to longer wavelengths as the pressure of the gas within the holes increased. This phase shift was further exacerbated when the gas in the holes was more polarisable. The modes that propagated along the PCF, recombined, and thus contributed to the interferogram, were calculated using an eigensolver analysis program. Using this we found that the beating co-propagating modes were two low-lying core modes with different phase indices. Despite the modes having a similar phase sensitivity with pressure giving a sensitivity value of only $f = 0.0078$, which is far from the optimal $f = 1$, our simple design is able to outperform nearly all existing in-fibre interferometers allowing us to measure the refractive index of several microliter-sized gas samples with an accuracy of better than 1 ppm.

The amplified FLCRDS experiment shown in Chapter 4 is also suited for very small volumes of samples. In our experiment the amplified FL-CRDS method was used to detect picolitre volumes of liquid alkynes down to 19% v/v in dodecane at a weak overtone band in the near infrared (NIR). The same setup had been previously used to detect acetylene using the weak P(13) line of the $\nu_1+\nu_3$ combination band down to concentrations of 50 ppm.[9] The amplified FLCRDS setup used for these measurements was designed based on the work by Stewart et al. and compensated for the additional losses in a fibre loop cavity by introducing a gain element such as an erbium doped fibre amplifier (EDFA).[10, 11] In this thesis, I demonstrated how the amplified FLCRDS setup could be used for chemical analysis. The setup used a two-loop system based on gain clamping to provide improved stability with a high sensitivity. The measurements highlight the versatility of the amplified FLCRDS technique to detect both liquids and gases in a spectral region of very weak absorption.

The fluorescence excitation emission matrix spectroscopy (EEMS) degradation studies shown in Chapter 6 and Chapter 7, show the versatility of EEMS as an analytical tool for kinetic analysis.[12, 13] The lubrication oil degradation studies built on earlier work by Omrani et al. and compared the fluorescence EEMS results with the linear sweep voltammetry (LSV) ASTM standard known as remaining useful lifetime evaluation routine (RULER).[14, 15] In this work, jet turbine oil was artificially aged under reflux at temperatures typical to a jet turbine engine. Samples were withdrawn at increasing time intervals for subsequent analysis by EEMS and RULER. EEM spectra were acquired for all samples and parallel factor (PARAFAC) analysis, a multivariate analysis technique, was run on all the 157 spectra. The PARAFAC analysis yielded two components within the spectra, which corresponded to the antioxidant phenyl-α-naphthylamine (PAN) and its dimer. The scores were fit to a simple kinetic model, which provided rate constants that were then used to determine activation energies. The comparative analysis of the LSV by RULER and fluorescence EEMS indicated that the total antioxidant concentrations obtained by both methods agreed very well. We also showed that EEMS has two noticeable advantages over the ASTM standard. First, it provides information on the chemical identity of the lubricants and thus is possible to generate a thorough understanding of the reaction kinetics involved as the oil degrades. Second, without the need for sample preparation, fluorescence EEMS is amenable for real-time, on-line measurements.

The fluorescence EEMS method was also applied to determine the stability of a scintillator solution under oxidative, thermal, and photochemical stress used by the Sudbury Neutrino Observatory (SNO) in an experiment to detect neutrinoless double beta decay.[16] For this experiment, the scintillator must remain functional over its experimental lifetime of ~7 years. Replica scintillator solutions were artificially aged at elevated temperatures in the presence of oxygen or under an inert atmosphere. Additional experiments were also performed to evaluate the effects from exposure to ultraviolet (UV) radiation.[13] As with the lubrication oil studies, samples were withdrawn in increasing time intervals and EEM spectra were obtained for all samples. Each EEM spectrum was obtained using a custom made bifurcated fibre probe that was simply

submerged directly into the sample without any prior sample preparation (other than the artificial ageing). PARAFAC analysis was performed on all 101 EEM spectra, which determined that there were three distinct components. The first and second components corresponded to the fluorescence of the scintillator compounds 2,5-diphenyloxazole (PPO) and bis(2-methylstyryl)benzene (bis-MSB) and the third component was attributed to dimers and oligomers formed as the solution was aged. In these studies, it was found that the presence of oxygen was detrimental to the scintillator solution and the level of O_2 must be kept below 24 ppm_v in the headspace (or a dissolved amount of 7.1 ppb_w) to ensure the solution remains 90% fluorescent over the 7 years. Additionally, we found that after purging the scintillator with purified N_2, and keeping the SNO+ scintillator solution under inert gas, the solution is expected to remain usable for much longer than 7 years. Further studies involving photo-degradation show that measures must be taken to ensure that the concentration of UV photons in the vessel remains lower than $0.138 \pm 0.009 \times 10^{-11}$ photonmol L^{-1}. The degradation study of the SNO+ scintillator solution highlights the precautions required for the SNO+ experiment to ensure the solution remains useable for the full experimental 7-year duration. These steps have been adapted in the liquid handling strategy and procedures for SNO+ experiment. All containers involved in the handling of the SNO+ scintillator solution such as filling tanker trucks, storage vessels, pipes and the SNO+ detector will be purged with purified N_2 and the scintillator will be stored in dark vessels. This preliminary study into the stability of the SNO+ scintillator solution highlights the requirements to ensure the longevity of the ~780 tonne liquid to prevent economic and environmental loss and ensure the post-experiment resale value of the compounds used. Since the solutions in our study did not contain tellurium, we expect that a similar study will have to be conducted in the future on the finalised SNO+ scintillator to investigate the oxidative, thermal and photochemical stability of the tellurium complex.

Both studies, on lubricants and on scintillator liquids, used EEM spectroscopy and involved offline spectral acquisition. Each EEM spectrum had an acquisition time of ~30 mins, which meant that offline sample

analysis was required. The solutions were artificially aged and samples were withdrawn for subsequent analysis. It became apparent that conventional EEM techniques are not ideal for such kinetic measurements, as they are much too slow, cannot be easily implemented for direct on-line and real-time sample analysis, and require a skilled worker to acquire and analyse the samples. Therefore, a method described in Chapter 9 in this thesis, utilises wavelength division multiplexing (WDM) to acquire EEM spectra at a much faster rate. Each excitation wavelength is encoded with a distinct binary Hadamard frequency using an array of excitation masks displayed on a digital micromirror array (DMA). The encoded excitation light is coupled into a bifurcated fibre probe and used to excite the sample. The fluorescence spectrum of the sample then depends on the excitation wavelengths that pass through each Hadamard excitation mask. Each Hadamard mask is used in sequence to generate an array of emission spectra that correspond to the modulation of the excitation light. The true EEM is then obtained through a simple matrix multiplication with the weighted inverse of the Hadamard matrix used to generate the excitation masks. This process can be done in a matter of seconds as compared to the double slit spectrometer that takes ~1 hour to produce a spectrum with the same resolution. A "first generation" instrument was built as a proof-of-principle and was shown to acquire the EEM spectra of sulforhodamine in ethanol ~120 times faster than using the conventional *Varian* Cary Eclipse spectrometer.

The same spectrometer was also used to monitor the dissolution of acid as tea was brewed in water as was shown in Chapter 10 in this thesis. As tea brews in the order of a few minutes, this was a great example to highlight the application of the Hadamard transform (HT) EEM spectrometer for monitoring a process in real time. To measure this process, water was spiked with a combination of pH sensitive dyes, fluorescein and dichlorofluorescein, which both show quenched fluorescence as the solution becomes acidic. The HT EEM spectrometer was able to follow the dissolution process during this time by acquiring an EEM spectrum every 30 s, a task that is impossible for the conventional spectrometer. Obviously, this process

can be done using a single excitation wavelength or a simple pH probe but it does highlight the HT EEM spectrometer's ability of monitoring kinetic processes in real-time.

11.2 Overall conclusions

This thesis described a multitude of optical techniques used for chemical sensing involving the life, death, and rebirth of a photon. Optical techniques are fast, sensitive, and non-destructive methods that can be used to detect chemical analytes. Furthermore, optical techniques can be used to monitor chemical reactions, measure their kinetics, and obtain thermodynamic information about a system. In addition to simply being used for the detection of analytes, optical spectroscopy can be used to investigate the fundamental (quantum) properties of molecules. The optical methods included in this thesis for chemical detection were based on refractive index, absorption and fluorescence measurements. Being optical, these techniques can all be modified for use with optical fibres to allow for sensing in inaccessible sites, over large distances, in strong magnetic fields and in harsh environments. Additionally, optical fibres allow these techniques to be made smaller, cheaper and more portable, which is essential for on-line field measurements. The techniques involved in this thesis all used optical fibres to guide the light to and from the chemical analyte used for sensing. These include, an in-fibre HC-PCF interferometer used for gas sensing, a double fibre loop amplified CRDS setup used to measure liquids, and a front face bifurcated fibre probe for fluorescence EEM spectroscopy. These techniques all involve small and relatively inexpensive components and can be easily modified and packaged for commercial field sensing applications.

The work discussed in this thesis, highlights the strategies of developing chemical sensing methods used to detect and understand complex systems. Additionally, I present the development of a smaller faster instrument for measuring fluorescence EEM spectra in real-time and on-line with zero prior sample preparation. Both these developments can be combined to design a suitable instrument for field measurements of complex samples. This device could have a large number of possible applications ranging from environmental sensing such as monitoring the levels of dissolved organic matter in our waterways,

product control and determining the quality of the product as it is made on-line in a factory, and ensuring the correct functioning of machinery through real-time remaining useful life measurements. This product will be invaluable as it will reduce cost, improve yield and potentially save lives.

11.3 Future directions

The optical techniques described in this thesis are all useful methods for chemical detection. However, significant improvements can be applied to each technique to enhance their sensitivities, detection limits and applicability for on-line sample detection. In the following section I present future improvements to the current optical setups, which can act as a guide for future students to continue on this work. Doing the following improvements should improve each optical method towards commercial products for on-line chemical sensing.

As was shown in this thesis, the in-fibre PCF interferometer is limited in sensitivity by its bending radius of 30 mm. Simulations of the modes that beat within the fibre, predict that the sensitivity should be enhanced if the PCF segment is made linear. This is in agreement with preliminary studies done by Camiel van Hoorn, which showed an enhanced phase-shift response when a linear PCF was filled with 2% acetylene in Helium.[17] Therefore, future work should be done to construct a linear in-fibre PCF interferometer. Doing this should enhance the sensitivity by at least a factor of 10 to $f \approx 0.1$.

A further approach to enhance the sensitivity of the in-fibre HC-PCF interferometer is to couple light between two modes in which one travels exclusively through the sample and the other one travels through material that is not affected by the sample medium. Such a setup would require a balanced in-fibre Mach-Zehnder interferometer consisting of one mode traveling entirely through the hollow core, which also contains the sample gas, and beating against a single second mode that propagates through, for example, a solid glass core contained in the same fibre. To our knowledge such a fibre does not yet exist. An alternative approach to enhance the sensitivity is to couple the core and cladding modes together using long period

gratings.[18] Beating between core and cladding modes within a HC-PCF will produce a larger effective refractive index difference than coupling between two core modes. Cladding modes guide a larger proportion of light through the glass of the PCF so they will have smaller interaction volumes with the sample gas compared with the core modes. Additionally, further improvements to the sensitivity can be done by sealing the cladding holes so that the cladding modes do not interact with the detection gas.[19]

An interesting direction of the project will be to investigate the temperature effects of the in-fibre HC-PCF interferometer. This will evaluate the interferometers usefulness to monitor gases over a range of temperatures and thus have potential for commercial applications. Alternatively, one can investigate the interferometers sensitivity in the visible region and investigate whether similar interference effects can be observed.

The PCF interferometer can be further utilised by combining it with the amplified FLCRDS setup. The HC-PCF can be inserted into the fibre loop and used as a gas cell. This experiment may allow for trace gas sensing in a small volume due to the enhanced optical pathlength from FLCRDS. However, combining the HC-PCF into the CRDS system will likely scramble the interferometric information only allowing for the detection of gases through absorption. Alternatively, the CRDS system can be adapted for cavity ring-down polarimetry (CRDP) to measure circular birefringence and circular dichroism of chiral analytes.[20, 21] The FLCRDS system can be used for CRDP by replacing all the fibres with polarisation maintaining fibres to control the polarisation of the circulating light. CRDP has been conducted using free space optics but to my knowledge has not been attempted for measurement within a fibre loop.

Regarding the EEM degradation studies, future studies can further explore and understand the degradation of lubrication oil. Engines contain heated moving metal surfaces, which likely hasten the degradation process. Therefore, I propose to construct a rig that better represents a working engine rather than a simple reflux apparatus. This rig will pump lubrication oil from a sump through a heated section containing metal

shavings and is circulated back towards the sump. The fibre probe will then be placed into the sump oil and used for continuous EEM acquisition. The RUL can then be determined in real time as the oil degrades. Additionally, the quantity and morphology of metal shavings can be investigated for their effects on the degradation rate. To achieve this however, one needs a faster method of acquiring EEM spectra than is feasibly possible with the commercial *Varian* Cary Eclipse spectrometer. An obvious solution to this is to employ the HT EEM spectrometer presented in this thesis. Being that the current HT EEM setup is wavelength limited to 450 nm, further work will be required to shift the wavelengths further into the UV so that the HT EEM spectrometer can be used to monitor the antioxidants within the lubrication oil. This can be achieved by replacing the white light emitting diode (LED) array with a UV source such as a deuterium or xenon flash lamp. Furthermore, the DMA window limits the light down to 350 nm and thus replacing the anti-reflection coated window with UV transparent quartz will allow further excitation into the UV. Applying these changes to the HT EEM setup will then allow for the on-line monitoring of the degradation of lubrication oil in real time. Additionally, as the HT EEM spectrometer is able to acquire EEM spectra at a much faster rate, the temperature effect on the degradation can be more extensively evaluated to allow for a more thorough analysis of the reaction kinetics. Further temperature studies will need to be conducted to evaluate the fibre probes robustness with regards to thermal stress. However, if the probe is submerged in the sump of the engine, which is much cooler than the engine, this may not be required. Additionally, it will be interesting to monitor the lubricity of the oil in parallel with the RUL measurements obtained from the HT EEM spectra. This will generate correlations between the RUL and lubricity of the oil. With these studies a RUL fluorescence signal intensity value could be determined as a threshold, and when exceeded an indicator could be used to tell the operator an oil change is required. Additionally, further investigations can be conducted to evaluate whether spiking additional antioxidants into the oil will prolong the oil's RUL.

For the SNO+ scintillator degradation research, an interesting future direction will be to investigate the solutions stability at room temperature and check for any noticeable absorption after a number of months. This will further the studies usefulness and investigate whether there are separate mechanisms for degradation at lower temperatures typical to the mine in Sudbury. More importantly a future study would have to use a SNO+ scintillator that is loaded with ^{130}Te, since this might affect thermal, oxidative and photochemical stability.

The HT EEM spectrometer presented in this thesis can be further improved by replacing the USB4000 array spectrometer with one that is more sensitive and also does not have memory effects. This will enhance the acquired EEM spectra and allow the spectrometer to potentially monitor systems with weaker fluorescence such as tea directly. With this it should be possible to monitor the diffusion of the tea compounds into water in addition to the dissolution of acid. An alternative improvement to the HT EEM spectrometer will be to modulate both the excitation and emission light. This can be done by replacing the emission array spectrometer with a second DMA to encode the emission light. Alternatively, a cheaper approach would be to use the top half of the DMA for excitation and the bottom half for emission. This will apply the WDM advantages to both the excitation and emission light, and will allow for a photo multiplier tube (PMT) to be used as the detector. PMTs are much more sensitive and have a faster acquisition rate than charged coupled device (CCD) arrays, which will hasten the EEM spectral acquisition. Furthermore, the excitation or emission light can be modulated using a Fourier system as with Peng et al.[22]

The HT EEM spectrometer is not solely limited to monitoring the degradation of lubrication oil. With the faster acquisition rates, many other systems can be investigated, for example, the reaction of n-bromosuccsinimide or n-iodosuccinimide with fluorescein to form eosin or erythrosine respectively could be observed.[23] Additionally, the HT spectrometer could be used to monitor the diffusion of tea as it brews, oxidation of wine, adulteration of olive oils, and Förster resonance energy transfer. Furthermore, as the HT

EEM spectrometer is able to acquire EEM spectra in real time, it can be applied to measure the concentration of DOM in surface water, detect the presence of oil spills and even as a detector for high performance liquid chromatography (HPLC). This would allow for easier chemical characterisation between fluorescent compounds with similar elution times. Obviously, these are only a handful of examples and the investigation of many other systems are possible. Applying these improvements to the optical instruments described in this thesis will therefore, enhance their ability to be used for commercial on-line field sensors.

11.4 Bibliography

1. N. L. P. Andrews, R. Ross, D. Munzke, C. van Hoorn, A. Brzezinski, J. A. Barnes, O. Reich and H.-P. Loock, In-fiber Mach-Zehnder interferometer for gas refractive index measurements based on a hollow-core photonic crystal fiber. *Optics Express* **2016,** *24*, 14086.
2. X.-D. Wang and O. S. Wolfbeis, Fiber-optic chemical sensors and biosensors (2008–2012). *Analytical Chemistry* **2013,** *85*, 487-508.
3. X.-D. Wang and O. S. Wolfbeis, Fiber-optic chemical sensors and biosensors (2013–2015). *Analytical Chemistry* **2016,** *88*, 203-227.
4. J.-N. Wang and J.-L. Tang, Photonic crystal fiber Mach-Zehnder interferometer for refractive index sensing. *Sensors* **2012,** *12*, 2983-2995.
5. J. N. Dash and R. Jha, Temperature insensitive PCF interferometer coated with graphene oxide tip sensor. *IEEE Photonics Technology Letters* **2016,** *28*, 1006-1009.
6. Y.-S. Zhu, H.-W. Wang and Y.-C. Hsu, The measurement of sucrose concentration by two-tapered all-fiber Mach–Zehnder interferometer employing different coupling structures and manufacture processes. *Optical Review* **2016,** *23*, 662-677.
7. P. S. J. Russell, Photonic-crystal fibers. *Journal of Lightwave Technology* **2006,** *24*, 4729-4749.
8. J. Villatoro and J. Zubia, New perspectives in photonic crystal fibre sensors. *Optics & Laser Technology* **2016,** *78, Part A*, 67-75.
9. N. L. P. Andrews, J. Litman, D. Stroh, J. A. Barnes and H.-P. Loock, Near-infrared absorption detection in picolitre liquid volumes using amplified fibre loop ring-down detection. *Optical Fiber Technology* **2013,** *19*, 822-827.
10. G. Stewart, K. Atherton, H. Yu and B. Culshaw, An investigation of an optical fibre amplifier loop for intra-cavity and ring-down cavity loss measurements. *Measurement Science and Technology* **2001,** *12*, 843-849.
11. G. Stewart, K. Atherton and B. Culshaw, Cavity-enhanced spectroscopy in fiber cavities. *Optics Letters* **2004,** *29*, 442-444.
12. N. L. P. Andrews, J. Z. Fan, H. Omrani, A. Dudelzak and H.-P. Loock, Comparison of lubricant oil antioxidant analysis by fluorescence spectroscopy and linear sweep voltammetry. *Tribology International* **2016,** *94*, 279-287.
13. N. L. P. Andrews, J. Z. Fan, R. L. Forward, M. C. Chen and H.-P. Loock, Determination of the thermal, oxidative and photochemical degradation rates of scintillator liquid by fluorescence EEM spectroscopy. *Physical Chemistry Chemical Physics* **2017,** *19* (1), 73-81.

14. H. Omrani, A. E. Dudelzak, B. P. Hollebone and H.-P. Loock, Assessment of the oxidative stability of lubricant oil using fiber-coupled fluorescence excitation–emission matrix spectroscopy. *Analytica Chimica Acta* **2014,** *811*, 1-12.
15. R. E. Kauffman and W. E. Rhine, Development of a remaining useful life of a lubricant evaluation technique. Part I: Differential scanning calorimetric techniques. *Lubrication engineering* **1988,** *1*, 154-161.
16. M. C. Chen, The SNO liquid scintillator project. *Nuclear Physics B - Proceedings Supplements* **2005,** *145*, 65-68.
17. C. van Hoorn, *Chemical sensing using hollow-core photonic crystal fibres*, Queen's University, Kingston, Ontario, 2011.
18. Z. He, Y. Zhu, J. Kaňka and H. Du, Core-cladding mode coupling and recoupling in photonic crystal fiber for enhanced overlap of evanescent field using long-period gratings. *Optics Express* **2010,** *18*, 507-512.
19. L. Xiao, W. Jin, M. S. Demokan, H. L. Ho, Y. L. Hoo and C. Zhao, Fabrication of selective injection microstructured optical fibers with a conventional fusion splicer. *Optics Express* **2005,** *13*, 9014-9022.
20. T. Müller, K. B. Wiberg and P. H. Vaccaro, Cavity ring-down polarimetry (CRDP): A new scheme for probing circular birefringence and circular dichroism in the gas phase. *The Journal of Physical Chemistry A* **2000,** *104*, 5959-5968.
21. T. Müller, K. B. Wiberg, P. H. Vaccaro, J. R. Cheeseman and M. J. Frisch, Cavity ring-down polarimetry (CRDP): Theoretical and experimental characterization. *Journal of the Optical Society of America B* **2002,** *19*, 125-141.
22. L. Peng, J. A. Gardecki, B. E. Bouma and G. J. Tearney, Fourier fluorescence spectrometer for excitation emission matrix measurement. *Optics Express* **2008,** *16*, 10493.
23. A. L. Theodore,*United States Pat.*, US3111528 A, 1963.